THE UNIVERSITY *of* EDINBURGH

Filling the sensor gap: Applying UAS technology to land-use research

By

Simon Gibson-Poole

Doctor of Philosophy

Scotland's Rural College

And

The University of Edinburgh

2019

Declaration

I declare that this thesis has been composed by myself and has not been submitted in any previous application for a degree. The work described is my own except where stated otherwise.

Simon John Gibson-Poole

June 2019

Lay summary

The rapid development of unmanned aircraft systems (drones) has resulted in these small aircraft being much easier to operate, through the use of tablet computers or phones, allowing the aircraft to fly themselves. They can be bought as “ready to fly” for a price that is within reach of most people. Drones are potentially very useful tools for research and education as well as to farmers and people working in conservation and the environment, as they allow an overhead view of crops, field boundaries, forests and all manner of other types of land, and can fly over difficult terrain that would otherwise not be easy to access.

Drones usually only carry ordinary digital cameras, but recent photogrammetry techniques (being able to make measurements from photographs) have allowed the images captured by drones to be turned into orthomosaics (visual maps of the area surveyed) and as these techniques work in a similar way to which we see the world (through our stereoscopic vison) they can also be used to create height maps of the area surveyed, allowing the development of plants or other features to be measured.

In this study the author designed and built a drone, equipped it with two digital cameras, with one modified to capture near infra-red light (which we can normally not see) and used it to survey different trials of potatoes. The results indicate that drones are very useful tools for monitoring the development of potatoes and can detect the onset of disease. Their use would allow more information about the plants to be gathered that would lead to improvements in understanding the effects of treatments (fertiliser, pesticides etc.) that are normally applied to potato fields.

Further to this the drone was also tested experimentally to enable the mapping of invasive non-native species (non-native plants that have spread and taken over from native vegetation) and to assist with the identification of greenhouse gas emissions from two different types of land use (forestry and grasslands). Both of these experimental uses showed promise and indicate that drones equipped with digital cameras can be used for a variety of research and monitoring applications.

Abstract

Collecting data at ground level typically yields the most detailed information on a subject, however it is limited by the spatial extent that can be covered within a specific timeframe. Remote sensing from an aerial platform increases this spatial extent and the deployment of unmanned aircraft systems (UAS) can provide this ability directly to researchers at an affordable cost and at data resolutions that are very applicable for site specific surveys. Further to this, developments in photogrammetry software allow the creation of orthorectified spectral and structural data that can that can be classified via pixel or object-based analysis methods and applied to a wide variety of different land-use research areas. In this study a sensor package was created consisting of two off the shelf digital cameras, one un-modified and the other modified to be sensitive to near infra-red wavelengths of light. A multi-rotor aerial platform utilising an open source autopilot was assembled to enable data collection and a processing pipeline was devised to transform RAW camera imagery into georeferenced and orthorectified data, using computer vision software following the structure from motion (SfM) approach. This remote sensing tool was applied to a variety of land-use research study sites in central Scotland and Northern England with two main areas focused on. (1) The use of spectral and structural data for the detection of disease within a potato (*Solanum tuberosum L.*) crop revealed that UAS could be an effective tool for mapping the distribution of diseased plants. (2) Comparisons between aerial data and traditional manual assessments of a trial crop of potatoes revealed that the earliest stages of plant emergence could not be detected but later plant counts, and ground cover estimates correlated well, indicating that UAS could be an effective trials monitoring tool, giving extra structural data and potentially a more representative measure of canopy ground cover compared to traditional manual techniques. This study also showed results from experimental applications investigating the mapping of invasive non-native species and ways of enabling upscaling of greenhouse gas emissions from different land use types. Therefore, this study demonstrates that UAS equipped with basic imaging technology can be of use to a variety of land-use research areas and look set to become an invaluable remote sensing tool, which will improve further with the addition of calibrated multi-spectral sensor payloads, high precision global navigation satellite systems and relaxation in regulations governing their use.

Acknowledgements

Firstly, I would like to thank my wife Catherine for assisting me with occasional fieldwork, letting me off from doing any housework as deadlines approached and not complaining (too much) when I'm spending all my time doing this PhD. I would also like to thank my supervisor Dr Alistair Hamilton for his enthusiasm for the project (and getting me signed up for it in the first place), steering me in the right direction whenever I got lost and encouraging me when needed. I would also like to thank my other supervisors, Caroline Nichol and Bob Rees for supporting me when needed and giving advice and Mathew Williams, my advisor of studies, for being perpetually optimistic.

Many thanks must go to Tom Wade from Airborne Geosciences, for letting me use Samson (the computer) almost constantly over the years and for allowing me to "borrow" various bits of kit. Also, to the SRUC trials team, Alastair Drysdale and Douglas Goodall, whom I have bombarded with emails from time to time, but they have always had the time to give me guidance on the crops being grown. Likewise, to Brian Fenton and Roger Griffin-Walker, who have suffered my questions and told me quite a lot about potatoes. To the guys and girls at NERC GEF (Alan Hobbs, Colin Kay and Kyle Caparoso), thank you for helping me out with all things GNSS and to the NERC FSF guys (Christopher MacLellan and Alasdair MacArthur) and Elias Berra, thank you for your spectral assistance.

To my assistants, Jason Graham and Tom Flatman; thank you for helping me out and humping kit about in odd locations filled with either invasive species or potatoes, and to my Intern, Callum Tyler, who suffered my presence for quite some time and helped me to get that damned elusive Piksi to work. To all my fellow collaborators (you know who you are), thank you for giving me the opportunity to test the UAS in strange places, and thanks to Juliette Marrie, for always being positive (your thesis is next!) and Jakob Assmann for keeping me informed about artic shrubbery.

And finally, thanks must go to SRUC for funding this PhD and to the Scottish Funding Council Knowledge Exchange program, for providing me with the means to purchase the equipment and training I needed to complete this project.

Table of Contents

List of Figures

List of Tables

Chapter 1. Introduction

1.1 Definition of a UAS

Unmanned Aircraft Systems (UAS) are aircraft that are intended to be operated remotely and without a pilot on board. They are often termed in different ways, including Remotely Piloted Vehicles (RPV), Remotely Operated Aircraft (ROA), Unmanned Aerial Vehicles (UAV), Remotely Piloted Aircraft Systems (RPAS), or just simply drones, which is a term often used by the media (Colomina & Molina, 2014). RPAS is the latest term being used by the International Civil Aviation Organization (ICAO) to indicate that unmanned vehicles are still controlled by people (ICAO, 2018), however the UK's Civil Aviation Authority (CAA) still currently refer to the shorter term of UAS, of which an Unmanned Aircraft (UA), is part of and defined as:

"An aircraft which is intended to operate with no human pilot on board, as part of an Unmanned Aircraft System. Moreover a UA:

- *is capable of sustained flight by aerodynamic means;*
- *is remotely piloted or capable of autonomous operation;*
- *is reusable; and*
- *is not classified as a guided weapon or similar one-shot device designed for the delivery of munitions."* (CAA CAP 722, 2015)

A UAS is further defined by the CAA as:

"An Unmanned Aircraft System (UAS) comprises individual 'System Elements' consisting of the Unmanned Aircraft (UA) and any other System Elements necessary to enable flight, such as a Remote Pilot Station, Communication Link and Launch and Recovery Element. There may be multiple UAs, RPS or Launch and Recovery Elements within a UAS." (CAA CAP 722, 2015)

1.2 Remote sensing from an aerial platform

Remote sensing (RS) is the science (and art) of gathering information about an object from a distance (Aber, 2010), through observing its radiative qualities within the electromagnetic spectrum. This can be achieved through the use of a wide variety of sensors (e.g. cameras or spectrometers), deployed from numerous types of platform (e.g. aircraft, satellites, or just a human). The sensors can be passive (e.g. digital cameras), relying on the reflective properties of objects at the current environmental conditions (e.g. the amount of sunlight), or they can be active (e.g. LIDAR; Light Detection and Ranging), where electromagnetic pulses are emitted by the sensor and the reflections of those pulses are recorded (Colomina & Molina, 2014).

RS from an aerial viewpoint essentially started in 1858 by the French photographer and balloonist, Gaspar Felix Tournachon, known as "Nadar", who captured scenes of a French village from a hot air balloon 80 m up in the air (figure 1-1a; Rees, 2013). This naturally evolved into the taking of images from aircraft to produce maps, with numerous developments from the First World War onwards (Stichelbaut, 2006; figure 1-1b), before the development of space-based imaging from satellites orbiting the earth, resulting in the Landsat series of satellites (from 1972; figure 1-1c). These were the first satellites designed specifically to monitor the Earth's surface for civilian purposes and used a multi-spectral imager to captured images covering narrow bands of the electromagnetic spectrum (Bernstein, 1976), allowing a wealth of research possibilities.

Figure 1-1: (A) "Nadar élevant la Photographie à la hauteur de l'Art" (Nadar elevating Photography to Art). Lithograph by Honoré Daumier, appearing in Le Boulevard, May 25, 1863 (Brooklyn Museum, 2004); (B) A sergeant of the Royal Flying Corps demonstrates a C type aerial reconnaissance camera fixed to the fuselage of a BE2c aircraft, 1916 (© IWM (Q 33850); IWM, 2018); (C) a sketch of the Landsat 1 satellite (NASA, 2018).

1.3 A brief history of UAS

Cook (2007) outlines the history of development of UAS, which unsurprisingly started life as a tool to aid in warfare. Essentially the first concepts of UAS were developed shortly after manned flight, as remote control of planes was achieved during the First World War (around 1916) leading to the development of remotely operated weapons (Cook, 2007) such as Archibald Montgomery Low's "Ruston Proctor Aerial Target" (Hardin & Jensen, 2011). These developments continued into the Second World War, with the Germans developing V-1 flying bomb, and continuing since then. Their development is still seen as being key for both remote reconnaissance and delivery of guided munitions, as they only cost a fraction of a

manned aircraft and can therefore be used in more hostile conditions without the concern of having pilots killed or captured should the aircraft be shot down (Cook, 2007).

From the late nineteen-seventies, some researchers saw the potential in using this technology for remote sensing (Colomina & Molina, 2014), however the explosion in use of UAS for civilian purposes has occurred over the last decade, with multiple types of UAS being developed and used (figure 1-2). This was due to advances in the miniaturisation of the electronic components required to operate UAS, the battery technology used to power many of them, the low cost of effective airframes and the availability of low-powered micro radio transmitters and has led to an increase in the use of UAS for numerous different research and commercial activities (Chao *et al.* 2010; Colomina & Molina, 2014; Chabot, 2018).

Figure 1-2: Example UAS of the three main types of UAS that have been used for remote sensing over the last decade; (A) a helicopter UAS (RPH2; Subaru, Tokyo, Japan) used to study riverbeds (Nagai et al., 2007); (B) A multi-rotor UAS (custom built) used to study heathlands (Gademer et al. 2010; (C) A fixed wing UAS (custom built) used to study tropical wildlife (Koh & Wich, 2012).

1.4 UAS and the regulations governing their use

There are many different types of UAS, including balloons, kites, blimps, fixed wing aircraft, helicopters and multi-rotor aircraft. They can vary in both size and capability but from a regulatory standpoint it is their mass that is important, and within the United Kingdom (UK) they classified into three broad categories (table 1-1). Regulations governing the use of UAS differ around the world (with some countries currently not having any regulations concerning their use), but for the purposes of this project only the UK regulations are of concern.

Table 1-1: Mass categories for UAS and to which regulatory body they apply to. (SUA are small unmanned aircraft and EASA is the European Aviation Safety Agency)

Mass Category	Mass (kg)	Responsible Regulatory Body
SUA	0-20	National Aviation Authority
Light UAS	> 20 to 150	National Aviation Authority
UAS	> 150	EASA

The full regulations covering the operation of full size UAS and light UAS are out with the scope of this project as they require airworthiness certificates (CAA CAP 722, 2015), making the aircraft themselves essentially as expensive (or more so) to operate as conventional manned aircraft (Everaerts, 2009). They include aircraft such as Global Hawk (Northrop Grumman, Virginia, USA; figure 1-3a), a full size UAS with a 24-hour endurance and has been used for a variety of research purposes including by NASA to monitor hurricanes at very high altitudes (Braun, 2016). In contrast to this, Hodgson *et al.* (2013) used a ScanEagle (Insitu Inc., Washington, USA; an SUA that also has a 24-hour endurance; figure 1-3b) to monitor marine mammals off the coast of Australia, but from a much lower altitude.

Figure 1-3: (A) NASA's Global Hawk being readied for deployment to track Hurricane Mathew in 2016 (Hughes, 2016); (B) a Boeing Insitu ScanEagle entangled within in its arresting cable used for landing (Hodgson et al., 2013); The size of both aircraft can be seen in relation to the ground support crew.

The regulations regarding small unmanned aircraft (which will be termed as UAS from this point onwards) are laid out in The Air Navigation Order 2016 (ANO2016) and the very recently released The Air Navigation (Amendment) Order 2018 (ANAO2018), to ensure that UAS cannot interfere with more conventional flights and are not a danger to the general public. However, these restrictions cause some issues for UAS operators as they limit the way in which the UAS can be used,

primarily as the UA must be within un-aided visual sight of the operator, meaning that missions must be planned to take account for this.

The main articles within the amended ANO2016, are 241, 94 (and 94 A~G) and 95, which essentially restrict the use of UAS based off of three take-off mass categories (this mass includes payload and batteries, but not fuel). The key article (241) that applies to all mass categories is that the UAS must not endanger persons or property, with table 1-2 outlining the general restrictions for these different mass categories (specifically for UAS equipped with a camera, there are more subtleties that are not listed).

*Table 1-2: General restrictions for the use of UAS with a mass of 0~20 kg within the UK. * Indicates that this regulation does not come into effect until November 2019.*

Take-off mass	**< 250 g**	**250 ~ 7 kg**	**> 7kg ~ 20 kg**
Registration required*	No	Yes	Yes
Competency verified*	No	Yes	Yes
Maximum altitude AGL	400 feet	400 feet	400 feet
Maximum distance from operator (must be within visual line of site)	500 m	500 m	500 m
Minimum distance from an airport boundary	1 km	1 km	1 km
Minimum distance from a congested area	150 m	150 m	150 m
Minimum distance from crowds of more than 1000 people	150 m	150 m	150 m
Minimum distance from people	50 m	50 m	50 m
Minimum distance from vessels, vehicles and structures	50 m	50 m	50 m
Limitations to flying within controlled airspace	No	No	Yes

There are further restrictions based on whether the operation is considered commercial work or not (i.e. being paid for the data produced from the UAS). If this is the case, the UAS operator must have completed a certification course with a National Qualified Entity, that includes ground and aerial based assessment (CAA CAP 722, 2015), however once completed this also reduces the requirement to stay 150 m away from congested (e.g. urban) areas, to just 50 m. Other concessions can also be made via consultation and agreement with the CAA, such as increasing the distance from the operator from visual line of site (VLOS, which is typically to a maximum of 500 m) to extended visual line of site (EVLOS), although this would still require observers (more flight crew) to be able to maintain VLOS to the aircraft (CAA

CAP 722, 2015). Beyond visual line of site (BVLOS) UAS operation is currently only permitted within segregated airspace (airspace specifically for UAS operations).

Whether university research using UAS is considered as commercial work is a grey area, however the CAA have clarified this with the below statement:

"Whilst every case should be judged on its own merits, some types of arrangements are not generally considered by the CAA to be Commercial Operations:

- *Any other imagery or data collection task where the video, photographic stills or other data collected, are used exclusively for the drone operator's own use.*

  Example: A university research team wants to use a drone to gather survey data or imagery to help with their research project. This is legitimate as long as the research project was not directly funded by a business that intends to use the results of the data for its own business purposes (including any material or research into its products or services). Clearly university research is funded through a variety of means (grants, charitable and alumni donations, etc) and for varying purposes. The exact arrangements would need to be considered in each case. Where an academic organisation is openly advertising their capabilities to external organisations and a business relationship is entered into with an external organisation, the use of a drone for that purpose is likely to be construed as Commercial Operations. In order to alleviate difficulties with varied funding models, universities and other similar organisations should consider applying for permission from the CAA so that their services can be offered without constraint." (CAA, 2018).

1.5 The pros and cons of using a UAS for remote sensing

Due to the regulations covering UAS operations in the UK, the size of area that could be surveyed within a single flight is considerably smaller (~1 km^2) than what could be achieved by using a manned aircraft, which depending on their size are capable of collect regional scale imagery (up to 10,000 km^2), or satellites, which can provide global coverage (Everaerts, 2009). However, both of these more traditional platforms can be inoperable in cloudy conditions as the cloud obscures the ground (for satellites more so than manned aircraft) and the resolution of the data produced is not always high enough for certain tasks (Koh & Wich, 2012; Matese *et al.*, 2015). Typically, the resolution of optical data is within the 1~30 m per pixel range for satellites and 0.1~1 m per pixel for manned aircraft, but if the objects to be monitored are only a few cm in diameter (e.g. the emergence of agricultural crops), then these resolutions would not be sufficient, as to effectively recognise an object it must be viewed at a resolution 3-5 times finer than its size (Aber *et al.*, 2010).

This gives some advantages to the use of UAS, as they are restricted to low altitude flights, so clouds are not usually an issue (they are operating below cloud level) and the spatial resolution of optical data is considerably higher, typically within 0.01~0.1 m per pixel (Zhang & Kovacs, 2012). Cost and flexibility is also a significant factor, as UAS (with a mass of < 20 kg) have quite low purchasing and operational costs when compared to the acquisition of data from satellites and manned aircraft, the latter of which also typically require scheduling in advance, reducing their flexibility (Everaerts, 2009; Husson *et al.* 2014; Zhang & Kovacs, 2012). This low cost and flexibility in use of UAS improves the chances of reliable temporal data collection, as a UAS can be deployed whenever the weather conditions are suitable (Zhang & Kovacs, 2012; Husson *et al.* 2014, Shahbazi *et al.* 2014).

There are however disadvantages, as the aircraft are considerably smaller their payload capacity is also reduced and therefore choice of sensors is more limited or compromised compared to the larger sensors available to manned aircraft or satellites (i.e. less spectral resolution; Zhang & Kovacs, 2012; Shahbazi *et al.* 2014). There are also limitations relating to the weather as small UAS are less capable of handling high wind speeds and are often not waterproof and due to restrictions in regulations they have a reduced spatial footprint of data collected per flight, potentially requiring more flights to cover the area of interest, which in turn can lead to increased time and cost of data processing (Zhang & Kovacs, 2012; Shahbazi *et al.* 2014).

1.6 Photogrammetry

Despite the reduced payload capacity of UAS a range of sensors are available, including multi-spectral, hyperspectral and thermal cameras, however out of all the different sensors that can be deployed on a UAS, standard digital cameras are considered to be the most available and have been widely adopted in many studies (Colomina & Molina, 2014). In order to take measurements from images captured from a UAS the science of photogrammetry has to be employed (making precise measurements of three-dimensional objects from two-dimensional photographs), which has been in existence for approximately 150 years, essentially since photography itself was invented (Aber *et al.*, 2010). Relatively recent advances in computer vision techniques have enabled software to be created that use the principles of photogrammetry to produce detailed three-dimensional (3D) models of

the scene being viewed from essentially unordered collections of two-dimensional (2D) digital images (Snavely *et al.*, 2008; Dandois & Ellis, 2010).

One of the main techniques used is termed Structure from Motion (SfM; Ullman, 1979), which requires that the imagery to be processed is overlapping. The movement of the camera with the overlapping imagery allows the extraction of key points (matching feature points in one image to the next; figure 1-4) using other computer vision algorithms such as scale-invariant feature transform (SIFT; Lowe, 1999), which allow matching points to be found despite changes in scale between images (Whitehead & Hugenholtz, 2014). Once these key points have been identified, the location, orientation and internal parameters of the camera (e.g. focal length, the principal point location and lens distortion coefficients) can be identified and optimized using bundle adjustment of all of the images to produce a sparse 3D point cloud of the scene viewed (Dandois & Ellis, 2010; Verhoeven *et al.*, 2012).

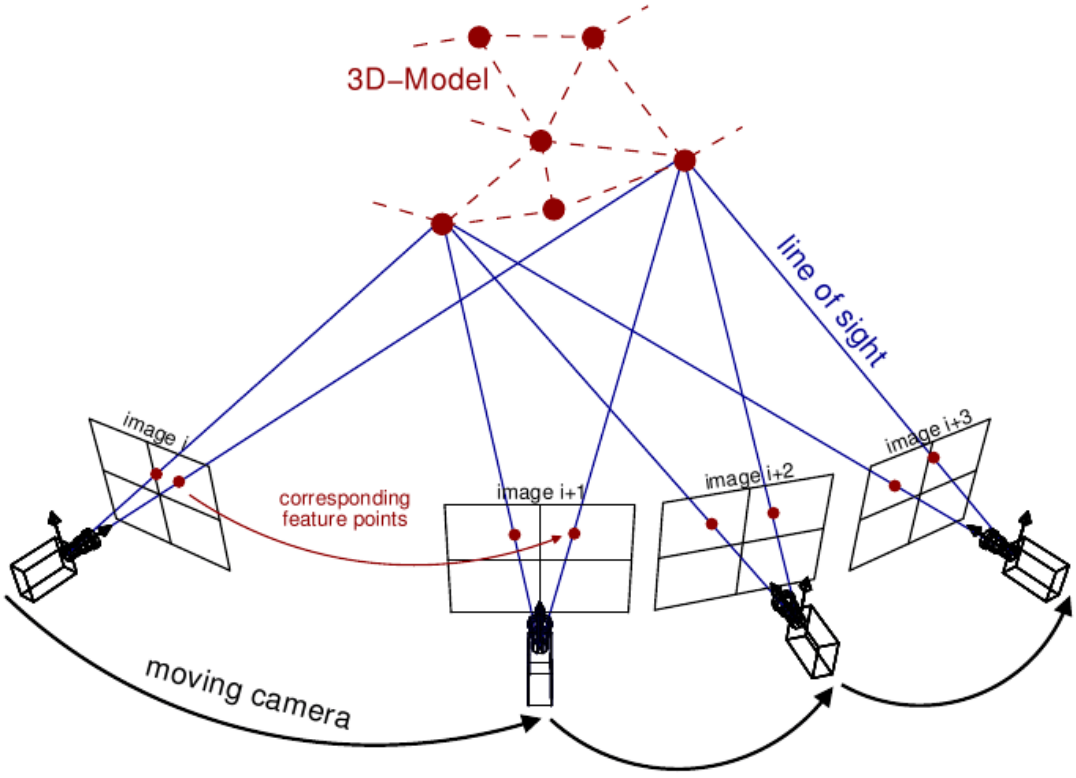

Figure 1-4: Example of identification of 3D points from four sperate but overlapping 2D images (Sweeny, 2016).

Further algorithms can then be used to densify and then convert this point cloud into a digital surface model (DSM), a 2D image showing a height model of the scene, which in turn can be used to orthorectify each image (the geometric correction of an

image to a known surface) and mosaic them together into a single orthomosaic of the scene viewed (Verhoeven *et al.*, 2012). Open source and commercial software is available to process imagery using these techniques, which are ideally suited to the imagery produced from a UAS and can allow relatively high levels of automation (Whitehead & Hugenholtz, 2014).

1.7 Classification and analysis

To be able to effectively utilise the data produced from these photogrammetry processes, other software is required that can extract the salient information, through interrogation of the spectral and spatial aspects of the imagery. For instance, in a sunlit scene, the material (features) within a surface being viewed will exhibit differing spectral characteristics, as the features will either reflect, absorb, transmit, emit or scatter different regions of the electromagnetic spectrum. These spectral characteristics are termed spectral signatures (typical reflectance properties) and can be used to identify one feature from another depending on the sensor being used and its spectral resolution (Govender *et al.*, 2007).

An initial stage of this is often thresholding of the imagery to separate it into the features of interest (e.g. vegetation) from those that are not (e.g. soil) and is typically done via the application of a vegetation index (VI) (Govender *et al.*, 2007). There are many different VIs covering a large range of different spectral wavelengths and the selection of a suitable VI will be based on the type of sensor available, its spectral characteristics (what wavelengths of light it can sense) and the spectral signature of the features being investigated. For instance, the spectral signature of green vegetation shows low reflectance for red wavelengths of the electromagnetic spectrum, with a high reflectance of NIR wavelengths (in stark contrast to dry soil; figure 1-5a). This means that a VI such as the normalised difference vegetation index (NDVI; Rouse *et al.*, 1973) is ideal to enable the effective separation of vegetation from soil, as it highlights the difference between red and near infra-red (NIR) reflectance (Rabatel *et al*., 2014).

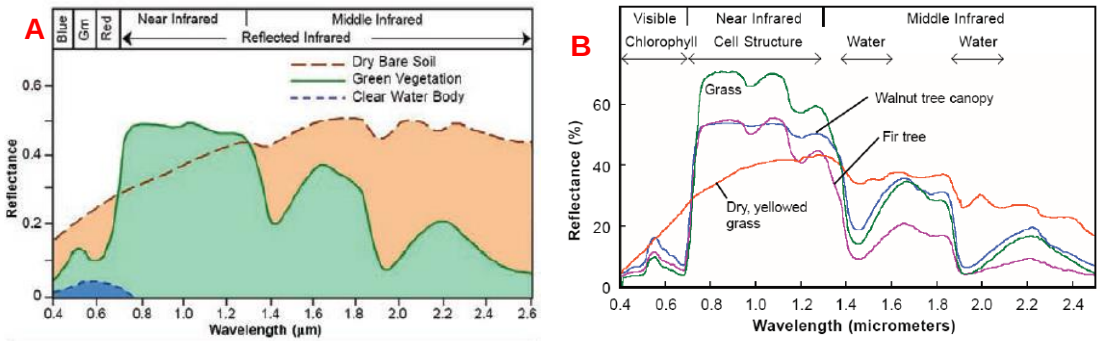

Figure 1-5: (A) Example spectral signatures of green vegetation, dry bare soil and clear water (Govender et al., 2007); (B) Example spectral signatures of varying types of vegetation, including healthy grass (green) and dry, yellowed grass (orange) (Govender et al., 2007).

Different types of vegetation will have unique spectral signatures, which will vary depending on the health of the plants (figure 1-5b), as the variation within vegetation for the visual portion of the electromagnetic spectrum (lower reflectance of red and blue wavelengths) is due to the absorption by chlorophyll as part of the plants photosynthesis. If photosynthesis is disrupted for some reason (e.g. disease) then the amount of chlorophyll could be reduced, altering the plants spectral signature (Govender *et al.*, 2007).

These spectral signatures can be used as part of a classification process, to identify what features are present within a scene being viewed. Computer software to enable this classification follows two main forms, either pixel based, where each pixel is queried directly and classified depending on its spectral value, or object based, where pixels are grouped into objects and the mean of their value determines the classification (Blaschke, 2010). Although pixel-based methods are generally faster to implement, they can result in 'salt and pepper' noise in the final classification of very high-resolution imagery (Blaschke, 2010; Weih *et al.*, 2010) due to intra-class variations (e.g. gaps and shadows within a canopy; Torres-Sánchez *et al*., 2015).

Therefore, for imagery derived from a UAS, object-based image analysis (OBIA) is the preferred method for classification, as different segmentation algorithms can be used to split the scene into distinct objects (e.g. individual plants; Torres-Sánchez *et al*., 2015). The mean of the spectral information for each object can be queried as well as spatial and contextual information, such as object height (if a height model was available), or the presence or distance to other objects that may have already been classified, as well as the shape and texture (the change in frequency and

pattern of tones) of an object (Blaschke *et al.*, 2014). Other sources of data can also be used as part of an OBIA classification (e.g. other thematic layers such as ground sourced information) and the classification routine can be automated once defined, making OBIA a very powerful classification tool for which both open source and commercial software solutions are available.

1.8 Rise in research using UAS

Although there are disadvantages in using UAS over other platforms for RS, researcher' enthusiasm in embracing this new technology has not been dampened, as a review by Shahbazi *et al.* (2014) shows a steady increase in the number of published papers making use of UAS for natural resource management from 2000~2013 (figure 1-6a), with agriculture being the topic most pursued (figure 1-6b). Further to this a recent study by Chabot (2018) again shows an increase in the number of papers referencing UAS (figure 1-6c), with the largest area being that of engineering (i.e. the development of UAS themselves), although agriculture and environmental sciences feature strongly indicating that the development of these platforms and how they can be used is continuing apace.

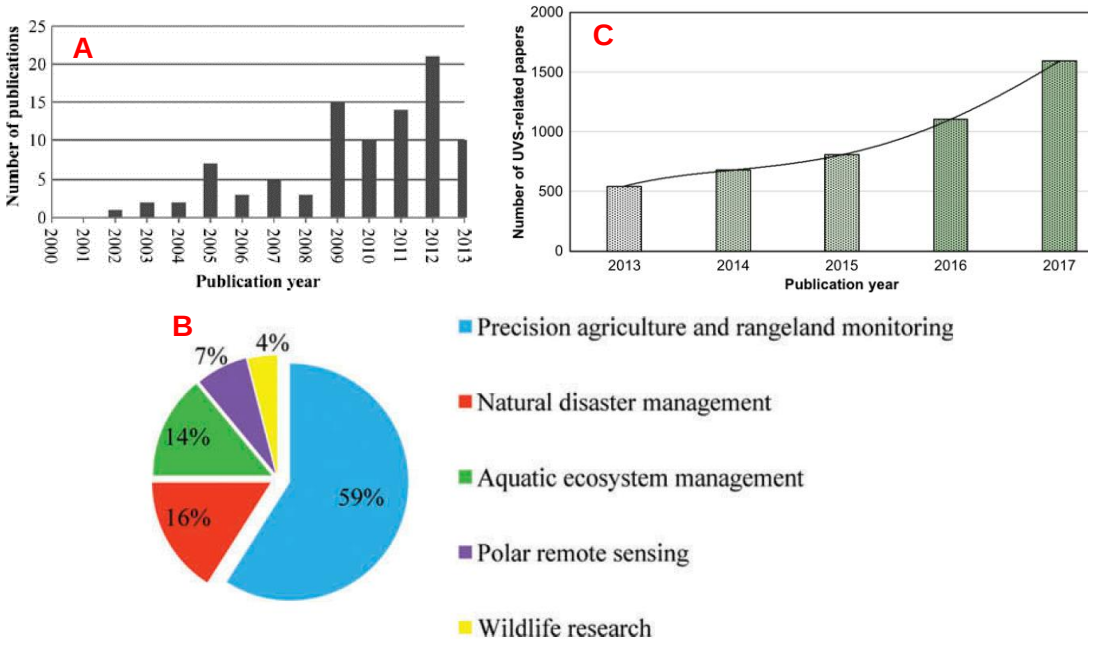

Figure 1-6: (A) The number of publications from 2000~2013 that have utilised UAS for natural resource management (Shahbazi et al. 2014); (B) The specific fields of research publications in (A) were based on (Shahbazi et al. 2014); (C) The number of publications from 2013~2017 that are related to the development and use of UAS (Chabot, 2018).

1.9 Example uses of UAS as remote sensing platforms

Due to the flexibility of small UAS, they have been used across a wide range of research disciplines and over a wide variety of geographical locations. For instance, Lucieer *et al.* (2014) used a multirotor UAS equipped with a digital camera to produce highly detailed digital surface models of Antarctic moss in the Windmill Islands region, East Antarctica. These could then be used to identify the hydrology of the area and its influence on the health of the moss. In complete contrast to this, Mori *et al.* (2016) also used a multirotor UAS equipped with gas sensing equipment to sample the plume from an active volcano (Mt. Ontake, Japan), where the results indicated a likely lessening of volcanic activity.

For wildlife research, Chabot & Bird (2012) used fixed wing UAS to survey flocks of Canada geese (*Branta canadensis*) and snow geese (*Chen caerulescens*) during their spring migration in Quebec, Canada. They confirmed that the UAS did not cause a disturbance to the flocks and the camera they used was more effective in counting snow geese over Canada geese. Koh & Wich (2012) also used a fixed wing UAS to survey varied stretches of tropical rainforest in the Gunung Leuser National Park in Sumatra, Indonesia. They successfully used the imagery produced to identify different land uses that were occurring (e.g. logging, habitation and palm tree plantations) as well as being able to detect large mammals such as the critically endangered Sumatran orangutan (*Pongo abelii*).

UAS can also be used to aid relief efforts when humanitarian disasters occur as the aircraft can be deployed rapidly to collect imagery over an impacted city, providing up to date data on the state of buildings, roads, bridges and other infrastructure that can help inform the relief response. Xu *et al.* (2014) successfully demonstrated such a system directly after an Ms7.0 earthquake occurred in Lushan County, Sichuan Province, China, covering some 25 km^2 of affected area using a fixed wing UAS. In contrast, Fernández-Hernandez *et al.* (2015) demonstrated the effectiveness of using small multirotor UAS as an archaeological tool, producing high resolution and accurate digital elevation maps of an Iron Age hillfort (Las Cogotas) in Ávila, Spain, enabling many measurements of the site to be made.

Different types of vegetation have also been monitored using UAS, such as identifying the condition and species composition (with accuracies of over 80 %) of aquatic habitats (the riparian zone) of two lakes and a river system in Northern

Sweden using a fixed wing UAS (Husson *et al.*, 2014). Jensen & Mathews (2016) also used a fixed wing UAS to identify the variability of forest canopy height, with high levels of correlation with ground-based measurements ($R^2 \geq 0.89$) over Central Texas, USA. However, one of the larger areas of research using UAS to survey vegetation is for precision agriculture (Shahbazi *et al.*, 2014; *Chabot, 2018*)

1.10 UAS and precision agriculture

Precision agriculture (PA) makes use of remote sensing and other techniques, including the use of satellite imagery, aerial imagery, tools such as geographical information systems (GIS) and global navigation satellite systems (GNSS), to identify variations in soil and crop qualities at site specific levels, to enable more effective management decision to be made using agricultural vehicles that are designed to allow a more targeted application of crop treatments (e.g. fertilizer and pesticide; McLoud *et al.*, 2007; Zhang & Kovacs, 2012).

Many studies have already been made using UAS for PA, including weed detection (Peña *et al*. 2015; Pérez-Ortiz *et al.*, 2016), monitoring crop biomass using spectral means (Honkavaara *et al*. 2013) and through the identification of crop height (Bendig *et al*., 2014; Bendig *et al*., 2015), identification of water status and stress (Baluja *et al*., 2012; Kyratzis *et al.*, 2017) and monitoring for the spread of disease (Sugiura *et al*., 2016; Albetis *et al*., 2017). Various sensors have also been employed to enable PA from UAS, including standard digital cameras (Torres-Sánchez *et al*., 2014; von Buren *et al*. 2015), modified digital cameras that are sensitive to near infra-red wavelengths of light (Hunt *et al*., 2011; von Buren *et al*. 2015), narrow band multispectral cameras (Baluja *et al*., 2012; von Buren *et al*. 2015; Torres-Sánchez *et al*., 2013), hyperspectral cameras (Honkavaara *et al*. 2013), thermal cameras (Baluja *et al*. 2012; Chapman *et al*. 2014) and standalone spectrometers (Link *et al*. 2013; von Buren *et al*. 2015).

A range of different types of crops have already been investigated to identify if UAS can be effectively used for PA (Zhang & Kovacs, 2012), including some of the key crops for Scottish agriculture, such as spring barley, winter wheat, potatoes and oil seed rape (Scottish Government, 2018). For instance, a study by Rasmussen *et al.* (2018), investigated the ability of pre-harvest weed mapping for both wheat and barley crops, using in-expensive commercial availably UAS and standard digital cameras. Their pixel-based classification approach gave accuracies above 90%

showing that easily available UAS technology can be used effectively to cover field scale (10 ha) areas and provide weed maps that can be used to control weed species such as creeping thistle (*Cirsium arvense*). However, their classification solution was not fully automatic (it required manual thresholding), so highlights the limitations of un-calibrated standard digital cameras.

For potatoes, late blight (*Phytophtora infestans*) is one of the key diseases to effect potato crops in Scotland (SRUC, 2019c). Recently a study by Duarte-Carvajalino *et al.* (2018) used a commercially available multirotor UAS equipped with a modified digital camera (to enable the detection of near infra-red wavelengths) to detect the presence of late blight. Their analysis routine used a deep learning convolutional neural network (a machine learning algorithm) to identify the severity of late blight infection and their results suggest that it would be effective enough to replace the visual estimation that is typically carried out on the ground. Due to the requirements of the deep learning algorithm requiring large numbers of training samples (a time-consuming manual process), their method still needs more work. It also only considered late blight being the source of any disease, however it shows promise that machine learning can be used to assist with fungicide management decisions to thwart this particular disease.

For yield assessment, an interesting study by Wan *et al*. (2018) used digital and multispectral cameras with a pixel-based classification method to identify the number of flowers present from an oil seed rape crop (which can give an estimate of oil yield). The results using the digital camera showed a high correlation ($r^2 = 0.89$) indicating that this method was effective at identifying potential yield and that this assessment could be improved with these two sensors used in conjunction, as further plant growth measures could then also be identified (i.e. not just the number of flowers). However, their UAS had to be flown very low and slow to obtain effective data capture, limiting its commercial potential, as it could only be used to cover small areas.

Therefore, UAS appear to be well placed to add value to PA however as Zhang & Kovacs (2012) point out, to gain traction with the farming community their use needs to be easy to implement, give timely results that can be easily integrated into existing management and application systems, and most importantly are cheap to

operate and give a good cost to benefit ratio. To enable this, the UAS technology itself and the regulations governing their use will play a part but the technology behind the processing and analysis of the data captured is key to enabling the adoption of this technology.

1.11 Project aims

Essentially all the elements required to perform RS via UAS are in place, from the regulations to govern their use, to methods to enable data collection, processing and classification that can be used to identify the state of features that are being remotely sensed. Therefore, given the rise in use of UAS in many applications, this study sets out to determine how low-cost UAS could be developed and applied in situations relevant to land management that are in concordance with the research, education and consultancy aims of Scotland's Rural College (SRUC).

"*SRUC exists to deliver comprehensive skills, education and business support for Scotland's land-based industries, founded on world class and sector-leading research, education and consultancy. The integration of these three complementary 'knowledge exchange' services is of significant value to all with an interest in land-based activities – be they learners, businesses, communities or policy-makers*" (SRUC, 2019a).

SRUC's mission is to "*drive the future needs of a dynamic, innovative and competitive rural sector in Scotland and to solve the biggest global agrifood challenges*" with a vision to be "*a unique, market-led and mission diverse 21st Century rural university*" (SRUC, 2019b). The areas of research undertaken at SRUC covers a wide range of rural concerns, including rural policy, animal and veterinary science, environmental science and crop and soils science and they have four overarching global aims:

- "*To create SRUC academic resources which have national impact and global influence.*
- *To be an international leader in land-based research and consultancy services.*
- *To be a sustainable, well-resourced organisation with exemplary environmental credentials and real ownership amongst students, staff and stakeholders.*
- *To continue to build on our assets and reputation."* (SRUC, 2019b)

Given the wide range of research activities undertaken at SRUC, the areas of environmental science and crop and soils science were identified as those that would directly benefit from the application of UAS technology, and so were addressed through the following broad objectives:

1. Identify, assemble and test a sensor package that can be applied to a variety of land use areas that are key to SRUC research aims.

2. Determine the UAS requirements of key SRUC research aims, and design, build and test an appropriate UAS that can accommodate the sensor package.

3. Determine software requirements linked to sensor and data requirements, and design appropriate data processing workflows.

4. Through collaboration with existing projects, demonstrate the utility of UAS acquired data to these projects by addressing specific questions within those projects.

1.12 Project outline

This introductory chapter has given an overview of RS and how UAS are being used as a new tool to enable the deployment of sensors at low altitude, giving very high-resolution data that was not easily available prior to the introduction of UAS.

Chapter 2 explores the identification and modification of a sensor package using consumer off the shelf (COTS) digital cameras, that could be used to capture data of over different land-use types for a variety of research aims. The spectral characteristics of the cameras (and others) are explored to identify how they could be used.

Chapter 3 investigates the design and testing of a custom built UAS, the integration of the sensor package and tests to reveal the limitations of the design in relation to flight planning and mission design. Further development and analysis are also carried out on the sensor package to identify how the imagery can be processed to produce a final product that will enable further analysis to occur, including an investigation into the geometric qualities of the processed data outputs.

Chapter 4 applies the UAS to the detection of disease within a trial plot of potatoes over time. This novel application of a UAS includes modelling of the development of individual plants over time, making use of the structural changes in the plants to indicate the onset of disease. The resulting accuracy of disease detection is indicated as effective but still requiring further development for real world application.

Chapter 5 is a time series investigation using the UAS to monitor the development of trial plot of potatoes, to be able to indicate the timing of emergence and estimation of canopy ground cover. The results were compared with traditional ground-based assessment revealing that emergence detection is not as sensitive (due to image resolution) but canopy cover estimation correlated well, despite a high level of weeds within the trial.

Chapter 6 investigates the environmental concerns of invasive non-native species and utilises the UAS to monitor the spread of one such species (giant hogweed), along a riparian habitat. The classification accuracy of this pilot study indicates that more work is required but it highlights the potential benefits that could be gained from identifying the species ability to spread to neighbouring areas.

Chapter 7 demonstrates how UAS could be used to assist in measures to mitigate climate change. The exploratory studies highlight how the UAS can be used to detect topographical features from two different land use types (forestry and grasslands), which in turn can be used to upscale expected greenhouse gas emissions.

Chapter 8 discusses the output from the studies in the earlier chapters and highlights areas that are effective or need further exploration. It also details areas of collaboration to show the utility and applicability of UAS to a range of different land use areas and finally concludes this thesis with an indication of what may come to pass in the future with regards to UAS.

Chapter 2. Sensor selection, modification and testing

2.1 Introduction

The primary purpose of most UAS is as some form of data collection platform, so identifying a sensor package that will fulfil the intended task, is within available budget and is as light as possible is required. For this PhD project the main focus of the research was to construct a remote sensing platform that could be used primarily for surveying and classifying vegetation, so that features such as plant growth, weed and disease detection, and other areas important to the agricultural and environmental aims of SRUC could be facilitated. Therefore, being able to capture a scene in NIR as well as visual wavelengths would be preferred as this would enable the use of a wider range vegetation indices (e.g. NDVI), allowing the use of potentially more effective methods for separating vegetation from soil (Rabatel *et al.*, 2014). Ideally a dedicated multispectral camera such as the Tetracam Mini-MCA (Tetracam Inc, California, USA) would have been selected, as this has already been used successfully to investigate disease resistance in a sugar beet crop (Bendig *et al.*, 2012), water stress within a vineyard (Baluja *et al.*, 2012), and Antarctic moss plant health (Turner *et al.*, 2014).

However, this sensor was well beyond the available budget and was quite heavy at ~720 g for the 6-sensor version (Bending *et al.*, 2012). Further studies by Von Bueren *et al.* (2015), looking at the variability of ryegrass pasture and Torres-Sánchez *et al.* (2013) identifying weeds within a sunflower crop, also used this senor and compared it with modified and un-modified consumer of the shelf (COTS) digital cameras. These studies both showed that COTS cameras give the advantage of higher spatial resolution but with a reduced spectral resolution due to the COTS cameras broad band nature. Due to the budgetary constraints of the project, using COTS cameras seemed obvious, especially as Von Bueren *et al.* (2014), and others (Rabatel *et al.*, 2014; Lebourgeois *et al.*, 2008; Dare, 2008) had already demonstrated that they could be modified to capture near infra-red (NIR) wavelengths of light, thereby increasing their spectral resolution.

This chapter address the 1st objective of this PhD project, as it details the identification and characterisation of sensors that were then used as the primary sensor package for all other chapters within this thesis.

2.2 Sensor choice

There were four main deciding points for the selection of suitable sensors for this project; (1) they had to be relatively light weight; (2) they had to be within a very limited budget (ideally less than £100); (3) they had to be modifiable in order to become sensitive to NIR wavelengths and (4) they need to be able to capture raw image files (RAW), as RAW imagery can be processed in a linear fashion rendering it more suitable to quantitative analysis compared to Joint Photographic Experts Group (JPEG) imagery (Lebourgeois *et al.*, 2008; Verhoeven, 2010).

Most consumer grade digital cameras use CMOS (complementary metal-oxide-semiconductor) or CCD (charge coupled device) sensors, which are essentially monochrome sensors that use photodiodes which are typically sensitive to wavelengths of light from 350 nm to 1100 nm (Nijland *et al.*, 2014, Hunt *et al.*, 2011). These can be made sensitive to specific wavelengths of light through the use of a colour filter array (CFA) positioned above the photodiodes of the sensor itself (Verhoeven, 2010). These CFAs can allow a variety of different wavelengths of light to pass through to the sensor (figure 2-1), however one of the most commonly used is the Bayer colour filter array (Bayer, 1976) which has twice as many green filters compared to red or blue, as green wavelengths are more important to the human visual system when picking out visual details (Verhoeven, 2010)

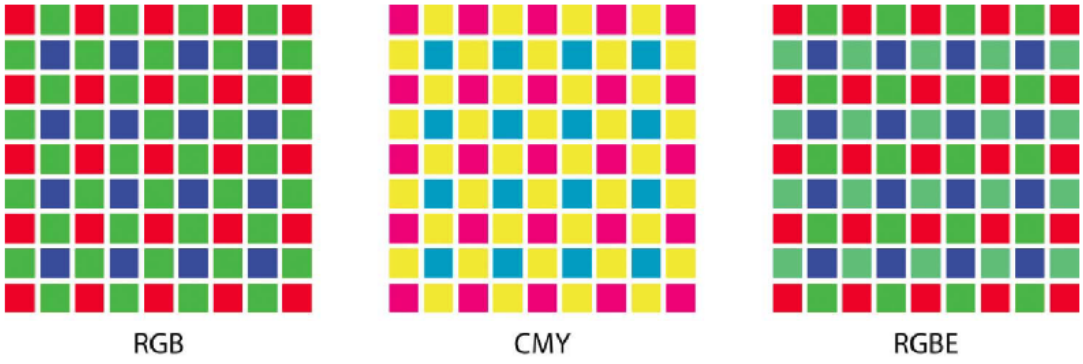

Figure 2-1: Examples of different colour filter arrays; (RGB) Red-Green-Blue Bayer pattern; (CMY) Cyan-magenta-yellow; (RGBE) Red-Green-Blue-Emerald (Verhoeven, 2010).

The Bayer CFA allows the sensor to capture red, green and blue wavelengths of light and output 3 colour channels (layers) that are combined and processed within the camera for elements such as white balance and sharpness, to produce the visually appealing JPEG imagery one would expect from a digital camera. However, if RAW imagery is being captured then the process of creating an image can be

manipulated, allowing customisation of how the pixels of each colour channel are reproduced, which can permit the creation of images with a linear response that have not been interpolated to the same extent that a typical JPEG image would have been (Verhoeven, 2009; Verhoeven, 2010).

Most of the digital cameras available that could capture RAW imagery were either well outside of the budget available or were older digital single-lens reflex (DSLR) type cameras that were too heavy to be deployed effectively on a small UAS. However, some cheaper consumer grade “point and shoot” cameras made by Canon can have their firmware modified to enable the capture of RAW imagery, even though the default camera firmware does not officially support it (CHDK, 2018a). This opened several possibilities as cheaper, light weight “point and shoot” style cameras could therefore be modified to not only capture RAW imagery, but also run custom scripts such as an intervalometer to allow the continuous capture of data, which would also be a very favourable feature to have within a camera system onboard an UAS.

As the human visual system is most responsive to the visual range of the electromagnetic spectrum around 400 nm to 720 nm (Palczewska *et al.*, 2014; figure 2-2), ideally images produced from a digital camera should also be within this range. As the CMOS and CCD sensors within digital cameras are sensitive to NIR and the CFA itself does not fully block these longer wavelengths, digital cameras have an internal NIR blocking filter in order to produce images that represent a scene as humans would see it. Removing this filter allows the full spectrum of the sensor to be accessed as demonstrated by Lebourgeois *et al.* (2008), Dare (2008) and Nijland *et al.* (2014) on larger DSLR type cameras, however the more compact “point and shoot” style cameras can also be modified, the results of which have been recorded through the citizen science webpages of Public Labs (PublicLabs, 2018).

Therefore, two Canon A2200 (Canon, Tokyo, Japan) digital cameras were selected for the main sensors used in this project as they met the four main requirements. (1) They were relatively light weight (135 g each); (2) they were very cheap when bought second hand (~£25 each); (3) they had been shown to be modifiable to allow the capture of NIR wavelengths (Horning, 2012) and (4) their firmware could be modified to allow them to capture RAW imagery (CHDK, 2018b). The cameras themselves have an integrated 5~20 mm zoom lens (28~114 mm, 35 mm

equivalent), a fixed aperture (f2.8~5.9, depending on zoom) and can produce a 14.1-megapixel image using a compact 1/2.3 inch CCD sensor. They also have an audio/visual output port that can be used to transmit the current view of the camera, and a mini universal serial bus (USB) port which can be used to trigger the camera, both of which would be of benefit as part of a UAS.

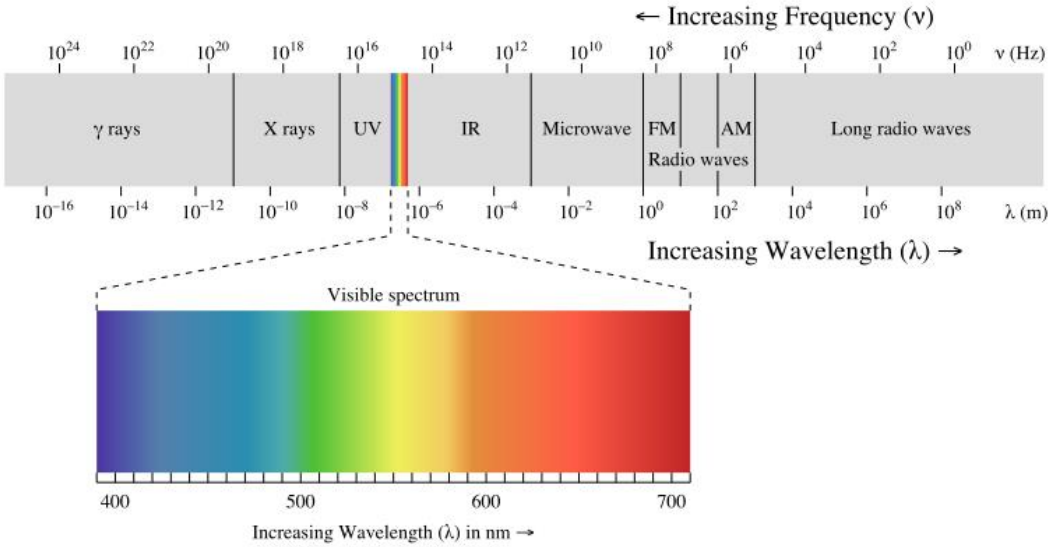

Figure 2-2: Electromagnetic spectrum (Ronan, 2007).

2.3 Sensor modification

One of the cameras was left un-modified and the other had its internal NIR filter removed so that the sensor was sensitive to its full spectral range. Previous studies by Lebourgeois *et al.* (2008) and Dare (2008) have shown that all three colour channels of modified digital cameras are usually sensitive to NIR wavelengths, although Hunt *et al.* (2011) indicates that this is not true for all types of digital camera. Therefore, an additional filter is required on the modified camera in order to obtain at least one colour channel that only captures NIR wavelengths. Two potential ways of achieving this are through the use of a band rejection filter that can effectively block certain wavelengths (e.g. red light), such as that used by Hunt *et al.* (2011), or through the use of a long pass filter that attenuates shorter wavelengths (e.g. blue light or everything below the NIR range) as shown by Rabatel *et al.* (2014) and others (Dare, 2008; Nijland *et al.*, 2014).

As the studies by Rabatel *et al.* (2014), Lebourgeois *et al.* (2008), Dare (2008) all used Canon cameras that showed that all three colour channels were sensitive to NIR, the decision was made to use a long pass filter for the modified camera that

would block any blue wavelengths of light, so an acrylic long pass filter with a transmission range of 585 nm to 2200 nm was selected for testing (figure 2-3a). This acrylic filter was chosen as it was considerably cheaper than attempting to get a custom-made filter that would fit inside the camera and was thinner, lighter and had slightly higher and flatter transmission profile up to 1100 nm compared to a glass filter of similar size and spectral qualities (figure 2-3b). Ideally a 550 nm long pass filter would have been selected as this would have allowed green, red and NIR wavelengths to be captured whilst rejecting blue (Nijland *et al.*, 2014), however this could not be sourced.

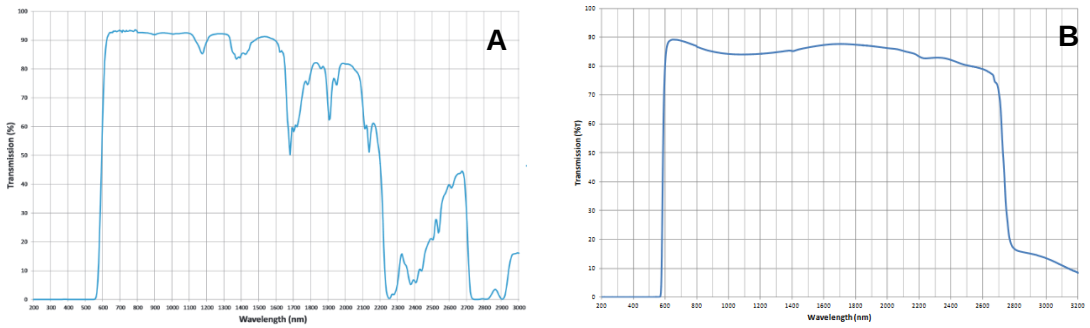

Figure 2-3: Transmission profiles of the (A) acrylic 585 nm cut-on long pass filter (KnightOptical, 2018a) and (B) glass 590 nm cut-on long pass filter (KnightOptical, 2018b).

The filter was 1 mm thick and 25 mm in diameter, making it an almost exact match to the dimensions of the lens housing on the Canon A2200 and so could be easily mounted externally with some adhesive (figure 2-4). Both cameras were equipped with 16 GB, class 10 secure digital memory cards (SanDisk, Milpitas, California) which had the Canon Hack Development (CHDK) v1.2 (CHDK, 2018a) installed and configured to allow the simultaneous capture of JPEG and RAW imagery in Adobe DNG format (v1.3). The cameras could be triggered to take a picture via the use of the shutter button on the camera itself or remotely by applying a 5 volt pulse to the cameras USB port.

Figure 2-4: The unmodified camera (a) and modified camera (b).

2.4 Spectral sensitivity testing

Although the typical spectral sensitivity of a digital camera is expected to be from 350 nm to 1100 nm (Nijland *et al.*, 2014; Hunt *et al.*, 2011) the actual response of the Canon cameras was not known as this information was not provided by the camera manufacturer. Bongiorno *et al.* (2013) used a linear variable edge filter (a spatially varying bandpass optical filter that passes wavelengths of light from 380nm to 745nm) to identify the spectral sensitivity of an un-modified Canon A2000 (likely to be very similar to the A2200), however this camera was only capturing JPEG imagery and still had its internal NIR blocking filter, so the full spectral response when capturing RAW imagery was also unknown.

The method typically used to identify spectral sensitivity is to take images of a monochromatic light source, which can be altered to output different wavelengths of light (Darrodi *et al.*, 2015; Jiang *et al.*, 2013; Suzuki *et al.*, 2009; Verhoeven *et al.*, 2009). Therefore, an experiment was undertaken in collaboration with Elias Berra (Newcastle University) and Alasdair MacArthur (The University of Edinburgh), making use of the laboratory facilities of the Natural Environment Research Council Field Spectroscopy Facility (NERC FSF) based at The University of Edinburgh. Both of the Canon A2200's and several other camera models were tested, and a paper detailing the results (Berra *et al.*, 2015; see below) was submitted and presented at the Unmanned Aerial Vehicles in Geomatics conference in Canada, August 2015.

2.5 Estimation of the spectral sensitivity functions of un-modified and modified commercial off-the-shelf digital cameras to enable their use as a multispectral imaging system for UAVs

E. Berra[1], S. Gibson-Poole[2], A. MacArthur[3], R. Gaulton[1], A. Hamilton[2]
[1]School of Civil Engineering and Geosciences, Cassie Building, Newcastle University, Newcastle upon Tyne, NE1 7RU, UK. *e.f.berra@newcastle.ac.br
[2]Scotland's Rural College, Peter Wilson Building, Kings Buildings, West Mains Road, Edinburgh, EH9 3JG, UK.
*Simon.Gibson-Poole@sruc.ac.uk; *Alistair.Hamilton@sruc.ac.uk
[3]NERC Field Spectroscopy Facility, Grant Institute, The King's Buildings, James Hutton Road, Edinburgh EH9 3FE, UK

2.5.1 Abstract

Commercial off-the-shelf (COTS) digital cameras on-board unmanned aerial vehicles (UAVs) have the potential to be used as multispectral imaging systems; however, their spectral sensitivity is usually unknown and needs to be either measured or estimated. This paper details a step by step methodology for identifying the spectral sensitivity of modified (to be response to near infra-red wavelengths) and un-modified COTS digital cameras, showing the results of its application for three different models of camera. Six digital still cameras, which are being used as imaging systems on-board different UAVs, were selected to have their spectral sensitivities measured by a monochromator. Each camera was exposed to monochromatic light ranging from 370 nm to 1100 nm in 10 nm steps, with images of each step recorded in RAW format. The RAW images were converted linearly into TIFF images using DCRaw, an open-source program, before being batch processed through ImageJ (also open-source), which calculated the mean and standard deviation values from each of the red-green-blue (RGB) channels over a fixed central region within each image. These mean values were then related to the relative spectral radiance from the monochromator and its integrating sphere, in order to obtain the relative spectral response (RSR) for each of the cameras colour channels. It was found that different un-modified camera models present very different RSR in some channels, and one of the modified cameras showed a response that was unexpected. This highlights the need to determine the RSR of a camera before using it for any quantitative studies.

2.5.2 Introduction

A new era of fine-scale remote sensing has emerged with the arrival of unmanned aerial vehicles (UAVs), which have the advantage of being lightweight, low-cost and operationally easy to deploy as safe remote sensing acquisition platforms (Berni *et al.*, 2009; Zhang & Kovacs, 2012).

Commercial off-the-shelf (COTS) digital cameras are typically used as imaging systems on-board UAVs due to their low-cost and researchers often want to make further use of them as multispectral imaging systems due to their ability to detect near infra-red light (Darrodi *et al*., 2015; Suzuki *et al.*, 2009; Lebourgeois *et al.*, 2008), once modified by removing the hot mirror filter (Rabatel *et al.*, 2014; Verhoeven *et al.*, 2009).

However, this is hampered by a lack of knowledge of the spectral sensitivity of the camera, as COTS camera manufacturers typically do not publish this information. Also, when cameras have been modified (with the addition of a long pass or notch filter) by an external party, the wavelengths that could be transmitted through that filter are also not always known (as is the case with two of the modified cameras in this study). Therefore, users need to either measure or estimate their cameras sensitivity (Darrodi *et al.*, 2015; Jiang *et al*., 2013).

A standard and accurate methodology for measuring the sensor sensitivities is to take photographs of monochromatic light produced by a monochromator (Darrodi *et al*,. 2015), where the digital numbers (DN) recorded on the images are expected to have a linear response to the radiation output of the monochromator (Verhoeven *et al.*, 2009).

Even though previous studies have measured the spectral function of different digital still cameras using monochromators (Darrodi *et al*., 2015; Jiang *et al*., 2013; Suzuki *et al*., 2009; Verhoeven *et al.*, 2009), there is a lack of a detailed methodology in how to do so, which has motivated us to present an open-source workflow to process the images after image acquisition. In this paper, we aim to identify and to present a step-by-step methodology for identifying the spectral sensitivity of modified and un-modified low-cost digital cameras using open source software, in order for them to be used as multispectral cameras for UAV systems and compare the results for a range of COTS and modified cameras.

2.5.3 Methodology

2.5.3.1 Camera types and settings

Six physical cameras (two of each model), which have been used as imaging systems on-board different UAVs, were selected for spectral sensitivity estimation. The cameras were either un-modified and therefore only sensitive to visible light (VIS) or modified (MOD) to also be sensitive to near infra-red (NIR) wavelengths. The modified cameras have had their internal NIR filter removed, thereby turning them into a full spectrum (FS) camera, which was then replaced with either an internal or external long pass or notch filter to alter the cameras spectral sensitivities.

A preliminary image acquisition of monochromatic light was carried out in order to determine the optimal settings for each camera, as presented in Table 1. For each of the cameras, the ISO was set to 100 in order to gain a high signal to noise ratio, and the aperture and shutter speed were altered to ensure that the image was not overexposed. The optimal exposure settings were chosen when the monochromatic light with the highest signal intensity (~540 nm for VIS and between 600~700 nm for NIR) came close too (but not actually) saturating the images digital numbers (DN).

The defined settings (table 2-1) were then kept unchanged throughout the acquisition period and the images were recorded in both JPEG and RAW formats. RAW format is necessary as it assumes that the cameras sensor detects and stores radiance without applying any processing or compression to it, i.e. the original signal reaching the sensor is not modified (Verhoeven, 2010).

Table 2-1: Camera types, exposure settings and modifications. Each camera used an ISO of 100 throughout the experiment.

Camera Model	Aperture; Shutter Speed	Short Name; Notes
Panasonic DMCLX5	f-2; 1/5	PAN_VIS -Un-modified
Panasonic DMCLX5	f-2; 1/3.2	PAN_MOD -No internal NIR filter -External long pass filter (manufacturer and cut on wavelength not known)
Canon A2200	f-2.8; 1/2	CAN_VIS -Un-modified
Canon A2200	f-2.8; 1/2	CAN_MOD -No internal NIR filter
Canon A2200	f-2.8; 1/2	CAN_MOD_585 -No internal NIR filter -External acrylic long pass filter, 585 nm cut on (KnightOptical, 2018a)
Sony Nex7	f-2.8; 1/5	SON_VIS -Un-modified -HGX 49 mm UV filter
Sony Nex7	f-2.8; 1/3	SON_MOD -No internal NIR filter -Internal notch filter (MaxMax LDP LCC G-R-NIR, exact transmission properties not known) - HGX 49 mm UV filter

Both the Panasonic and Sony cameras were able to record JPEG and RAW files natively; however, the Canon camera could not. Therefore, modified firmware (CHDK v1.2; CHDK, 2018a) was used to allow JPEG and RAW (Adobe DNG v1.3 format) images to be produced, as well as to allow the shutter speed to be set at a constant value.

2.5.3.2 Monochromatic light image acquisition

The spectral sensitivities of each camera were measured by recording their response to monochromatic light produced by a double monochromator (OL 750-M-D Double Grating Monochromator (Additive), Optronic Laboratories, Inc., Orlando, Florida, USA) and reflected by an integrating sphere attached at the monochromators exit slit. The light beam is reflected by the spheres interior surface from where images were acquired through a detection port in the integrating sphere (figure 2-5).

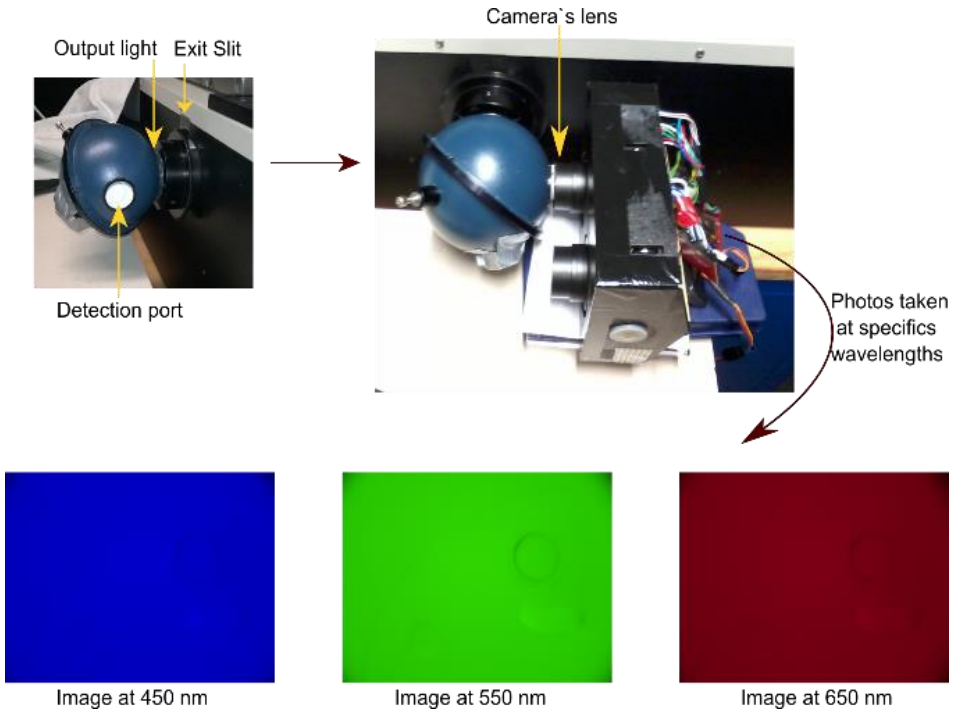

Figure 2-5: The monochromator and camera setup and three example images of the inside of the integrating sphere at different wavelengths.

The monochromator was located in a temperature-controlled dark room and the lens of each camera was positioned touching the integrating spheres detection port. The sphere and camera were also covered by a low reflectance black cloth in order to avoid any external light contaminating the result.

Each camera was exposed to monochromatic light ranging from 370 nm to 1100 nm in 10 nm steps, with two images being captured at each step (most of the cameras were tested across only a portion of this complete range). Therefore, the selected nominal half bandwidth (HBW) was 10 nm (using 1200 g/mm gratings), which is achieved by combining 5 mm slits at the entrance, middle and exit ports (Optronic, 2002). Due to the range of wavelengths being sampled, it was also necessary to vary the lamp voltage and the type of internal filter used. The settings selected on the monochromator and the wavelength interval from which images were acquired to measure the cameras spectral response, are presented in table 2-2.

Table 2-2: Monochromator lamp voltage and internal filter settings used for specific wavelengths being sampled.

Lamp Voltage (v)	19	17	17
Filter (nm)	345	345	599
Wavelengths sampled (nm)	370-500	510-620	630-1100

Dark images were also acquired for the Panasonic cameras in order to correct for effects of noise create by the dark current signal (Verhoeven *et al.,* 2009). Photographs were taken inside the dark room with the camera lens covered by the black cloth and the room light switched off.

2.5.3.3 Imaging processing

Each camera recorded its RAW image file using a different format dependant on the camera manufacturer, so the open source software DCRaw (v9.25; Coffin, 2018) was used to convert the RAW files into TIFF images that maintained a linear relationship with the original RAW data (Gehrke & Greiwe, 2014; Verhoeven *et al.*, 2009). During this step, the Panasonic images were also corrected for the effects of the dark current signal as DCRaw can utilise the dark image taken at the same time as the images of monochromatic light, generating dark-corrected linear TIFF images. The script command used with explanation is present in Appendix A.

The TIFF image DNs were averaged within a 9 x 9 pixel area in the centre of each image, in order to avoid issues related with the variance of the radiance within the integrating sphere and any differences in the individual pixel response across each camera's image sensor (Darrodi *et al.*, 2015). To obtain the mean and standard deviation values from the 9x9 pixel window of each image, a macro was created using the open source software ImageJ (v1.49k, Fiji distribution; Schindelin *et al.*, 2012). Figure 2-6 details the workflow used to capture these values and a detailed step-by-step guide is presented in Appendix A and the ImageJ macro script used is presented in Appendix A.

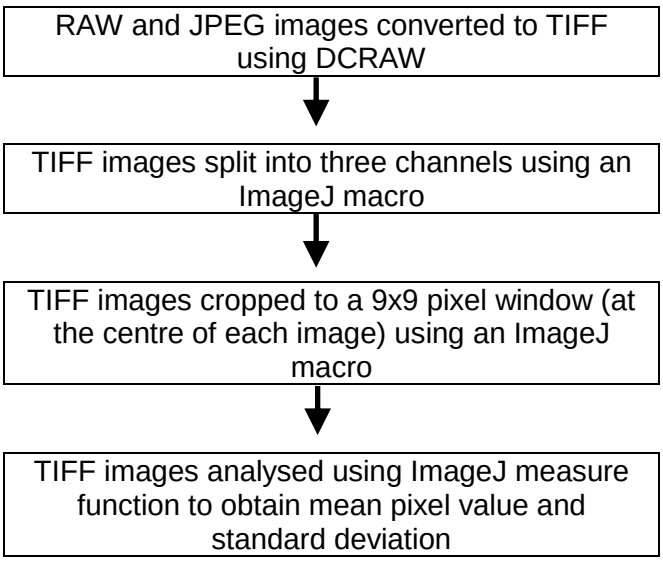

Figure 2-6: Post processing steps to convert RAW and JPEG images and to obtain mean and standard deviation digital number values for further analysis.

2.5.3.4 Retrieving RSR from the cameras

The light intensity from the monochromator and its integrating sphere were independently measured using a reference silicon photodiode (OL DH-300C S/N: 12101253, Optronic Laboratories, Inc., Orlando, Florida, USA) in order to identify the relative spectral radiance at each measured wavelength (figure 2-7a). The settings used mirrored those used at the image acquisition phase (table 2-2).

Two lamps voltages were used (figure 2-7b), with the 17 V lamp was used in combination with the 345 nm and 599 nm filter, however for the lower wavelengths (<500 nm) the lamp voltage was increased to 19 V in order to generate monochromatic light with an intensity that would be strong enough to be detected by the cameras sensors on wavelengths ~400 nm. This is because the CCD (charge coupled device) or CMOS (complimentary metal oxide semiconductor) sensors which are usually fitted in COTS cameras are likely to sense wavelengths lower than 400 nm (Nijland *et al.*, 2014).

The RSR of the RGB channels for a given wavelength λ were calculated as per Eq. 2-1 (Suzuki *et al*,. 2009) and a linear relationship between the input radiance and the output signal is assumed (Darrodi *et al.*, 2015).

$$R(\lambda) = \eta \frac{r(\lambda)}{I(\lambda)}, \quad G(\lambda) = \eta \frac{g(\lambda)}{I(\lambda)}, \quad B(\lambda) = \eta \frac{b(\lambda)}{I(\lambda)} \qquad (2\text{-}1)$$

Where r, g, and b = the mean spectral response from each camera channel (red, green and blue channels, respectively) given in DN values and calculated from the 9x9 window (output signal);
I = the light intensity (monochromator and sphere) given in relative spectral radiance units (input radiance);
η = the normalized coefficient.

Instead of using absolute physical units, the η coefficient is applied to generate a relative spectral response, as it results in lower calibration uncertainties (Darrodi *et al.*, 2015). For each camera, the mean spectral response over all of the wavelengths were normalized (η) by the maximum signal detected among the RGB channels, yielding dimensionless units with a peak equal to 1.

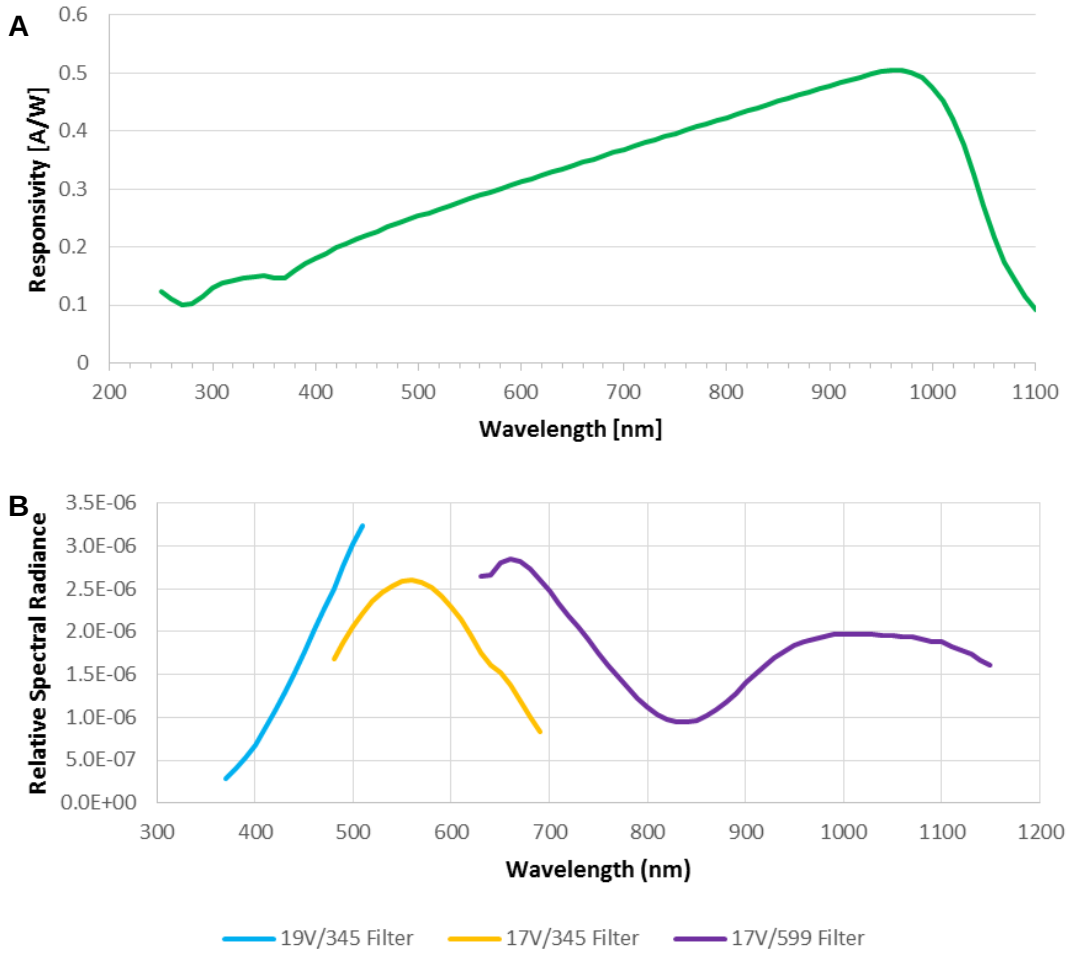

Figure 2-7: The responsivity of the silicon photodiode (A); The relative spectral radiance of the monochromator at given voltages using specific filters (B).

2.5.4 Results

All of the un-modified cameras showed similar ranges within the visual spectrum as would be expected (400~700 nm; Figure 2-8), with almost all of the RGB channels covering this range but with varying degrees of sensitivity. The green channel for each camera showed the highest peak response due likely to all cameras being using a Bayer colour filter array, which has twice as many green filters compared to red or blue, as this more closely resembles how the human eye sees the world (Lebourgeois *et al.*, 2008; Verhoeven, 2010) and improves luminance sampling and image sharpness (Verhoeven *et al.*, 2009; Verhoeven, 2010).

However, a closer analysis on both shape and intensity of the RSR curves reveals differences among the camera models, and most noticeable are the differences of the Sony cameras compared to the other two models (Figure 2-8). The red channel of the Sony camera (Figure 2-8c) has a much lower peak response (0.58) compared to Panasonic (Figure 2-8a) and Canon (Figure 2-8b) red channels, which both peak with a response of ~0.8. The green channel curve of the Sony also shows a narrower shape than both Panasonic and Canon. For the blue channel, the Canon and Sony tend to have very low sensitivity after around ~560 nm; however, the Panasonic keeps on sensing until around 680 nm.

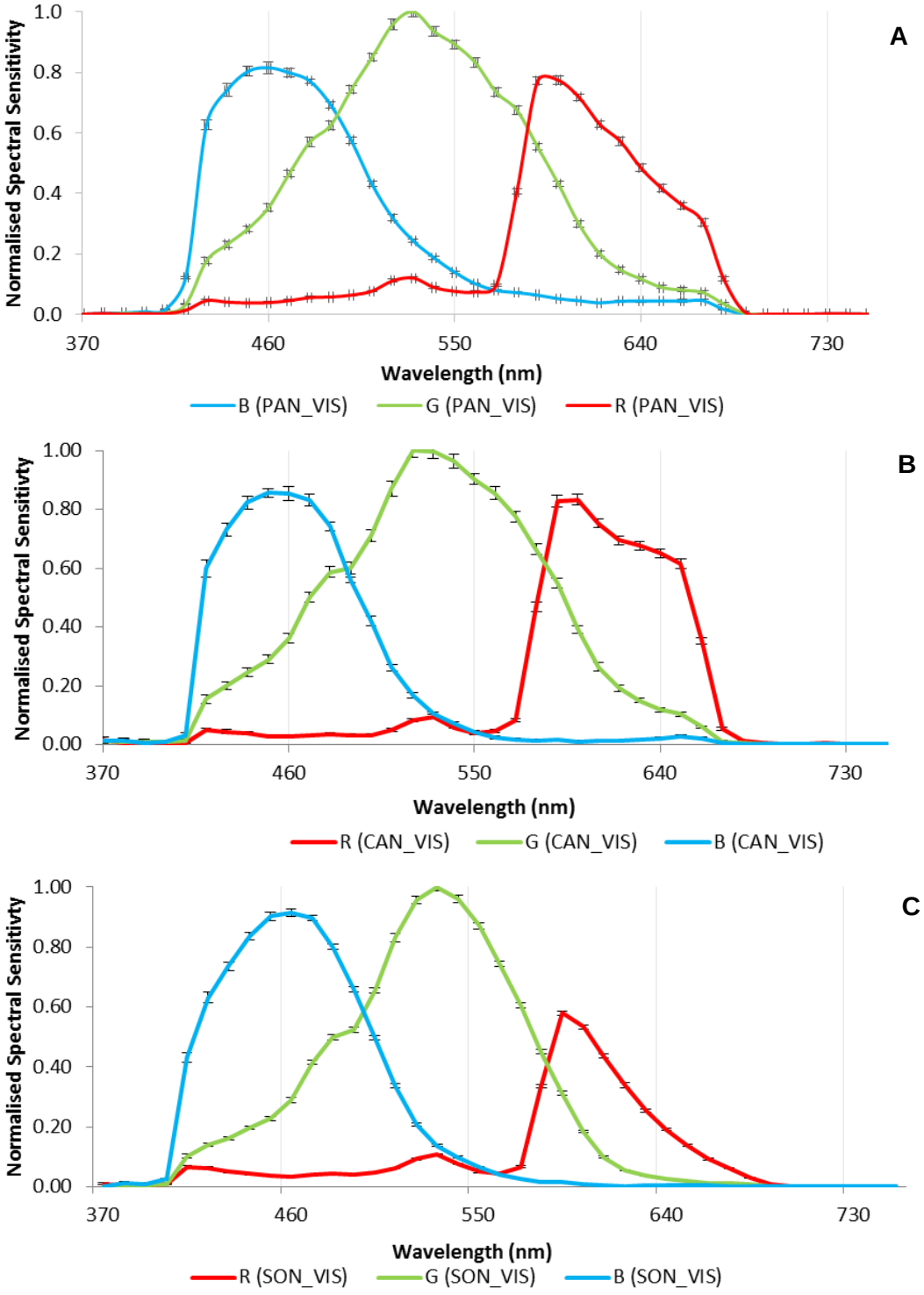

Figure 2-8: Spectral responses from the un-modified Panasonic (A), Canon (B) and Sony (C) cameras, normailised to the peak value of each cameras green channel.

The FS Canon camera (figure 2-9) shows the full spectral sensitivity of the Canon sensor, with responses from 370~1020 nm for all of the channels, revealing the expected COTS cameras sensitivity to NIR wavelengths when the internal NIR blocking filter is removed (Verhoeven *et al.*, 2009). The blue channel has a very low response from 560~770 nm with a peak at 820 nm (well within the NIR band), which is accordance with what could be expected from a Bayer filter (Nijland *et al.*, 2014).

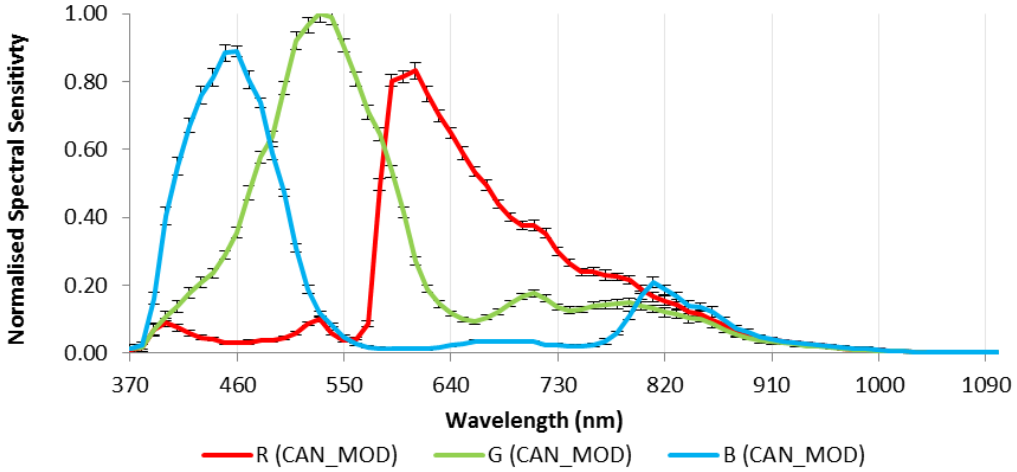

Figure 2-9: Spectral response for the modified to full spectrum Canon camera normalised to the peak of the green channel.

With a 585 nm long pass filter attached to the FS Canon camera (figure 2-10a), the NIR peak in the blue channel could potentially be exploited as the blue channel is now the only channel that is predominately sensitive to NIR wavelengths and is beyond the red edge feature of 700~720 nm (Hunt *et al*., 2010). This same characteristic is not observed with the blue channel of the modified Panasonic (figure 2-10b), as its sensitivity increases rapidly after 670 nm, detecting some wavelengths within the red region of the spectrum and across the red-edge feature. It is noticeable for both cameras (Figure 6) that their blue channels have a much lower intensity than the red channels.

Both modified Panasonic and modified Canon cameras have the red channel as the most sensitive to NIR light, however the Panasonic peaks at 710 nm, within the red-edge feature, meanwhile the Canon peaks at 620 nm, within the red region of the spectrum (figure 2-10). The green channels have an intermediate sensitivity between blue and red channels (figure 2-10).

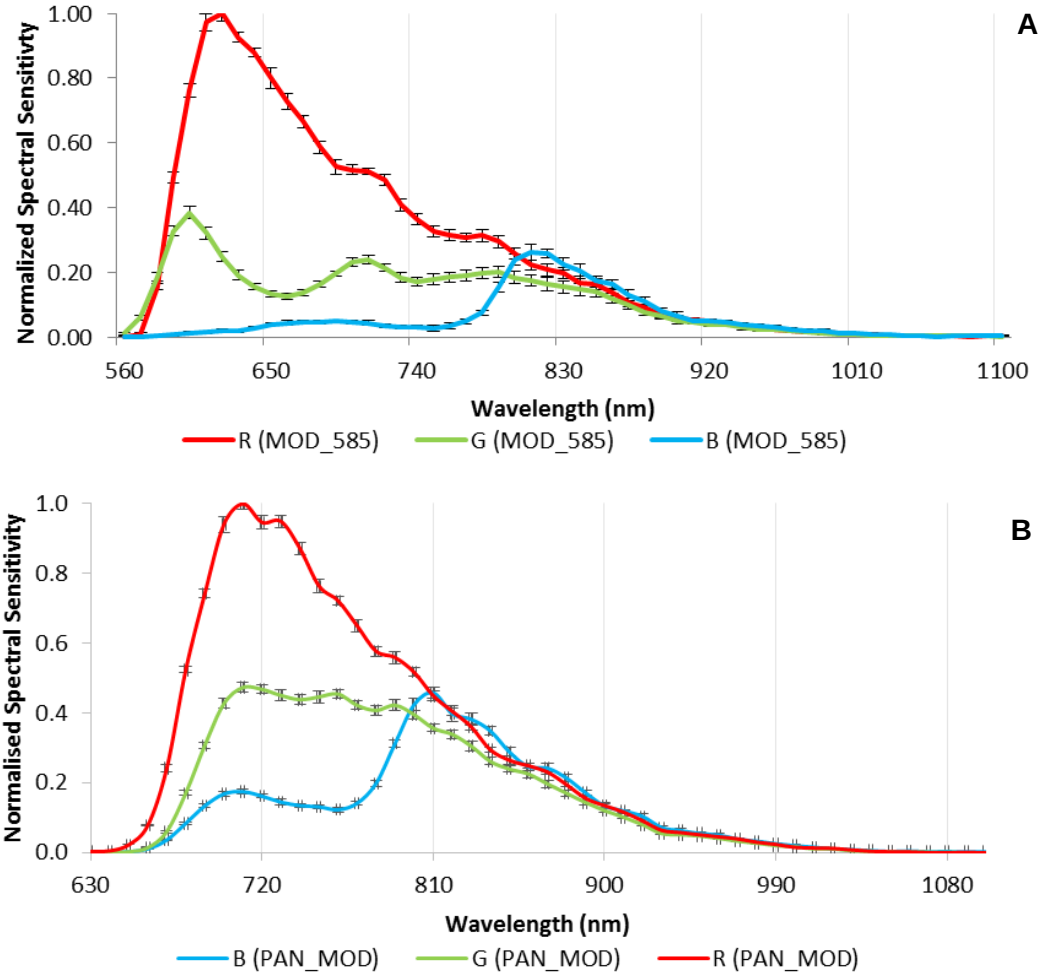

Figure 2-10: Spectral response for the modified to full spectrum Canon with with a 585 nm long pass filter (A) and for the modified Panansonic camera (B), both normailised to the peak of the red channel.

The red and green channels of the modified Sony camera (figure 2-11) have well characterized curves peaking in the green and red wavelengths respectively, that are narrower and of a more equal intensity compared to the same channels in the un-modified Sony camera (figure 2-8c). The blue channel however has a much lower sensitivity than the green and red, with two main peaks at 400 nm and 830 nm, meaning that this channel may not be suitable to be used as the source of a NIR signal.

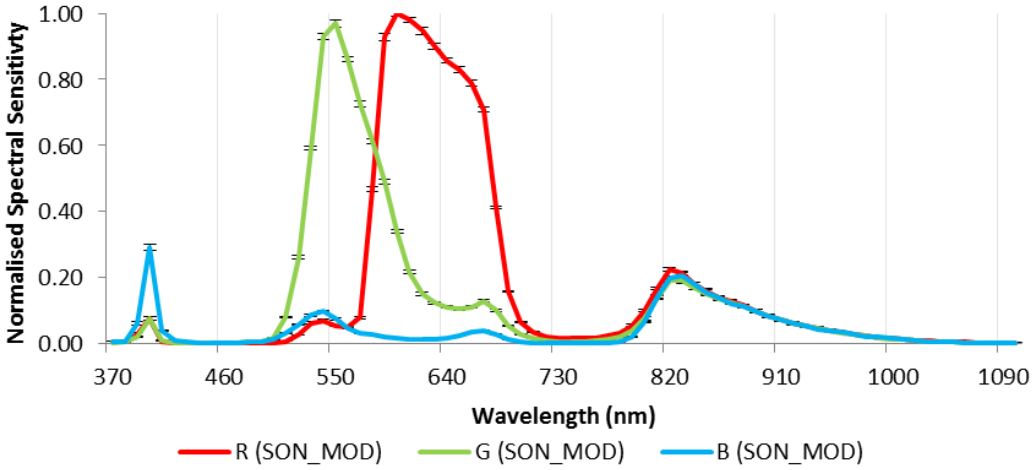

Figure 2-11: Spectral response for the modified Sony camera, normailised to the peak of the red channel.

2.5.5 Discussion and conclusions

The image acquisition method employed is a relatively standard technique, variations of which have been employed by numerous studies (Darrodi *et al*., 2015; Jiang *et al*., 2013; Suzuki *et al*., 2009; Verhoeven *et al.*, 2009) and is known to give accurate results but it does require expensive and specialised laboratory facilities and equipment (Bongiorno *et al.*, 2013; Darrodi *et al*., 2015). Other methods could be employed instead, such as those indicated by Bongiorno *et al.* (2013), who themselves used a linear variable edge filter to characterise the spectral response of several COTS cameras; However, they may not be able to cover the entire range of wavelengths sampled in this study.

In the image processing stage, the use of DCraw (or a distribution/modification of) as a tool to convert RAW images into linear TIFF files is also widely acknowledged in the literature (Lebourgeois *et al.*, 2008; Rabatel *et al.*, 2014; Verhoeven *et al.*, 2009), but often we see the further processing of these converted images using proprietary software such as ENVI (Hunt *et al*., 2010) or MATLAB (Verhoeven *et al.*, 2009). Using an open source program such as ImageJ to process the images means that this technique can be used by anyone, and the macro and batch processing options available meant that processing a large volume of images (over 200 for FS Canon camera alone) is both quick and simple.

The data presented here has not gone through any corrections to account for extra noise that may be present, as some of the cameras did not have dark images taken. So, the results are representing the response of the sensor to the photons hitting it,

plus any dark current signal and bias signal (Verhoeven *et al.*, 2009). The bias signal is likely to be small, but the dark current signal could be quite large depending on the temperature at the time of taking the image and the ISO and exposure settings used (Verhoeven *et al.*,2009).

This unwanted noise reduces the signal to noise ratio (SNR) and can be corrected for by taking dark images at the same time as momochromatic light image acquisition and using DCraw to subtract a dark frame as indicated in Appendix A. Other points of possible error that would need to be corrected for are the identification and interpolation of bad pixels within the image (pixels that fail to sense light levels), which can also be corrected though the use of DCraw, and vigenetting. Vignetting is where the brightness of an image reduces away from the centre of the image and can be caused due to physical effects of the cameras lens as well as the angle of the light source in relation to the lens (Lebourgeois *et al.*, 2008). The reasoning behind having a small and central 9 x 9 pixel sampling window in the image processing phase was partly due to this phenomenon and for imagery that is to be used for remote sensing this would need to be corrected by following a method similar to that of Lebourgeois *et al.* (2008).

A final source of error that was overlooked at the time of image acquisition is that of reflections off of the camera lenses themselves (and any external filters), back into the integrating sphere (as the lens was positioned so close to the detection port of the integrating sphere). The properties of any anti-reflective coating of the camera lenses or filters used is not known, however it is likely that its effect would be small in the visual region of the spectrum and perhaps more pronounced towards the NIR region, as the cameras were principally designed to detect visual wavelengths of light.

With these potential sources of error acknowledged, the results of the experiment can be investigated, and they reveal that the RSR differs between the un-modified camera models and therefore we cannot assume that all COTS digital cameras have a standard Bayer array response or internal NIR filter response, which echoes that of other studies (Darrodi *et al*., 2015; Jiang *et al.*; 2013). Once the spectral sensitivity of a camera is known, judgments can be made on what the camera could be used for (e.g. vegetation monitoring), how it can be used (e.g. singularly or in

combination with another camera) and what filters could be applied in order to capture desired wavelengths of light.

For instance, monitoring vegetation with COTS digital cameras usually requires the combination of visible and NIR wavelengths in order to exploit the well-known spectral characteristics of healthy plant leaves, namely the low reflectance of visible wavelengths due to chlorophyll absorption and high reflectance in the NIR wavelengths due to plant cell structure. This behaviour results in a spectral contrast which is the basis for many vegetation indices (VI), such as the Normalized Difference Vegetation Index (NDVI) (Rouse *et al.*, 1973).

In relation to this Hunt *et al.* (2010) found that certain colour channels (blue and green) of some COTS digital cameras are not very sensitive to NIR wavelengths, allowing a red light blocking filter to be used to create a single camera multispectral sensor that outputs blue, green and NIR bands and could be used to estimate the Green Normalised Difference Vegetation Index (GNDVI) for agricultural crop monitoring purposes.

In contrast to Hunt *et al.* (2010), a study by Rabatel *et al.* (2014) used a single COTS camera with all channels sensitive to NIR (as is the case with the cameras of this study) and investigated the use this camera as a multispectral sensor to estimate NDVI. A blue light blocking filter was used to allow NIR wavelengths to be captured in the blue channel and red+NIR wavelengths in the red channel. It utilised an orthogonal projection method to simulate the separation of the red and NIR wavelengths to allow NDVI estimates to be made of agricultural crops.

Alternatively, two cameras could be combined, one un-modified and the other modified to capture NIR, so that separate red and NIR bands can be acquired and registered together to allow NDVI estimation (Dare, 2008). This approach can have issues with the geometric alignment of the bands as they come from two separate instruments (Dare, 2008), which of course would not be an issue with a single camera approach (Rabatel *et al.* 2014), however the dual camera method has other advantages such as more control of the shape of the NIR band, reduced concerns about SNR and the fact that standard RGB colour images can be produced at the same time (Rabatel *et al.*, 2014).

From the results displayed we can say that our three models of camera are sensitive to NIR wavelengths of light, and this confirms the common knowledge that COTS digital cameras in general are responsive to NIR and could potentially be used as a remote sensing tool (Lebourgeois *et al.*, 2008; Rabatel *et al.*, 2014; Suzuki *et al.*, 2009; Verhoeven *et al.*, 2009). However, the comparison of the spectral responses shows that there might be some implications for combining different cameras or combining channels from the same camera.

For the Panasonic cameras in this study, the dual camera method could be applied as the red channel from the unmodified Panasonic (Figure 4A) could be used as the red band and the red channel from modified Panasonic as the NIR band (Figure 6B), as it has the highest SNR. However, there is some overlap between these bands, in the region of 650-690 nm, which might cause some band correlation (Nijland *et al.*, 2014). Also, the red channel from the modified Panasonic peaks within the red-edge feature (710 nm) and so may not show as strong a NIR response compared to longer wavelengths, as green leaves present their maximum reflectance after 740 nm (Brandelero *et al.,* 2012).

Likewise, for the Canon cameras, the dual camera method could also be applied as the modified camera with a 585 nm filter shows a peak NIR response at ~820 nm (Figure 6A), which could prove more useful than that of the Panasonic camera if used for vegetation monitoring however, it has a considerably reduced sensitivity (~20% compared to the red channel of the same camera) which could lead to issues with SNR. Interestingly the single camera method employed by Rabatel *et al.* (2014) could also be attempted with this modified camera, and in conjunction with a dual camera setup, allowing comparisons between the two methods to be made.

The modified Sony camera has the most interesting spectral response due to the internal notch filter employed, that appears to block wavelengths between 410~510 nm and 690~790 nm. It was expected that this camera would be responsive to red and green wavelengths (in their respective channels) with NIR wavelengths only available in the blue channel. However, the blue channel also has a peak response at 400 nm, meaning that it does not have a predominately NIR response and so may not be effective if used with a dual camera or single camera setup. An alternative method will likely have to be devised to make use of this camera's spectral sensitivity.

In conclusion, although this paper made use of expensive and sophisticated laboratory equipment in order to capture spectral images of known spectral radiances, it does also demonstrate a quick and cheap method of processing images using open source software in order to identify a cameras spectral sensitivity. Our results showed that different COTS cameras might have very different sensitivities, which highlights the importance of determining the spectral response function if using COTS cameras for quantitative applications.

2.5.6 Acknowledgements

Thanks to the Natural Environment Research Council Field Spectroscopy Facility (NERC FSF) for allowing us to use their laboratory facilities and equipment and especially to Christopher MacLellan (NERC FSF) for his advice and help with setting up monochromator and identifying its relative spectral radiance per wavelength. E. Berra would also to thanks Science without Borders Brazil (grant 1121/13-8) for funding his PhD.

2.6 Concluding remarks

The lightweight nature of the sensors and their ability to be remotely triggered means that their deployment could be very flexible, and therefore they could be integrated into a variety of UAS types (e.g. multirotor or fixed wing). The investigation into the spectral sensitivity of the cameras revealed that the modified camera can be used to capture NIR data and therefore, in combination with the un-modified camera, has utility to aid in vegetation surveys through the use of vegetation indexes such as NDVI. However, to satisfy the 1st object of this PhD project, further testing is required to fully appreciate the effectiveness of the sensors as a combined sensor package, and to identify what limitations may apply.

Chapter 3. Aircraft design and image processing

3.1 Introduction

At the time of starting this PhD project in 2014 it was more cost effective and flexible, from a sensor integration and flight planning perspective, to source individual components and build a UAS rather than purchase a ready to fly “off the shelf” system. However, due to the rapid pace of development in this technology (Heaphy *et al.*, 2017) this is now not necessarily true, as manufacturers of popular ready to fly systems such as the DJI Phantom series of multirotor UAS (DJI, Shenzhen, China), have increased their aircrafts capability considerably, in both flight capability and mission planning, as well as sensor package integration. Nonetheless, for maximum understanding of UAS capability, and flexibility in operation, being able to build from components can be vital.

This chapter addresses the 1st, 2nd and 3rd objectives of this PhD project as it describes building a UAS, including integration of its sensor package and methods used to produce orthorectified imagery for further analysis. The UAS created was then used as the primary aerial platform to collect and process data for all other chapters of this thesis.

3.2 Identifying the type of UAS to use

As mentioned in chapter 1 UAS come in many different shapes and sizes but for many research projects UAS below 7 kg are more likely to be used as these are generally cheaper, easier to transport to study locations and have less regulatory issues surrounding their use. They are also typically battery powered and generally only two types of UAS are used, either rotorcraft or fixed wing, although the use of more novel platforms such as powered paragliders can have benefit for certain situations (Thamm, 2011; Dunford *et al.*, 2009). One of the main differences between rotorcraft and fixed wing designs is that of endurance and speed of flight, which may have a large influence on the choice of aircraft type depending on the nature of the study being undertaken.

Rotorcraft typically take the form of a multirotor aircraft (figure 3-1a) and are arguably the most popular design due to their mechanical simplicity (Dvořák *et al.*, 2015) as only the rotors are moving. They are relatively easy to operate manually as the autopilot stabilises the aircraft allowing it to hover in place or fly at very slow speeds if necessary and they can also take off and land vertically (VTOL), so require

a minimal amount of space to operate from. Single rotor rotorcraft (helicopters, figure 3-1b) share many of these advantages, however are mechanically more complex due to the variable pitch nature of their rotor blades and are therefore a less commonly seen.

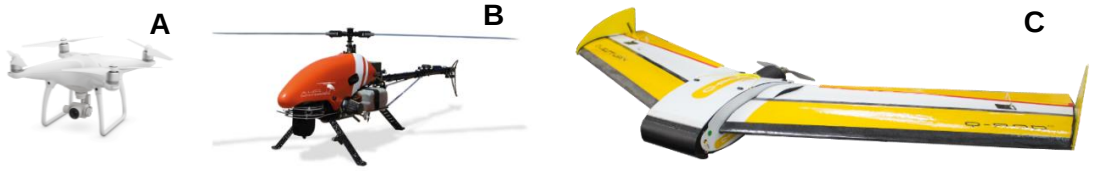

Figure 3-1: Example UAS; (A) A DJI Phantom 4 Multirotor (DJI, 2018a); (B) Alpha 800 helicopter (AlphaUAS, 2018); (C) Quest Q200 fixed wing (QuestUAV, 2018a).

Fixed wing aircraft (figure 3-1c) are mechanically more complex compared to multirotor designs due to the control needed for flight surfaces (e.g. rudder, elevator, ailerons and for some aircraft flaps as well). As the aircraft require constant forward flight to avoid stalling, they typically operate at higher airspeeds, so require sensors that have a shorter integration to allow effective capture of imagery. This also means that they require more attention from the pilot if being controlled manually as they cannot be made to hover (Dvořák *et al.*, 2015), although this is not an issue when the autopilot is in full command of the aircraft. Depending on their size they also require more space for take-off and landing, with smaller aircraft being hand launched, but larger, heavier ones requiring assistance (e.g. a catapult launcher) to get into the air (figure 3-2)

Figure 3-2: (A) A Quest Q200 being bungee launched (QuestUAV, 2018b); (B) A Quest Datahawk^{AG} being hand launched (QuestUAV, 2018c).

More recently the concept of hybrid aircraft that have elements of both multirotor and fixed designs have started to appear (figure 3-3). At the time of starting this project these types of aircraft were very much in the design stage and not mature enough to be used as a reliable aerial platform due to the complexity of their design

but in the future, they are likely to be very popular designs combining the endurance of a fixed wing aircraft with the VTOL ability of a multirotor.

Figure 3-3: The FireFLY6 hybrid VTOL UAV (BirdsEyeView, 2018)

With this in mind it would seem that multirotor aircraft are far more flexible from a sensor deployment perspective, are simpler to operate (both in flight and for take-off and landing) and therefore of ideal use for a varied range of applications. However, the biggest difference between the two types of aircraft is that of endurance. Multirotor aircraft have very limited lift surfaces (essentially just the rotor blades themselves) so use far more power to stay airborne compared to a fixed wing design that benefits from the lift provided by its wings. Multirotors by their very name have multiple rotors (engines) in order to supply enough thrust to keep aircraft airborne, typically four (quadcopter), six (hexacopter) or eight (octocopter) rotors are used. In contrast a fixed wing will only require one or two rotors to provide enough thrust for forward flight. Figure 3-4 shows an example of different multirotor and fixed wing designs (both of the shelf and custom made) and the amount of energy each one requires during flight and the resulting range (endurance) of each design.

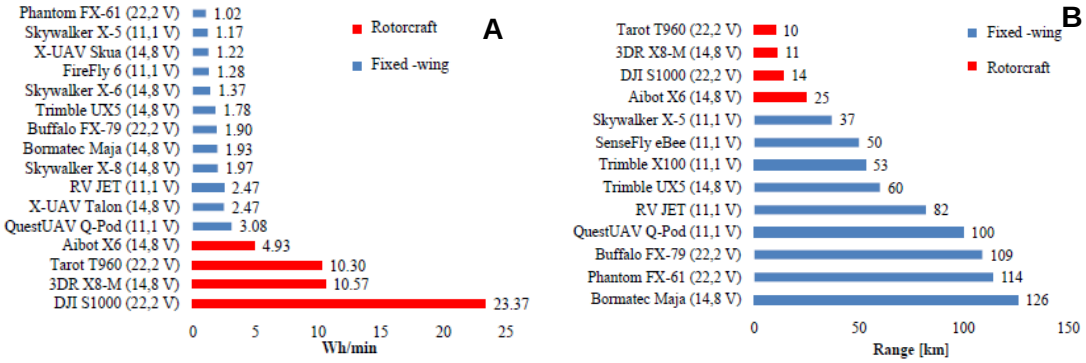

Figure 3-4: (A) The energy requirements (Wh per minute) for various fixed wing (blue) and multirotor (red) aircraft (Dvořák et al., 2015); (B) The expected endurance (km) for various fixed wing (blue) and multirotor (red) aircraft (Dvořák et al., 2015).

There is therefore a clear distinction in the use of either a multirotor or fixed wing design based on the level of endurance required and if larger areas are to be surveyed a fixed wing design would be the obvious choice. However, as this project was primarily investigating relatively small areas such as agricultural trials (typically < 5 ha) that would require flying at low level and therefore at low airspeeds (to enable effective image capture), only multirotor aircraft were considered as the basis for the aerial platform for this project.

3.3 Composition of a multirotor aircraft

A multirotor aircraft is made up of three main parts; (1) the airframe, which is the fuselage of the aircraft along with elements such as the landing gear; (2) the propulsion system, which includes the motors, electronic speed controllers (ESC), propellers and power source (e.g. a battery) and (3) and command and control system, which includes a radio control transmitter and receiver (for manual control), a ground control station (GCS) with radio telemetry and the autopilot onboard the aircraft itself (Quan, 2017).

3.3.1 The airframe

The simplest type of multirotor airframe is the quadcopter (Sidea *et al.*, 2014; Koslosky *et al.*, 2017, Quan, 2017) as its four rotors (with propellers of a fixed pitch) allow six degrees of freedom (figure 3-5). This permits transitional movement along the X (forward/backward), Y (left/right) and Z (up/down) axes and rotational movement around the X (roll), Y (pitch) and Z (yaw) axes (Koslosky *et al.*, 2017).

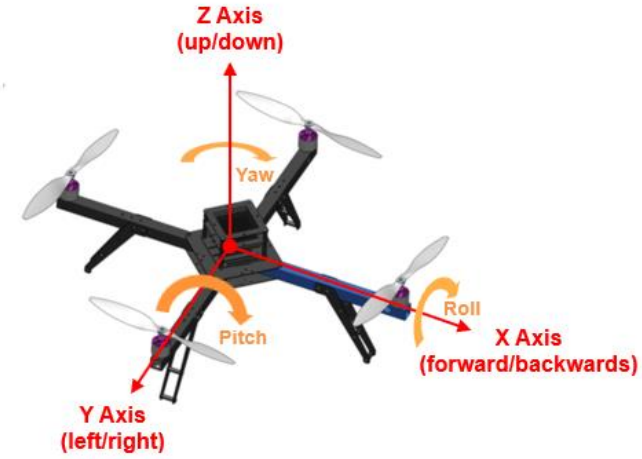

Figure 3-5: Transitional and rotational movement of a quadcopter (adapted from Arducopter, 2012).

A quadcopter is configured to have counter rotating pairs of rotors so that two always spin clockwise and two anticlockwise, counteracting each other and reducing the total angular momentum to zero whilst allowing sufficient thrust to counteract gravity and allow the aircraft to remain airborne (figure 3-6a). Angular momentum is calculated by multiplying the angular velocity by the moment of inertia, therefore rotational movement is controlled via changes in the speed (torque) of each rotor. For the aircraft to rotate on its Z axis (yaw), one counter rotating pair must decrease in speed and the other must increase in speed in order to increase angular acceleration around the Z axis whilst maintaining overall thrust (Quan, 2017; Koslosky *et al.*, 2017; figure 3-6b).

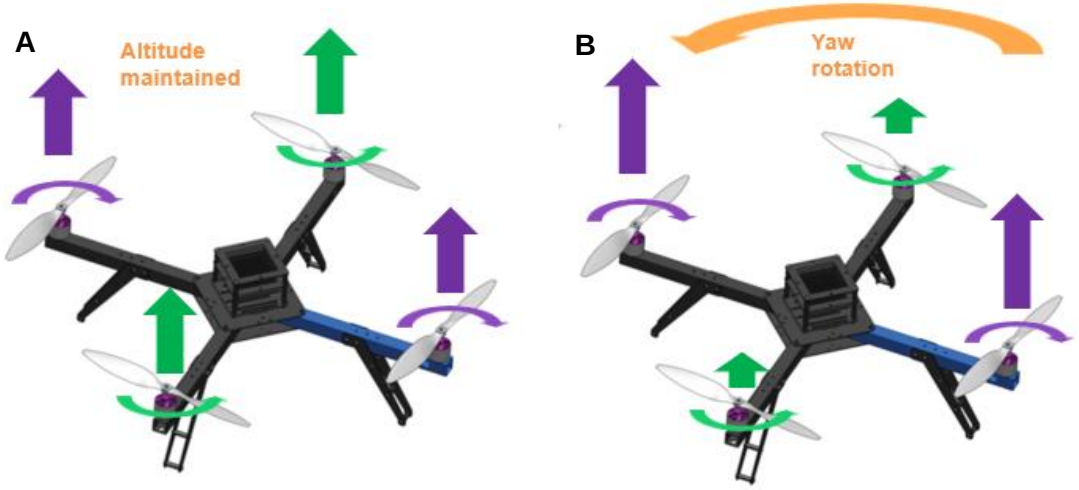

Figure 3-6: (A) Angular momentum is zero with equal thrust on all motors; (B) Angular acceleration is increased around the Z axis as one counter rotating pair is reduced in speed, whilst the other increases (adapted from Arducopter, 2012).

For the aircraft to move forwards or backwards, the aircraft must rotate along its Y axis (pitch) to create a pitch angle by decreasing the speed of the rotor in the desired direction of travel and increasing the speed of the rotor in the opposite direction in order to maintain overall thrust (figure 3-7a). Likewise, to move the aircraft to the left or right, the aircraft must rotate along its X axis (roll) to create a roll angle by decreasing the speed of the rotor in the desired direction of travel and increasing the speed of the rotor in the opposite direction in order to maintain overall thrust (Quan, 2017; Koslosky *et al.*, 2017; figure 3-7b).

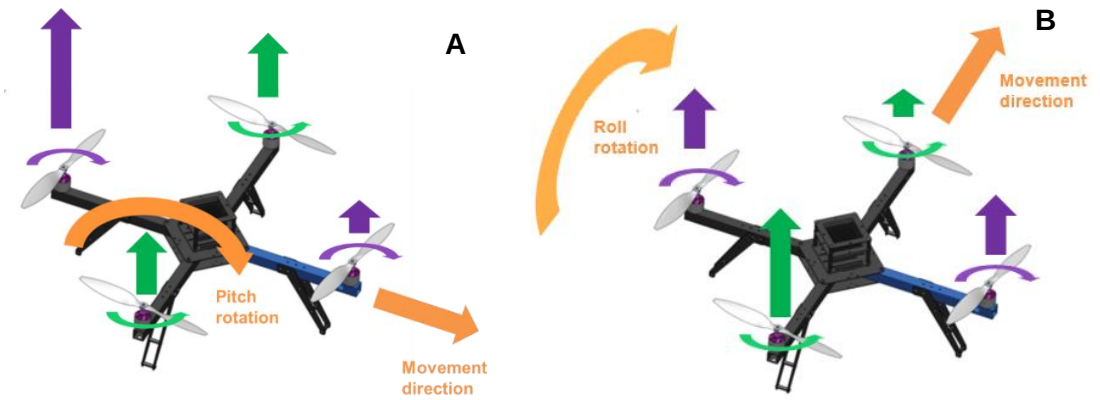

Figure 3-7: (A) Forward movement due to rotation on the Y axis as rear motor speeds up and forward motor slows down; (B) Movement to the right due to rotation on the X axis as the left motor speeds up and the right motor slows down (adapted from Arducopter, 2012).

The majority of multirotor airframe types follow this same principle of movement but simply with a varying number of counter rotating pairs. For instance, hexacopters have three counter rotating pairs (figure 3-8a), octocopters have four (figure 3-8c), with the extra motors giving the aircraft more lifting capacity (thrust) and redundancy should a rotor fail (Quan, 2017) but at the expense of a larger, heavier aircraft that uses more power. Not all airframes have their motors orientated in the same direction as some designs have coaxial rotors, with each arm of the airframe having two motors facing in opposite directions (figure 3-8b & 3-8d). Coaxial airframes provide more thrust but from a smaller airframe, however they do suffer some penalties in efficiency and thrust compared to airframes with the more typical "flat" positing of the rotors, due to the lower propeller being within the prop wash of the upper propeller (Bondyra *et al.*, 2016)

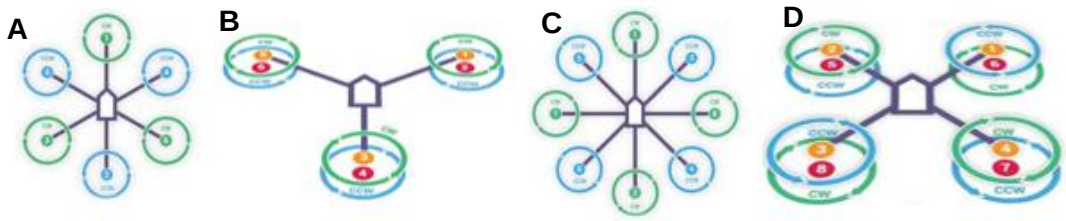

Figure 3-8: Configuration of different multirotor frames and propeller direction (green clockwise, blue anti-clockwise); (A) Hexacopter; (B) Coaxial hexacopter; (C) Octocopter; (D) Coaxial octocopter (Ardupilot, 2016a).

3.3.2 The propulsion system

The propulsion system has to be able to allow the aircraft to maintain stable flight and manoeuvre whilst carrying itself and the sensor package and therefore must be designed based on the airframe type that has been selected. The propulsion system

can be electric, or fuel based (figure 3-9), which can give significant benefits to aircraft endurance, however the vast majority of current multirotor aircraft use an electrical population system powered by a battery.

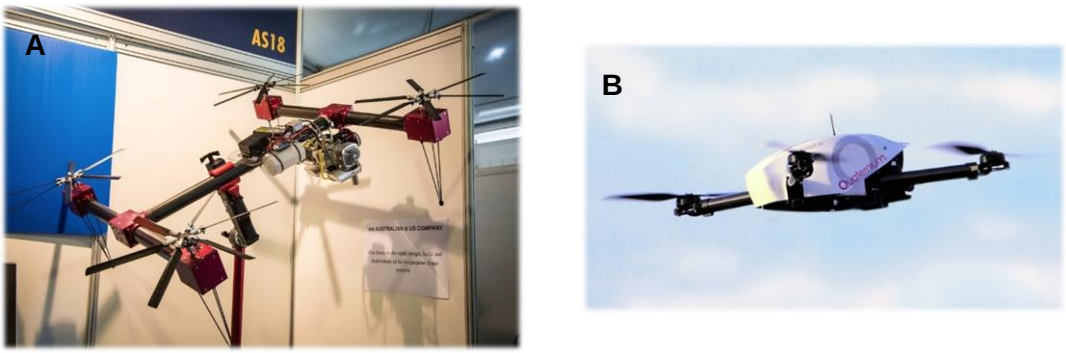

Figure 3-9: (A) The Belias, a prototype heavy lift (10 kg payload) variable pitch petrol powered quadcopter with an expected three-hour endurance (Blain, 2017). (B) The HYBRiX.20, a prototype hybrid fuel-electric multirotor with a 2.5 kg payload and two-hour endurance (Quaternium, 2017).

3.3.2.1 Propellers

Propellers provide the main lifting surface for a multirotor and are made from a variety of materials (e.g. plastic, wood or carbon fibre) and come in a variety of sizes, blade pitch and numbers of blades, although this is typically only two as this configuration is more efficient (Quan, 2017). The materials used dictate the strength of the propeller (carbon fibre being the strongest) but also the moment of inertia, as lighter propellers will have faster responses to changes in motor speed. The size of the propeller (both length and width) dictates how much thrust can be generated, as larger propellers create a larger disc area and therefore lifting surface but at the expense of requiring more torque from the motor. The blade pitch determines how far a propeller will move through the air for each rotation of the motor, with higher pitched propellers allowing faster movement if the motor revolutions are the same, but again requiring more torque from the motor (Quan, 2017).

3.3.2.2 Motors

Electric motors also vary in size and abilities, with smaller motors typically producing lower torque and being able to spin smaller, shallow pitched propellers at higher revolutions per minute (RPM), whereas larger motors with higher torque are able to spin larger propellers (with potentially a steeper pitch) but at a slower RPM. The unit of measurement used to understand how fast a motor can rotate is termed Kv, which indicates the RPM of an unloaded motor (i.e. no propeller) when 1 V (volt) is

applied to it (e.g. an unloaded 100 Kv motor will spin at 100 RPM if 1 V is applied to it; Quan, 2017). Lower Kv motors (typically < 400 Kv) produce higher torque and so can drive larger propellers and are often seen used with larger multirotor platforms where higher thrust is required (figure 3-10a). High Kv motors (typically > 1000 Kv) have low torque and can only be used with smaller propellers and are typically seen used on very small multirotors that are used for recreational activities such as racing (figure 3-10b), as the small motor and propeller combination can react faster making the aircraft far more agile.

Figure 3-10: (A) Raven heavy lift coaxial octocopter (VulcanUAV, 2016); (B) Connex Falcore mini racing drone (GetFPV, 2018).

3.3.2.3 Electronic speed controllers

Electronic speed controllers are used to vary the speed of each motor (one ESC is connected to each motor) via the pulse width modulated (PWM) signals received from the command and control system (the autopilot). ESCs can convert the direct current (DC) power source (the battery) into an alternating current (AC) power source required to drive the motors. The main parameter of interest with ESC is that of their maximum continuous current rating, as depending on the motor and propeller combination used, the ESC needs to be able to cope with the expected maximum current draw. Typically, ESC overrated by 20 % are used (Quan, 2017), so if a motor propeller combination is likely to require 20 amps (A) when running at full power, a 24 A ESC will be used to ensure a safety margin.

3.3.2.4 Batteries

Batteries for multirotors are typically lithium-ion polymer (LiPo) and will have varying numbers of cells in series that allow different terminal voltages. LiPo cells have a nominal voltage of 3.7 V, which rises to 4.2 V when fully charged (Quan, 2017), so

to create a battery that outputs 14.8 V when charged, the LiPo battery must contain four cells arranged in series (termed 4S). Batteries can also be arranged in parallel to increase capacity whilst maintaining voltage, so the terminology for two, four cell batteries in series is 4S2P. The capacity of batteries is usually indicated in milli-Ampere-hours (mAh) and is an indicator of how long the battery will last (e.g. a 10,000 mAh battery will last for 1 hour under a 10 A load) and also how much current can be drawn from the battery continuously before it fails (its discharge rate; eq. 3-1; Quan, 2017).

$$\text{Discharge Rate (C)} = \frac{\text{Current of Discharge (mA)}}{\text{Capacity (mAh)}} \quad (3\text{-}1)$$

The maximum discharge rate of a battery depends on its quality, so batteries that are lighter usually have lower C ratings compared to heavier more robust batteries. The maximum discharge rate required depends on the number and maximum power requirements of the motor propeller combination. For instance, a quadcopter that requires 20 A for each motor when running at maximum will need to be able to draw 80 A and therefore a 4000 mAh battery will need to have a C rating of at least 20 to be able to fulfil the motors requirements without failing (4000 mAh x 20C = 80 A). Most batteries will give two C ratings, one for continuous current output and a second to indicate an allowable burst current output for a very limited time (typically twice the continuous current but for only a few seconds).

3.3.2.5 Power distribution

There also needs to be a way of distributing power from the battery around the airframe to each of the motors, the command and control system and any other ancillary equipment present. Typically, this is handled by a power distribution board and like the ESCs, the power distribution board also needs to be able to cope with the potential maximum current draw from all of the motors and other equipment when running at full power.

3.3.3 Command and control system

To be able to manually control a multirotor, the operator needs to have a radio control (RC) transmitter configured with flight sticks and switches to allow movement and other actions on the aircraft to be commanded. On the aircraft itself an RC receiver is required that can convert those radio signals into a format suitable for the autopilot to understand (Quan, 2017). Radio telemetry from the aircraft is often also

used to update a ground control station (GCS), so that the status of the aircraft can be ascertained (e.g. battery capacity remaining, altitude, speed etc.), but the most important command and control system is the autopilot itself (figure 3-11).

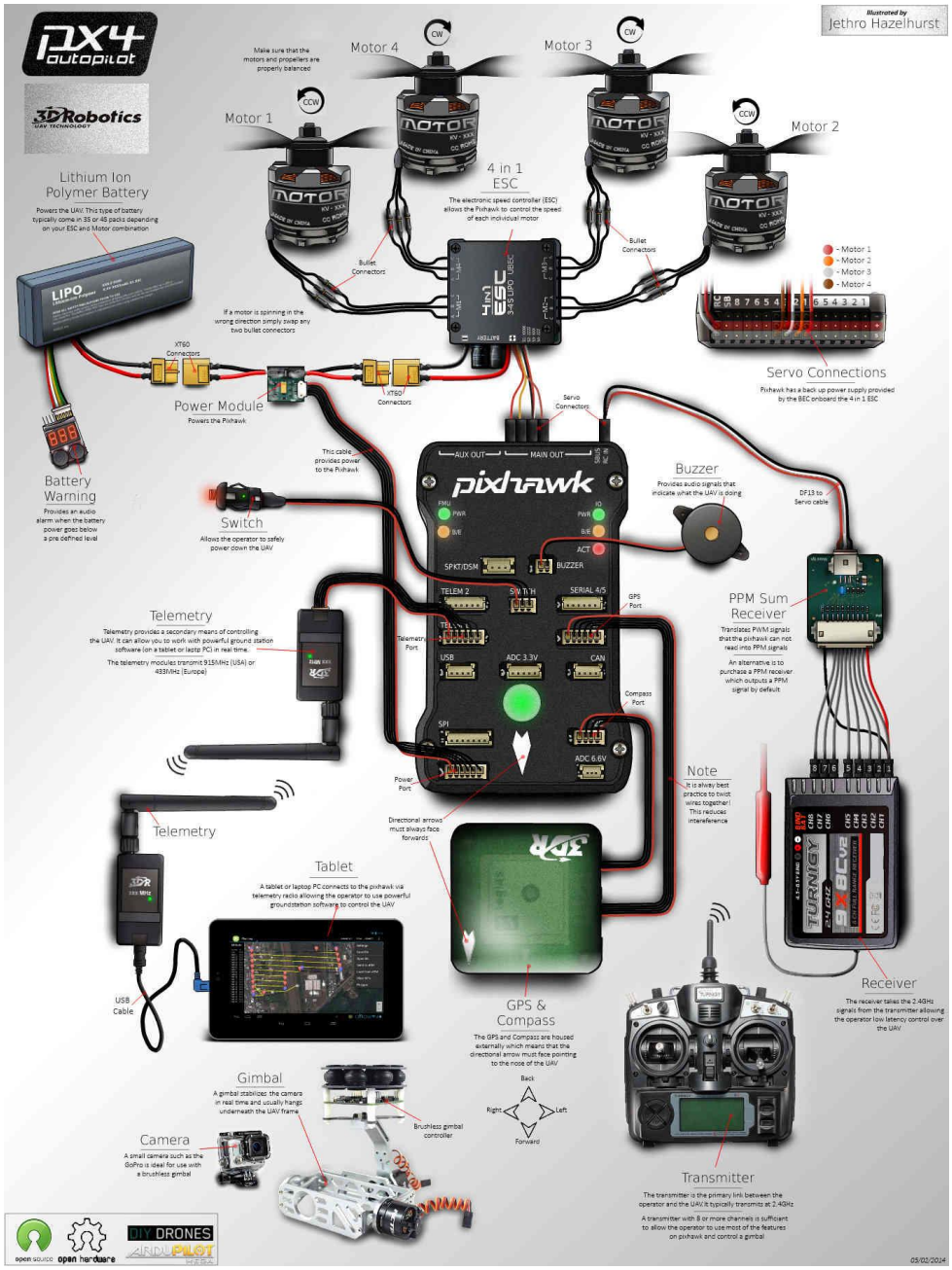

Figure 3-11: Expanded diagram showing the major components of a multirotor and their connections to a Pixhawk autopilot (Hazelhurst, 2014).

3.3.3.1 Flight controllers (autopilot) and avionics of a quadcopter

Quadcopters are inherently unstable (Sidea *et al.*, 2014; Lim *et al.*, 2012) as the four rotors require constant manipulation in order to maintain stability and allow the aircraft to manoeuvre. This would not be possible to control manually so a flight

controller (from here in called an autopilot; essentially a small computer) is required to handle the thrust requirements of each rotor. The autopilot can vary the speed of the motors by communicating with the ESC attached to each motor (figure 3-11), however to know what speed changes are necessary an autopilot requires a suite of sensors so that it can understand the forces being applied by the aircraft (the results of its own commanded movement) and to it (e.g. wind).

The sensor suite is comprised of a number of Micro-Electro-Mechanical Systems (MEMS) that are widely used in other electronic devices such as smartphones (Loianno *et al.*, 2015). The Inertial Measurement Unit (IMU) provides the quadcopter with an understating of its current attitude and is typically comprised of a three axes gyroscope to measure rotational changes across each axes; a three axes accelerometer to measure acceleration rate along each axes; and a magnetometer to measure the magnetic field and identify aircraft heading (Koslosky *et al.*, 2017). Further to this a barometer is used to measure altitude and a global navigation satellite system (GNSS) receiver is used to provide a 3D position in space.

Within the autopilot a control framework is required in order to analyse and react to the information coming from the IMU, barometer and GNSS, which first need to be filtered for noise before forming part of the control system. Typically, an Extended Kalman Filter (EKF) is used to filter and fuse the different sensor inputs and give a current estimated state of the attitude of the aircraft (Quan, 2017; Lim *et al.*, 2012). This estimated state then forms part of the control process by being an input within a Proportional-Integral-Derivative (PID) control loop feedback mechanism (figure 3-12).

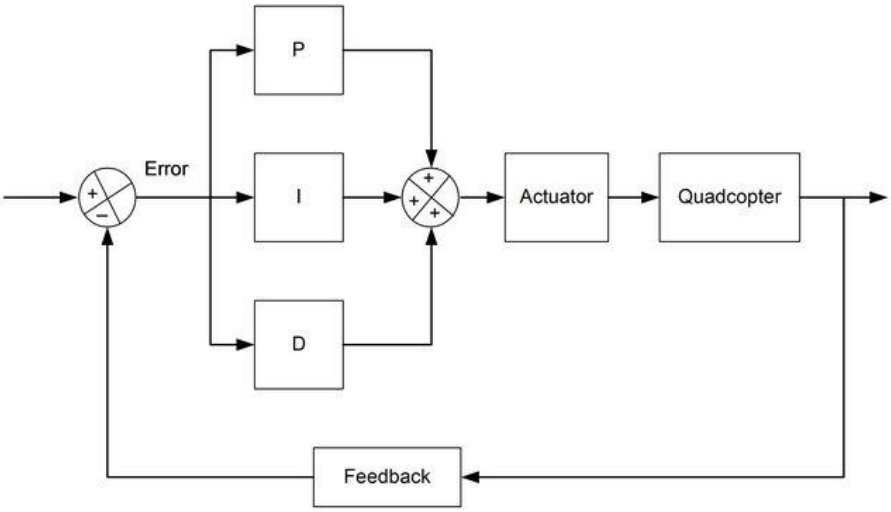

Figure 3-12: Process diagram of a PID control feedback loop (Hanafi et al., 2013).

The purpose of PID controllers is to correct a difference (error term) between the value that has been measured (the process variable; e.g. the current altitude of the quadcopter) and the desired value that is required (the set point; e.g. an increase in altitude). The proportional element is a gain of this error signal (proportional to the error) and will give a large output if the error is large, which the aircraft will respond to (i.e. it increases thrust and starts increasing its altitude) with the changes in its current attitude being feedback into the PID controller. However, if the gain is set too high, then an overshoot of the desired set point could occur (i.e. the aircrafts altitude is now higher than desired) leading to an oscillating effect as the PID controller attempts get to the desired set point (National Instruments, 2011).

The integral element sums the error term over time, so even a small error will result in an eventual change to ensure that the error becomes zero, driving the steady-state error to zero (the steady-state error is the final difference between the process variable and the set point). For instance, the aircraft is requested to hold its position, but its altitude is slowly reducing as thrust is not sufficient to maintain a stable altitude (e.g. wind is affecting it). Therefore, an increase in thrust would be requested that would keep increasing over time until the desired altitude is reached. This however can also lead to oscillations, so the derivative element helps to control this effect by reducing the output proportionally to the rate of change in the process variable as it gets closer to the set point, essentially dampening the outputs made by the proportional and integral elements (National Instruments, 2011)

Several PID controllers will be used to control the various aspects of the aircraft attitude (e.g. roll, pitch, yaw etc.) and all need to be tuned in order for the aircraft to be stable in flight. The tuning can vary depending on what role the aircraft is to perform, therefore an aircraft to be used for racing would be tuned aggressively so that control inputs respond sharply, however an aircraft intended for surveying would have more relaxed tuning as a smoother flight response would be desirable.

3.4 Multirotor aircraft design

In order to design a multirotor that will be able to carry the required sensor package whilst giving an endurance sufficient to satisfy the survey requirements, the weight of all the components is required. This will then allow identification of thrust to weight ratio of the aircraft, which can then be investigated and altered by the selection of different motors and propeller sizes. Ideally a thrust to weight ratio of 2:1 is to be sought (Portlock & Cubero, 2008), resulting in the aircraft hovering at 50 % of its maximum throttle and leaving sufficient remaining thrust for each motor to allow the aircraft to manoeuvre effectively and resit environmental factors (e.g. wind).

3.4.1 Sensor package airframe integration

There are two methods of deploying an optical sensor to a UAS, either fixed mount, where the sensors are mounted directly to the aircraft, often at a slight angle to compensate for the pitching angle of the aircraft during forward flight or gimbaled (figure 3-13). Gimballing a sensor gives more guarantee of nadir image capture as changes to the pitch and roll of the aircraft will be compensated for directly, however it does add extra weight and further power requirements, both of which will reduce the endurance of the aircraft. Capturing nadir imagery is important as different surfaces (especially vegetation) do not necessarily reflect light evenly in all directions (they are not Lambertian). Their reflective properties are based on the angle of incident light and the angle of view of the sensor and can be described using complex bidirectional reflectance distribution functions (BRDF; Aber *et al.*, 2010).

Figure 3-13: Side and underside views of a 3DR Solo UAS fitted with 3 axes brushless gimbal with GoPro camera attached, and a tilted fixed mount with MAPIR camera attached (green camera; MAPIR, 2018).

There are also two main types of gimbal that can be used, either brushless motor based (figure 3-13), or servo based, where smaller servo motors are actuated to change due to the attitude of the aircraft. Brushless motors give a faster and smoother response to changes in the attitude of the aircraft and are the de facto standard for videography applications, however they are heavier, typically require a separate controller to control all of the axis and can consume more power. As the primary purpose of the UAS in this study is as a remote sensing survey platform, the decision to use a servo-based gimbal was taken as it would still give more guarantees for capturing nadir imagery, whilst not adding too much extra weight (figure 3-14a).

To mount the sensor package onto the gimbal, a custom camera rig was created from aluminium sheeting that could be used to house both cameras securely, whilst still allowing access to the memory cards, batteries USB port, camera screen and control buttons (figure 3-14b). Finally, a vibration dampening plate was also used as this can help remove vibrations coming from the airframe, which could otherwise affect image capture from the sensors (reducing the likelihood of blurred imagery). The total weight of the sensor package with its integrating components was ~600 g.

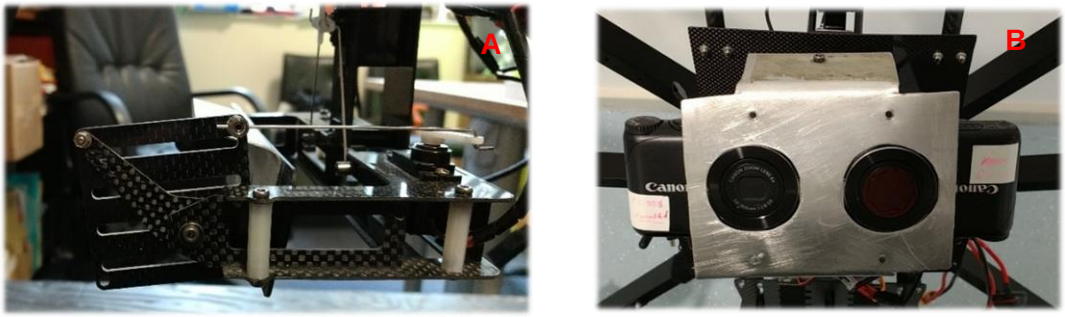

Figure 3-14: (A) The 2 axes (roll and pitch) servo-based carbon fibre gimbal; (B) The aluminium custom camera rig with two Canon A2200 cameras installed.

3.4.2 Airframe and propulsion system modelling

With the knowledge of the size and weight of the sensor package and its integrating components, a suitable airframe and propulsion system can be selected and configured in order to be able to carry it. The web application eCalc (xcopterCalc; Muller, 2018a) was used to identify the abilities of a multirotor (once the weight and type of all of the components were known), as it models how the multirotor will perform based on the inputs given. eCalc gives a good estimation (accuracy of ± 15%; Muller, 2018a) of the main functions of the aircraft (e.g. thrust to weight ratio, maximum speed, endurance etc.) as well as warnings regarding components that could be under stress at maximum power (e.g. ESCs, battery etc.).

3.4.3 Existing aircraft - airframe and propulsion system

At the start of this project the author already had an existing multirotor aircraft (a quadcopter, figure 3-15, table 3-1), available from a previous project (Gibson-Poole, 2013). However, this aircraft was unlikely to produce sufficient thrust to effectively carry both cameras at the same time, as eCalc indicated a thrust to weight ratio of 1.7:1 with an expected all up weight of the aircraft at 2.05 kg when carrying the sensor package. Therefore, the aircraft would be able to lift the sensor package but would have reduced manoeuvrability and poor endurance (Muller, 2018b), indicating that it would not be an ideal option to be used as the main aerial platform for the project. However, it was used in a limited capacity to test image capture using only a single Canon A2200 (attached to a smaller servo gimbal) and as a videography platform using a single GoPro Hero (GoPro, San Mateo, USA) action camera, as this is what it had originally been designed to carry.

Figure 3-15: The quadcopter equipped with GoPro camera in small servo gimbal.

Table 3-1: Limitations of the quadcopter when equipped with a GoPro camera.

Feature	Limitation
Max flight time	9 minutes
Max range at 5 m/s	2.7 km
Max speed	9.7 m/s
Max constant wind speed	5 m/s
Max gusting wind speed	7.7 m/s
Max temperature	35 °C
Min temperature	-5 °C

3.4.4 New aircraft - airframe and propulsion system

As a new aircraft needed to be designed to carry the sensor package effectively, extra funding was sought and supplied by SRUC from the Scottish Funding Council Knowledge Exchange program. This significant increase in budget allowed for a wide choice of airframe and propulsion system components, however as the funding had objectives out-with that of this PhD project, it needed to be designed to carry potentially heavier and far more expensive sensor packages than those already created for this project.

3.4.4.1 Airframe considerations and selection

With this in mind the type of airframe to be used was limited to an octocopter design in order to give maximum redundancy in case of motor, ESC or propeller failure. If a single rotor (either, motor, ESC or propeller) fails in a quadcopter, then the aircraft will be unlikely to have sufficient thrust to maintain height and will not be able to manoeuvre, although algorithms to allow a degree of control (albeit with a rapidly rotating aircraft) have been developed (Lanzon *et al.*, 2014; Lippiello *et al.*, 2014). Hexacopters and octocopters both a give a level of redundancy in situations such as this as more overall thrust is available, and some element of control can still be maintained, however an octocopter would give the highest level of redundancy but would be a heavier and more expensive aircraft.

To achieve the highest level of thrust and endurance, a “flat” airframe was selected instead of a coaxial design and although this would mean having a larger sized airframe, this was also seen as an advantage as it allowed the possibility of

deploying larger and more cumbersome sensors or other equipment (e.g. testing aerial sprayers). The 1080 mm Vulcan Skyhook Octo airframe was selected (Vulcan UAV Ltd, Mitcheldean, UK) as this allowed for propeller sizes up to 15 inches in diameter to be used and could be fitted with high clearance landing gear (350 mm) to provide very stable landing even if carrying bulky sensors or other equipment.

3.4.4.2 Propulsion system considerations and selection

To avoid potential regulatory issues due to the weight of the aircraft, the decision was made to keep the all up weight (AUW; the weight of the entire aircraft, batteries and sensors when airborne) of the aircraft to a maximum of 7 kg. This helped narrow the potential choice of propulsion system, allowing modelling using eCalc to find the lightest and most efficient motor, propeller and battery combination.

The T-Motor U3 700 Kv motor (Tiger Motor, Nanchang, China), paired with T-Motor 13 x 5 inch beechwood propellers (Tiger Motor, Nanchang, China) were selected as this combination gave a thrust to weight ratio of 1.8:1 when at the maximum AUW of 7 kg. This ratio, whilst not ideal, would still allow the aircraft to manoeuvre effectively (Muller, 2018b). Larger propeller sizes could have been used to give higher endurance but would have required larger and heavier motors, reducing the overall potential sensor payload due to the imposed 7 kg AUW limit. The motors required a 14.8 V power source to provide the level of thrust required, so Turnigy Multistar 10,000 mAh 4S LiPo batteries were selected (Hobbyking, Hong Kong, China) as they were considerably lighter than most other brands. However, they had a maximum discharge rate of 10 C (i.e. 100 A) so two packs needed to be used at the same time to provide a sufficient safety margin (in relation to potential maximum power draw) whilst increasing total battery capacity.

Finally, T-Motor 35 A ESCs (S-series S35, Tiger Motor, Nanchang, China) were selected to ensure a 20 % overhead over the maximum expected current draw of 27 A per motor and a 250 A power distribution board (Vulcan UAV Ltd, Mitcheldean, UK) was used to route power from the batteries to each ESC and motor.

3.4.5 New aircraft - Command and control system considerations and selection

There are many different autopilot systems that can be used within a custom build multirotor, however the author had prior experience with systems that make use of

the Arducopter flight control firmware (Arducopter, 2018). This firmware is an offshoot of the open source Ardupilot project (Lim *et al.*, 2012) and is a continually evolving flight control system that is well supported with documentation and web-based forums that can be used to help diagnose unexpected problems, and crucially it allowed full waypoint navigation using GNSS (Lim *et al.*, 2012).

The 3DR Pixhawk autopilot (3D Robotics, Berkeley, USA), was selected as the autopilot hardware (figure 3-16a) as it was robust and a well-tested autopilot that could make use of the Arducopter firmware. A 3DR UBlox GPS + Compass Module (3D Robotics, Berkeley, USA) was selected as the primary navigation sensor, using the USA Global Positing System (GPS), and a Piksi (v2) RTK GPS (Swift Navigation, San Francisco, USA) was selected as a secondary navigation sensor to allow the possibility of gaining centimetre positional accuracy using a real-time kinematic (RTK) GPS system (although this was not used in the initial build of the aircraft due to autopilot firmware issues at that time).

Figure 3-16: (A) 3DR Pixhawk autopilot (3DR, 2018); (B) Example of the mission planer GCS primary screen (indicates aircraft attitude via wireless telemetry).

Autopilots running Arducopter firmware can be configured and controlled using a variety of different GCS software, however Mission Planner (Oborne, 2016) was selected (figure 3-16b) as it had also been used previously by the author and was a fully featured and regularly updated GCS software platform that would run on a small field notebook computer. To enable telemetry from the aircraft to the GCS, a pair of 433 Mhz 3DR Radios (v2; 3D Robotics, Berkeley, USA) were selected and equipped with Dipole antennas in order to increase the communication range.

For direct manual control of the aircraft, a 2.4 Ghz FrSky Taranis X9D (FrSky Electronic Co. Ltd, Wuxi, China) RC transmitter was selected as it is highly

configurable, allowing customisation of the switches and controls to suit the pilots needs. This was paired with a Frysky X8R (FrSky Electronic Co. Ltd, Wuxi, China) RC receiver on the aircraft, as this could have up to 16 separate command channels configured, allowing for a variety of commands to be ordered directly from the RC transmitter if desired. Finally, an ImmersionRC 25 mW 5.8 Ghz video transmitter with clover antenna (ImmersionRC, Hong Kong, China) was installed on the aircraft to allow video transmission from the sensor package to an ImmersionRC Uno V2 5800 5.8 Ghz video receiver (ImmersionRC, Hong Kong, China). The output from this receiver could be viewed through the GCS, allowing the pilot to see in real time the extent of view from the sensor package.

3.4.6 New aircraft – Build

The initial build, configuration and ground testing of the aircraft took approximately four days to go from a selection of parts (figure 3-17a) to a complete aircraft ready for flight testing (figure 3-17b). Due to the modular nature of the frame, the build itself was fairly simple requiring only a limited amount of soldering to connect the propulsion system into the power distribution board, but more attention was required to ensure a good configuration of the autopilot firmware.

Figure 3-17: (A) Main propulsion components of the UAS before assembly; (B) The completely assembled UAS carrying a dummy payload to simulate the gimbal and sensor package weight.

Arducopter v3.2.1 was installed on the autopilot and configured and calibrated to match the airframe type and propulsion system and to give effective control of the sensor package gimbal. Attention was given to the failsafe features of the firmware to ensure that the aircraft would automatically return to its take-off position should manual control be lost between the RC transmitter and receiver, and a geofence

configured so that it would return if it exceeded the maximum distance limits from the pilot in either horizontal (500 m) or vertical (122 m) directions as stipulated by the CAA in The Air Navigation Order 2016. The aircraft was also configured to land at its current location in the event of a lost or corrupted GPS navigation signal (a GPS glitch) or return to its launch point if the battery capacity remaining was below 30%.

The aircraft in its complete form, with sensor package and batteries had an AUW of ~6.4 kg. eCalc estimated that that would give a thrust to weight ratio of 2:1, a maximum speed of ~9.5 m/s and endurance of ~13 minutes with 30% of the battery capacity remaining. Some capacity must be left in the battery to allow for changeable weather conditions resulting in a higher load on the battery and to avoid deep discharge of the battery, as Lipo batteries are very sensitive to this (Quan, 2017; Baronti *et al.*, 2011) and could be damaged if discharged too far.

3.4.7 New aircraft – Flight testing and limitations

Initial flight testing was carried out to ensure that the aircraft was performing as expected with regards to its endurance and navigation abilities when flying autonomously, and to identify how well the aircraft could be controlled manually as the default configuration of the autopilots PID controllers were very relaxed, meaning that the aircraft was sluggish in its response to controls. The PIDs of each axis were tuned automatically via the use of a special flight mode that tests each of the axes in turn (Ardupilot, 2016b). This tuning made the aircraft much more responsive, especially when yawing, meaning that it would be an effective platform for conducting aerial survey work.

Endurance tests gave results close to those estimated by eCalc (around 13 minutes), which gives an estimated range of ~4 km if travelling at a speed of 5 m/s (the default waypoint navigation speed used for arducopter). Speed tests revealed that the aircraft could reach and maintain the expected 9.5 m/s in forward flight and that the aircraft could be pushed beyond this and reach speeds up to 17 m/s. However, this would result in a loss of altitude as the aircraft was unable to maintain the high forward speed as well as altitude, but it does indicate that the aircraft should be able counteract occasional gusts of unexpected high wind speeds as long as they only occur for a few seconds at a time.

Limitations to the operation of the aircraft in relation to wind speed at ground level can be estimated using power law (Eq. 3-2), with a default power law exponent of 1/7. This gives an indication of the likely vertical wind shear (increase in wind speed at different altitudes) but is difficult to know exactly as it will vary depending on aspects such as atmospheric stability, surface roughness, changes in surface conditions and terrain shape (Manwell *et al.*, 2009). With this in mind, constant wind speeds in excess of 5 m/s measured at ground level are likely to cause navigation issues (reduced speed or deviation from expected flight lines) and are therefore a limiting factor when operating the aircraft.

$$\frac{U(z)}{U(z_r)} = \left(\frac{z}{z_r}\right)^{\alpha} \quad (3\text{-}2)$$

Where $U(z)$ is the wind speed at height z, $U(z_r)$ is the reference wind speed at height z_r, and α is the power law exponent (Manwell *et al.*, 2009).

The other main operational limitations of the UAS are also environmental, in that precipitation of any kind would stop flights as the aircraft and sensors are not waterproof (extremely light drizzle might still allow flights to occur). Temperature is also a factor, so limitations of a maximum of 35°C were imposed as this could lead to the motors overheating when running at maximum. Likewise, a limit of -5°C was also imposed, primarily because the capacity of Lipo batteries will reduce in low temperatures (Quan, 2017), however this can be remedied by using battery warmers. The full limitations to the operation of the UAS (figure 3-18) can be seen in table 3-2.

Figure 3-18: The completed UAS with sensor package attached and connected to the autopilot.

Table 3-2: Limitations of the UAS when equipped with its sensor package (AUW of 6.4 kg).

Feature	Limitation
Max flight time	13 minutes
Max range at 5 m/s	4 km
Max speed	9.5 m/s
Max constant wind speed	5 m/s
Max gusting wind speed	7.7 m/s
Max temperature	35 °C
Min temperature	-5 °C

3.5 Integration of sensor package with command and control system

In order to be able to use the sensor package effectively as part of a UAS, it needs to be integrated with the command and control system of the aircraft so that it can be triggered on demand via the autopilot as part of an autonomous mission, or manually by the pilot. Autonomous missions themselves will also be limited by the integration time and speed of response of the sensor package, as more time required to capture and store an image could be a limiting factor on the speed of the aircraft depending on the amount of image overlap required.

3.5.1 Triggering

As the remote triggering feature of the sensor package required a 5 V pulse to the USB port of each camera, a custom cable was constructed that would convert a 3.3 V relay signal from the Pixhawk autopilot into a 5 V signal that could be fed to both cameras at the same time, allowing for synchronous image capture. A channel was also configured on the RC transmitter to allow the pilot to command synchronous image capture when desired.

3.5.2 Managing camera exposure

Initial testing of the automatic settings within the camera revealed that even modestly overcast environmental conditions would result in the cameras increasing their ISO to levels that returned very noisy images (e.g. an ISO of 800 or more) and shutter speed would be reduced to levels that would often result in blurred images due to the speed that the aircraft was traveling at. This is due to the camera's compact lens design and small sensor size, as one downside of cameras of this type is their ability to capture good quality imagery in lower light conditions. This is because the pixel size on smaller sensors is also smaller and therefore, they require either a higher ISO (signal gain) or lower shutter speeds in order to get a good exposure (Nakamura, 2006).

3.5.2.1 KAP UAV Exposure Control Script configuration

The default installation of CHDK allows the user to setup a host of set parameters (ISO, shutter speed etc.) as well as allowing the cameras to be triggered remotely. However, as changes in light conditions could occur during a survey, being able to vary those parameters to suit the conditions without creating overly noisy or blurry images was required.

The open source KAP UAV Exposure Control Script (v3.1; CHDK, 2016) allows configuration of the camera shutter speed and ISO settings within specific bounds and by default it is configured towards ensuring that the shutter speed stays high enough (e.g. 1/1000 of a second) to minimise image blur. This 'ideal' shutter speed can be configured within a range (minimum, ideal and maximum) so that it will alter if it cannot reach the ideal for a good enough exposure but will not exceed the range. The ISO can also be varied in the same way to ensure a good exposure, with lowest ISO value within the range used where possible. The aperture can also be configured, however the aperture of the cameras in the sensors package was fixed and so could not be altered.

The script was installed onto each camera and configured to use the ranges below for shutter speed, ISO and aperture:

- Shutter speed range set to 1/200 – 1/2000 with 'ideal' set at 1/640 second.
- ISO range set to 80 – 400 (using higher than 400 ISO produced very poor images).
- The aperture is fixed at 2.8 (no way to change this as the camera has a fixed aperture).

The script can also be configured to run either as an intervalometer (e.g. take an image every 2 seconds) or to take a picture on command via a 5 V pulse to each cameras USB port. The latter was selected as it gives much more control of the number and location of images taken within a survey and allows images to be captured manually by the pilot when desired. The script was also configured to force the camera to lock its focus to infinity, removing the need for the camera to attempt to autofocus for each image. This reduced the time required between successive images and reduced the possibility of the autofocus failing to correctly set to infinity, which can result in out of focus images.

3.5.3 Sensor integration time and speed of response

The cameras were then tested for their speed of response when capturing a continuous stream of images, as this would be a limiting factor for mission planning. The CHDK KAP script was altered to use an intervalometer to trigger the camera every two seconds and take a maximum of 12 images. The camera was mounted on a tripod to ensure it did not move and was pointed at a computer screen running a

digital stopwatch (black screen with white numeric). The light levels in the room were reduced to ensure that the camera used the lowest shutter time (1/200) and highest ISO (400) permissible by the CHDK KAP script, in order to simulate poor environmental conditions and identify the slowest response of the cameras.

The average, maximum and minimum times between successive image captures was then identified through interrogation of the images of the digital stopwatch as captured by the camera. When capturing JPEG imagery only, the maximum time recorded between images was 3.81 seconds. When capturing JPEG and RAW imagery, the maximum time between successive images was 5.63 seconds (table 3-3).

Table 3-3: The minimum, maximum and average time required between successive image captures, when capturing JPEG only or JPEG and RAW imagery.

JPEG image capture only (seconds)			JPEG and RAW image capture (seconds)		
Minimum	**Maximum**	**Average**	**Minimum**	**Maximum**	**Average**
3.03	3.81	3.17	4.93	5.63	5.10

3.6 Image collection and mission planning considerations

As the primary purpose of the UAS was to survey vegetated areas, identification of the best way to collect imagery that could then be processed to produce an orthorectified image of the entire scene surveyed was required. Orthorectification is the geometric correction of an image to a known surface such that its scale is uniform allowing measurements of distance to be made. The scale (spatial resolution) of the orthorectified image indicates the dimensions of each pixel within the image and varies depending on the height above ground level (AGL) at which the image was taken, the focal length of the camera and the on-sensor pixel size. The term ground sampling distance (GSD) is typically used to indicate the spatial resolution of an image and can be identified by eq. 3-3 (Aber *et al.*, 2010).

$$GSD = pixel\ size * \frac{H_g}{f} \qquad (3\text{-}3)$$

Where H_g is the height above ground level, f is the focal length of the camera and $pixel\ size$ is the on-sensor pixel size of the camera (Aber *et al.*, 2010).

To be able to set the scale of an orthorectified image to units of a known value, positional information is required (altitude, longitude and latitude), and this will also

allow the georectification of the image to a specified coordinate reference system (CRS). Georectification is the transformation of an image from its local coordinate system to a given CRS so that it is positioned correctly on a map or other imagery using the same CRS. As the UAS is equipped with a GPS receiver and barometer, the positional information of the aircraft at the point of image capture can be obtained and applied to each image (termed geotagging).

The geotag of each image can be used by photogrammetry software to enable the orthorectification of imagery, however the navigation grade GPS used by the UAS is only accurate to ±2.5 m (U-blox, 2017), so the resulting positional accuracy will not be exact as other studies have indicated (Turner *et al.*, 2014). To improve positional accuracy, ground control points (GCP) should be used and surveyed with survey grade GNSS that give positional accuracies of (ideally) a few centimetres. These can then be used by photogrammetry software to produce a more accurate georectification of the imagery, as long as a sufficient number (ideally at least 10) have been evenly dispersed across the area to be surveyed (Photoscan, 2018).

3.6.1 Mission planning method and limitations

Due to the restrictions in maximum altitude AGL for UAS, a single image is unlikely to cover the entire area of interest being surveyed at sufficient resolution, therefore a collection of images is required that can each be orthorectified before being merged together to show a single image of the entire scene surveyed (an orthomosaic). Relatively recent developments in computer vision software have made this process simpler for images captured by UAS, but they require a high overlap of imagery to work effectively, typically 80 % forward overlap and 60 % side overlap (Colomina *et al.*, 2014), and so this needs to be planned for when designing autonomous missions.

The GCS software Mission Planner (Oborne, 2016) was used to design all of the autonomous missions flown within this project, as it provides very customisable waypoint navigation. Autonomous missions can be created by first drawing a polygon around an area of interest (figure 3-19a) before generating a flight plan automatically (figure 3-10b). The flight plan can be configured for a particular camera (i.e. on-sensor pixel size, focal length and resolution are known), allowing the UAS operator to vary the height of the mission to match the GSD desired. Collecting imagery at the correct GSD is important if trying to recognize particular

features or objects within the scene, as typically a GSD 3-5 times smaller than the object itself is required in order for it to be effectively recognizable (Aber *et al.*, 2010).

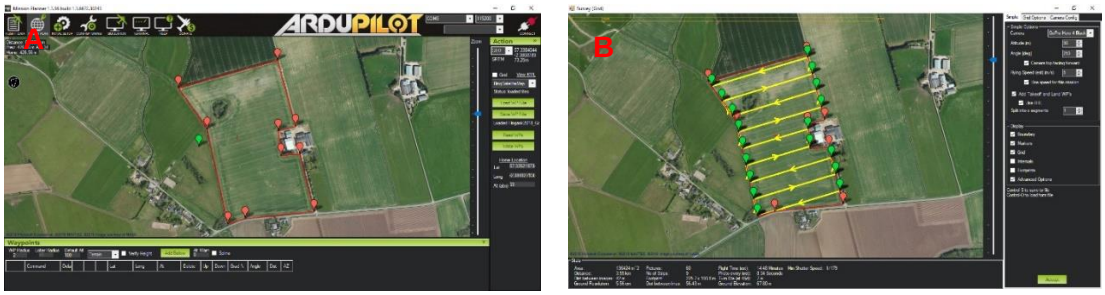

Figure 3-19: (A) Selecting the area to survey by drawing a polygon around its boundaries; (B) Using mission planner autonomous waypoint generating options to produce a flight plan that covers the area of interest.

However, the limitations of the aircraft and sensor package also need to be addressed to ensure sufficient overlap of imagery is made. This could mean that if flying close to the ground to get highly detailed imagery, the aircraft may have to have its default speed slowed down to enable effective overlap due to limitations in the image capture speed of the sensors, and this in turn could result in the desired flight plan exceeding the endurance of the aircraft. Once all of these factors have been addressed, the flight plan (or plans if multiple flights are required to cover the area of interest) can then be uploaded onto the aircraft and enabled at any point during the flight.

3.7 RAW image pre-processing

As the cameras were set to capture both JPEG and RAW imagery, after the images had been captured the JPEG data could be used directly once it had been geotagged with the positional information from the UAS logs. However, the RAW imagery needs to be processed to convert into linear 16-bit TIFF files, that can then be further processed by photogrammetry software into orthomosaic data. An automatic pre-processing workflow was devised and coded as a macro within ImageJ (v1.49k, Fiji distribution; Schindelin *et al.*, 2012) and utilised a number of other open source software programs to enable the conversion, correction and geotagging of all of the images from a single survey at once (figure 3-20; see appendix B for the script itself).

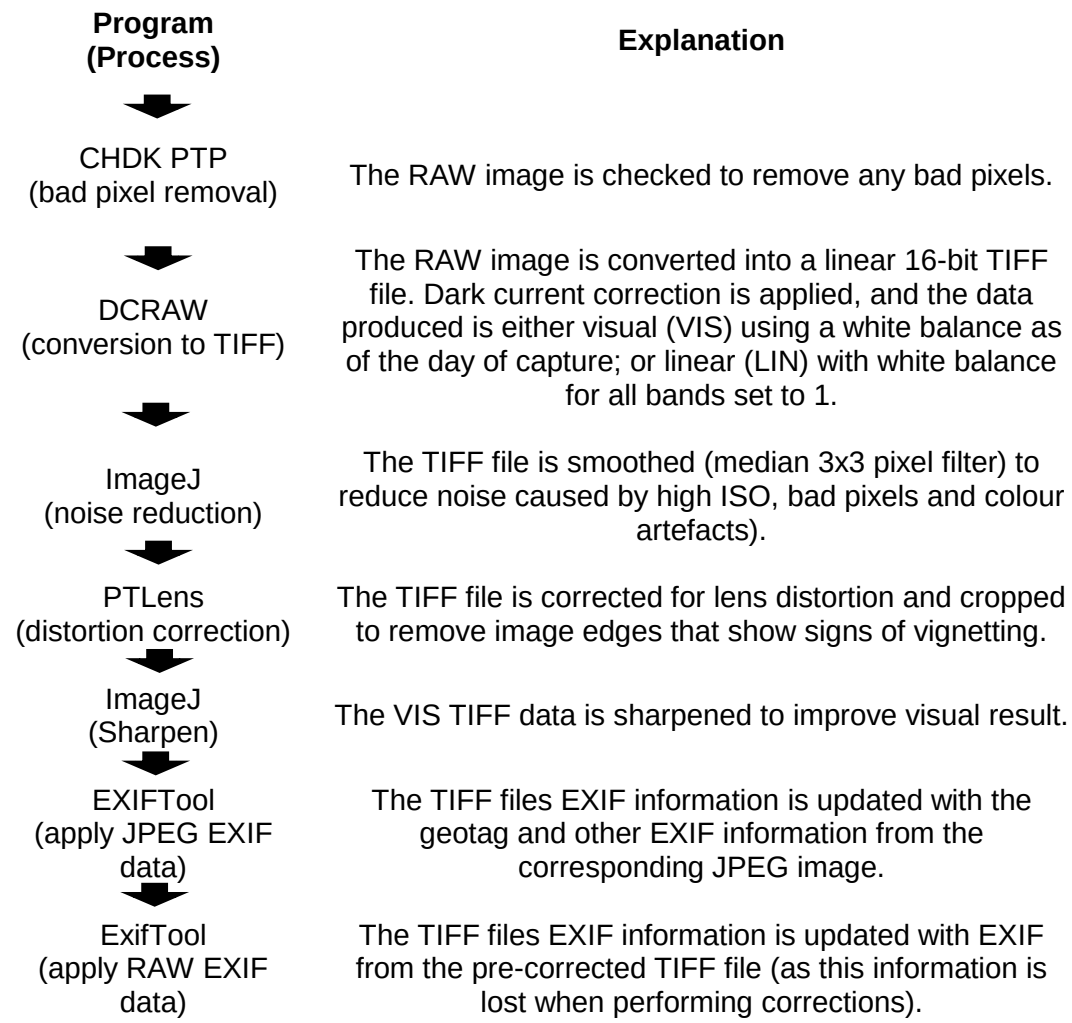

Figure 3-20: Image pre-processing workflow. More detailed explanations for each process are shown in the following sections.

3.7.1 Bad pixel removal

Bad pixels are faults on the senor itself where no data will be captured for a particular pixel resulting in a black or brightly coloured pixels appearing in the final image (figure 3-21a). The JPEG imagery is corrected by the camera itself as no bad pixels could be seen (figure 3-21b). CHDK generates RAW files using the Adobe DNG v1.3 format, where bad pixels are not corrected on the camera but simply marked within the file in order to improve the speed of response of the camera (CHDKPTP, 2014). Therefore, CHDKPTP (v3; CHDKPTP, 2014) was used to process each RAW file in order to remove any bad pixels (figure 3-21c).

Figure 3-21: Example image of a conifer sapling; (A) the converted RAW image showing bad pixels (black and coloured speckles across the scene); (B) JPEG image with no bad pixel visible; (C) the converted RAW image after processing with CHDKPTP to fix the bad pixels (none can be seen).

3.7.2 RAW conversion to TIFF

The process of converting the RAW imagery into linear 16-bit TIFF files has already been covered in chapter 2, however some differences were made to improve the final image output and also to produce a separate set of data with improved visual clarity, as this would help with manual image analysis. The open source program DCRAW (v9.25; Coffin, 2018) was used for all of the conversions, but its command inputs would vary depending on the type of imagery to be produced (either linear or visual) and the attributes of the image to be converted (ISO and shutter speed used for its capture).

3.7.2.1 Dark current signal correction

The dark current signal of a camera sensor can be generated even if there is no light getting to the sensor as it is noise produced by the sensor itself. It changes depending on the integration time of the camera (shutter speed), the ISO (signal gain) used and the temperature of the sensor (Verhoven *et al.*, 2009; Figure 3-22). Dark images (images taken in the absence of any light) can be used to correct some of this noise as well as detect and remove hot pixels (very bright pixels), which can occur when higher ISO and low shutter speeds are used (Verhoven *et al.*, 2009).

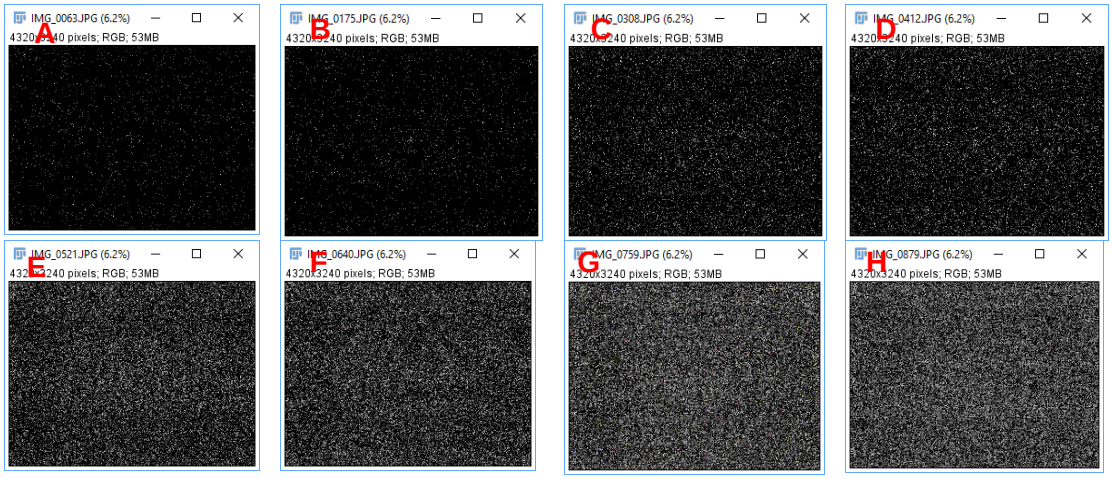

Figure 3-22: Example dark current signal noise due to increasing ISO (images have had their histograms equalised to enhance the noise). All dark images captured using a shutter speed of 1/200 and an ISO of (A) 80; (B) 100; (C) 125; (D) 160; (E) 200; (F) 250; (G) 320; and (H) 400.

A series of dark images were captured at room temperature (~19 °C) for each camera using a range of ISO and shutter speed settings (to match the permissible range used within the CHDK KAP script). Unfortunately, the shutter speed of the cameras could not be set exactly via the camera's normal settings menu (unlike the ISO) and the CHDK firmware would only allow a coarser range of settings to be used, so getting exact dark image to captured image exposures was not possible.

ISO range:

- 80, 100, 125, 160, 200, 250, 320 and 400

Shutter speed range (seconds):

- 1/200 (0.005), 1/250 (0.004), 1/320 (0.003), 1/500 (0.002) and 1/1000 (0.001)

15 dark images were captured for each ISO and shutter speed combination (600 images for each camera) and converted using DCRAW into dark frame images. The intention was to produce an average dark frame from each set of 15, however this averaged dark frame was not acceptable to DCRAW for use as a dark frame (despite being in the correct format), so only a single dark frame from each set was used for dark current correction. Dark images were selected based on the ISO and shutter speed of the image to be corrected. As the entire expected range of shutter speeds could not be captured, a dark image with next slowest shutter speed would always be used (i.e. an image captured a 1/640 second would use a dark image captured at 1/500 second).

The use of a single dark frame did considerably reduce the dark current signal (figure 3-23) although did not completely remove it, as the only way to ensure removal would be to take a dark image directly after intended image capture using the same settings (and with the sensor at the same temperature). This could be done using CHDK but would have slowed the camera response time considerably (essentially doubling it), making the sensor package impractical to deploy on a UAS.

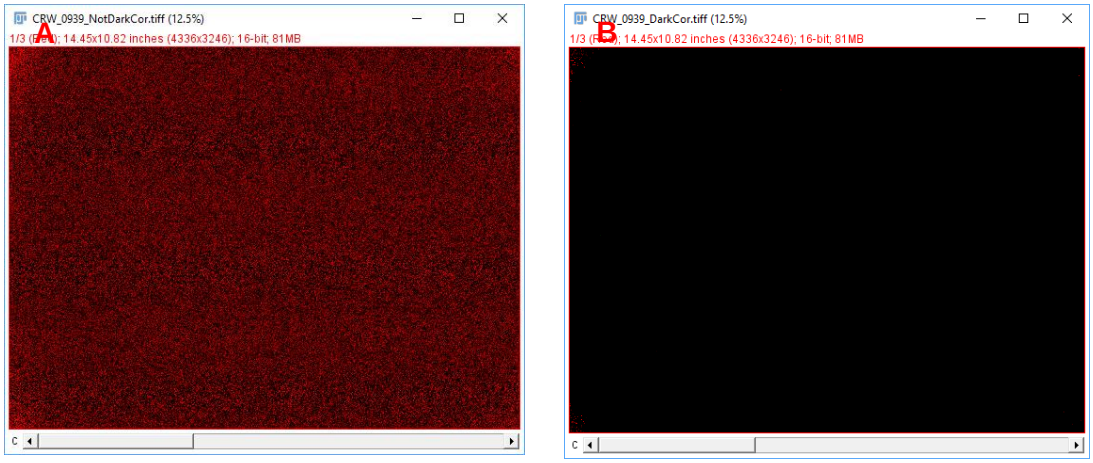

Figure 3-23: Enhanced contrast dark images (saturation 0.4 %, equalised histogram); (A) dark image that had not been corrected (mean DN 125.573 ±137.705, minimum DN 0, maximum DN 65534); (B) dark image that had been corrected by using another dark frame within its set (mean DN 0.022 ±2.728, minimum DN 0, maximum DN 3320).

3.7.2.2 Linear conversion

Conversion to linear 16-bit TIFF utilised the same DCRAW command inputs irrespective of whether the images were sourced from the modified or unmodified camera. The command input was changed slightly from that used previously in chapter 2 to produce linear images, as that used low-quality bilinear interpolation to create the TIFF image from the RAW file to allow high speed processing. However, artefacts were noticed when this was used (figure 3-24) so a higher quality interpolation routine was applied (VNG, Variable Number of Gradients) that interpolated the RGB channels as 4 colours in order to remove the artefacts (Coffin, 2015).

DCRAW command:

- dcraw -r 1 1 1 1 -f -o 0 -4 -j -t 0 -T -K “darkframe”

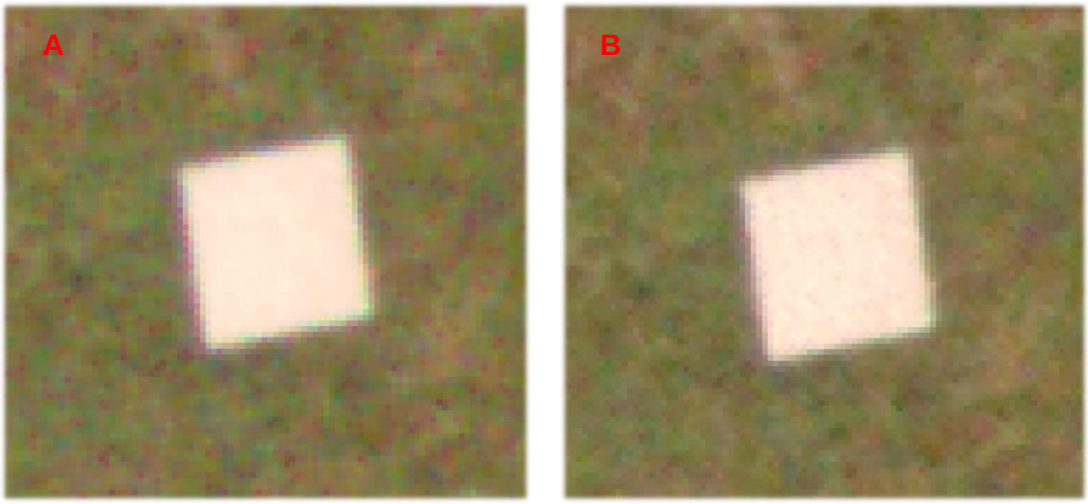

Figure 3-24: Example of bilinear (A) and VNG (B) interpolation looking at a grey calibration target. Coloured artefacts can be seen around the edges of the calibration target in (A) but are not present in (B).

3.7.2.3 Visual conversion

A set imagery with improved visual clarity was required for any direct visual (manual) image analysis, as linear conversion of the images with the white balance set to 1 for all channels could not be used effectively for this purpose (colour representation was poor in relation to the human visual system). Visual conversion of the data was not strictly necessary as the JPEG imagery produced would have been sufficient for this purpose, however this often suffered from over exposure of brighter areas of an image (e.g. very white objects such as white flowers) and was quite noisy when using higher ISO settings (figure 3-25a), making visual analysis more difficult. One of the advantages of using RAW imagery is that it can be recreated to remedy issues such as this, so DCRAW was used to produce improved visual clarity TIFF imagery using the white balance as set on the day of image capture, with highlight recovery options to improve image quality (figure 3-25b).

DCRAW command:

- dcraw -w -f -o 1 -H 2 -4 -j -t 0 -T

Figure 3-25: Example of a JPEG (A) and TIFF (B) image interpolated from the RAW file. More image noise and over exposure of bright objects can be seen in (A); Highlight recovery shows far more detail in (B) and less noise, but some brighter features get a pinkish tint (e.g. the fluorescent jackets).

3.7.3 Noise reduction

Noise was still apparent even after bad pixel removal and dark current correction, especially when images were taken using higher ISO and lower shutter speeds (figure 3-26a). To reduce this effect all of the converted TIFF images were smoothed within ImageJ using a 3 x 3 pixel median filter (figure 3-26b).

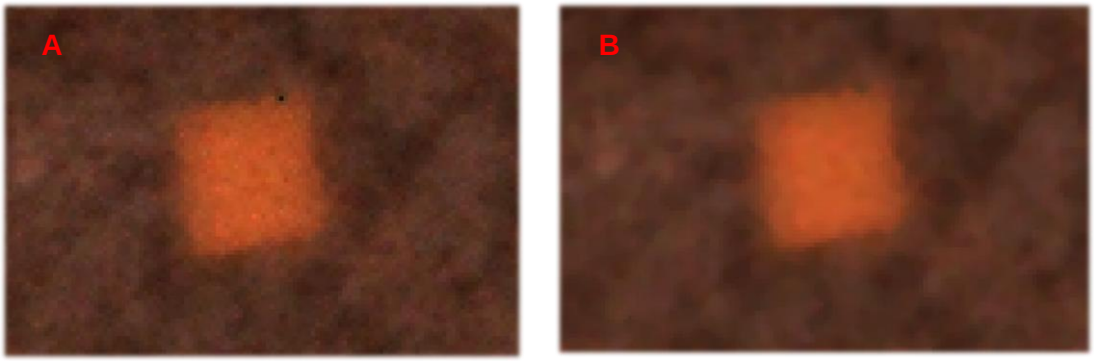

Figure 3-26: Example image from the modified camera showing a grey calibration target (ISO 400, 1/500 second shutter speed). Noise is apparent before smoothing is applied (A) and is greatly reduced after the use of a 3 x 3 pixel median filter (B).

3.7.4 Distortion correction

The default size of the JPEG image produced was 4320 x 3240 pixels (~14 mega pixels), however the size of the actual RAW image (once converted to TIFF) was 4336 x 3246 pixels (~14.1 mega pixels). This is because some on camera processing is occurring when it is generating the JPEG image, in order to correct distortion created by the lens of the camera and to remove the outer edges of the

image to reduce vignetting effects (image darkening in a circular gradient from the image centre to its borders; Lelong *et al.*, 2008; Lebourgeois *et al.*, 2008). PTLens (v9; Niemann, 2018) was used to perform a fisheye distortion correction with image crop to each of the TIFF images to replicate the correction made to the JPEG images (figure 3-27). An almost exact replication could be made, however the image crop was reduced to maintain a larger image footprint, as this would allow for a greater image overlap at the later orthomosaic processing stage, whilst still removing the worst areas of vignetting (essentially the far corners of each image).

PTLens settings:

- Fisheye correction 65, crop factor 6 (to match the JPEG).
- Fisheye correction 65, crop factor 3 (used to allow a larger image footprint).

Figure 3-27: (A) An uncorrected TIFF image (note curve of fence line); (B) a corrected and cropped TIFF image; (C) a corrected and cropped TIFF image overlaid with its corresponding JPEG image to show extent of extra image footprint.

3.7.5 Sharpening visual data

To improve the clarity of the visual data it was sharpened within ImageJ using a weighted average of the 3 x 3 pixel neighbourhood (figure 3-28). As sharpening can accentuate noise it was not applied to the linear imagery, but as the visual data was only intended for direct visual analysis (and not part of any automatic classification), this was not seen as a potential source of increased error.

$$\begin{matrix} -1 & -1 & -1 \\ -1 & 12 & -1 \\ -1 & -1 & -1 \end{matrix}$$

Figure 3-28: Weighted average filter used by ImageJ to sharpen images (Ferreira & Rasband, 2012)

3.7.6 Adding EXIF information

The Exchangeable Image File Format (EXIF) information is standardised metadata attached to each image file so that information such as date of capture, ISO, shutter speed etc. can all be recorded. As the RAW files are processed though the various stages of the processing workflow, some of the original EXIF information is lost, so the open source program EXIFTool (v10.05; Harvey, 2018) was used to replace the lost information and to copy the geotag information from the JPEG images onto the processed TIFF files.

3.8 Orthomosaic generation workflow

Once the RAW images have converted into TIFF files, corrected and geotagged, they are then ready to be processed into an orthomosaic to show a uniformly scaled image of the entire scene surveyed. Software that uses computer vision to process digital images have become very popular for processing imagery from UAS as more traditional aerial photogrammetry techniques can struggle to process the high-resolution imagery from low altitude surveys causing large perspective distortions (Turner *et al.*, 2012).

Agisoft Photoscan (Agisoft LLC, St. Petersburg, Russia) was chosen as the photogrammetric software to use for this project, as it has been used successfully in many studies, including investigating the spectral and structural changes in agricultural crops (Bendig *et al.*, 2015), estimating tree canopy heights (Jensen & Mathews, 2016), identifying changes to landslides over time (Lucieer *et al.*, 2013) and monitoring the spread of invasive plant species (Müllerová *et al.*, 2016). It uses several different computer vision algorithms over different stages (figure 3-29), with the first stage being image alignment.

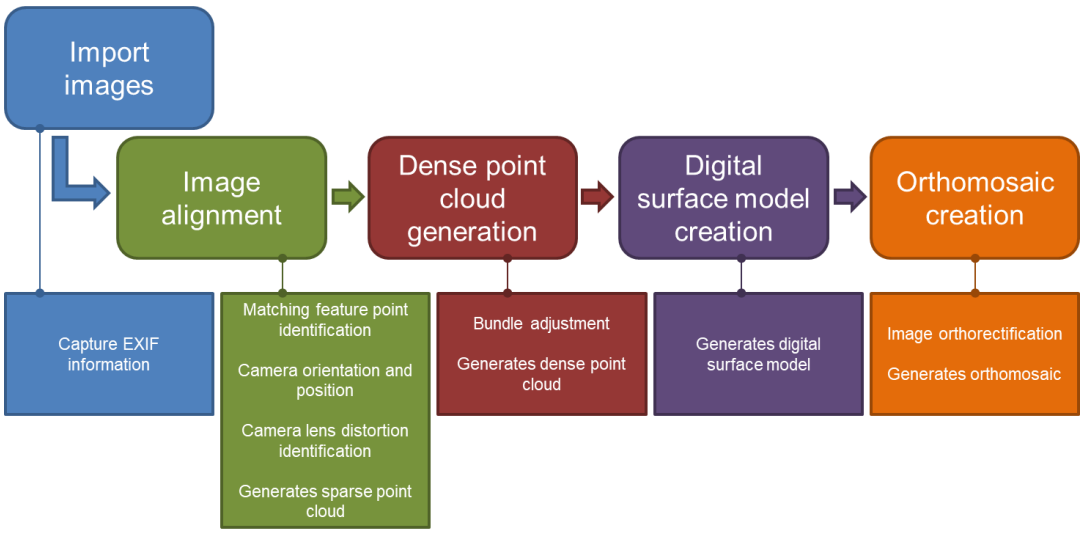

Figure 3-29: Agisoft Photoscan image processing workflow.

Image alignment uses a technique called structure from motion (SfM; Ullman, 1979), along with other algorithms similar to scale-invariant feature transform (SIFT; Lowe, 1999) which detects feature points within each image (distinctive features such as object edges), matches them to similar points in other images and monitors their change in position in successive images. If available, camera location information (from the geotag of an image) will be used to accelerate the matching process (collocated images can be checked more quickly). This allows a three dimensional (3D) sparse point cloud of the matched feature points to be created (figure 3-30a), as well as give an understanding to the camera position and orientation at the moment of image capture and internal calibration parameters to account for lens distortions (Verhoeven, 2011). GCPs can also be used (once their position in each image is marked), allowing the alignment to be further optimised to improve the accuracy of the sparse point cloud geometry.

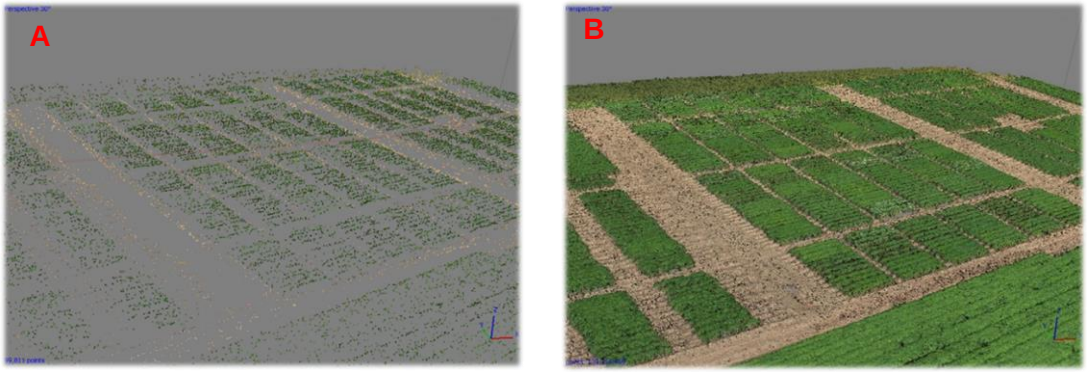

Figure 3-30: (A) An example sparse point cloud of a trial crop of potatoes; (B) an example dense point cloud of the same scene, showing far more detail and 3D geometry.

The second step uses a dense multi-view stereo algorithm to bundle adjust the images (adjusting all of the images based on their estimated positions and calibration) to produce the scene geometry in detail (using pixel values rather than matched feature points), generating dense 3D point cloud (Verhoeven *et al.*, 2012; figure 3-30b). The third step uses this dense 3D point cloud to create a digital surface model (DSM), essentially a two-dimensional (2D) image whose pixels represent elevation values (figure 3-31a). Finally, an orthomosaic can be generated (figure 3-31b) by orthorectifying all of the bundle adjusted images, using the DSM as a height field. The DSM and orthomosaic can then be exported for further analysis (as 32-bit and 16-bit TIFF files respectively) using any given CRS.

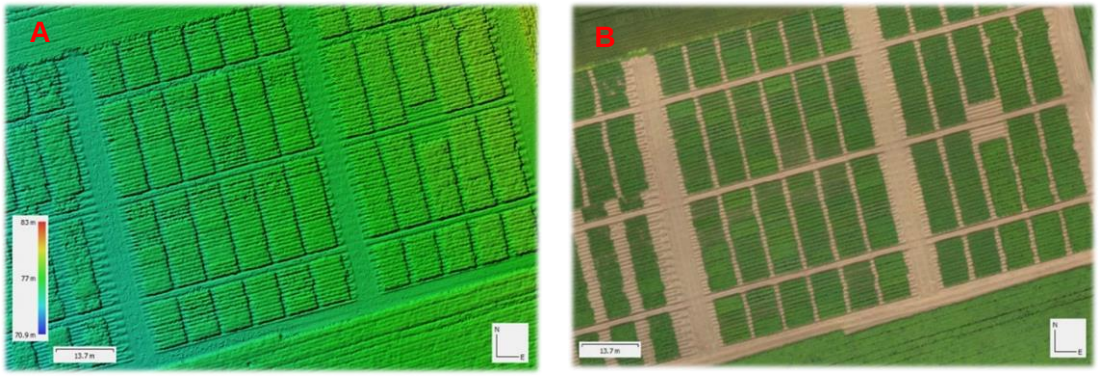

Figure 3-31: (A) A digital surface model showing the elevation profiles over a trial crop of potatoes; (B) an orthomosaic of the same scene, formed from approximately 30 images that had been orthorectified using the DSM.

As two cameras were being used in this project and visual as well as linear data was required, the workflow in figure 3-29 had to be run three times for each survey completed. This was not ideal as processing could take several hours per dataset (on an Intel i7 6 core computer with 64 GB RAM and twin AMD R400 graphics cards), depending on the reconstruction parameters specified and number of images involved. Once processing was complete, three sets of orthorectified data would be available for further analysis; a visual orthomosaic generated from the unmodified RGB camera; a linear orthomosaic and DSM created from the unmodified RGB camera; and a linear orthomosaic created from the modified NIR camera (figure 3-32).

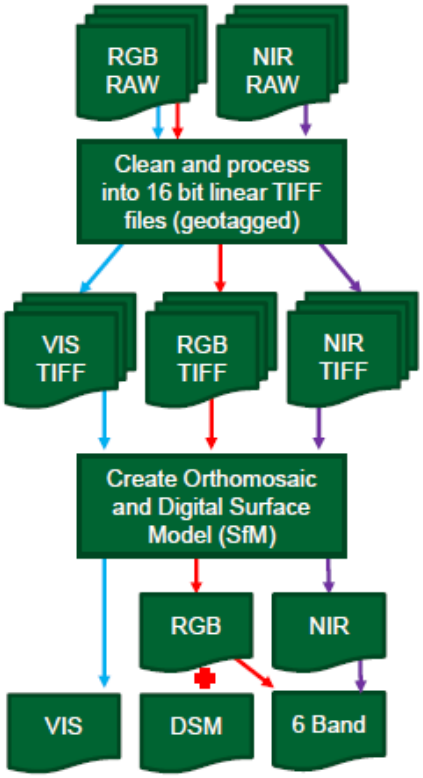

Figure 3-32: Overview of project image processing workflow, from pre-processing to orthomosaic and DSM generation, resulting in a 6 band orthomosaic (containing all bands from the modified and unmodified cameras), a digital surface model and an improved visual clarity orthomosaic.

3.9 Digital surface model quality investigation

The purpose of this study was to investigate the qualities of the DSM data produced from Photoscan using example imagery processed following the processing methodology indicated in section 3.8. Other studies have already shown that Photoscan can be effective in producing accurate scene geometry (Kršák *et al.*, 2016; Gross, 2015), so the data was processed using different dense cloud generation options and filtering in order to identify which options could be the most suitable to use for future studies within this PhD project.

3.9.1 Methodology

The trial site used was located at Fingask farm (Oldmeldrum, Scotland), with the subject being a SRUC trial of different potato (*Solanum tuberosum*) varieties and treatments (figure 3-33). The survey was conducted on 7th August 2015 at around midday under mixed sunny/cloudy conditions with light winds (< 2 m/s). The Vulcan UAS was flown at an altitude of 70m AGL to give an expected GSD of ~2 cm per

pixel, using a standard lawn mower survey pattern to give a forward image overlap of 78% and side overlap of 60 %. The speed of the UAS was limited to 3 m/s to allow for the integration time of the sensors, with 79 images captured in total. 12 GCP (orange discs of 20 and 30 cm diameter) were placed in and around the trial area and measured with a Leica GPS 1200 survey grade RTK GPS (Leica Geosystems, Heerbrugg, Switzerland) with an expected accuracy of ±2 cm (Leica, 2008). All of the images produced were geotagged within mission planner using the UAVs on-board 3DR GPS (Ublox LEA-6H), with expected accuracies within ±2.5 m (U-blox, 2017).

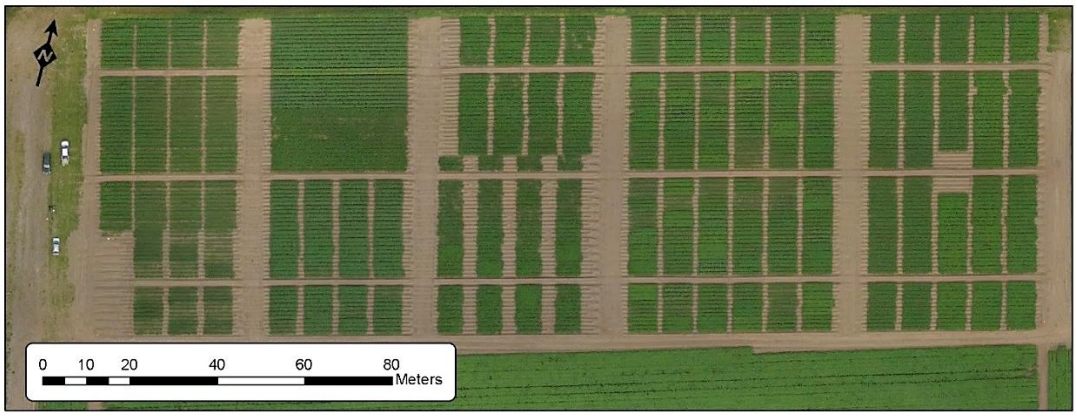

Figure 3-33: Orthomosaic of the entire trial site (~2 ha) showing all plots.

3.9.1.1 Data processing

The data was processed for visual analysis but was not sharpened, thereby simulating the expected DSM data output, but with better visualisation. This data was then processed using different parameters within Photoscan (v1.2.0; table 3-4), including alterations to the quality of the dense point cloud and its depth filtering. All of the GCPs were marked in each image where visible and optimized within Photoscan with a measurement accuracy 0.15 m to allow for possible errors in identification of the GCP centres, as the GCP themselves did not have obvious markings of their centre points (the geotag of each image was not used as part of the optimisation, only for initial image alignment).

Table 3-4: Photoscan image processing options used for each dataset, with GSD of DSM created.

Data set	Image Alignment	Dense cloud	Depth filtering	DSM GSD (cm)
1	Highest	Ultra	Aggressive	1.88
2	Highest	Ultra	Mild	1.82
3	Highest	High	Mild	3.77
4	Highest	Medium	Mild	7.54

3.9.1.2 Data analysis

All of the data was then analysed within ArcGIS (v10; ESRI, Redlands, USA). The box used to transport the UAS (figure 3-34a) was measured (118.5 x 45 x 56.5 cm; 0.301 m^3). Obvious ground points around the box were marked and used to create a digital terrain model (DTM) of the ground surface (figure 3-34b) and used to generate a height model for the box (for each dataset). The top of the box was then also marked to enable the volume to be identified for each set of data. 100 randomly generated points (at least 2 cm apart from each other) where then created within the boundary of the top of the box (figure 3-34c), before being queried to identify the height at each point for each set of data (which in an ideal world should all have matched the actual height of the box).

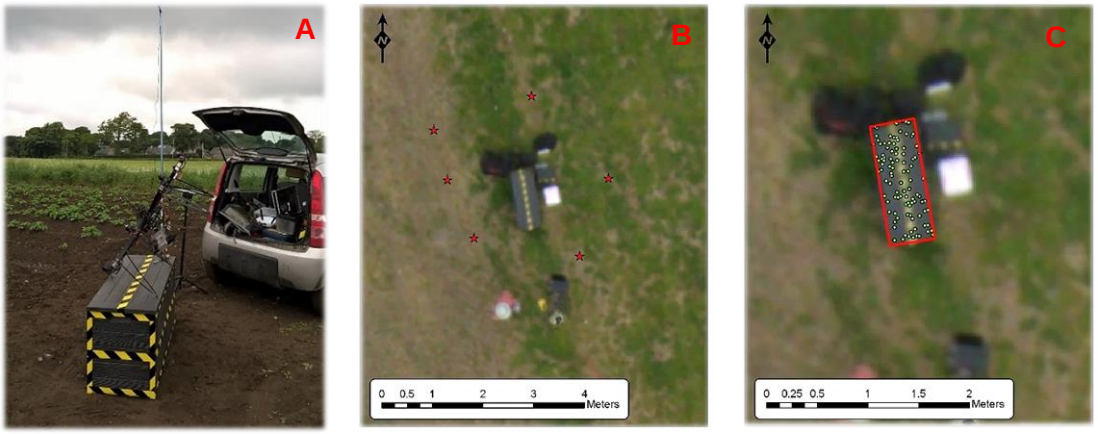

Figure 3-34: (A) The UAS transport box; (B) ground points (red stars) around the box used to generate a DTM; (C) the outline of the box used to measure its volume and within it, the random points (green dots) used to measure its height.

3.9.2 Results

The box volumes reported varied between datasets, with datasets 2 & 3 showing a slight increase of 2~4 % of expected volume, but datasets 1 & 4 showing a decrease of 12~17 % of expected volume (table 3-5). The box heights also varied, with dataset 1 & 4 under reporting the mean height and sets 2 & 3 slightly over reporting it. Set 1 also showed a larger standard deviation of the mean, with points

above and below the expected height value. Sets 2 & 3 showed less standard deviation of the mean and less outlying data, with set 4 being the most consistent and showing the smallest deviation (figure 3-35).

Table 3-5: Reported volumes from each dataset and the difference in volume compared to the actual volume of the box (0.301 m^3).

Data set	Volume reported (m^3)	Difference in volume
1	0.265	-12.11 %
2	0.306	1.65 %
3	0.312	3.62 %
4	0.250	-16.99 %

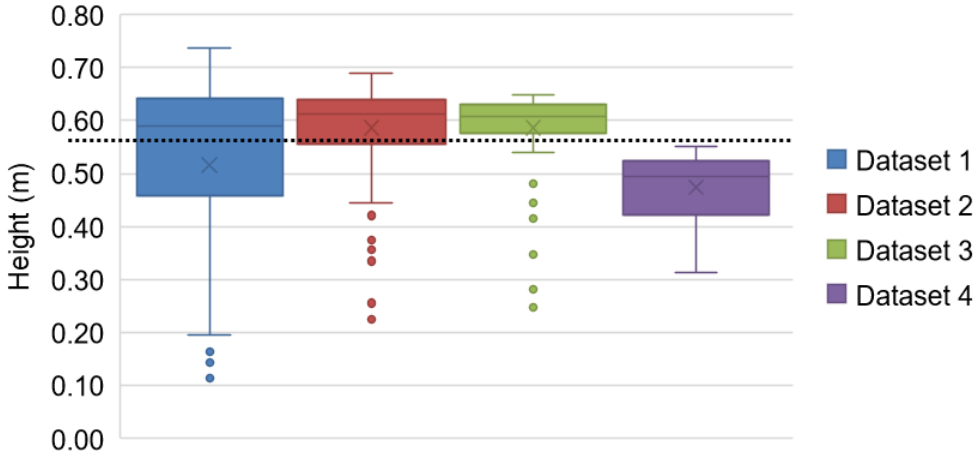

Figure 3-35: Box plot of 100 points of height measurements (mean, median, standard deviation and outliers shown for each dataset). The black dotted line denotes the true height of the box.

3.9.3 Discussion and conclusion

The results were as expected in relation to the higher quality dense cloud datasets giving the closest estimation to the actual volume of the box, as at Ultra quality, the dense cloud is created using the images at their full resolution, whereas this is downscaled for each lowering of quality (High is 50 %, medium is 25 %). This means that the GSD becomes larger for each reduction in quality, resulting in the shape of the box not being well formed at all in dataset 4 (medium quality; figure 3-36d). However, the aggressive filtering in dataset 1 did not represent the true dimensions of box well at all (figure 3-36a), so this would not be a good option if trying to identify volumes of relatively small objects within a scene. Holman *et al.*, (2016) also reported that more accurate height estimations were made when using

mild depth filtering for their analysis of wheat plots, indicating that for smaller features this would be the better option.

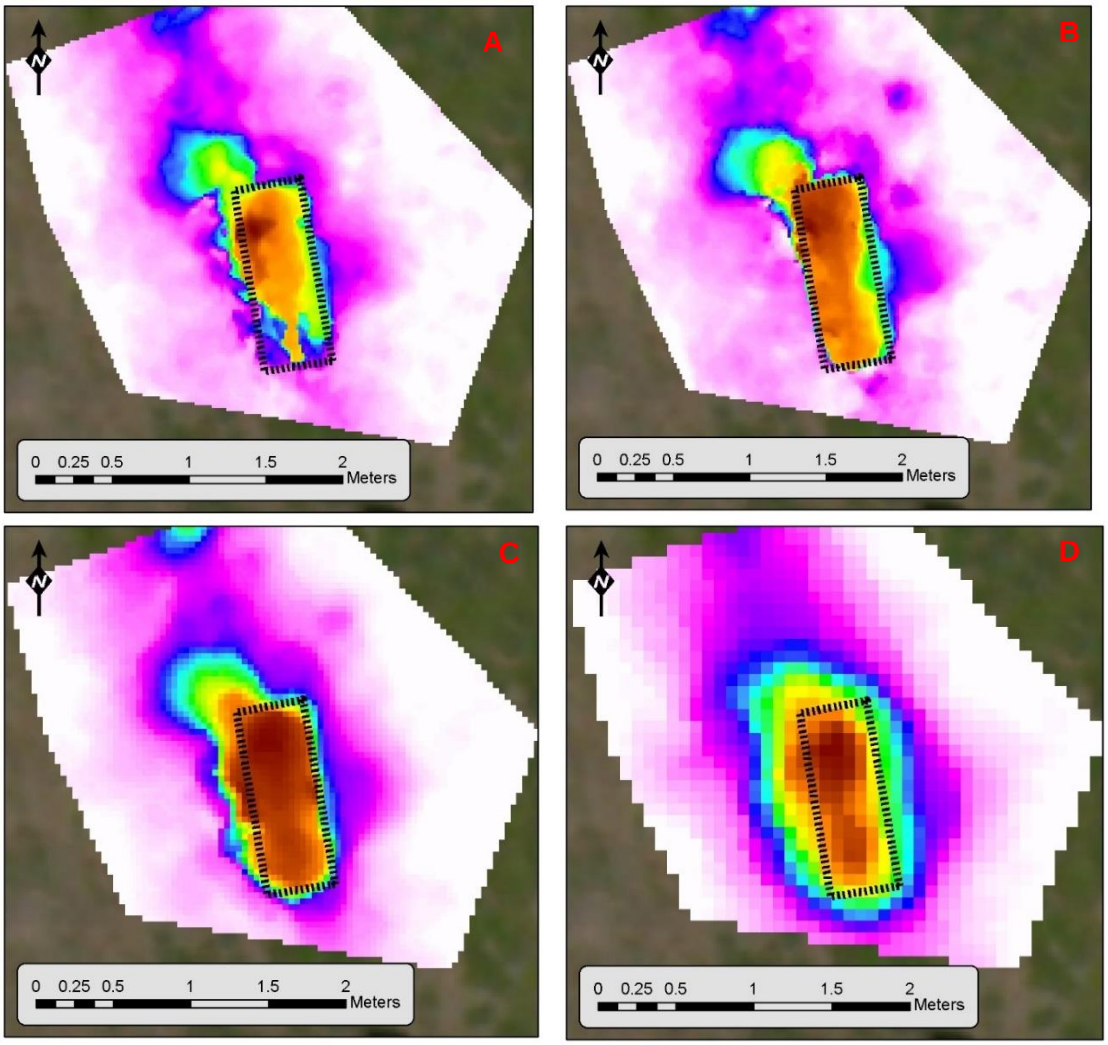

Figure 3-36: Height models for each dataset (white is ground level, dark red are highest points, black rectangle represent location of the box); (A) the height model for dataset 1, where the geometry of the box is poorly formed; (B) the height model for dataset 2, showing well-formed box geometry; (C) the height model for dataset 3, showing that the edges of the box are not as clearly defined; (D) the height model for dataset 4, showing very poorly defined box edges due to low GSD.

The difference in the results for volume estimation and height were very similar for datasets 2 & 3 (figure 3-36b & 3-36c), with the coarser dataset 3 showing slightly less variation in its indications of the height of the box. The main difference between these two datasets was the amount of time required to process the data within Photoscan. Processing using Ultra quality took ~50 minutes (for the dense cloud step), whereas when only using High quality, this took ~10 minutes. This difference in processing times could become more of an issue if the dataset includes a large

number of images, especially if computer processing power was limited. Ideally the Ultra quality setting would always be used, however if the GSD of the generated DSM processed using High quality settings was enough for the intended task, then processing time savings could be made.

Therefore, as the image processing methodology identified for this project requires the creation of three sets of data for each survey, limiting dense point cloud quality to allow faster processing times makes sense as long as the GSD of the DSM will be sufficient for the analysis task at hand, as the orthomosaic will always be created at the GSD of the original images.

3.10 Orthomosaic normalisation methodology

As light intensity changes throughout a day and between different days, normalisation for image brightness is required to allow comparisons between different surveys. Scaling each of the colour channels for each camera independently to a uniform reflectance level allows normalisation of changes in brightness between different surveys. A panel or target that has a flat reflectance spectrum across all of the wavelengths being captured is required and ideally it should be a Lambertian surface (Troscianko & Stevens, 2015) and at least ten times larger than the GSD of the image (Wang *et al.*, 2015).

3.10.1 Calibration target reflectance identification

A camera exposure and calibration kit, consisting of grey, white and black cards constructed of a matt textured plasticised material (20 x 25 cm in size) was selected to be used as the calibration target. It was tested with assistance from NERC FSF under laboratory conditions (figure 3-37) using an SVC LC-RP Pro contact probe (Spectra Vista Corporation, NY, USA) attached to an SVC HR-1024i field spectrometer (Spectra Vista Corporation, NY, USA).

Figure 3-37: The SVC contact probe and spectrometer in use measuring a grey card target.

The reflectance properties of the cards were measured over the visible to short wave infrared range (350-2500 nm) at a sampling interval of 1.5 nm (350-100 nm), 3.8 nm (1000-1890 nm) and 2.5 nm (1890-2500 nm), to produce reflectance spectra for each card (figure 3-38). None of the cards showed a truly flat profile, however the grey card only varied from approximately 16 - 20 % between the area of interest within the visual to NIR range (420-860 nm), and reflectance values in this range (up to 50%) are less likely to cause the cameras to over expose when capturing the calibration target (Troscianko & Stevens, 2015).

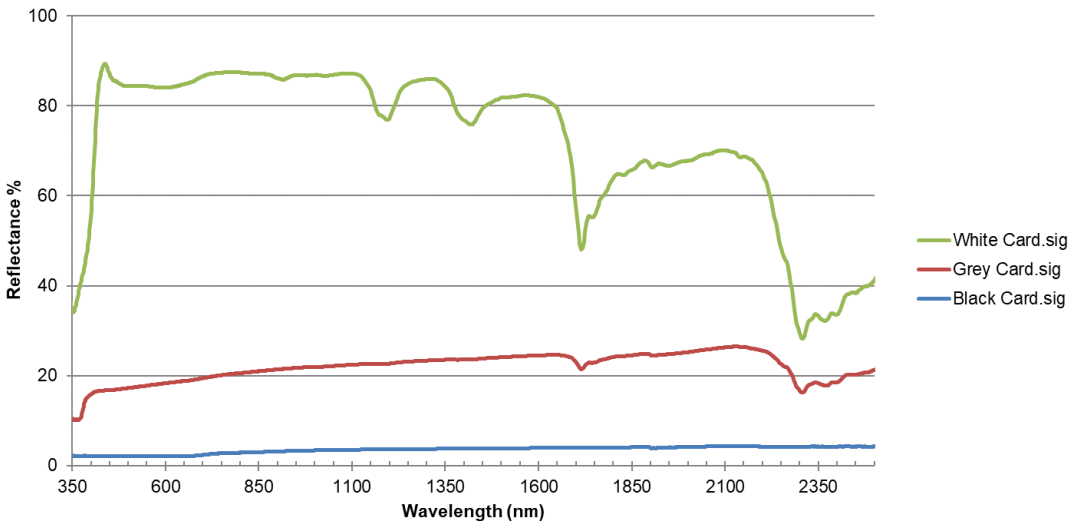

Figure 3-38: Reflectance spectra of the white, grey and black calibration cards.

The reflectance of the grey card was identified for both the modified and unmodified cameras by identifying the average reflectance across the full width at half maximum (FWHM) spectral response for each individual band (table 3-6).

*Table 3-6: Peak wavelength, FWHM range and average grey card reflectance values for each band of each sensor. ***** The green channel of the modified camera was not processed as the band is to be discarded due to it not having a distinct peak wavelength.*

Sensor	Band	Peak wavelength (nm)	FWHM (nm)	Average grey card reflectance (%)
Unmodified	Blue	450	420-490	16.81
	Green	520	470-590	17.56
	Red	600	580-650	18.46
Modified	Blue	810	790-860	20.76
	Green*			
	Red	620	600-710	18.88

3.10.2 Image normalisation methodology

To normalise the output of each camera, for each survey undertaken the calibration targets were placed flat on the ground near the take-off position with a clear view of the sky and not overshadowed by any nearby vegetation. An image of the calibration targets was then made at the beginning of each autonomous mission, from directly above the targets at an altitude of ~5 m (figure 3-39a). This essentially served two purposes, to enable the normalisation itself plus a check to ensure that each camera lens had deployed and locked autofocus to infinity. The average DN of the grey calibration target for each band were then captured after the mission using ImageJ (v1.49k, Fiji distribution; Schindelin *et al.*, 2012), with the region of interest being measured being well within the target to avoid any shading effects from the edges (figure 3-39b).

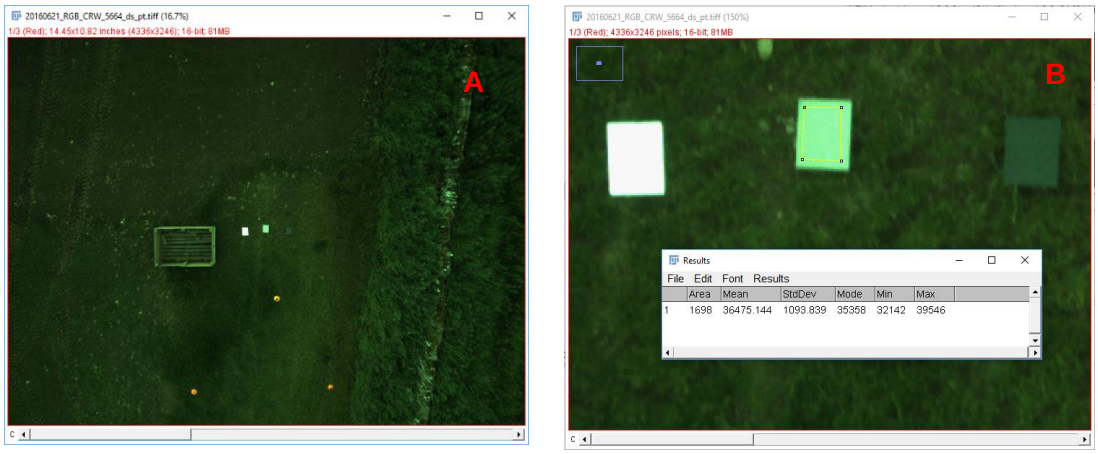

Figure 3-39: (A) Example RGB image showing typical positioning of the calibration targets (centre of image) and altitude used to capture normalisation image; (B) Example measuring of grey calibration target using ImageJ, yellow polygon is the area being measured (1698 pixels).

To normalise the DN (linear pixel values) of each image, the equation outlined by Troscianko & Stevens (2015) was used (eq. 3-4) and applied to each band of both cameras. As this normalisation will convert the linear 16-bit TIFF images into 32-bit TIFF images, the storage space requirements and processing time required to convert each image individually were deemed excessive. Therefore, the normalisation process was only applied to the completed orthomosaic using ArcGIS (ESRI, Redlands, USA), by first separating each linear 16-bit orthomosaic into its individual bands, before applying the normalisation equation and then recomposing the bands back together into a 32-bit orthomosaic.

$$V_{norm} = V_{linear} \frac{\left(\frac{S}{100}\right)65{,}535}{G} \qquad (3\text{-}4)$$

Where V_{norm} are the normalised pixel values, V_{linear} are the linear pixel values, S is the grey standard reflectance value and G is the mean pixel values of the grey calibration target (Troscianko & Stevens, 2015).

3.11 Piksi RTK GPS accuracy assessment

The Piksi RTK GPS (v 2.3.1) unit is an open source centimetre-accurate relative positioning carrier phase RTK device that can output at position at 10 hz (Swift Navigation, 2016). Unfortunately, it could not be used on the UAS during this project as it required modified firmware to be able to integrate with the 3DR Pixhawk autopilot, and in order to get accurate positioning of each image taken by the UAS, it would require feedback from the cameras when their shutters actuate (e.g. by use of the flash hot shoe). This was not possible for the cameras used to create the sensor package (they did not have a flash hot shoe) so the Piksi was instead converted to be used on the ground, to enable surveying of GCPs to a high level of accuracy.

3.11.1 Methodology

As this is an RTK device, it requires a non-moving base station to provide reference measurements to the moving rover unit that is actually taking measurements, with communication between the two units provided via 3DR 433 Mhz radios (v2; 3D Robotics, Berkeley, USA). The base unit was attached to a tripod (figure 3-40a) and the roving unit attached to a collapsible pole (figure 3-40b). Both the rover and base units were attached (via USB) to Panasonic Toughbook CFU1 field computers (Panasonic, Tokyo, Japan) running the Piksi console software (v0.26, firmware

version 0.16). The roving Piksi unit was configured to output NMEA messages at 2 hz with a Baud rate of 4800 and the freeware software GPSUtility (v5.26; Murphy, 2016) was installed onto its field computer so that it could be used to capture the NMEA data being output from the roving Piksi unit.

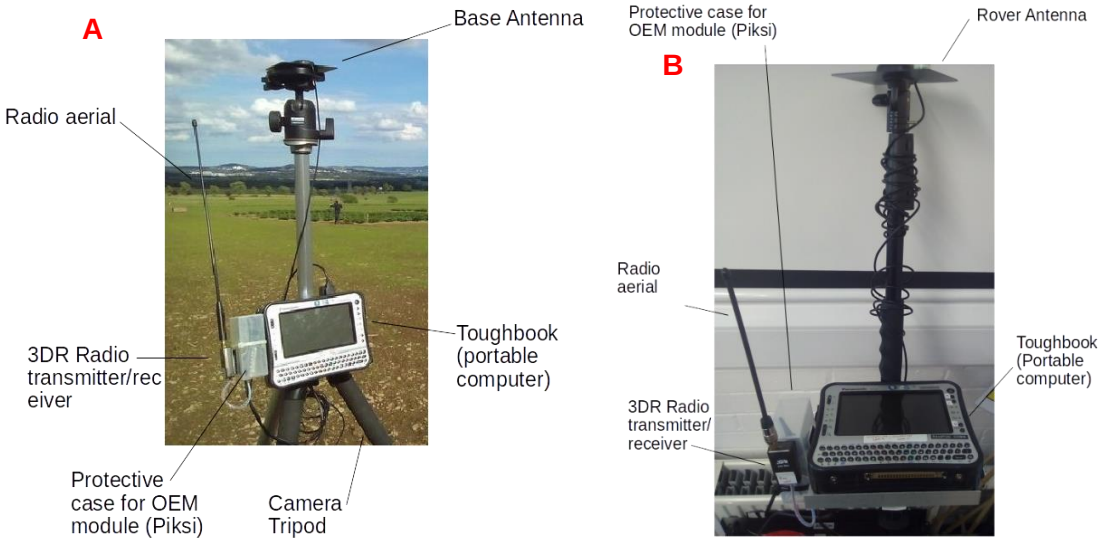

Figure 3-40: The configuration of the Piksi base station (A); The configuration of the Piksi roving unit (B).

To test the accuracy of the Piksi units, 30 GCPs were deployed within a ~1 ha area of a field to the West of Edinburgh. With assistance from the NERC Geophysical Equipment Facility (Allan Hobbs & Kyle Caparoso) and an SRUC intern (Callum Tyler, Queensland University of Technology), the GCP points were measured using a Leica VIVA GS10 RTK GNSS (Leica Geosystems AG, Heerbrugg, Switzerland) with an expected accuracy of ±8 mm horizontal and ±15 mm vertical (Leica, 2018). The points were then re-measured using the Piksi roving unit (the base station was positioned on a pre-surveyed point of known location) and the difference between the two compared to identify the accuracy of the Piksi.

3.11.2 Results

One of the GCP was missed (the point could not be located) so was omitted from the test. The remaining 29 were compared to identify the maximum horizontal (X and Y) and vertical (Z) difference between the two measures and root mean square error (RMSE). RMSE takes the difference between the observed value and estimated value for each user-defined point, squares it, finds the mean squared value, and then finds the square root of that mean (Roze *et al.*, 2014). The horizontal difference (RMSE XY) was worse than expected at nearly 8 cm, with a

maximum difference in Y of 13 cm for one measurement. However, vertical measurements (RMSE Z) gave a good comparative result at ~3 cm (table 3-7).

Table 3-7: Accuracy results (RMSE) of the Piksi RTK GPS unit.

	X (m)	Y (m)	Z (m)
Mean difference	0.023 ±0.026	0.042 ±0.053	-0.019 ±0.021
Maximum difference	0.072	0.131	0.059
RMSE	0.035	0.067	0.029
RMSE XY	0.076		

3.11.3 Conclusions

It was not expected that the accuracy of the Piksi units would be to the cm level, however the larger than expected maximum difference noticed for RMSE Y was surprising, especially as errors of 10 cm or more occurred at least 5 times, whilst much smaller errors were noted for RMSE X. The reason for this is unclear but it could be due to the way the Piksi rover was being operated, as even though a spirit bubble had been added to ensure the survey pole was level for each measurement, slight movements of the operator as they request a measurement were likely to affect the results. The RMSE Z was better than expected as vertical accuracy is typically worse than horizonal accuracy, which again highlights the likelihood that the operator or the construction of the survey pole (or both) were contributing to the RMSE XY error. However, the error is still considerably smaller than that of the navigation grade GPS used on the UAS, which is only accurate to ±2.5 m (U-blox, 2017) and therefore higher positional accuracy could be gained by using the Piksi to survey GCP for use in optimising imagery when being processed by Agisoft Photoscan.

3.12 Concluding remarks

This chapter has outlined the development of the main components of a UAS (the airframe, its propulsion system, command and control and sensor package), identified its operational limitations and modus operandi for field deployments, and indicated the methods to be used to process the imagery captured into products that can be used for further analysis. The UAS is ideally suited to conduct field scale research (i.e. areas < 10 ha) as ~10 ha can be covered within a single flight at maximum altitude, giving image with a GSD of ~3.5 cm per pixel using the combined sensor package. However, as multiple battery sets can be used, this UAS could be

used to capture up to 40 ha a day, if all four battery sets were utilised (potentially more if field capable battery recharging options were available).

It does however have limitations with its design that preclude its use for certain environmental conditions as it is not waterproof, and its large physical size restricts its use somewhat to areas that are more easily accessible (a smaller system would be much easier to pack into a rucksack). Due to the requirements to use RAW imagery from a camera that was not really designed to capture RAW imagery, image capture is slow and pre-processing to a product fit for analysis is long winded, however it should perform well and be comparable with other studies that have used similar sensor packages (von Bueren *et al.*, 2015; Koh & Wich, 2012; Jensen & Mathews, 2016; Rasmussen *et al.*, 2016).

The ability of the sensor package to show visual, near infra-red and height information at very high resolutions should enable it to have a wide range of utility for both agricultural and environmental research areas of interest to SRUC (e.g. plant growth parameters, terrain slope analysis and identification of varied microtopographical features). Therefore, this chapter has met the 1st and 2nd objectives of this PhD project as the field scale level of endurance of the UAS is ideal for the majority of SRUC's agricultural research work, which is typically concentrated on smaller scale crop trials of around 10 ha or less. Similarly, environmental research is also likely to only be concerned with field scale areas, although surveying longer linear features such as rivers or in out of the way places may prove more of a challenge as the size of the aircraft would make it difficult to transport to preferred areas of operation. The 3rd objective is only partially met, as this chapter only indicates the software and processing routines to enable the imagery captured to be created into products for further analysis (e.g. orthomosaic and corresponding digital elevation model). Further software and data processing requirements need to be identified to enable the classification of features of interest from within these data, that are important for specific use cases.

Chapter 4. Agricultural applications - Disease detection within a trial crop of potatoes

4.1 Introduction

Agriculture around the world has to deal with the ever increasing need to improve yield in order to supply a growing human population (Motavalli *et al.*, 2013), whilst reducing impacts on the environment and reacting to climatic changes that could bring pests and disease to new areas (Abberton, 2016). Precision agriculture is a key management approach that could assist with these challenges (McLoud *et al.*, 2007), with UAS forming part of the management solution by providing remotely sensed data that could be used to help identify fertilizer requirements or detect disease and pest infestation. Being able to detect the onset of disease within an agricultural crop would allow for fine tuned decision making with regards to when and where to apply products (e.g. fungicides, pesticides), potentially reducing the amount of product applied, which would be of benefit to the farmer by reducing their costs and would result in less impact to the wider environment (Zhang & Kovacs, 2012).

UAS have already been used to successfully monitor crops such as wheat (Torres-Sánchez *et al*., 2014) and barley (Bendig *et al.*, 2015) and detect the onset of disease in crops such as rice (Zhang *et al.*, 2017), soybean (Brodbeck *et al.*, 2017) and potatoes (Nebiker *et al.*, 2016; Sugiura *et al.*, 2016). However, to date no studies using UAS have looked at the particular potato disease commonly named blackleg (*Pectobacterium spp.*), which is a major contributor to the loss of potato crops worldwide (Toth *et al.* 2011).

This chapter addresses the 3rd and 4th objectives of this PhD project and explores the use of an UAS to detect the onset of disease within a trial crop of potatoes and is based on the results of an experiment carried out with colleagues from The James Hutton Institute (Sonia Humphirs and Ian Toth). A paper detailing early results of the visual and automatic analysis (Gibson-Poole *et al.*, 2017) was submitted and presented at the European Conference on Precision Agriculture in Edinburgh, UK (July 2017) and can be seen in appendix C. The rest of this chapter is an expansion of those early results and seeks to identify if the onset of disease can be automatically classified based on the structural qualities of the plants (i.e. their growth rate, height, volume and canopy cover).

4.2 The potato

The potato (*Solanum tuberosum L.*) was first grown as a crop in the south Americas (Andean region) 8000 years ago (Ortiz & Mares, 2017) and was not brought to Europe until the 16th century (Hawkes & Francisco-Ortega, 1993). Its introduction in Europe led to a significant increase in the European population, however over reliance on the crop and a lack of genetic diversity lead to the rise of disease (late blight) which spread to Europe in the 1840s causing the great famine in Ireland from 1845-49 (Ortiz & Mares, 2017). The potato plant is a herbaceous perennial (figure 4-1) that is typically used as an annual crop in agriculture, where it is grown from seed tubers of particular varieties (Struik, 2007).

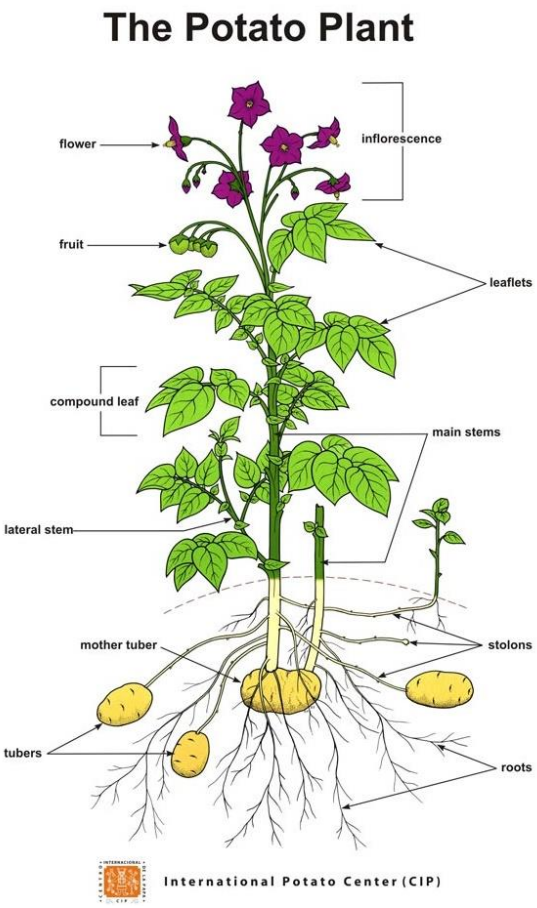

Figure 4-1: The above and below ground elements of a potato plant (International Potato Centre, 2018).

The plant itself can be grown from true potato seed, although this is typically only done by plant breeders in order to create new varieties (Bradshaw, 2007). All parts of the plant contain the compound glycoalkaloid solanine, which contributes to the flavour of the tubers but can be bitter and toxic to humans at high concentrations (Cantwell, 1996). The potato is now an integral part of the worlds food supply, being the world's fourth largest food crop after wheat, maize and rice (Ahmadi *et al.*, 2014, Lacomme *et al.*, 2017), with over 4000 cultivars being grown in more than 100 countries (Bradshaw, 2007).

4.2.1 Growth stages

The potato plant goes through a number of growth stages before it dies back (senescence) at the end of the growing season (figure 4-2), with the BBCH (Biologische Bundesanstalt, Bundessortenamt und CHemische Industrie) scale indicating 10 distinct stages (Kolbe & Stephan-Beckmann, 1997). Understanding these growth stages are important in predicting when tubers will start to form (tuber

initiation; O'Brien *et al.*, 1998) and are therefore key in informing when specific treatments should be applied (e.g. fertilizer; Kolbe & Stephan-Beckmann, 1997) and when the crop could be harvested to supply tubers at a specific size or for a maximum yield (O'Brien *et al.*, 1998).

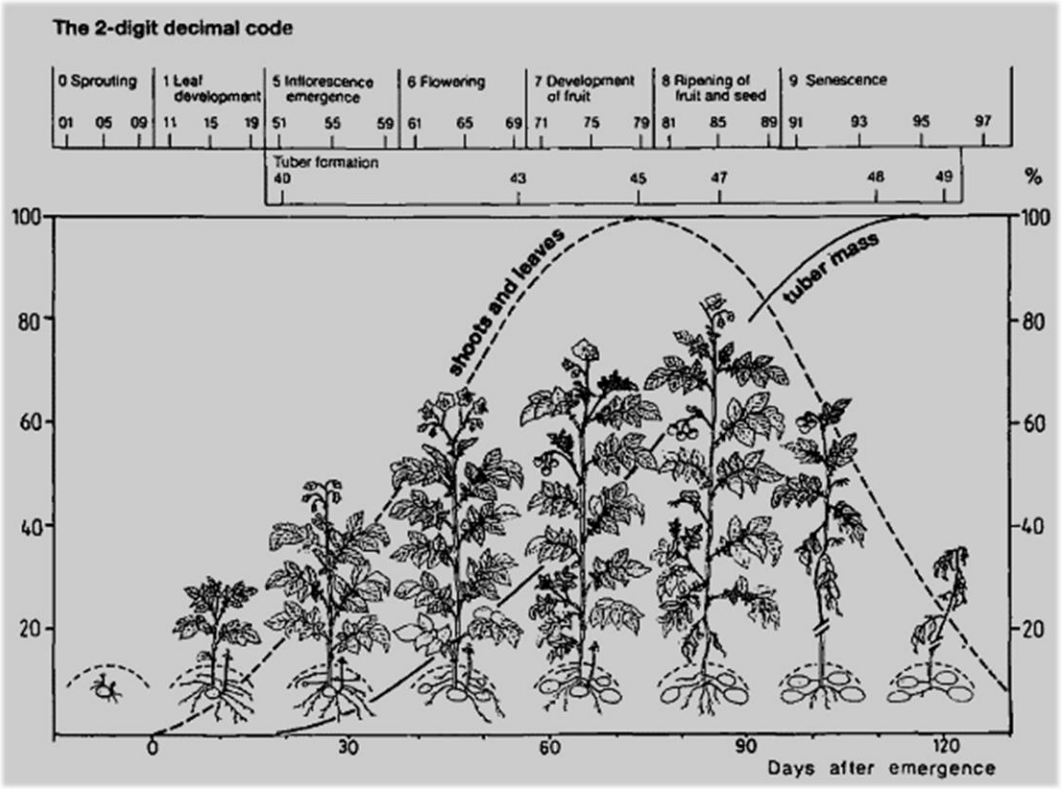

Figure 4-2: The phenological growth stages of the potato crop, with 2-digit decimal identification code for each stage (Kolbe & Stephan-Beckmann, 1997). Diagram does not show stage 2, the formation of basal side shoots, or stage 3, main stem elongation (Hack et al., 2001).

4.3 Seed and ware potatoes

There are two main crop types of potatoes grown for two specific markets. Ware crops are grown for direct consumption or processing into other products for consumption (e.g. bagged crisps) and form the largest volume of UK potato production (AHDB, 2016). Seed crops are not for direct consumption but rather to supply seed tubers of known varieties for the next seasons ware crops. In 2014 the UK was ranked as the 19th largest producer of potatoes in the world (AHDB, 2016), with yield still increasing (figure 4-3) despite the area being used to grow potatoes (and therefore total production) reducing (AHDB, 2016).

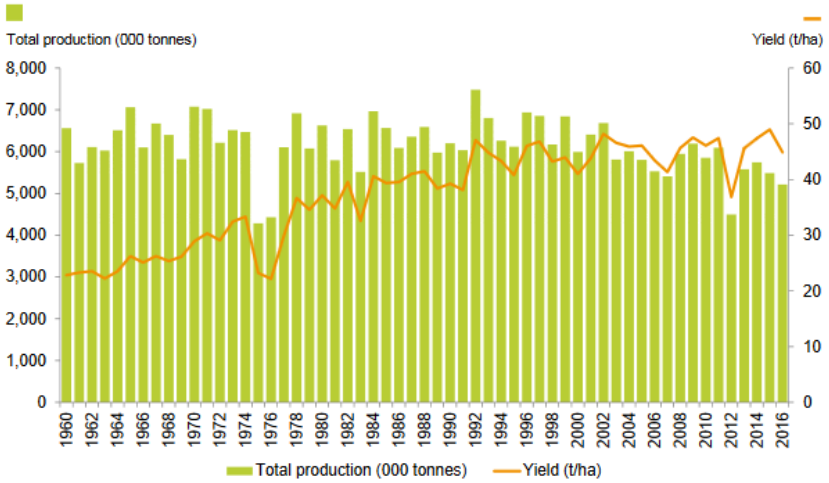

Figure 4-3: Yield per ha and total production from 1960-2016 in the UK (AHDB, 2016).

A large proportion of UK grown potatoes are exported, especially the seed crop, with Egypt purchasing 58 % of all UK seed potato exports 2016/17 (Wright, 2017). Scotland produced 23% of all of the potatoes grown in the UK in 2016 (figure 4-4a), with seed production accounting for 47 % of all the potato crops grown in Scotland (AHDB, 2016; figure 4-4b).

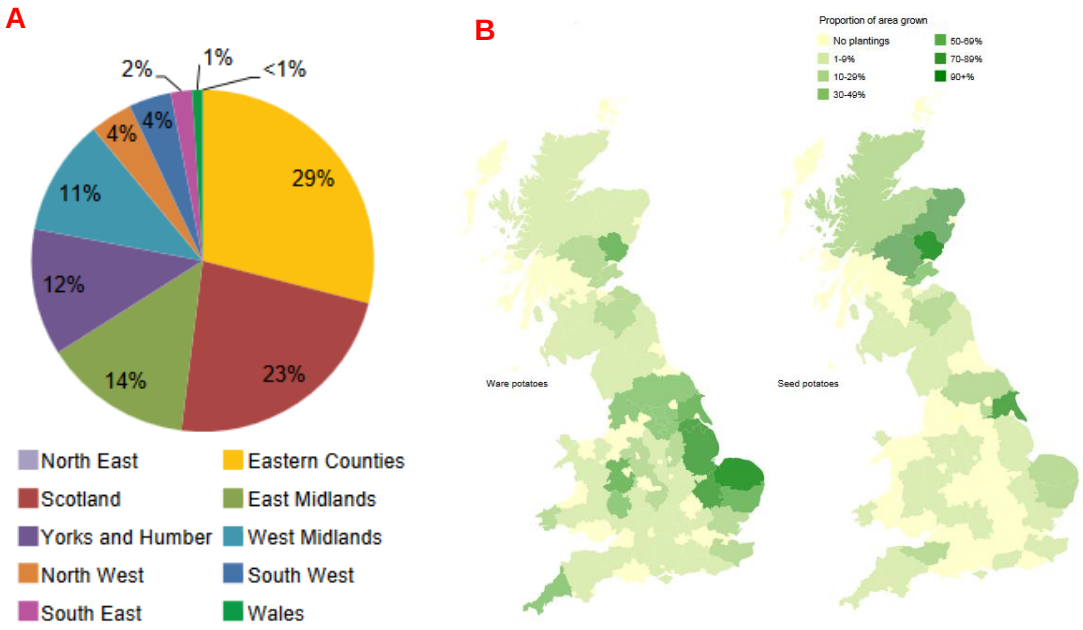

Figure 4-4: (A) Proportion of planted area in the UK by region in 2016 (AHDB, 2016); (B) 2016 main production areas in the UK for ware and seed potatoes (AHDB, 2016).

4.4 Scottish seed potato classification scheme

Scotland is recognised within the EU as a producer of high greed seed potatoes, but before seed potatoes can be marketed, they must meet the requirements of The Seed Potatoes (Scotland) Regulations 2015. To ensure this, the Scottish Government employs inspectors to verify that seed crops are healthy (free or within tolerance levels for specific disease or viruses) and of sufficient purity (i.e. they are the variety they are supposed to be), enabling them to be certified under the Seed Potato Classification Scheme (SPCS; SASA, 2017).

Potatoes can be affected by a number of viruses and bacterial infections that can transfer to daughter tubers (the progeny), therefore seed potatoes are initially created from nuclear stock (micro plants propagated under protected conditions) which generate mini tubers. These pre-basic (PB) tubers must be 99.99 % pure, true to type (i.e. no variations of variety) and completely free from specific viruses and disease, including blackleg and over a number of field generations (growing cycles), their progeny becomes the initial seed potato stocks (termed BASIC S; SASA, 2017).

BASIC S seed tubers can then be propagated for up to 5 field generations and can be marketed if they are within tolerances for certain diseases, with the tolerance for blackleg being 0.1 % of the crop. If they fail to meet this classification (or exceed the number of field generations) then they can be downgraded to BASIC SE (blackleg tolerance 0.5 %) or BASIC E (blackleg tolerance 1 %) or fail to be classified at all if the disease load is too high (SASA, 2017). The inspection process occurs at least twice, initially in early July and then a few weeks later, with a third inspection if required within the last week of July (SASA, 2015). These inspections form the basis of the crop inspection report, however the crop will be subject to ongoing assessments throughout the growing season and therefore roguing occurs throughout. Roguing is the physical removal of plants showing signs of disease (or other undesirable traits) and requires teams of people to walk through the crop to check for and remove diseased plants. This activity can itself cause damage to the canopy of the crop and could possibly spread disease such as blackleg if the conditions are wet, although more research is required to verify this (Toth *et al.*, 2016).

Crop inspection requires a person(s) to walk through potato fields and visually identify and record plants showing signs of disease. However, this is very time consuming, it increases the chance of damage to the crop canopy, diseased plants can be difficult to identify (especially if symptoms are not yet developed or in the early stages), and their spatial distribution is difficult to assess. Recording spatial distribution is currently not carried out, but it would be particularly useful in modelling disease spread (Skelsey *et al.* 2016). The outcome of a crop inspection is central to certification and determines the overall grade (and therefore the price) of a seed crop and allows growers to make decisions regarding the best way to store and subsequently sell the crop, as well as manage it in future generations.

4.5 Blackleg disease

Blackleg disease of potato plants and tubers is caused by different bacterial pathogens belonging to the genera *Pectobacterium* and *Dickeya*, formerly *Erwinia* species (Charkowski, 2015). In Scotland, the disease is largely caused by *Pectobacterium atrosepticum* (Pba), via contaminated seed tubers (Pérombelon, 2002). Worldwide, blackleg disease is a major contributor to the loss of potato crops, and in some countries is the main cause of seed tuber failure and downgrading, e.g. in the Netherlands strict tolerances for certification have led to direct losses of up to €30M annually (Toth *et al.* 2011).

The bacteria causes rotting of the seed tuber if it is contaminated, either through planting (or harvesting) equipment or due to overwintering storage and if soil moisture and temperature favour the development of the pathogen it can spread through the soil and contaminate progeny tubers (Toth *et al.*, 2003; Charkowski, 2015). It is mobile in water so can spread to neighbouring plants and can be transmitted via insects (Charkowski, 2015).

The disease is called blackleg as the most characteristic symptom caused by infection is a slimy black rot lesion that spreads from the rotting seed tuber up the stems (Czajkowski *et al.* 2011; figure 4-5a). This typically occurs under wet environmental conditions but if dry, stunting, wilting, yellowing and desiccation of stems and leaves can occur (Czajkowski *et al.* 2011; figure 4-5b). Unlike infections by fungi, oomycetes and insects, there are no chemical treatments for these pathogens, and breeding for disease resistance has been minimal, making it

necessary to control disease through crop inspections and certification of the resulting seed potatoes (Czajkowski *et al.* 2011).

Figure 4-5 : (A) Close up image of a potato plant stem showing typical "blackleg" symptom (SASA, 2018); (B) Example of wilted potato plant due to blackleg infection.

4.6 Aim of the case study

The aim of this case study is to identify if a UAS equipped with COTS cameras can detect and map the onset of disease within a crop of potatoes, with an effective level of accuracy. Both visual analysis and automatic assessment of the imagery will be compared with conventual ground based disease inspection results.

Due to time pressures at the time of starting analysis to get sufficient data to enable the creation of Gibson-Poole *et al.* (2017) and difficulties with identifying a suitable normalisation method, the imagery captured was not normalised as indicated in chapter 3. Therefore, this analysis was conducted primarily from the viewpoint of the structure and growth of each individual plant, modelling its development from emergence to maturity (or death if it became diseased), with limited reliance on the spectral qualities of the imagery.

4.7 Materials and Methods

4.7.1 Trial layout

The trial plots used for this experiment were located to the west of Dundee, Scotland and were part of a set of varied trial plots designed to show either different potato varieties or treatments as part the Potatoes in Practise 2016 display (James Hutton Institute, 2016). Planting occurred on 5/5/2016 and the trial was composed of 2 plots of 16 rows (figure 4-6), each containing 12 tubers of the variety Hermes that had

been planted by hand with ~30 cm spacing between tubers (91 cm between rows). All of the tubers had been exposed to blackleg forming bacteria (*Pectobacterium atrosepticum*) before planting, and the reason for the trial was to demonstrate best practise tuber storage and haulm destruction methods.

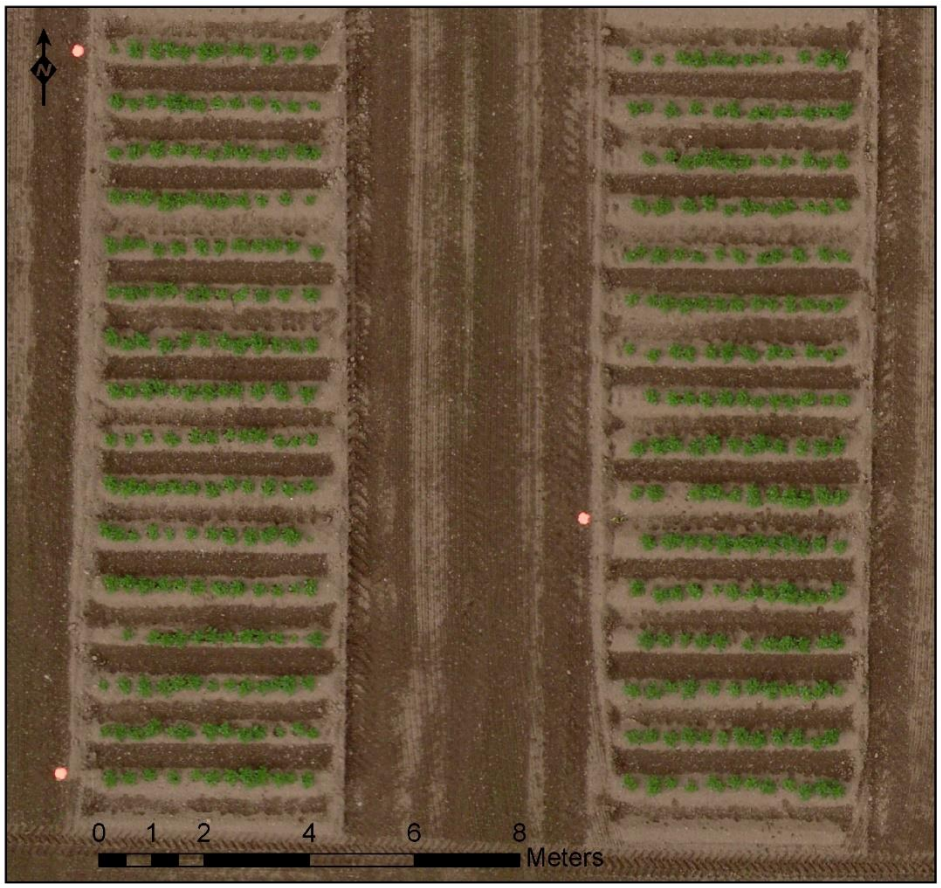

Figure 4-6: The layout of the trial showing plant growth at 47 days after planting. The orange discs are GCPs.

4.7.2 Ground data collection

A visual assessment (ground truth) was carried out by an experienced observer 70 days after planting (DAP), to identify the number of emerged plants ($GROUND^{emerge}$) and show the presence or absence of disease for each emerged plant ($GROUND^{disease}$), along with an indication of the disease symptoms displayed at that time.

4.7.3 Aerial data collection

Aerial data was acquired using the UAS and sensor package indicated in chapters 2 & 3, at 22 (pre- emergence), 28, 34, 39, 47, 52, 62, 67, 75 and 85 DAP, at varying times of the day and environmental conditions (full sunlight ~ overcast; table 4-1). Data was acquired using a pre-programed automatic flight at 35 m above ground level (AGL) to capture imagery with a GSD of ~1 cm per pixel and with an expected image overlap of 62% and side overlap of 87 %. The speed of the UAS was limited to 2 m/s to allow for the integration time of the sensors. Georectification of imagery was assisted by the placement of nine GCPs surveyed using a Piksi (Swift Navigation, San Francisco, USA) real-time kinematic GPS with an expected accuracy of ±8 cm.

Table 4-1: Time each survey conducted, and environmental conditions encountered.

DAP	Time	Conditions
22	13:00	Overcast
28	15:00	Cloudy/sunny
34	14:00	Sunny
39	19:00	Very overcast
47	16:00	Cloudy/sunny
52	11:00	Overcast
62	13:00	Overcast
67	15:00	Cloudy/sunny
75	14:30	Sunny
85	18:00	Overcast

4.7.4 Image processing

Image pre-processing was carried out as indicated in chapter 3 however normalisation was not performed. All three sets of data were processed using Agisoft Photoscan (v1.2.5; Agisoft LLC, St. Petersburg, Russia), using high settings (image alignment highest; dense cloud high quality; depth filtering mild) and optimised using the 9 GCPs placed around the trial plots (using an estimated accuracy of 0.15 m). Ideally there should have been 10 GCP to provide the highest level of accuracy (Photoscan, 2018), however the 10th GCP did not have sufficient image overlap to be reliable and so was not used.

4.7.4.1 Orthomosaic co-registration

The linear orthomosaic data from unmodified and modified cameras needed to be co-registered and combined into a single 6 band orthomosaic, however small shifts in position were noticed between the two. This was most likely caused due to slight

differences in viewing angle, both from the position of the cameras in the gimbal and due to extra distortion from the 585 nm long pass filter applied to the modified camera, leading to slightly different geometry between the orthomosaics. To remedy this, ArcGIS (v10; ESRI, Redlands, USA) was used to georeference the linear orthomosaic from the modified camera to that of the unmodified camera, using the adjust transformation with a minimum of 10 control points leading to root mean square (RMS) errors of < 0.01 m.

4.7.4.2 Plant height layer creation

A pre-emergence orthomosaic and DSM was captured at 22 DAP as this was intended to serve as the base ground height to allow crop height models to be created in the same fashion as Bendig *et al.* (2013). However, inaccuracies were encountered in the resulting crop height models, where the slope of the ground appeared to alter between sensing dates (figure 4-7). The reason for this is unclear but most likely due to inaccuracies of the GCP, an issue that Bendig *et al.* (2013) also encountered.

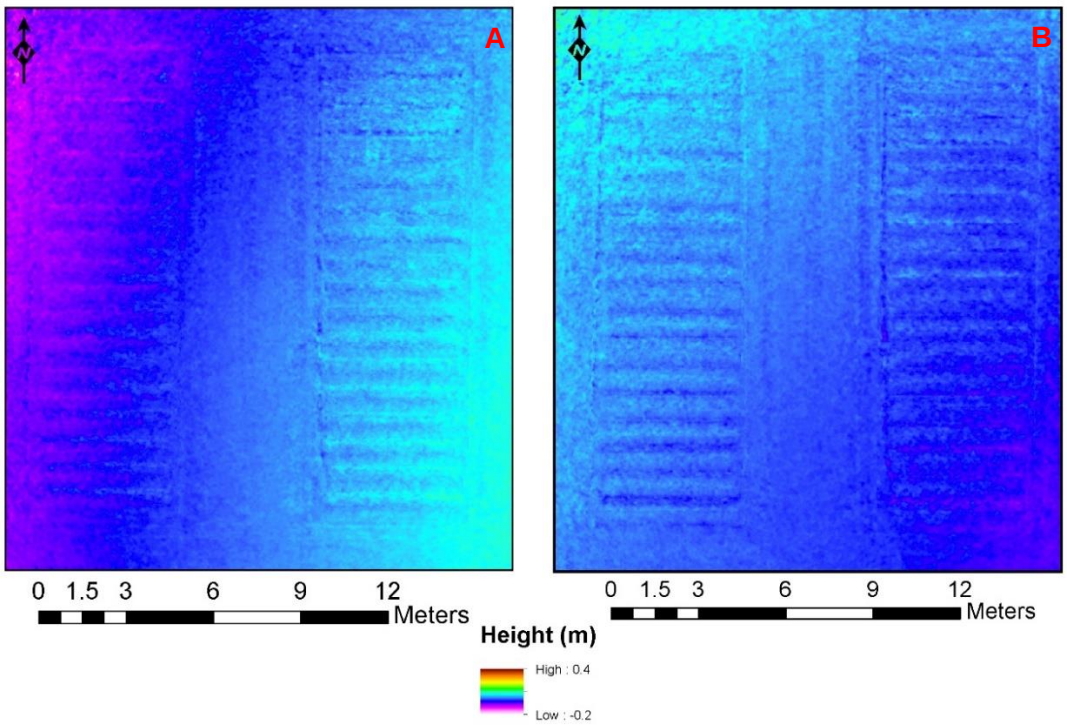

Figure 4-7: Changes in height from 28 – 34 DAP, both sensing dates set to display at the same scale (rows are visible due to slight shift in georeferenced position between sensing dates); (A) 28 DAP, ground appears to slope upwards towards the South East; (B) 34 DAP, ground appears to slope upwards toward the the North West.

To remedy this issue, ground surface points containing no (or minimal) vegetation were selected for each sensing date and used to create an interpolated DTM. 28 points were placed around the two plots (figure 4-8a) and their elevation captured for each sensing dates DSM. The ArcGIS spline command (regularised, default options of 0.1 weight and 12 for number of points) was used to create the interpolated DTM, allowing the crop height model to be created (DSM – DTM). This allowed for effective crop height models that included the ridge of each row (figure 4-8b), however as this remained constant across sensing dates this inaccuracy was ignored from a further processing perspective.

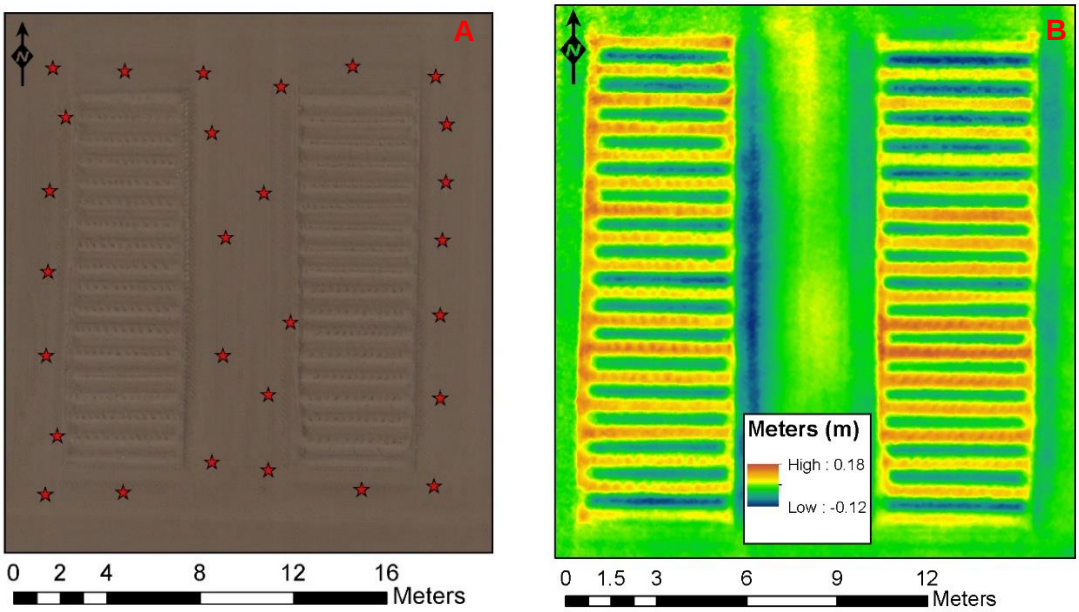

Figure 4-8: (A) Position of points used to estimate DTM for each sensing date; (B) Example crop height model at 28 DAP, showing that row ridges are included within the height captured for each plant.

4.7.5 Manual image analysis method

ArcGIS was used by an assessor (the author) to visually assess the imagery to identify if a plant had emerged or was diseased, using both true and false colour orthomosiac data. For each date a plant emergence point was added if the assessor was satisfied it was valid (not noise) and a plant would then be marked as diseased at a later date, if the assessor believed that signs of disease were showing (e.g. canopy discolouration, canopy loss or stunting). The assessor could go back in time through the data but not forward beyond the date they were currently investigating (the test was done blind; i.e. not referring to the ground data collected by the experienced observer). These methods are referenced as MAN^{emerge} for emergence results and $MAN^{disease}$ for disease detection results.

4.7.6 Automatic emergence and plant count analysis method

To automatically detect emergence, ArcGIS was used to create region of interest (ROI) across the top of each row, derived from a 15 cm buffer of a line manually drawn along the centre of each row, covering each point of planting. A normalised difference vegetation index layer (NDVI; Rouse *et al.* 1973) was created and thresholded manually for each date to delineate potato vegetation from soil, using the formula in eq. 4-1.

$$NDVI = \frac{DN_{NIR} - DN_R}{DN_{NIR} + DN_R} \qquad (4\text{-}1)$$

Where DN_{NIR} refers to the DN from the blue channel of the modified camera and DN_R refers to the DN from the red channel of the unmodified camera.

A model was formed in ArcGIS (figure 4-9a) that created potato vegetation and soil polygons from the NDVI layer of the date being processed, clipped to the ROI. These polygons were then fed into a second model (figure 4-9b) that removed the following sensing dates soil polygons from the current sensing dates vegetation polygons in order to reduce potential noise.

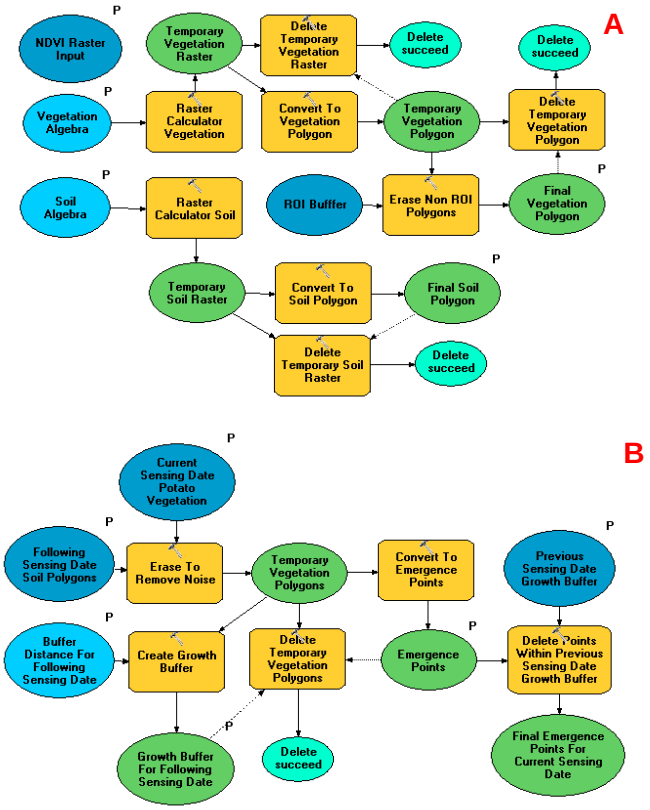

Figure 4-9: ArcGIS models (blue are inputs; yellow are processes; green are outputs); (A) thresholding model devised to create soil and vegetation polygons (clipped to each rows ROI) for each sensing date; (B) emergence model used to create emergence points from vegetation polygons as long as they were not within a vegetation buffer from the previous sensing date.

The model then marked the centre of each remaining vegetation polygon as an emergence point (figure 4-10b) and a buffer of 2 cm per day between the current and following sensing date was then applied to the current sensing date's vegetation polygons, to simulate the growth of the plants' canopy between sensing dates (figure 4-10c). Each subsequent date was processed using the same method, except that any new emergence points were ignored if they were within the vegetation buffer of the previous sensing date, as these were most likely from the same plant. This process was repeated until no new emergence points were discovered across all of the rows. Once all sensing dates had been processed, a central point for each plant needed to be identified from the emergence points to allow a plant count. As several emergence points could come from a single tuber, emergence points that were located within 15 cm of each other were classed as being from the same plant and were amalgamated into a central point (figure 4-10e). This method is referenced as AUTO^{emerge}.

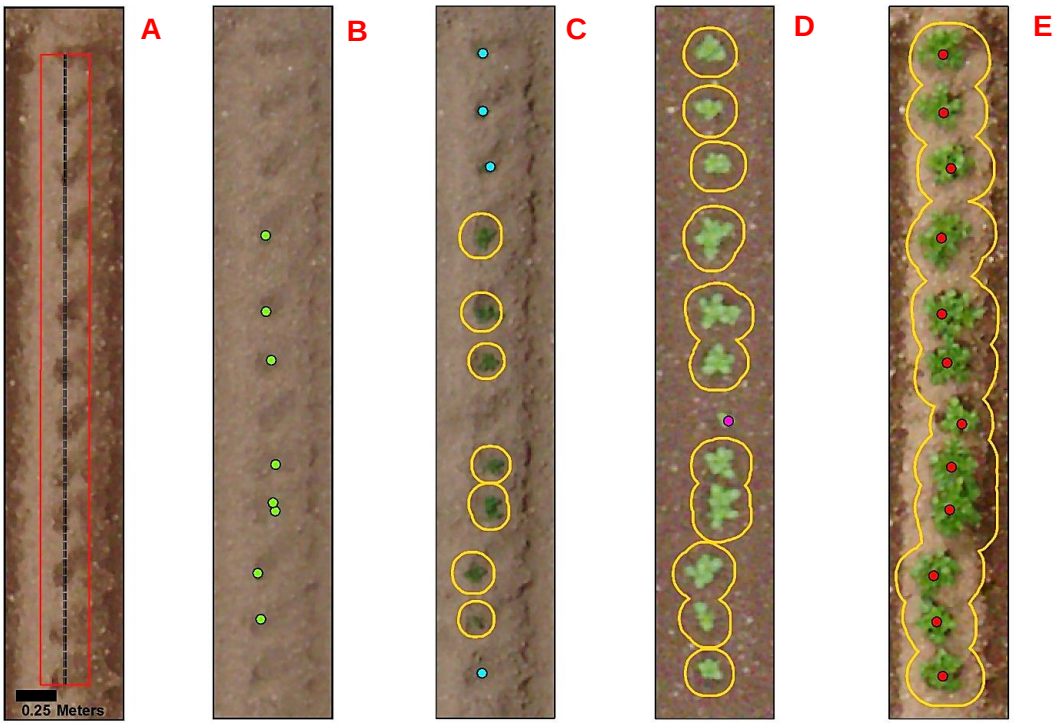

Figure 4-10: Example detection of emergence points using AUTO^{emerge}. (A) Pre-emergence, centre line of plot (black line) and region of interest (red box); (B) 28 DAP, emergence points detected (green dots); (C) 34 DAP, new emergence points (blue dots) but none recorded under the vegetation buffer (orange polygons) from 28 DAP; (D) 39 DAP, final emergence point detected (purple dot), but none recorded under the vegetation buffer (orange polygons) from 34 DAP; (E) Final plant points (red dots) created from amalgamated emergence points.

4.7.7 Automatic disease detection analysis method

4.7.7.1 Classification of potato vegetation

Although pixel-based thresholding of vegetation and soil had been carried out for the emergence count, it was not run against the entire dataset (it stopped after 100 % emergence) and did not account for potato flowers. Potato flowers would be marked as soil due to their low NDVI values, leading to potential gaps within the potato canopy at sensing dates were flowers were present. Therefore, the 6 band data sets for each date were classified using the open source OBIA software InterImage (v1.43; Camargo *et al.* 2012) in order to extract vegetation, flowers and identify areas of shadow.

Due to the image size limitations of InterImage (InterImage, 2010), an ArcGIS model was used to clip each row from the 6-band imagery layer using a 60 cm buffer around the centre line of each row (figure 4-11a). The semantic net (processing workflow) used three classes (potato, potato flowers and shadows) which were all

assigned using the TA_Arithmetic operator (a pixel-based thresholding operator) to denote either:

- Potato vegetation
  - $\frac{DN_{NIR}-DN_R}{DN_{NIR}+DN_R}$ >= (NDVI threshold for that sensing date)
- Areas of shadow
  - $\frac{DN_R+DN_G+DN_B+DN_{NIR}}{4}$ <= 2000
- Potato flowers
  - $\frac{DN_{NIR}-DN_R}{DN_{NIR}+DN_R}$ < NDVI threshold for that sensing date AND
  - Brightness (function) >= 15000

Where DN_{NIR} refers to the DN from the blue channel of the modified camera, DN_R refers to the DN from the red channel of the unmodified camera, DN_G refers to the DN from the green channel of the unmodified camera and DN_B refers to the DN from the blue channel of the unmodified camera.

Once all plots had been classified (figure 4-11b), vegetation and potato flowers were merged using ArcGIS into a single polygon layer (shadowed areas were ignored), to give the total vegetation for each sensing date.

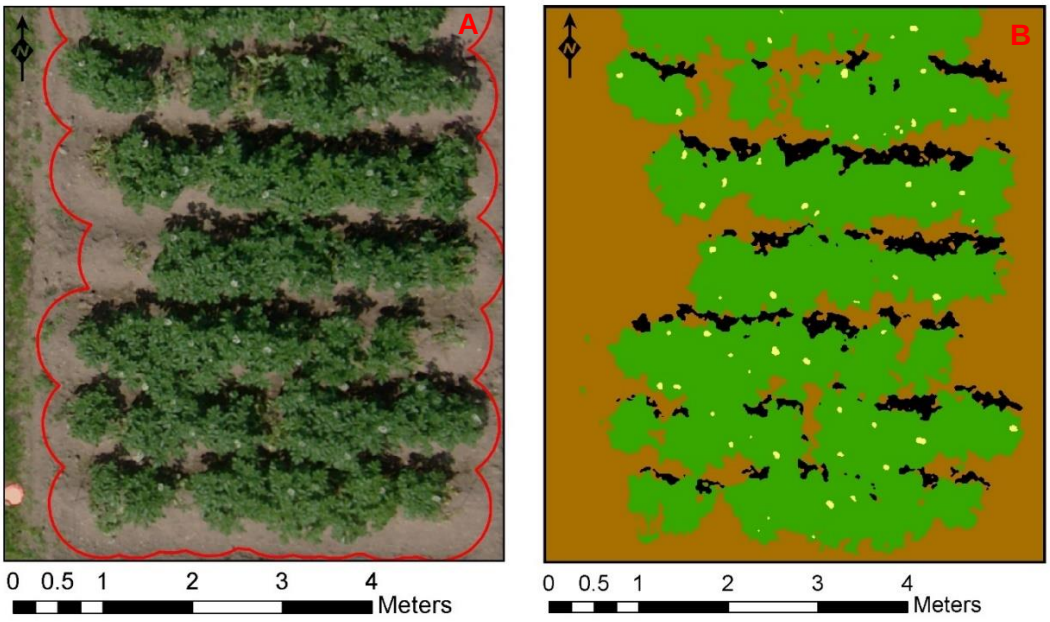

Figure 4-11: Part of trial plot at 75 DAP; (A) Visual image showing maximum extent of 60 cm buffer applied to each row (red polygon); (B) Classification of the same scene (green = vegetation, yellow = flowers, black = shadows and brown = soil).

4.7.7.2 ROI and measures

To monitor the structural changes in the canopy of each plant, further ROI were created using ArcGIS that would be specific for each plant being monitored. All of the emergence points previously detected were buffered by 7.5 cm (dissolved) in order to create emergence point regions of interest (e^{ROI}, figure 4-12a) and as each e^{ROI} could contain more than one emergence point, the centre of each e^{ROI} was marked as the location of a plant (the plant point). Plant regions of interest (p^{ROI}) were then created by delineating an area around each plant point using Thiessen polygons, clipped to a maximum of 60 cm from each plant point (figure 4-12b).

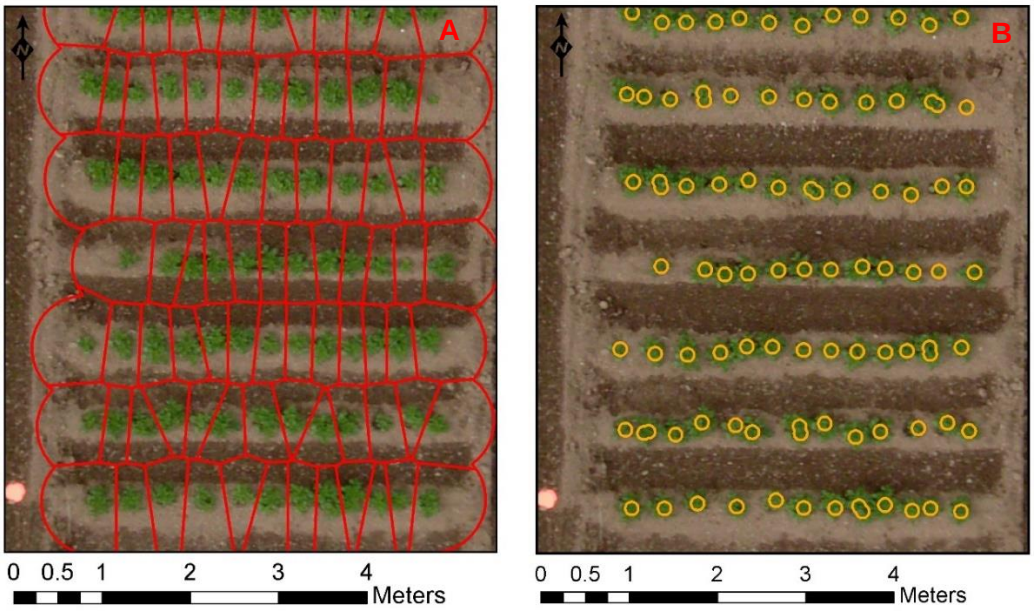

Figure 4-12: (A) Example p^{ROI} created from Thiessen polygons generated from plant points; (B) Example e^{ROI} created from buffering emergence points.

p^{ROI} are essentially the growing space allocated to each plant and can be used to identify changes in canopy ground cover and height within that space. However, as there are several days between sensing dates, an individual plant could die back within that time frame and their neighbouring plants could spread out into the p^{ROI} of the dead plant. This could confuse any measurements made so the e^{ROI} can be used to detect for this as it is much more focused on each individual plant and can also be used to detect any breakup of the plants' canopy. Various measures using the e^{ROI} and pROI were investigated manually to identify their viability in detecting disease, with those in table 4-2 being selected to use within the model.

Table 4-2: Description of measures to be used within the disease detection model.

Measure	Description
p^{GROWTH}	p^{ROI} percentage of canopy growth from previous to current sensing date for a single plant.
p^{GROWTH}_{MEAN}	Mean p^{ROI} percentage of canopy growth from previous to current sensing date for all plants not marked as diseased.
p^{GROWTH}_{STD}	Standard deviation of mean p^{ROI} percentage of canopy growth from previous to current sensing for all plants not marked as diseased.
p^{VOLUME}	p^{ROI} volume of vegetation for current sensing date for a single plant.
p^{VOLUME}_{MEAN}	Mean p^{ROI} volume of vegetation for current sensing date for all plants not marked as diseased.
p^{VOLUME}_{STD}	Standard deviation of mean p^{ROI} volume of vegetation for current sensing date for all plants not marked as diseased.
e^{HEIGHT}	e^{ROI} mean height of vegetation for current sensing date for a single plant.
e^{HEIGHT}_{MEAN}	Grand mean of e^{ROI} mean height of vegetation for current sensing date for all plants not marked as diseased.
e^{HEIGHT}_{STD}	Standard deviation of grand mean of e^{ROI} mean height of vegetation for current sensing date for all plants not marked as diseased.
e^{COVER}	e^{ROI} percentage of canopy cover for current sensing date for a single plant.

4.7.7.3 Disease detection model

A disease detection model was then built within ArcGIS (figure 4-13; figure 4-14 shows the step-by-step workflow for this complicated model) based around the concept that healthy plants will be increasing their growth within the p^{ROI}, until saturation occurs (i.e. the plants' canopy cover has filled its p^{ROI}) or the plants are beginning to senesce. To identify potential cases of disease, thresholds for each measure needed to be identified and initial work using fixed thresholds (Gibson-Poole *et al.*, 2017) revealed that that these needed to be able to adapt to the changes in the growth of the plants as they progress through their different growth stages. To facilitate this these thresholds were based on the mean and standard deviation of each measure for all of the plants within the trial that were known not to be diseased.

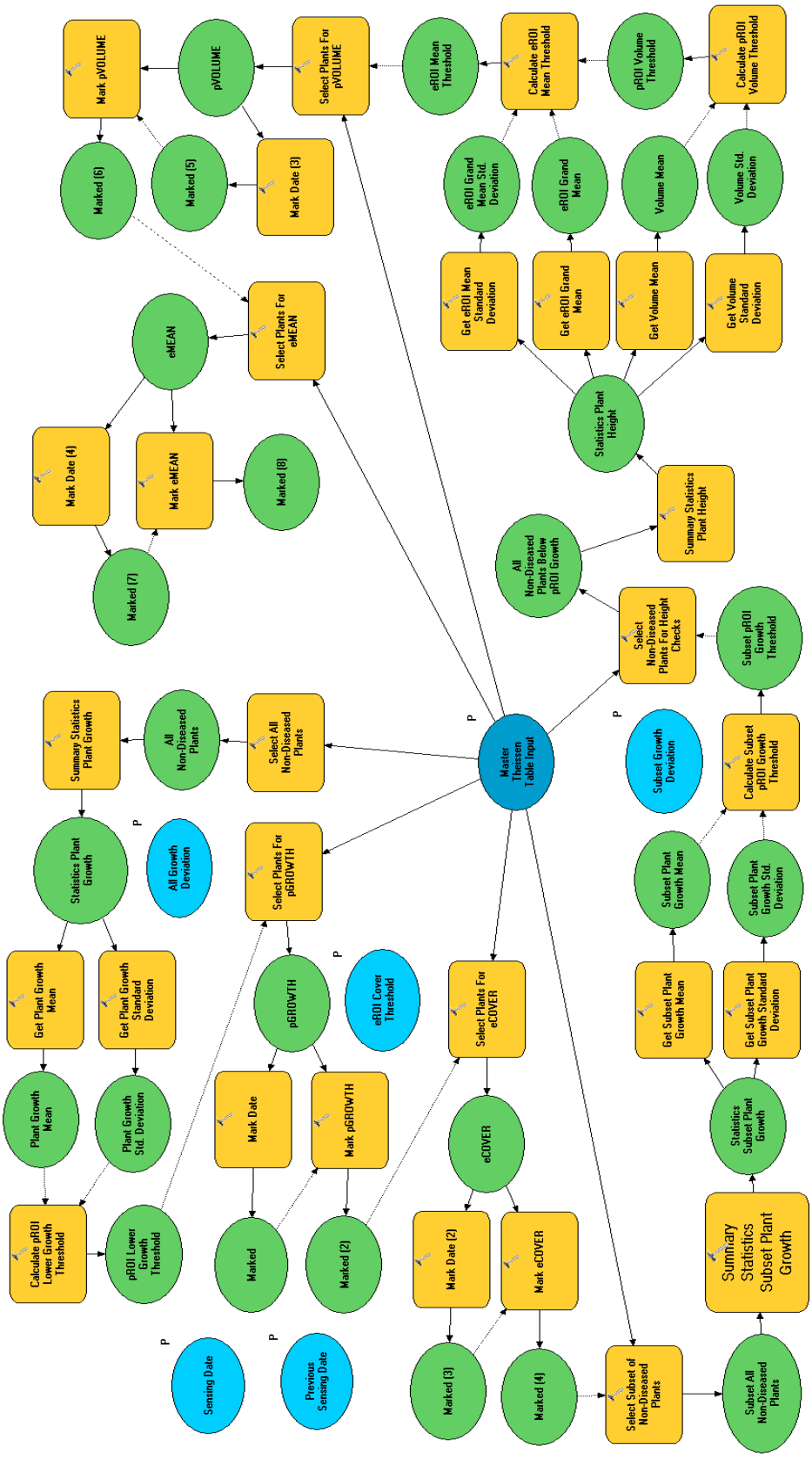

Figure 4-13: ArcGIS disease detection model (blue are inputs; yellow are processes; green are outputs), that utilises the four measures (p^{GROWTH}, p^{VOLUME}, e^{HEIGHT} and e^{COVER}) to identify if a plant is showing signs of disease, by comparing it with the average measures for the entire population of (known healthy) plants within the trial.

Some plants could lose a significant proportion of their canopy between sensing dates due to the onset of disease, which in turn could distort the p^{GROWTH}_{MEAN} and p^{GROWTH}_{STD} measures of the plant population. Therefore, the model tries to filter the most likely cases of diseased plants first, by identifying plants that show very low or negative canopy cover growth compared to their peers (figure 4-14).

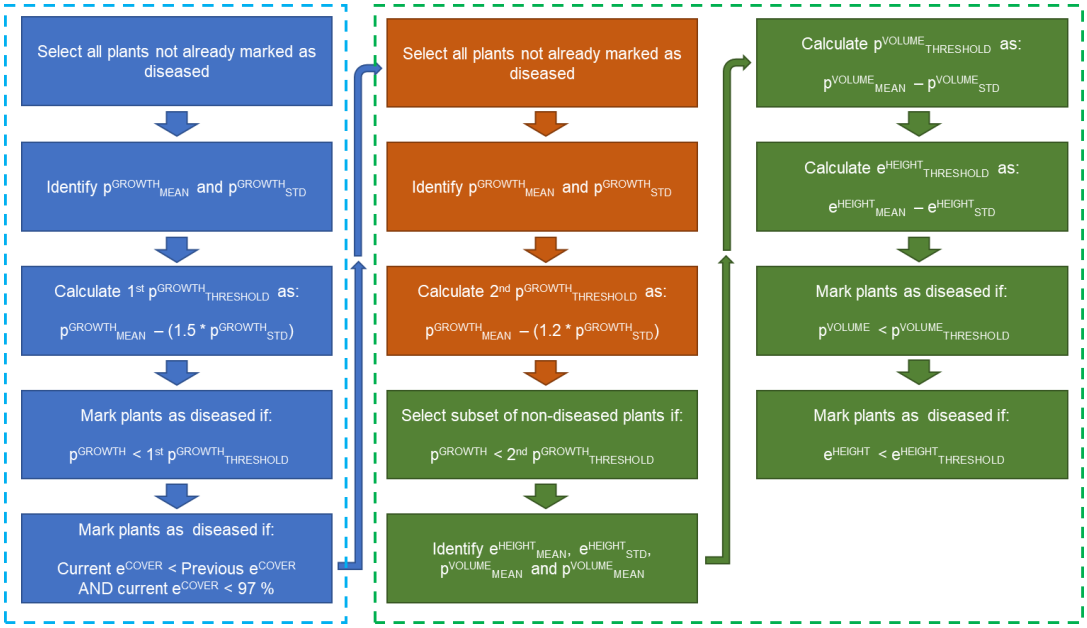

Figure 4-14: Workflow of the disease detection model. The blue section is the first pass to detect obvious disease plants. The orange section identifies a new set of non-diseased plants that does not include these obviously diseased plants. The green section marks remaining plants as diseased if their volume or height is less than the population mean.

The threshold used for this initial selection (1^{st} $p^{GROWTH}_{THRESHOLD}$) could be altered by applying a multiplication factor to the P^{GROWTH}_{STD} measure (figure 4-14), allowing different thresholds to be tested to identify which gave the best results. Plants that showed a reduction in their e^{COVER} measure from the previous to the current sensing date being reviewed could also be a sign of disease that might be missed by the p^{GROWTH} measure if neighbouring plants had encroached into the p^{ROI} of the diseased plant. The expectation is that the e^{COVER} measure should always be 100 % canopy cover, however the threshold used for this measure could also be altered to identify if more flexibility is required (figure 4-14).

With these potentially diseased plants marked, a new selection is made of the remaining plants that are showing lower than average growth compared to their peers. The threshold used for this second selection (2^{nd} $p^{GROWTH}_{THRESHOLD}$) could also

be altered by changing the multiplication factor to the P^{GROWTH}_{STD} measure (figure 4-14), to allow testing for an optimum selection. This final selection of plants were then marked as diseased if they showed a lower than average p^{VOLUME} or a lower than average e^{HEIGHT}.

4.8 Results

As the emergence and disease detection models are based at the plant level, they essentially creating maps of the spatial extent of emergence and disease throughout the trial. Therefore, measures of accuracy for detecting both emergence and disease were computed using error matrices with kappa (Ǩ) statistics (eq. 4-2) that consider the actual agreement between classes whilst taking into consideration the possibility of agreement by chance (Foody, 2002; Rogan *et al.*, 2002). The error matrix gives three main outputs, with the overall accuracy (OA) being an average of all of the correct matches (i.e. number of plants correctly identified as diseased / total number of plants). The users accuracy (UA) corresponds to the error of commission (inclusion; i.e. a plant was marked as diseased when it wasn't diseased) and producers accuracy (PA) corresponds to the error of omission (exclusion; i.e. a plant was not marked as diseased when it fact it was diseased).

$$\check{\mathrm{K}} = \frac{Po - Pc}{1 - Pc} \qquad (4\text{-}2)$$

Where Po represents actual agreement and Pc represents chance agreement (Weih *et al.*, 2010).

The level of accuracy required is subjective, with Foody (2002) indicating 85 % for OA, UA and PA, whereas others indicated OA 85 % and PA/UA of at least 70 % is adequate (Thomlinson *et al.*, 1999; Pringle *et al.*, 2009). A scale for Ǩ is given by Landis & Koch (1977), indicating that Ǩ < 0.41 is poor, 0.41–0.61 is moderate, 0.61–0.81 is good and >0.81 is excellent. Therefore, for the results to be considered as accurate and reflecting reality, OA should be >= 85 %, PA/UA should be >= 70 % and Ǩ should be > 0.61.

4.8.1 Emergence and plant count results

Actual date of emergence could not be verified as only one ground truth measure was available and as this was at 70 DAP, it was only useful for plant count analysis. $GROUND^{emerge}$ identified 385 plants in total, with one case of non-emergence and

two extra plants (left-over tubers had been planted). 385 plants were detected using both MAN^{emerge} and AUTO^{emerge} methods however, both methods identified two cases of non-emergence and three extra plants. Due to this disparity (which would also affect disease detection analysis results) GROUND^{emerge} was reviewed along with the aerial data by the experienced observer, resulting in the change of the ground truth to match that of what was observed with the aerial data, as it was clear from images before 70 DAP where cases of non-emergence and extra plants were present.

Therefore, GROUND^{emerge}, MAN^{emerge} and AUTO^{emerge} agreed exactly with regards to plant counts, but differences in date of plant emergence could still be compared between the two methods. MAN^{emerge} indicated that 69% of the plants had emerged by 28 DAP and all plants had emerged by 39 DAP. The AUTO^{emerge} differed slightly as it indicated that 71% of plants emerged by 28 DAP but did not detect that all had emerged until 47 DAP (due to one plant). Although AUTO^{emerge} did not detect all plants until a later date, it tended to identify emergence slightly earlier than MAN^{emerge}, with 13 plants detect at an earlier date and only 7 later, resulting in an excellent level of agreement between the two methods (OA 95 %, Ǩ 0.88; table 4-3).

Table 4-3: Error matrix of plant emergence at DAP for MAN^{emerge} and AUTO^{emerge}.

		Producer (MAN^{emerge})					
User (AUTO^{emerge})	**(DAP)**	**28**	**34**	**39**	**47**	**Total**	**UA**
	28	262	13	0	0	275	0.95
	34	5	102	0	0	107	0.95
	39	0	1	1	0	2	0.50
	47	0	0	1	0	1	0.00
	Total	267	116	2	0	(385)	
	PA	0.98	0.88	0.50	1.00		**OA** (0.95)

4.8.2 Disease detection results

As the emergence analysis detected anomalies with the ground truth and the remotely sensed data extended beyond 70 DAP, the experienced observer re-evaluated GROUND^{disease} through visual analysis of the imagery, to include all plants that showed obvious signs of disease at 75 DAP. This decision was made so that the ground truth would be more representative of the condition of plants by 75 DAP, especially as the signs and effects of blackleg disease could become apparent

within a 5 day period (Humphirs, 2016). Unfortunately, a final ground truth scheduled to take place just after 85 DAP was not undertaken as the plots had been prepared for the Potatoes in Practise event before this could be carried out (haulm destruction), so results cannot be compared directly at this final sensing date. By 70 DAP, GROUND^{disease} had initially identified 85 diseased plants, which rose to 98 to take into account plants that showed obvious signs of disease at 75 DAP.

4.8.2.1 Identification of model thresholds

Testing of the 1st p^{GROWTH} threshold independently from any other measures within the model revealed that a threshold multiplier of 1.7 resulted in 0 incorrect detections and if it were increased towards 2 then fewer correct detections were made, but if decreased towards 1 then more correct and incorrect detections were made (Table 4-4). Testing the e^{COVER} threshold independently from any other measure revealed that a canopy cover of 97 % within the e^{ROI} gave a high number of correct detections with minimal incorrect detections, and if this were increased towards 100 % then the number of incorrect detections rises faster than the number of correct detections, and if it was reduced towards 95 % then the number of correct detections would reduce by a larger amount of incorrect detections (Table 4-5).

Table 4-4: Independent testing results of 1st p$^{GROWTH}_{THRESHOLD}$ to 75 DAP.

Threshold multiplier	Correct Number of Diseased Plants	Incorrect Number of Diseased Plants	Incorrect Detections as Proportion of Population
1	76	52	13.5 %
1.1	72	34	8.8 %
1.2	68	26	6.8 %
1.3	63	15	3.9 %
1.4	60	8	2.1 %
1.5	57	3	0.8 %
1.6	52	2	0.5 %
1.7	47	0	0.0 %
1.8	43	0	0.0 %
1.9	38	0	0.0 %
2	35	0	0.0 %

Table 4-5: Independent testing results of e^{COVER} canopy cover % to 75 DAP.

Canopy Cover (%)	Correct Number of Diseased Plants	Incorrect Number of Diseased Plants	Incorrect Detections as Proportion of Population
100	73	46	12.0 %
99	66	13	3.4 %
98	65	7	1.8 %
97	65	6	1.6 %
96	63	5	1.3 %
95	62	4	1.0 %
94	60	4	1.0 %
93	60	3	0.8 %
92	58	3	0.8 %
91	56	3	0.8 %
90	54	3	0.8 %

The 1st and 2nd p$^{GROWTH}_{THRESHOLD}$ were then tested together with e^{COVER} fixed to 97%, to identify which combination of thresholds produced the most correct and least

incorrect detections (table 4-6). For each change in the 1st $p^{GROWTH}_{THRESHOLD}$ multiplier, the optimum 2nd $p^{GROWTH}_{THRESHOLD}$ multiplier of 1.2 always gave the best ratio between correct and incorrect results. If this threshold were decreased towards 1, incorrect results would increase by a larger amount than correct and if the threshold was increased towards 1.3, then correct results would decrease by a larger amount than incorrect (table 4-6).

Table 4-6: Identifying ideal disease model thresholds (using 1st and 2nd $p^{GROWTH}_{THRESHOLD}$) to 75 DAP.

1st Multiplier	2nd Multiplier	e^{COVER} Canopy Cover (%)	Correct Number of Diseased Plants	Incorrect Number of Diseased Plants	Correctly Identified Diseased Plants	Incorrect Detections as Proportion of Population	Selected Threshold Combinations
1.7	1	97	82	15	83.7 %	3.9 %	
1.7	1.1	97	82	13	83.7 %	3.4 %	
1.7	1.2	97	82	13	83.7 %	3.4 %	
1.7	1.3	97	80	13	81.6 %	3.4 %	
1.6	1	97	83	16	84.7 %	4.2 %	
1.6	1.1	97	82	13	83.7 %	3.4 %	
1.6	1.2	97	82	13	83.7 %	3.4 %	$AUTO^{disease1}$
1.6	1.3	97	80	12	81.6 %	3.1 %	
1.5	1	97	83	24	84.7 %	6.2 %	
1.5	1.1	97	83	18	84.7 %	4.7 %	
1.5	1.2	97	83	15	84.7 %	3.9 %	$AUTO^{disease2}$
1.5	1.3	97	81	14	82.7 %	3.6 %	
1.4	1	97	85	31	86.7 %	8.1 %	
1.4	1.1	97	84	24	85.7 %	6.2 %	
1.4	1.2	97	84	22	85.7 %	5.7 %	$AUTO^{disease3}$
1.4	1.3	97	82	20	83.7 %	5.2 %	
1.3	1	97	85	40	86.7 %	10.4 %	
1.3	1.1	97	84	32	85.7 %	8.3 %	
1.3	1.2	97	84	29	85.7 %	7.5 %	
1.3	1.3	97	83	24	84.7 %	6.2 %	

4.8.2.2 Accuracy assessment of methods

$MAN^{disease}$ and the three threshold combinations that showed the best ratio between correct and incorrect detections ($AUTO^{disease1}$, $AUTO^{disease2}$ and $AUTO^{disease3}$; table 4-7) were then compared with $GROUND^{disease}$ to identify which gave the most accurate representation of conditions on the ground.

Table 4-7: Disease detection accuracy by 75 DAP; expected number of diseased plants (E); observed number of diseased plants (O); correctly identified diseased plants (C); producers accuracy for disease present (PA); users accuracy for disease present (UA); overall accuracy (OA); and kappa statistic (ǩ).

Comparison	E	O	C	PA	UA	OA	ǩ
$GROUND^{disease}$ vs $MAN^{disease}$	98	80	80	82%	100%	95%	0.87
$GROUND^{disease}$ vs $AUTO^{disease1}$	98	95	82	84%	86%	92%	0.80
$GROUND^{disease}$ vs $AUTO^{disease2}$	98	98	83	85%	85%	92%	0.79
$GROUND^{disease}$ vs $AUTO^{disease3}$	98	106	84	86%	79%	91%	0.76

$MAN^{disease}$ identified 80 diseased plants by 75 DAP (all excluding the cases of non-emergence) and showed an effective level of accuracy and excellent agreement with $GROUND^{disease}$ (OA 95 % and ǩ 0.87). It produced no incorrect detections (false positive results) but produced the lowest number of correct detections (table 4-8). $AUTO^{DISEASE2}$ produced the highest accuracy scores out of the three automatic model combinations (85 % for all UA and PA) and was selected as the model for further analysis. It identified slightly more correct detections (83) compared to $MAN^{DISEASE}$ but it also produced 15 incorrect detections (table 4-9). However, $AUTO^{disease2}$ still showed an effective level of accuracy with a good level of agreement with $GROUND^{disease}$ (OA 92 % and ǩ 0.79).

Table 4-8: Error matrix of plant disease by 75 DAP for $MAN^{disease}$ and $GROUND^{disease}$; (D = disease present; ND = no disease present).

User ($MAN^{disease}$) \ Producer ($GROUND^{disease}$)	D	ND	Total	UA
D	80	0	80	1.00
ND	18	287	305	0.94
Total	98	287	(385)	
PA	0.82	1.00		OA (0.95)

Table 4-9: Error matrix of plant disease by 75 DAP for $AUTO^{disease2}$ and $GROUND^{disease}$; (D = disease present; ND = no disease present).

User ($AUTO^{disease2}$) \ Producer ($GROUND^{disease}$)	D	ND	Total	UA
D	83	15	98	0.85
ND	15	272	287	0.95
Total	98	287	(385)	
PA	0.85	0.95		OA (0.92)

4.8.2.3 Identification of most effective measure

$AUTO^{disease2}$ could not start detecting disease until 52 DAP, once $AUTO^{emerge}$ had identified all of the emergence points, however $MAN^{disease}$ did not detect any disease plants until this date either. Both methods also identified a few more valid diseased

plants by the final sensing date (85 DAP), with MAN^{disease} correctly identifying 84 diseased plants in total, and AUTO^{disease2} slightly higher at 85 (figure 4-15x).

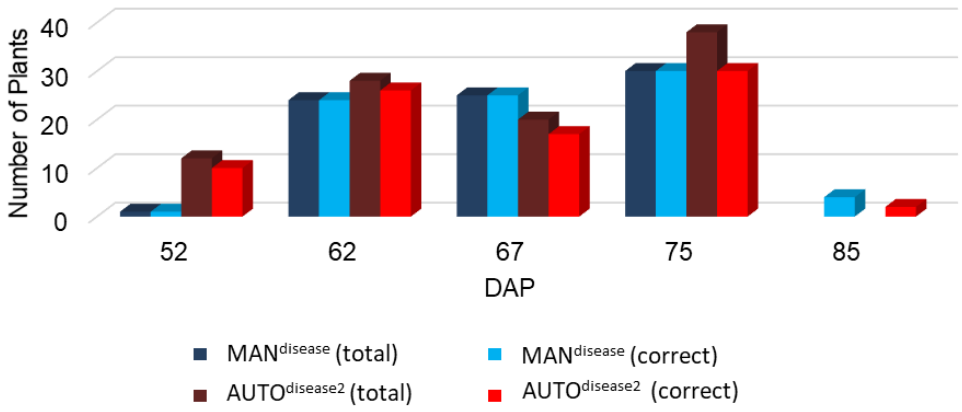

Figure 4-15: Total number of detections and number of correct directions for MAN^{disease} and AUTO^{disease2} at each sensing date.

As the visual analysis of MAN^{disease} is mainly taking into consideration the discoloration or loss of canopy, identification of the measures used by AUTO^{disease2} to successfully (or erroneously) identify disease was also undertaken to see which measures had the most impact. Nearly half of the diseased plants detected were identified from very low growth using the p^{GROWTH} measure, followed by the e^{COVER} measure, then p^{VOLUME} and lastly e^{HEIGHT}. A small number of incorrect detections were made using all of the measures, but the largest contribution of incorrect detections occurred using the e^{COVER} measure (table 4-10, figure 4-16). The majority of incorrect detections occurred on the last sensing date (75 DAP) for all measures except p^{GROWTH} (figure 4-1b).

Table 4-10: Correct and incorrect detections of diseased plants by each measure used in AUTO^{disease2} up to 75 DAP.

AUTO^{DISEASE2} Measures	Correct Detections	Correct Detections as Percentage of Total Detections	Incorrect Detections	Incorrect Detections as Percentage of Total Detections
p^{GROWTH}	48	49.0%	4	4.1%
p^{VOLUME}	12	12.2%	3	3.1%
e^{HEIGHT}	8	8.2%	2	2.0%
e^{COVER}	15	15.3%	6	6.1%

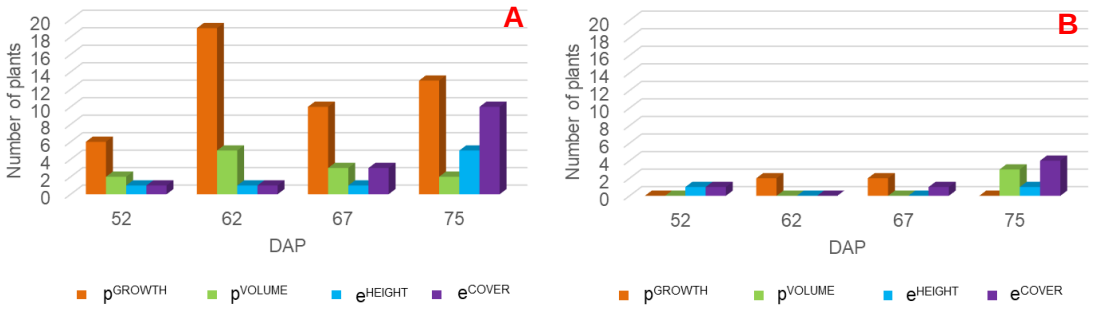

Figure 4-16: (A) Number of plants correctly identified as diseased at each sensing date for each measure used in AUTO^{disease2}; (B) Number of plants incorrectly identified as diseased at each sensing date for each measure used in AUTO^{disease2}.

Comparisons between MAN^{disease} and AUTO^{disease2} were also made with regards to which method detected valid cases of disease the earliest and whether they detected the same diseased plants, including valid detections made by 85 DAP (table 4-11). The agreement between the two methods was poor, showing an ineffective level of accuracy (OA 55%) and barely moderate agreement (Ǩ 0.42). This was because AUTO^{disease2} tended to detect disease earlier than MAN^{disease}, and although most of the valid cases of disease were detected by both methods (79 valid cases), there were 5 diseased plants detected by MAN^{disease} that were not detected by AUTO^{disease2} and 6 diseased plants detected by AUTO^{disease2} that were not detected by MAN^{disease}.

Table 4-11: Error matrix of disease detection at DAP for MAN^{disease} and AUTO^{disease2}.

		Producer (MAN^{disease})							
	(DAP)	**52**	**62**	**67**	**75**	**85**	**No Disease**	**Total**	**UA**
User (AUTO^{disease2})	**52**	1	5	3	0	0	1	10	0.10
	62	0	15	7	3	0	1	26	0.58
	67	0	2	9	5	0	1	17	0.53
	75	0	1	4	20	2	3	30	0.67
	85	0	0	0	1	1	0	2	0.50
	No Disease	0	1	2	1	1	8	13	0.62
	Total	1	24	25	30	4	14	(98)	
	PA	1.00	0.63	0.36	0.67	0.25	0.57		**OA** (0.55)

4.9 Discussion

4.9.1 Emergence and plant counts

The first sensing date post emergence (28 DAP) revealed that more than 50% of the plants had emerged (for both MAN^{emerge} and $AUTO^{emerge}$) however, as the ground truth was only carried out at 70 DAP, the actual date of 50 % emergence of plants could not be verified. This measure can be used to identify the future development of the plants as it enables prediction of tuber initiation (O'Brien *et al.*, 1998), however this measure was not important for the results of this trial although the number and position of each emerged plant was. Plant counts for both methods were excellent (exact in fact) once the ground truth had been amended to take into account the small number of anomalies identified during visual analysis. This demonstrates an advantage of using repeat aerial surveys, as data can be re-evaluated at a later date if results are not consistent with expectations, which is not so easily done if only paper-based records of ground surveys are available.

MAN^{emerge} relied on the assessor being able to recognise and filter out potential points of noise caused by defective pixels (primarily from the NIR camera), however for $AUTO^{emerge}$ their potential influence on the results was addressed through the use of a limited ROI for the detection (15 cm around the centre of each row) and the identification of what was vegetated (or not) for the following sensing date. This means that there will be a delay in effective emergence detection as it will always be a sensing date behind, however this could be remedied through the elimination of defective pixels in the cameras or the development of alternate ways to detect them. Having to manually identify the centre of each row to be able to create a ROI to enable the $AUTO^{emerge}$ method to work satisfactorily is also not ideal but was required to reduce the number of possible emergence points due to noise or the detection of non-potato vegetation (e.g. weeds) between rows. MAN^{emerge} did not require the ROI as the assessor could make judgements directly as to whether an emergence point was noise or a weed in between rows but the creation of the ROI could have been more automated through the use of high accuracy GNSS to mark the start and end of each row, either through a ground based manual survey or attached to any automatic planting equipment that might be being used. Alternatively, automated crop row detection could be attempted using the Houghton transform technique, as demonstrated by (Pérez-Ortiz *et al.*, 2015).

When compared to a similar study on potato emergence by Sankaran *et al.* (2017), it could be said that the AUTO^{emerge} method is superior (although potentially computationally more expensive), especially as the use of a daily growth buffer allowed the detection of newly emerged plants at later stages, even after within-row canopy closure had occurred for the majority of plants. However, in this trial the tubers had been placed by hand and so were well spaced, plus weed control had been effective with only a limited amount of non-potato vegetation present within the emergence period. Spacing of tubers and weed control are important factors to ensure effective growth within the crop (Bussan *et al.* 2007), but less optimal conditions in these factors may decrease the effectiveness of AUTO^{emerge} detection method.

Similarly, the use of a hard growth factor for the vegetation buffer (at 2 cm per day) may not be applicable in all circumstances and may need to be varied based upon weather conditions and fertilizer inputs made within the sensing period. The growth factor value was determined through visual analysis and as the model created allowed for variation of this factor, different values could be attempted (2 cm per day happened to work well for this trial). The use of this buffer also influenced the final position allocated to each plant, which was good in general (i.e. ~30 cm spacing between plants was achieved) but could be slightly offset if the growth buffer of one plant had encroached onto the vegetation of a newly emerging neighbour. The final position of each plant is important in being able to delineate a “growth space” to be used as a ROI for disease detection (the p^{ROI} and e^{ROI}), so errors at this stage could affect the disease detection results. An addition to the model, perhaps incorporating Sankaran *et al.* (2017) concepts of binary thresholding and plant vegetation sizing, or by looking more closely at the maximum height of each potential plant, could allow for improved placement of each plant point.

4.9.2 Vegetation thresholding

The disease detection and emergence automatic methods relied on a thresholded NDVI value in order to separate vegetation from soil. In this study this value was set manually though a visual assessment for each survey date, but ideally the automatic detection of this value should be made. This was investigated using a similar method to Rabatel *et al.* (2014) by thresholding the computed NDVI layer within ArcGIS using the binary thresholding function. This function uses the Otsu (1979) method of creating two classes (a high value and a low value class) with minimal

interclass variance (originally intended to distinguish between background and foreground of a greyscale image). However, it tended to overestimate the vegetative cover, included shadows and covering small details such as gaps within the canopy (figure 4-17) which could reduce the detection of disease.

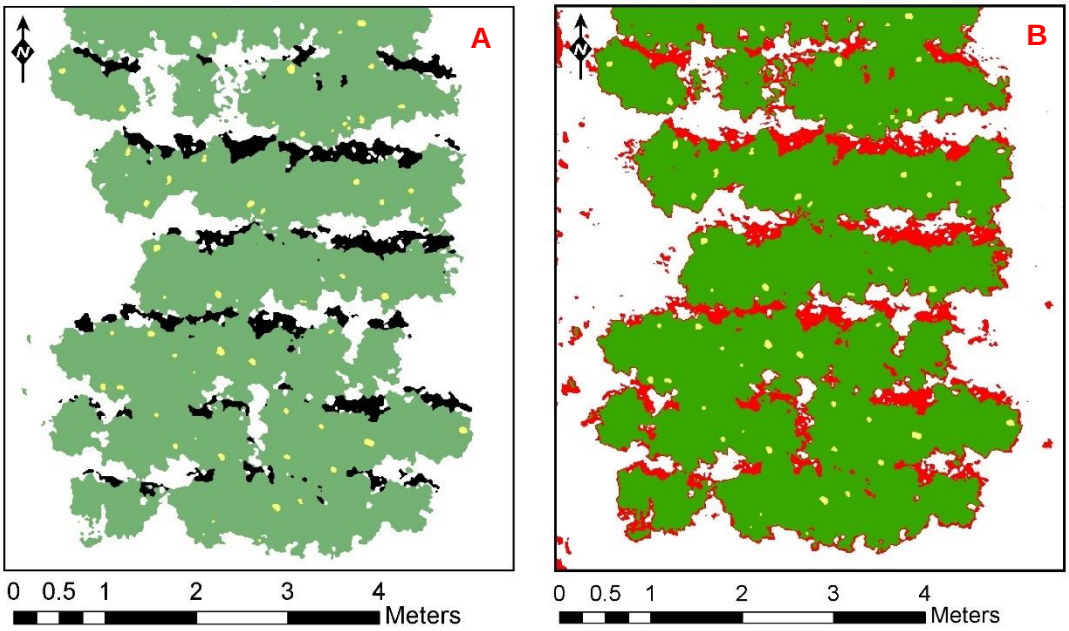

Figure 4-17: Example plot vegetation at 75 DAP; (A) Classified vegetation using manually thesholded NDVI layer (green = vegetation, yellow = flowers, black = shadow); (B) addition of binary thresholded layer (red) showing extra extent of expected vegetation due to inclusion of shadows (between rows) and dying potato plants (intra row).

It was also unable to generate a satisfactory threshold for the first sensing date (28 DAP), probably due to the fact that there was not enough vegetation present to form a significant second peak (bimodality) within the grey-level histogram of the NDVI layer (figure 4-18). The use of a more complex model for the vegetation thresholding could well remove the need for it to be set manually, as a study by Torres-Sánchez *et al.* (2015) indicated a high level of accuracy with minimal computation using an OBIA approach against aerial imagery of maize, sunflower and wheat crops.

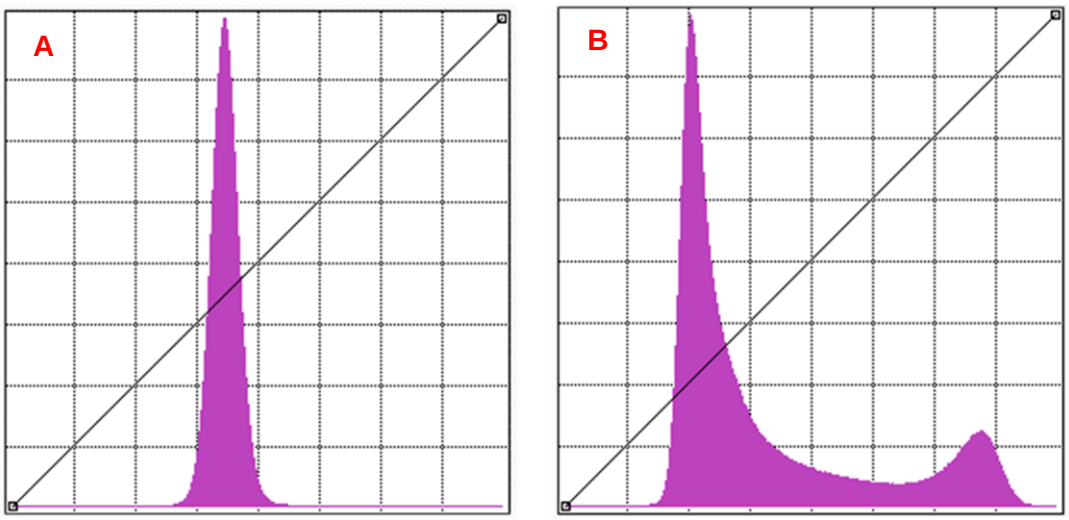

Figure 4-18: Histograms of the NDVI layer; (A) 28 DAP, no significant second peak can be seen; (B) 62 DAP, a significant second peak can be seen, allowing binary thresholding.

4.9.3 Pixel and object-based approaches

Previous studies of trials for disease detection often use pixel-based approaches to map the spread of disease within each plot (Zhang *et al.*, 2017; Brodbeck *et al.*, 2017; Nebiker *et al.*, 2016; Sugiura *et al.*, 2016), however an OBIA based method was used as its ability to segment and classify an image (based on shape, size, texture and spectral properties), is more appropriate for the high-resolution imagery captured by UAS (Blaschke, 2010; Kelcey &Lucieer, 2013). In this study the full power of the OBIA software was not used (no multi-resolution segmentation) as the imagery was essentially just thresholded, however errors were observed with the detection of some flowers. As the OBIA classification was primarily based on a manually derived NDVI threshold, its classification accuracy was only visually assessed and has not been directly verified within this study, but improvements to its classification of potato flowers could have reduced a small amount of false negative results, as misclassification of some flowers led to “holes” appearing within the potato vegetation canopy (figure 4-19).

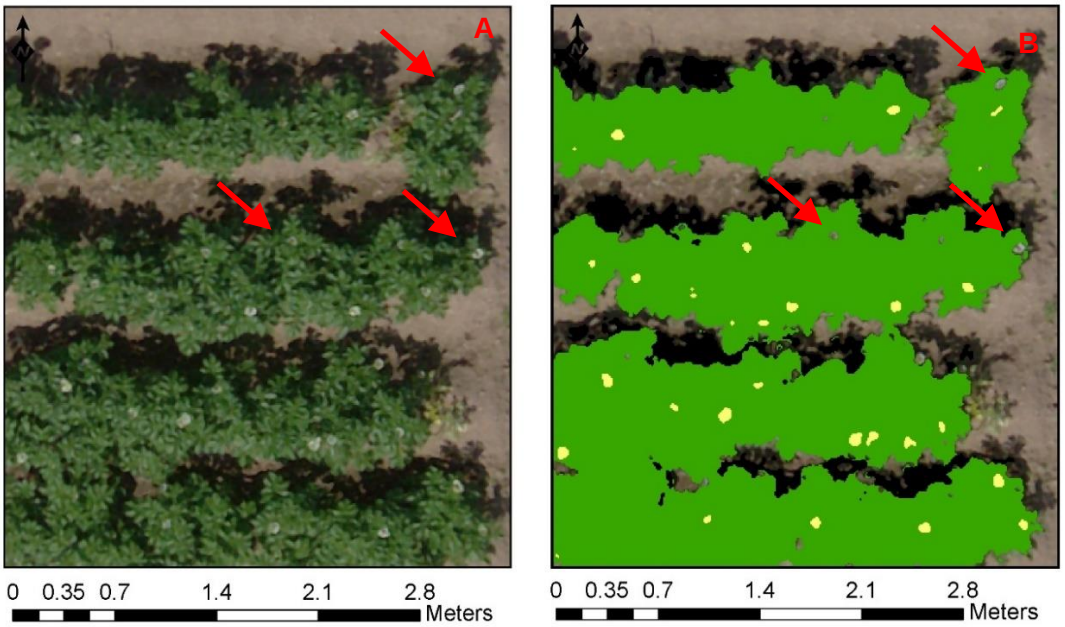

Figure 4-19: Part of the trial at 75 DAP when flowering was very visible; (A) visual layer highlighting flowers; (B) visual layer with classification overlaid (green = vegetation, yellow = flowers), misclassified flowers are highlighted.

OBIA could also have been used for emergence detection, however as weed control of the trial had been effective, a simple and far quicker pixel based NDVI thresholding method was preferred at that stage, especially as the OBIA software available (InterImage) had limitations on the size of imagery it can process (Clewley *et al.*, 2014), meaning that each plot had to be processed independently (a considerably slower processing method).

4.9.4 Delineating plant growth space

As the aim of this study was to identify and map diseased plants through changes in their canopy structure, a way of delineating and monitoring each individual plant was required. The concept of creating growth spaces for each plant (the p^{ROI}) seemed logical and was implemented using Thiessen polygons generated from the plant emergence points. Thiessen polygons are created around a set of points by dividing a given space and allocating it to the nearest point, so that any location within a Thiessen polygon is closer to the point it was allocated to, rather than any other point within the set (Yamada, 2016). As these p^{ROI} were created once the emergence points of all the plants were known (by 52 DAP), delays caused by late emerging plants would delay the disease detection process, potentially missing diseased plants at earlier stages of development, so ideally a model that combined

the detection of emerged plants and monitoring of them for disease from that point of detection needs to be identified.

The use of Thiessen polygons to delineate the p^{ROI} may not be the best method as not all of the plant points were perfectly spaced, leading to disparity in the size and shape of each allocated p^{ROI} (figure 4-20a). They are also not necessarily representative of the natural growth of the plants, which are unhindered by fixed boundaries, only by competition with their neighbours and resource availability (figure 4-20b). This would have attributed to some of the missed and false positive results, and because of the disparity in size of different p^{ROI}, changes to the percentage of canopy growth within each p^{ROI} was used as a measure of disease detection rather than the area or percentage of canopy within each p^{ROI}.

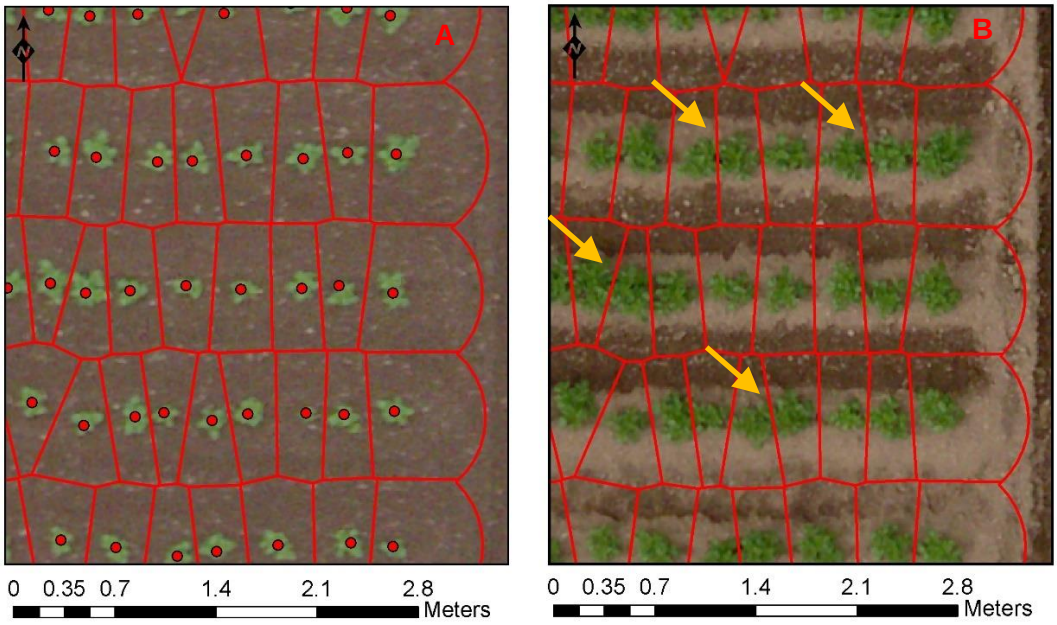

Figure 4-20: (A) Part of trial at 39 DAP, variations in size and of p^{ROI} (red polygons) can be seen due to estimate plant positions (red dots) with the end of rows having more space due to no competition with the 60 cm buffer used; (B) the same part of trial at 47 DAP, intra-row canopy closure is occurring for some plants (highlighted) and so can now only be differentiated by using the hard border of the p^{ROI}.

As these p^{ROI} were fixed based on the emergence results, further issues were encountered relating to the georeferencing of orthomosiac imagery between survey dates as slight differences in position were observed, most likely due to the accuracy of the equipment used to survey the GCPs. Although small, a drift of a few cm between survey dates would have influenced the results, so the use of higher accuracy GNSS (e.g. accuracy < 2 cm) to mark the GCPs would likely have

improved the results. This would also have improved height data processing as Bendig *et al.* (2013) showed effective identification of the height of crops through the use of a pre-emergence DTM, however this method could not be followed due to the variance in slope identified when initially processing the height data.

4.9.5 Automatic and manual disease detection

When thinking of how disease such as blackleg affects a potato plant (primarily wilting, stunting and canopy dieback), the main expectations leading into the study was that canopy discolouration and a reduction in canopy ground cover would be the primary indicators. Visual assessment of the imagery using the $MAN^{disease}$ method was based on these expectations and was relatively straight forward to implement, as the high resolution of the imagery and ability to quickly view current and previous images (in both true and false colour) enabled the assessor to make fast judgements. The assessor would likely improve in both speed and accuracy as they became more experienced, although this would become a tedious task over a much larger number of plots. The results showed a high level of accuracy with no false positive results and an excellent level of agreement with $GROUND^{disease}$ (OA 95 %, PA 82%, UA 100% and Ǩ 0.87). However, not all cases of disease were identified, which can be attributed to missing some cases of canopy discolouration and the fact that only effects to the top of the canopy (loss or discolouration) can be seen from the aerial viewpoint and diseases such as blackleg often show effects on the stems first (basal stem rot, giving the plant its 'blackleg'), with the disease becoming apparent within the canopy later (Czajkowski *et al.* 2011).

The $AUTO^{disease2}$ method relied on thresholded NDVI values to indicate changes in canopy ground cover and canopy discolouration, as discoloured canopy would give lower NDVI values and therefore not be classed as potato vegetation. It could also make more use of the height and volume data, both of which are not as easy to visualise compared to normal imagery and so were not used by $MAN^{disease}$. Initial work using fixed values as thresholds for measures such as canopy ground cover growth gave poor results (Gibson-Poole *et al.*, 2017), so allowing the thresholds to become variable and based on the growth of the entire potato plant population being surveyed was the next logical step. This concept is acceptable if all factors affecting the plants are expected to be the same for each plant (e.g. availability of water and nutrients), as this should result in a relatively uniform pattern of plant development. For this small trial it was expected that this would be the case, but for larger

commercial fields changes to the model may be required to account for in field variability in factors such as soil type and pH, both of which might affect the development rate of plants (Redulla *et al.*, 2002).

To make the threshold for each measure variable, the standard deviation of the plant population mean of each measure was used to identify plants that were either growing at a slower rate or loosing parts of their canopy. However, even for this small trial there were relatively large differences in canopy ground cover growth rate between plants as the plants emerged at slightly different times and so were exhibiting different rates of growth at each sensing date. Large established plants could also completely die back in between sensing dates (especially towards the later dates), which would result in large deviations of the mean within the population as a whole. To reduce this deviation an initial selection of plants is made using the p^{GROWTH} measure to identify plants that exhibited a considerably reduced (or negative) canopy ground cover growth rate compared to the mean plant population.

The 1st $p^{GROWTH}{}_{THRESHOLD}$ for this initial selection could be altered by changing the multiplication factor applied to $p^{GROWTH}{}_{STD}$. This multiplication factor was experimented with but a value of 1.5 produced the most correct detections with minimal incorrect detections, whereas decreasing it towards 1 would result in more correct and incorrect detections, whilst increasing it towards 2 would result in less correct and incorrect detections. A multiplication factor of 1.7 resulted in no incorrect detections, so could potentially be used for applications that required accurate detection of only diseased plants, although fewer diseased plants would be identified overall.

The second measure used in the first part of workflow (e^{COVER}) looked specifically at the canopy cover within the e^{ROI} of each plant as this was expected to always be 100% unless the plant was losing canopy due to disease. This was the only threshold that used a fixed value but would only be enacted if the e^{COVER} percentage of the current sensing date was lower than the e^{COVER} percentage from the previous sensing date. Within the model the e^{COVER} threshold could also be altered and so was experimented with to find an optimum value. Setting it to the ideal value of 100 % proved too sensitive and gave more incorrect results due to a combination of imperfect positioning of the e^{ROI} and slight shifts in orthomosaic georectification, as well as the misclassification of some flowers. Lowering the threshold to 97 % gave

some allowance for this whilst still enabling it to be a useful measure for disease detection, especially where neighbouring plants had encroached into the p^{ROI} of the diseased plant (figure 4-21).

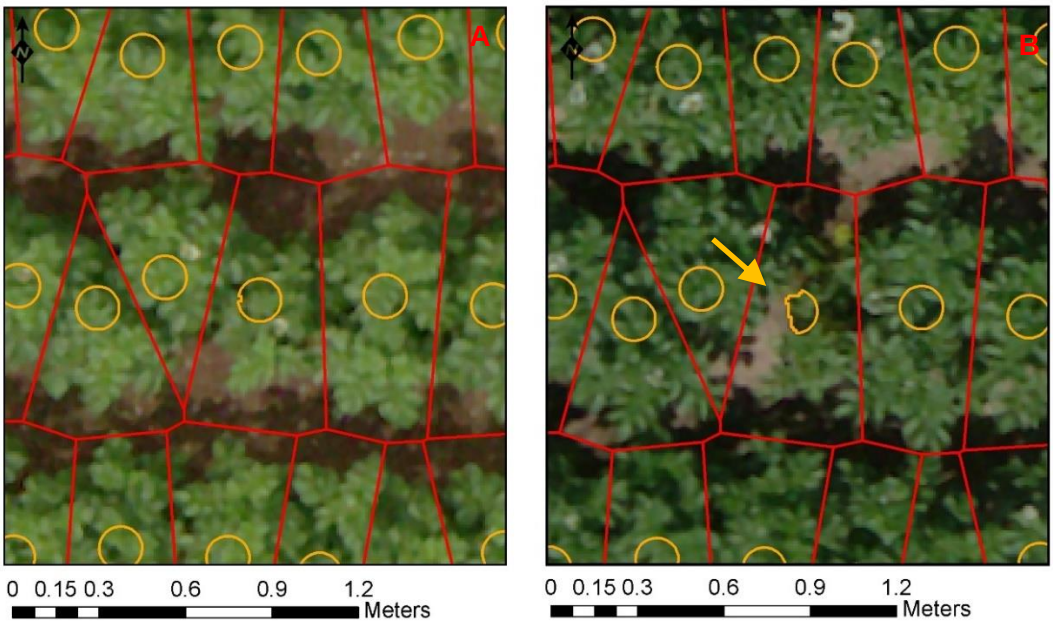

Figure 4-21: (A) part of the trial at 67 DAP, showing e^{COVER} areas generally at 100 % (orange circles); (B) the same section of the trial at 75 DAP, the central plant has lost canopy but was not detected by the p^{GROWTH} measure. Its e^{COVER} is greatly reduce (highlighted) allowing detection.

Both the p^{GROWTH} and e^{COVER} measures relied solely on the spectral element of the data and combined made up ~75% of total detections, so even if height data was not available then these measures alone would give an indication of disease pressure within the plant population. However, as height data was available it could be used to try and identify further cases of disease that were not easily picked up through canopy loss or discolouration. Due to the variability in plant development and growth, a subset of plants that showed lower growth than the population as a whole had to be used before interrogating each plants height and volume, otherwise later emerging plants would always be indicated as diseased, simply because they are smaller than earlier emerging and more mature plants.

Therefore, a 2nd $p^{GROWTH}_{THRESHOLD}$ was used in order to select a subset of slower growing plants from the remaining (i.e. not already marked as diseased) population of plants, again using a multiplication factor for p^{GROWTH}_{MEAN}. Experimentation revealed that a factor of 1.2 gave the best balance between correct and incorrect detections and appeared to be consistent no matter what 1st $p^{GROWTH}_{THRESHOLD}$ value

had been used. Decreasing it towards 1 would add too many plants to the subset, leading to more incorrect detections using the height measures, whereas increasing it towards 1.3 would result in too few plants being added to the subset and therefore fewer correct detections.

To select potentially diseased plants from the subset of slow growing plants, first the mean volume and standard deviation of all the plants in the subset was identified and used to create a threshold for the p^{VOLUME} measure (fixed at the mean volume minus one standard deviation). This produced a more correct detections at earlier sensing dates (62 and 67 DAP), with no incorrect results until 75 DAP. The reason for these incorrect results is unclear, but as the plants were more mature by this stage the already observed shifts in orthomosaic georectification between survey dates could have more influence with this measure, especially if neighbouring plants dying back had part of their canopy within the p^{ROI} being measured. This does indicate that volume measurements are potentially less reliable once the plants have matured and canopy closure (within and between rows) has occurred, simply because it is difficult to isolate one plant from its neighbours.

The final measure used within the subset looked at the mean height within the e^{ROI} of each plant as this should be less influenced by incursions from neighbouring plants. The grand mean and standard deviation of e^{ROI} height for the subset population was identified and used to create a threshold for the e^{HEIGHT} measure (fixed at the grand mean height minus one standard deviation). This detected only a few correct diseased plants for each survey date until 75 DAP, where it then detected a higher number. This can also be attributed to the fact that the plants were more mature at this stage and canopy closure had occurred, so this measure became more important in identifying diseased plants whose p^{ROI} had been encroached on by neighbouring plants.

Although the difference between $MAN^{disease}$ and $AUTO^{disease2}$ was small in relation to the number of correctly identified diseased plants detected (84 and 85 respectively by 85 DAP), there was some discrepancy between the methods. They both identified 79 out of a possible 98 diseased plants (by 85 DAP), so out of each methods total valid detections, a few plants were only detect by one method or the other (5 only for $MAN^{disease}$ and only 6 for $AUTO^{disease2}$). When looking at just the 79 valid cases that both methods detected, we can also see that $AUTO^{disease2}$ tended to

detect diseased plants slightly earlier than MAN^{disease}, especially at the earlier sensing dates (52 and 62 DAP) showing a potential advantage using this method (figure 4-22). More ground truth surveys would be required in order to identify if AUTO^{disease2} could detect disease earlier than from an actual visual inspection of the crop, but it is possible that modelling the growth of plants in detail could allow enable this.

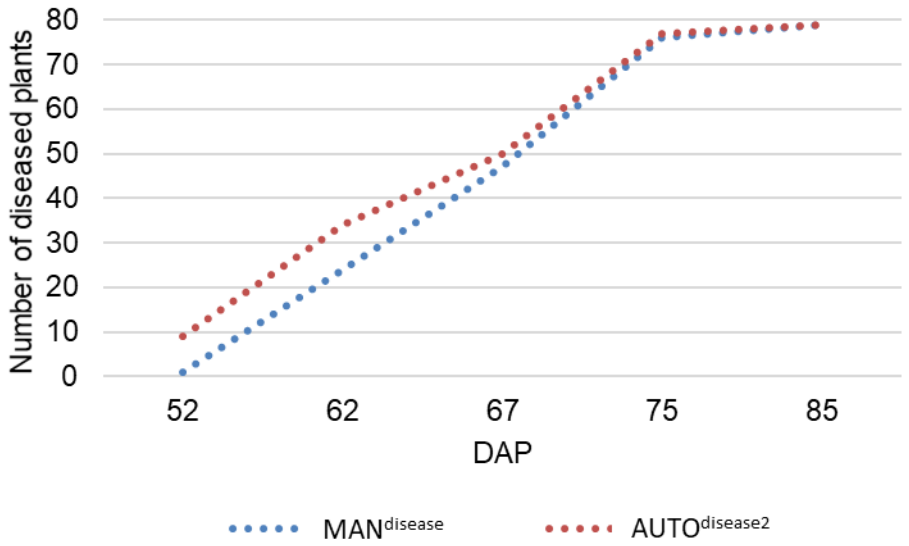

Figure 4-22: Total number of valid diseased plants detect by both methods up to 85 DAP.

4.9.6 Potential application

The primary application of a model such as this is to be able to produce maps of disease that could be used by government inspectors to identify the amount of disease in a crop, or by farmers to provide a map of the locations of disease (figure 4-23) to allow a more targeted response (i.e. only sending in roguers to areas that have known disease), thus minimising any damage to the canopy by unnecessarily walking through it. This spatial distribution of disease within a crop could also show the vectors of infection, as linear patterns could indicate contaminated equipment, whereas scatter cases or 'blanket' infection over a large number of plants could indicate an aerial source of dispersion (Skelsey *et al.* 2016).

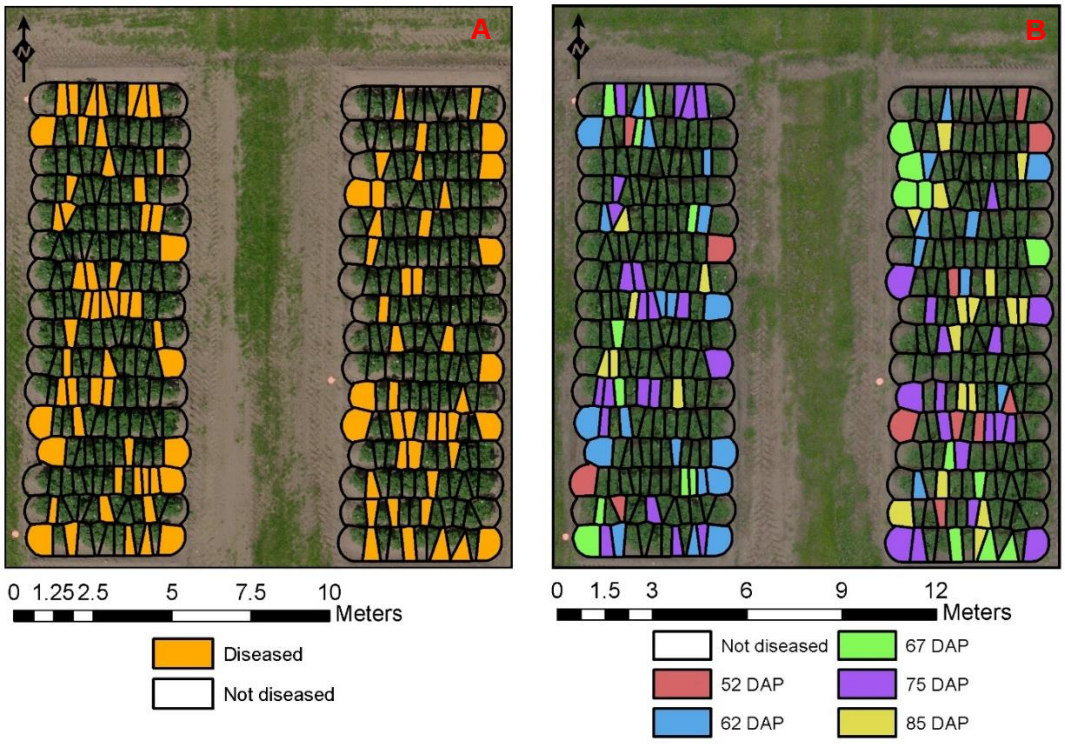

Figure 4-23: (A) Spatial distribution of disease by 75 DAP according to GROUND^{disease}; (B) Spatial distribution of disease by 85 DAP according to AUTO^{disease2}.

4.9.7 Limitations

4.9.7.1 Senescence

One element of the growing cycle of potatoes was not specifically covered within this study, that of senescence. As the crop was burned down (haulm destruction) before reaching this stage (in preparation for the Potatoes in Practise event) its effects on the AUTO^{disease2} model cannot be identified. As plants start to naturally die back at this stage, it is quite possible that the model will generate lots of false positive results, unless all the plants started to senesce at the same time. The mean volume of all of the known "healthy" plants (i.e. the 287 not indicated as diseased by GROUND^{disease}) was still showing signs of increase at 85 DAP (figure 4-24a) although the mean height was reducing (figure 4-24b) and growth had slowed (figure 4-24c), but from this it is difficult to conclude that senesce had begun. Spectral data would most likely be needed to give a better indication of senesce as for instance NDVI values are a good indicator (Bărăscu *et al.*, 2016; Islam *et al.*, 2008), however a drop in mean plant NDVI was also not apparent (figure 4-24d).

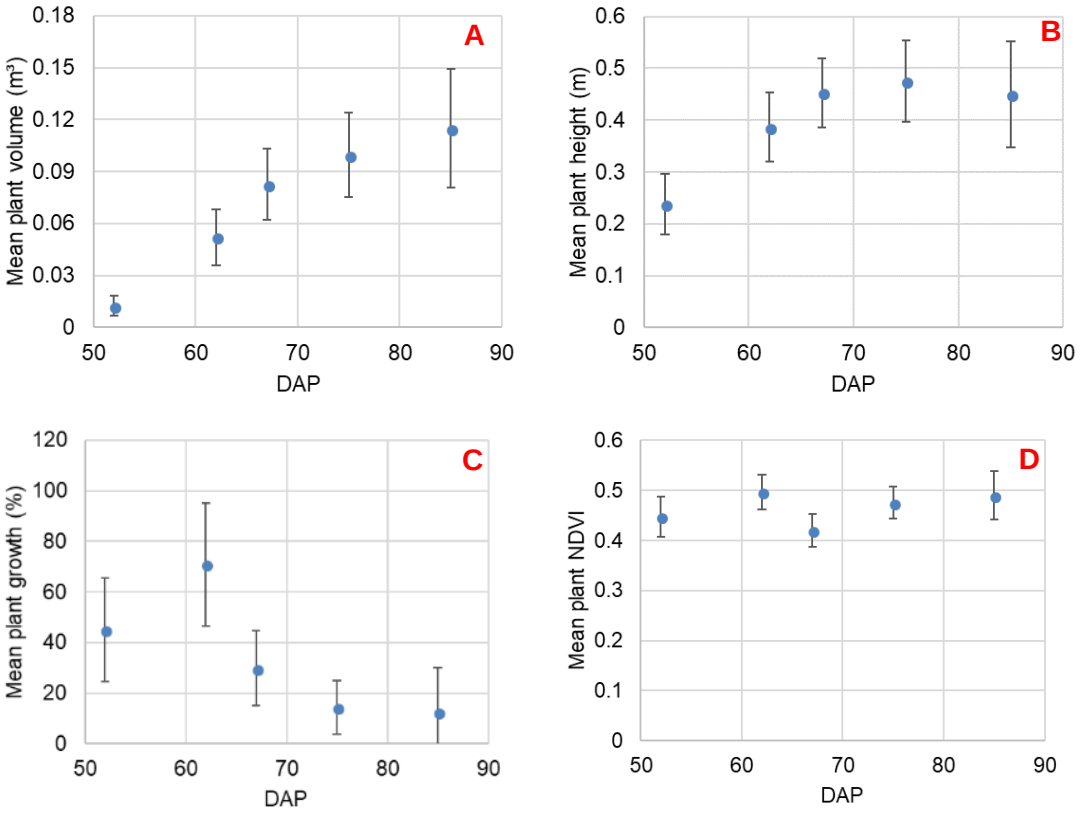

Figure 4-24: Mean p^{VOLUME} (A), e^{HEIGHT} (B), p^{GROWTH} (C) and NDVI (D) values for the "healthy" plant population (the 287 plants not indicated as diseased by $GROUND^{disease}$). Note that by 85 DAP more cases of diseased plants are likely to have been apparent, hence more deviation of the mean.

4.9.7.2 GCP accuracy

As the imagery produced for this project was very high resolution (GSD ~1cm per pixel), slight shifts in georeferenced position of the orthomosaic from one survey date to the next are not ideal, as essentially not all of the same plant is being measured for each survey date. The equipment used to survey the GCP should have had a horizontal accuracy of 2 cm and ~6 cm vertically (Swift Navigation, 2017), however validation of this (chapter 3) revealed that not to be the case (8 cm horizontal, 3 cm vertical), most likely due to error introduced from the way the equipment was deployed. The change in georeferenced position between survey dates was checked (table 4-12) to identify the shift using the root mean square error (RMSE) and revealed that the horizontal difference was within the accuracy margin although vertical error was worse than expected (which could account for the issues encountered with the DSM when attempting to generate crop height models).

Table 4-12: Changes in orthomosaic position between one survey date and its successor (all in meters).

DAP	RMSE X	RMSE Y	RMSE XY	RMSE Z
28-34	0.044	0.022	0.050	0.094
34-39	0.010	0.023	0.025	0.014
39-47	0.011	0.025	0.037	0.044
47-52	0.013	0.025	0.027	0.090
52-62	0.018	0.019	0.023	0.022
62-67	0.012	0.025	0.031	0.042
67-75	0.012	0.017	0.021	0.028
75-85	0.053	0.057	0.078	0.049

These shifts in position will have had an effect on the results as the p^{ROI} and e^{ROI} were static, so not all of the same plant will have been measured every time (more so for the later sensing dates than the earlier due to the size of the plants). As this study was specifically trying to monitor the development of plants in situ, this level of positional accuracy was far from ideal but considerably better than if relying on the accuracy of the GPS onboard the UAS alone. Therefore, ideally very accurate GCP survey equipment should be used to try and minimise errors caused by positional shift between survey dates, but this in itself is a limiting factor as this equipment is expensive and not always easily available (hence why the Piksi was used for this purpose).

4.9.7.3 Weather & survey effort

Weather limitations are an issue when using UAS as they are generally not waterproof and work best when wind speeds are light. Throughout this study the weather did dictate when data could be collected and although regular (approximately weekly) data collections did occur, they were not necessarily at the optimum time of day. Ideally remotely sensed imagery should be captured within two hours of solar noon and under cloudy conditions to minimise the generation of shadows and provide stable ambient light (Rasmussen *et al.* 2016). This was however not always possible simply due to the environmental conditions at the time when data needed to be collected (it was better to have data under sub-optimal conditions than have no data at all).

This leads onto the other main limitation of the AUTO^{disease2} model, in that for it to be effective, regular surveys must be carried out (ideally every week) so that the progress of plant development can be followed. If the time between datasets is too long, emergence counts could be disrupted due to intra-row canopy closure, or diseased plants could be missed simply because neighbouring plants extended their canopy into the space left by the diseased plant. This is potentially quite a high survey effort so may not be practical and adds risk to using the model, for if data capture is delayed, the model may give poor results.

Capturing the aerial data for this trial took less than 5 minutes of actual flying, but with aircraft setup and layout of ground control points, at least 30 minutes was required. Processing the data (orthomosaic generation and analysis) also took time (~2 hours per dataset), however much of the processing did not require continuous human interaction and with further automation (and the use of faster classification software) could be discounted almost entirely. One area that would significantly reduce collection and processing times would be to not use GCPs, although for this study they were required to ensure effective georectification of imagery between survey dates.

As this trial was very small, manual assessment of the trial was comparatively quick compared to the aerial survey (<30 minutes in total), however over larger areas of several ha the amount of time required increase significantly. For instance, potato inspectors typically work in pairs and don't physically inspect the entire area of crop being reviewed, but inspect sections using a zig zag pattern across the field. For a 10 ha field they would physically inspect ~0.2 ha, which would take them at best 30 minutes if no or limited signs of disease are found, but this would increase significantly if more signs of disease are seen (as closer inspection would be required) or if the size of the crop makes it more difficult to walk through (Ellicott, 2019).

Further to this the time required for roguing fields (which is typically done twice, before each inspection) is even longer. Depending on the level of disease found within a field, on average a team of 15 people would take ~3.5 hours per ha, as they have to inspect each plant and where disease is found, remove the effected plants and any tubers. Even where disease presence is low, ~1.75 hours per ha is required just to inspect each plant (Fleming, 2019).

Therefore, the use of a UAS to monitor fields weekly and provide disease maps could reduce the time required for roguing, as they could target their efforts into areas known to have issues. Likewise, as the potato inspectors only physically inspect sections of the field, the use of a UAS would help widen their survey, again allowing more targeted inspections into highlighted problem areas.

4.10 Conclusions and future thoughts

Modelling and mapping the development of individual potato plants to this level of detail has not been shown within another study to date (to the authors knowledge). This study has successfully shown that the onset of disease within a potato crop can be identified via interrogation of the change in plant structure using a UAS equipped COTS cameras. The level of accuracy is however subjective, for if the 3.9% error rate (false positive detections / plant population) of $AUTO^{disease2}$ were scaled linearly to a more typical commercial crop plant density of 40,000 plants per ha, then there could potentially be 1560 false positive results per ha. This may well not be accurate enough for real world use, so improvements indicated in the discussion will need to be made.

The main omission is the use of spectral data to help narrow down cases of potential disease. Ideally the use of calibrated multispectral sensors such as the MicaSense RedEdge (MicaSense Inc, Seattle, USA) would provide high quality spectral data to assist with this, as they have been used successfully to detect disease in rice (Zhang *et al.*, 2017) forests (Dash et al., 2017) and grapevines (Albetis *et al.*, 2017). However, sensors such as these are considerably more expensive than the COTS cameras used in this study. Another aspect that could reduce the error rate and help reduce the time taken for data collection would be the application of direct georeferencing from GNSS receivers on board the UAS. If accurate enough (ideally to a few cm), this would potentially negate the need for GCP thereby speeding up image capture and image processing. However, this too would require the use of more expensive GNSS receivers, but other studies have shown that accuracy of a few cm can be achieved by pursuing this technique (Turner *et al.*, 2014; Harder *et al.*, 2016).

This chapter meets part of the 4^{th} objective for this PhD project, in showing that structural plant growth parameters can be interrogated overtime and that this can be

used to as a method of detecting disease. Although this study only investigated potatoes, the use of structural data could be applied to a variety of trial crops, as well as to aid in the classification of other microtopographical features (e.g. different levels of native vegetation, such as trees, shrubs and grasses). It also adds to the evidence for the 3rd objective, in that it demonstrates the utility of both pixel and object-based image analysis to aid in the separation of plant material from soil, although the use of OBIA techniques in this chapter was fairly limited due to the limitations of the software package used.

Chapter 5. Agricultural applications - Comparison of aerial and ground-based methods for analysis of a trial crop of potatoes

5.1 Introduction

Agricultural trials are used for a variety of different purposes, with the primary aim being the identification of the development and potential yield of crops when within field like conditions and not in the controlled environments of laboratories or greenhouses (Sankaran *et al.*, 2015). However, collection of data from the ground can be laborious if there are many plots to process, or specific measures (such as crop height) are required (Sankaran *et al.*, 2015; Holman *et al.*, 2016). Field trials are required to evaluate new varieties of crops, in terms of their resistance to certain types of disease or response to environmental conditions (often termed high throughput phenotyping) and due to their flexibility of deployment, range of possible sensors and relatively low price, UAS are likely to become indispensable tools to support this activity (Chapman *et al.*, 2014; Haghighattalab *et al.*, 2016; Shakoor *et al.*, 2017).

Ground based assessed agronomy field trials are used to evaluate established varieties typically grown by farmers, covering all aspects of crop production (growth regulation, tillage, establishment, varieties, weed control, pest and disease control), which can be disseminated and fed back directly to farmers to help them manage the day to day development of their crops. For instance, Havis *et al.* (2014) conducted ground-based assessment of field trials over three years to identify varietal resistance of barley to the fungal pathogen *Rhynchosporium commune* (which can result in yield losses up to 40%), as well as inform on the effective timing application of targeted fungicides to combat its development. UAS have already been used to help monitor field trials investigating the resistance of crops to disease (Sugiura *et al.*, 2016) and tolerance to environmental conditions such as water stress (Kyratzis *et al.*, 2014), hard winters (Khot *et al.*, 2015) or damage caused by more extreme weather such as hail (Zhou *et al.*, 2016), so the application of UAS to aid in the monitoring of agronomy trials could enable more aspects of plant development to be captured and thus provide more informed feedback to farmers.

This chapter addresses the 3rd and 4th objectives of this PhD project as it explores the use of a UAS as an analysis tool to identify if it can produce results that are

comparable to that of traditional ground-based trials analysis. An experiment was carried out with colleagues from Scotland's Rural College (Brian Fenton and Roger Griffin-Walker), to monitor the emergence and canopy ground cover of a trial crop of potatoes, which became somewhat overrun with weeds partway through the trial. A paper detailing summary results of the manual and automatic analysis (Gibson-Poole *et al.*, 2018) was submitted and presented at the Crop Protection in Northern Britain conference in Dundee, UK (February 2018) and can be seen in appendix D. The rest of this chapter is an expansion of the summary paper, detailing the methods used for the comparison and explaining the issues encountered.

5.2 Aim of the case study

The aim of this case study is to identify if a UAS equipped with COTS cameras is able to detect the emergence and change in canopy cover of potato plants to the same fidelity as that of traditional ground-based techniques.

The aerial data collected for this study was of a series of trials investigating the effects of different treatments in a field system containing a high egg load of potato cyst nematodes (PCN). There are two species of PCN, *Globodera pallida* and *Globodera rostochiensis*, and exposure of potato plants to them results in reduced root growth, leading to a reduction in water uptake (plants become water stressed) as well as a reduction in key nutrients such as nitrogen, phosphorus and potassium (Ryan *et al.*, 2000). However, as the results of this trial were commercially sensitive, and the trial was disrupted due to the high level of weeds present, this study looks specifically at the differences between ground based and aerial based observations and the actual treatments and differences in their effectiveness are not directly reported on.

5.3 Materials and Methods

5.3.1 Trial layout

The trial plots used for this experiment were located to the east of Dundee, Scotland. The trial was composed of 48 plots, containing two beds (four rows in total, the outside two being guard rows) with 21 tubers per row (figure 5-1). All of the plots were planted on the 11/05/2016 and split into two varieties, 24 of Harmony and 24 of Maris Piper. Tubers were planted using a customised planter with an expected spacing of 25 cm and a drill width of 0.865 m.

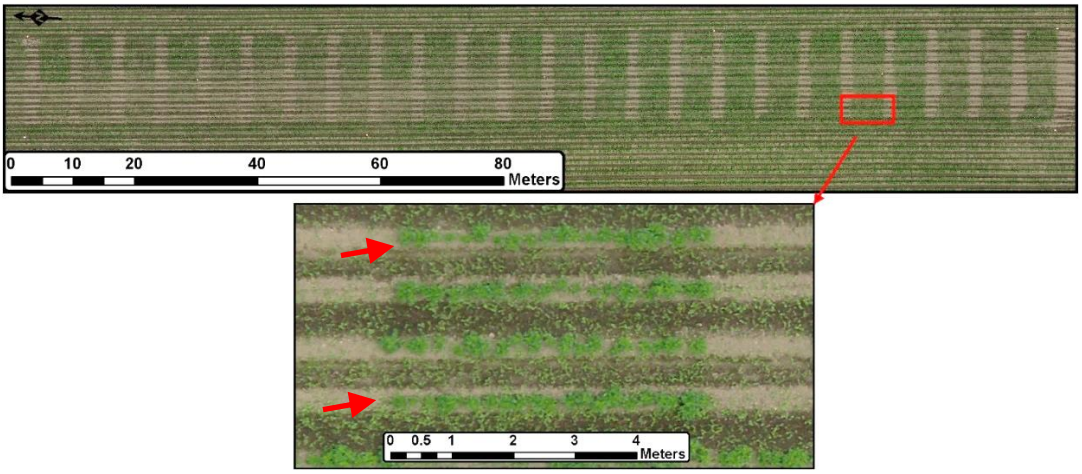

Figure 5-1: Overview of trial plot layout with detail insert of a single plot highlighting guard rows (red arrows).

5.3.2 Ground data collection

Two sets of manual data were acquired by an experienced observer, using standard techniques to record potato development (SRUC, 2017a; SRUC, 2017b). Emergence counts were conducted at 19, 23, 30, 33 and 37 days after planting (DAP), with emerged plants being estimated by grouping closely located emerged shoots ($GROUND^{emerge}$). Only the central two rows of each plot were counted (guard rows were ignored; figure 5-1), added together and if equalling 21 or higher, then the 50% emergence date would be set for that plot. Ground cover assessments were conducted at 54, 61 and 89 DAP ($GROUND^{cover}$) with percentage of potato leaf ground cover being estimated using a hand-held grid of 100 equal sized squares to view the central two rows (aligned to the trough-centres on outside of the rows), whilst ignoring the row-end plants (figure 5-2).

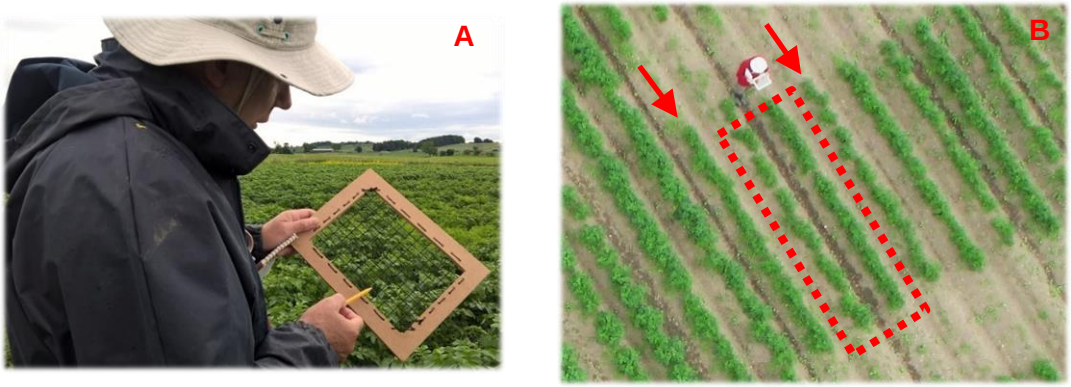

Figure 5-2: (A) Example of the hand-held grid square used for manual identification of canopy cover; (B) Example of grid square in use to monitor a plot (the two central rows, dashed red box), guard rows are indicated (red arrows).

5.3.3 Aerial data collection

Aerial data was acquired using two different aircraft and two different sets of sensors, with data acquired at 16, 22, 27, 33, 41, 46, 54, 61, 69 and 79 DAP, at varying times of the day and with varying environmental conditions (table 5-1). Nine sets of data were collected (by the author) using the custom-built multi-rotor UAS and sensor package as indicated in chapter 3 (UAS_1). The data acquired at 54 DAP was collected (by the trials team) using a 3D Robotics Solo (3D Robotics, Berkeley, CA, USA) quadcopter UAS (UAS_2) equipped with a single, fixed mount Canon ELPH 115 IS (Canon, Tokyo, Japan) capturing true colour imagery in JPEG format (ISO, white balance and aperture all set to automatic, exposure set to 1/1000 second).

Both UAS used pre-programmed automatic flights at 35 m above ground level to capture imagery with a GSD of ~1 cm per pixel, at a speed of 2 m/s and with an expected forward image overlap of 62% and side overlap of 87% for UAS_1 but only ~60/60% overlap UAS_2. The reduced overlap achieved from UAS_2 was due to inexperience of the trials team UAS operator, as its camera was set to take a picture every 2 seconds, but the aircrafts cruise speed was set too high (5 m/s) to allow for the intended 80% forward image overlap. Georectification of imagery was assisted by the placement of eleven GCPs surveyed using a Piksi (Swift Navigation, San Francisco, USA) real-time kinematic GPS with an expected accuracy of ±8 cm.

Table 5-1: Time each survey conducted, and environmental conditions encountered.

DAP	Time	Conditions
16	18:00	Overcast
22	12:00	Cloudy/sunny
27	11:30	Sunny
33	17:00	Overcast
41	13:00	Overcast
46	13:00	Cloud/sunny
54	12:30	Light cloud
61	12:30	Cloudy/sunny
69	12:00	Sunny
79	15:30	Overcast

5.3.4 Image processing

Image pre-processing was carried out as indicated in chapter 3 (including normalisation) for all the imagery captured by UAS_1. Imagery captured by UAS_2 did not undergo any pre-processing (except geotagging) as only JPEG format data was

available. All datasets were then processed using Agisoft Photoscan (v1.2.5; Agisoft LLC, St. Petersburg, Russia), using high settings (image alignment highest; dense cloud high quality; depth filtering mild) and optimised using the 11 GCPs placed around the trial plots (using an estimated accuracy of 0.15 m).

5.3.5 Orthomosaic co-registration

As was experienced in chapter 4, issues were encountered when attempting to co-register the linear orthomosaic data from the unmodified and modified cameras of UAS_1. Attempts were made to remedy this by using ArcGIS (v10; ESRI, Redlands, USA) to georeference the linear orthomosaic from the modified camera to that of the unmodified camera, however the results were not satisfactory across all of the plots (possibly due to the long and thin nature of the trial). This would have caused issues when attempting to identify emergence at the earliest stages, as some very small plants were unlikely get detected (they only consisted of a few pixels each). Therefore, attempts at co-registration were abandoned (left as per initial processing) and the layers were combined into a 5 band orthomosaic for future processing (the green channel from the modified camera was omitted to reduce image size as it was not going to be used). As only true colour imagery was available for UAS_2, no co-registration was required.

5.3.6 Emergence and plant count analysis method

5.3.6.1 Automatic methods

Two automatic methods of identifying plant emergence were attempted, and both followed the same methodology indicated in chapter 4 for the initial thresholding of vegetation. However, there was one divergence from this method as the NDVI layer was created from the red and blue channels of the modified camera using the formula in eq. 5-1, rather than the red channel from the unmodified and blue channel from the modified. This was done due to the issues encountered when attempting to co-register the orthomosaic data from the modified and unmodified camera. This solution was not ideal as all channels of the modified camera capture NIR wavelengths; however, this produced a satisfactory result that was enough to enable the manual thresholding of the scene into vegetation and soil.

$$NDVI = \frac{DN_{NIR} - DN_{R+NIR}}{DN_{NIR} + DN_{R+NIR}} \qquad (5\text{-}1)$$

Where DN_{NIR} refers to the DN of the blue channel of the modified camera and DN_{R+NIR} refers to the DN of the red channel of the modified camera.

As the emergence was still occurring by 54 DAP, the data captured by UAS_2 also needed to be separated into vegetation and soil and as the data was true colour only, the vegetation was threshold manually by using the excess green minus excess red index (ExGR; eq. 5-2) in a similar manner to Meyer & Neto (2008).

$$ExGR = (2 \cdot DN_G - DN_R - DN_B) - (1.4 \cdot DN_R - DN_G) \qquad (5\text{-}2)$$

Where DN_G refers to the DN of the green channel of the unmodified camera, DN_R refers to the DN of the red channel of the unmodified camera and DN_B refers to the DN of the blue channel of the unmodified camera.

The first automatic method for emergence counting ($AUTO^{emerge}_1$) followed the methodology indicated in chapter 4 to first detect emergence points and then create amalgamated plant points. After checking the initial results from $AUTO^{emerge}_1$, it was clear that estimates of emergence were below what was expected. This was due to the closer and less consistent plant spacing used within this trial and the much higher prevalence of weeds, so the model used for $AUTO^{emerge}_1$ was modified in an attempt to make it more robust to these conditions.

This second automatic method for emergence counting ($AUTO^{emerge}_2$) detected actual emergence points in a manner very similar to $AUTO^{emerge}_1$ (figure 5-3a), however it attempted to compensate for the more irregular planting of the tubers by 'snapping' each emergence point detected to the central line of each plot, in order to identify plant points for each set of closely situated emergence points (figure 5-3b).

Figure 5-3: ArcGIS models (blue are inputs; green are outputs; yellow are functions); (A) AUTO$^{emerge}{}_{2}$ model for emergence point detection; (B) AUTO$^{emerge}{}_{2}$ model for plant point identification.

Each emergence point detected (figure 5-4a) was first aligned with the centre line of the plot and any points within 7 cm of each other were amalgamated into a single central point (figure 5-4b). A 10 cm plant spacing buffer was then applied to the plant points before processing the next sensing date, with any newly detected emergence points being ignored if they were within the plant spacing buffer after alignment with the centre line (figure 5-4c). This process would be continued for each sensing date (figure 5-4d & 5-4e) until no more emergence points were detected.

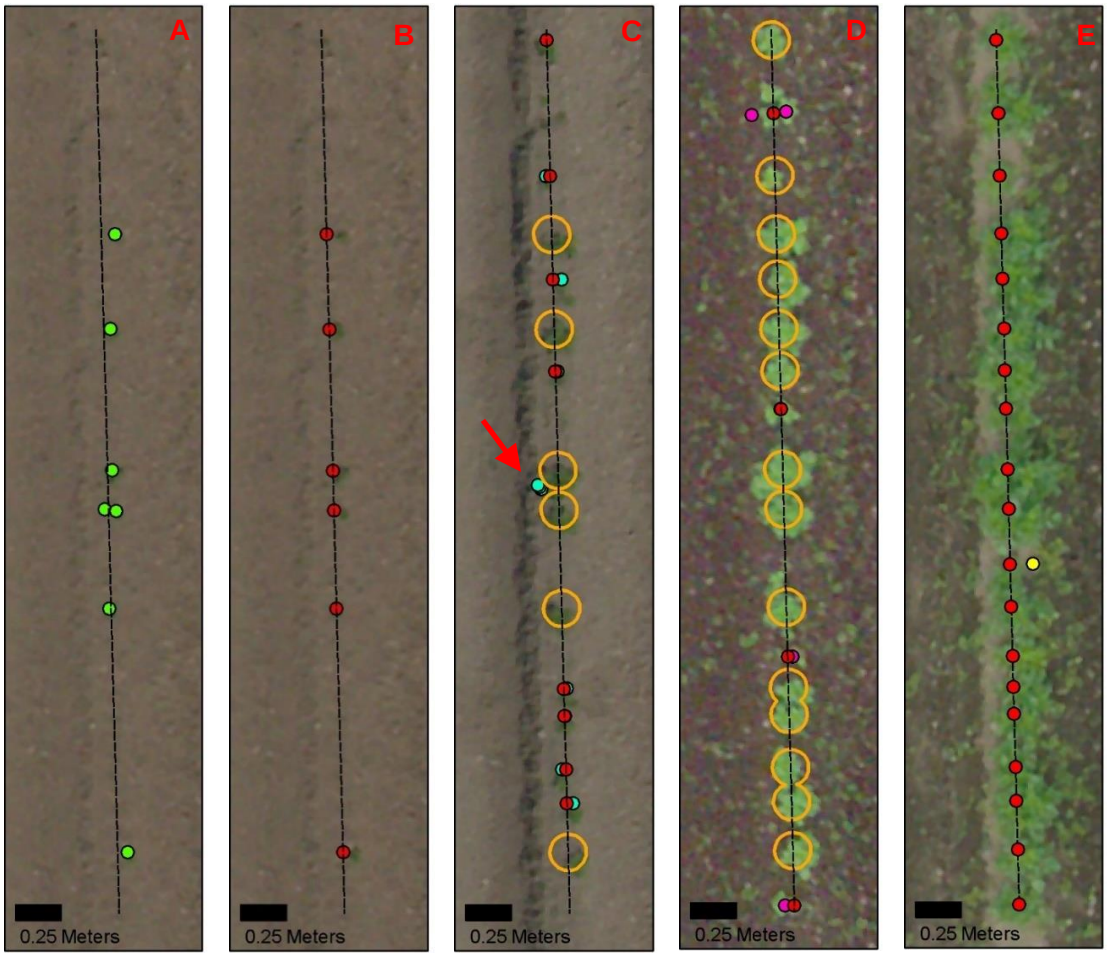

Figure 5-4: (A) Row development at 22 DAP showing emergence points (green dots) and row centre line (black dash); (B) row at 22 DAP showing amalgamated plant points snapped to centre line (red dots); (C) row at 27 DAP showing emergence points (blue dots), plant spacing buffer (orange polygons) and amalgamated plant points (red dots). Ignored emergence points are highlighted (red arrow); (D) row at 33 DAP showing emergence points (pink dots) and amalgamated plant points (red dots); (E) row at 41 DAP showing last emergence point (yellow dot) and final amalgamated plant points for the row (red dots).

5.3.6.2 Manual emergence method

Five plots from each variety were also randomly selected for direct visual analysis (MAN^{emerge}) of the aerial imagery. The experienced observer stepped through the visual imagery of each survey date in turn and counted what they believed were emerged plants per date. They could look backwards but not forwards in time from the date they were currently assessing.

5.3.7 Canopy cover analysis method

As two of the survey dates had crossover of both aerial and ground data collection, the aerial data at 54 DAP ($AUTO^{cover}_{54}$; originating from the unmodified camera of UAS_2), and 61 DAP ($AUTO^{cover}_{61}$; originating from the unmodified and modified cameras of UAS_1), were both classified using the object-based image analysis (OBIA) software eCognition Developer (v9.2.1; Trimble, Munich, Germany). Different classifications approaches were taken due to the different sensors available for each date, resulting in the orthomosaic data being classified into five potential classes; potato, potato flowers, weeds, shadow and soil.

5.3.7.1 Plant height

Height is not usually a metric that is captured for potato trials analysis, although measures of vigour (an estimation of the growth of the plant including its height) are sometimes taken if necessary. However, as this measure could be of benefit to trials analysis a pre-emergence orthomosaic and DSM was captured at 16 DAP with the intention for it to serve as the base ground height to allow crop height models to be created in the same fashion as Bendig *et al.* (2013). However, as with chapter 4, similar issues were encountered that made this method unusable, so an alternative was devised. The vegetation polygons that were created as part of the emergence process for each sensing date were buffered by 5 cm (to avoid any edge effects from the vegetation) and used to create a ground polygon layer. 100,000 points (with a minimum distance of 2 cm between each point) were randomly generated within this polygon, assigned with an elevation value from the corresponding DSM and used to create an interpolated DTM layer. A crop height model could then be created (DSM-DTM) and although this will have some inaccuracies, it would still give an estimation of height for each sensing date.

5.3.7.2 Initial segmentation of data

Rather than classify each row independently (as occurred in chapter 4), the data for both sensing dates was segmented into plots first to enable processing against only

those areas (plots were defined by buffering the centre line of each row by 0.43 m, the distance between two rows). Separate classification methods were then employed to classify the data from 54 and 61 DAP, as the data originated from different sensors.

5.3.7.3 Classification of true colour orthomosaic at 54 DAP ($AUTO^{cover}_{54}$)

At 54 DAP weeds were apparent between the rows of potatoes, with some occurrence of weeds within each row but no flowers or shadows were present. A process workflow was created within eCognition (figure 5-5) that initially used a chessboard segmentation to segment each plot, using the soil polygons created for the emergence process as constraining features. A large object size was used to ensure that the segmented scene resulted in objects that represented the manual thresholding carried out as part of the emergence process. Vegetation was then classified as objects that had a mean ExGR value >= 50 and were within 15 cm of each row centre line. Any unclassified objects remaining at this stage were either classified as soil (ExGR < 50) or weeds (ExGR >= 50).

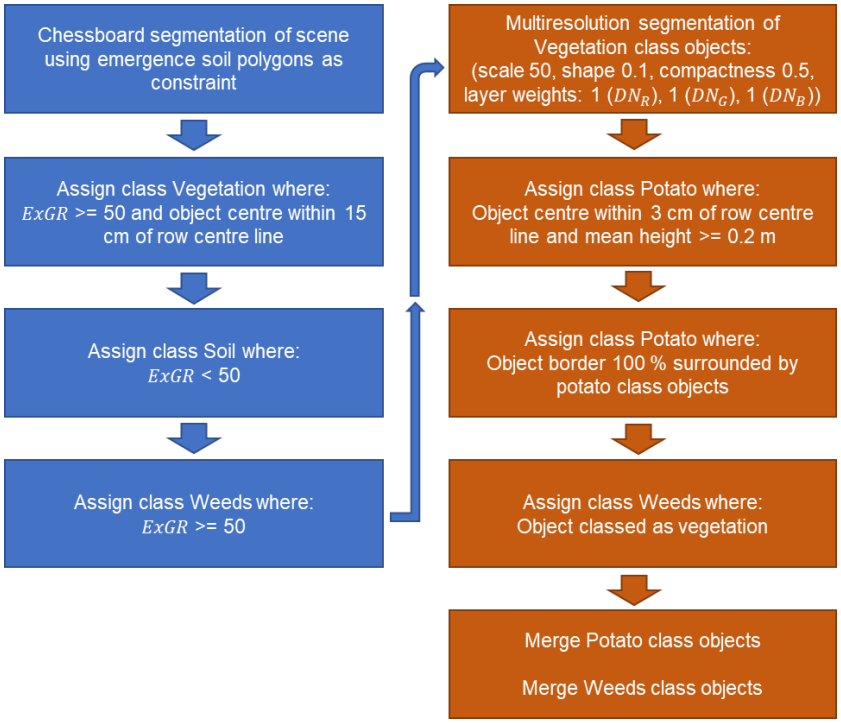

Figure 5-5: eCognition process workflow used to classify potatoes, weeds and soil at 54 DAP.

As the vegetation class objects contained both potatoes and some weeds, a multiresolution segmentation was used to split the vegetation into more discrete objects (scale 50, shape 0.1, compactness 0.5). These discrete objects had classes

assigned using several steps, with an initial classification as potato if the objects were within 3 cm of the row centre line or had a mean height of at least 0.2 m (at this sensing date the potato plants were taller than the weeds). Any remaining objects that were completely encompassed by potato vegetation were then also classed as potato (small areas of the internal canopy that were slightly shadowed). The remaining vegetation polygons were all classed as weeds, before the potato and weeds classes were merged (independently) and exported for further analysis.

5.3.7.4 Classification of 5 band orthomosaic at 61 DAP ($AUTO^{cover}_{61}$)

By 61 DAP weeds were well established between and within each row, making classification considerably more difficult. A process workflow was created within eCognition (figure 5-6) that also used an initial chessboard segmentation to segment each plot, using the soil polygons created for the emergence process as constraining features. Vegetation was then classified as objects that had mean NDVI value >= 0.36 and were within at least 15 cm of each row centre line or had a mean height >= 0.22 m with a mean NDVI value of >= 0.44 (the latter was to account for some rows of particularly large plants whose canopies had become joined across rows, resulting in their object centres being the centre of the trough between the rows). Any unclassified objects remaining at this stage were either classified as soil (NDVI < 0.36) or weeds (NDVI >= 0.36).

The vegetation class objects contained both potatoes and a considerable number of weeds (that were around the edge and within the canopy of the potato plants), therefore a multiresolution segmentation was used to split the vegetation class objects into a fine scale of discrete objects (scale 20, shape 0.8, compactness 0.5). Any object with a mean brightness <= 1000 was classified as shadows (brightness was defined as $\frac{DN_R+DN_G+DN_B}{3}$ - where DN_G refers to the DN of the green channel of the unmodified camera, DN_R refers to the DN of the red channel of the unmodified camera and DN_B refers to the DN of the blue channel of the unmodified camera). Objects that had a brightness >= 8000, mean DN_B of >= 3000, ExGR <= 1000 and NDVI >= 0.4 were classified as flowers. Any image object that had an NDVI >= 0.44 was then merged and classed as potato as this accounted for the larger healthy potato plants. Remaining vegetation class objects that had an NDVI <= 0.42 were then classed as weeds.

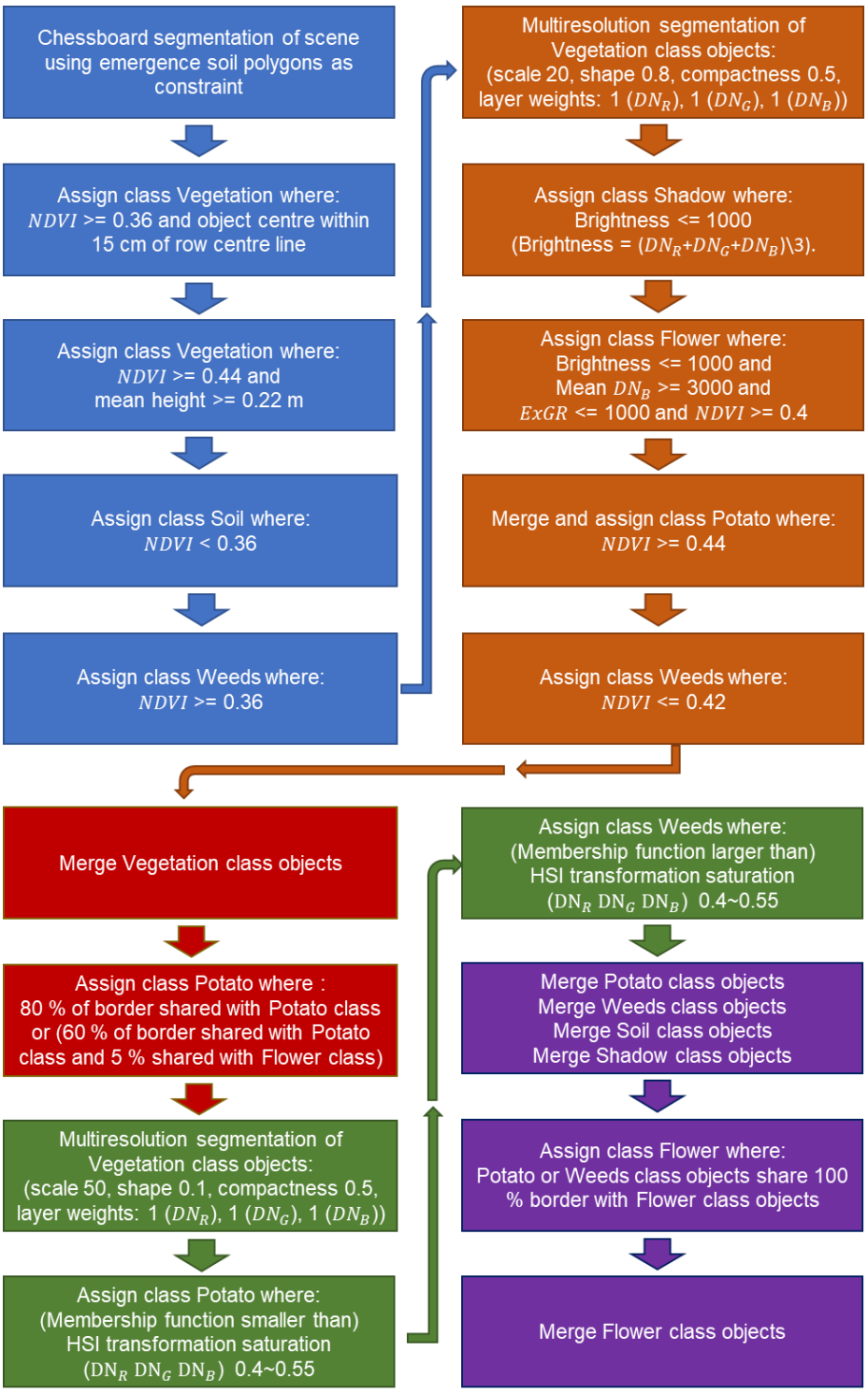

Figure 5-6: eCognition process workflow used to classify potatoes, flowers, weeds, shadow and soil at 61 DAP.

At this point a significant number of vegetation class objects remained, so they were merged before identifying objects as potato if they shared a border with other potato class objects of at least 80%, or they shared a border with other potato class objects

of at least 60% along with at least 5% shared border with flower class objects (this accounted for the small areas of slightly shadowed potato vegetation that were within the main canopy of each row). The remaining vegetation class objects were re-segmented again using a coarser multiresolution segmentation (scale 50, shape 0.1, compactness 0.8) before being classified as either potato or weeds based off of their membership function to an HSI (hue, saturation and intensity) transformation to saturation (figure 5-7; HSI saturation between 0.4~0.55).

Figure 5-7: Membership functions for (A) Weeds class and (B) Potato class, using an HSI transformation to saturation.

To complete the classification, each class of objects (except flowers) were merged (independently), before classifying potato or weeds class objects as flowers if they were completely encompassed by other flower class objects (this was to account for the occasional misclassification of the centre of a flower). The flower class objects were then merged before the entire classification was exported for further analysis.

5.3.7.5 Identification of ground cover per row

To enable the detection of ground cover for surveys conducted at 54 and 61 DAP, the same method employed in Gibson-Poole *et al.* (2017) (chapter 4) was used to segment each row using Thiessen polygons into plant regions of interest (p^{ROI}; bounded to a maximum of 0.43 m for rows around the edges of the trial). The area of each p^{ROI} was then identified along with the area of ground potato leaf ground cover, before then combined to give totals for each row, which was then used to generate a percentage of potato leaf ground cover per row.

5.4 Results

For the emergence and ground cover results, statistical analysis was carried out using Microsoft Excel (Microsoft, Redmond, WA, USA) to calculate the Pearson correlation coefficients (*r*) and probability values (*p*).

5.4.1 Emergence

GROUND^{emerge} revealed that all Maris Piper plots had reached 50% emergence by 23 DAP and all Harmony plots by 30 DAP. AUTO$^{emerge}{}_1$ and AUTO$^{emerge}{}_2$ reached the same level by 27 DAP and 41 DAP respectively. However, MAN^{emerge} reached 50 % emergence by 22 DAP for the Maris Piper plots and by 33 DAP for the Harmony plots. This indicates that the automatic methods may not be as sensitive as the manual method in detecting emergence (although MAN^{emerge} was looking at a smaller number of plots), but in general, GROUND^{emerge} detected more emerged plants earlier than any of the other methods and AUTO$^{emerge}{}_1$ detected the least number of emerged plants overall (figure 5-8).

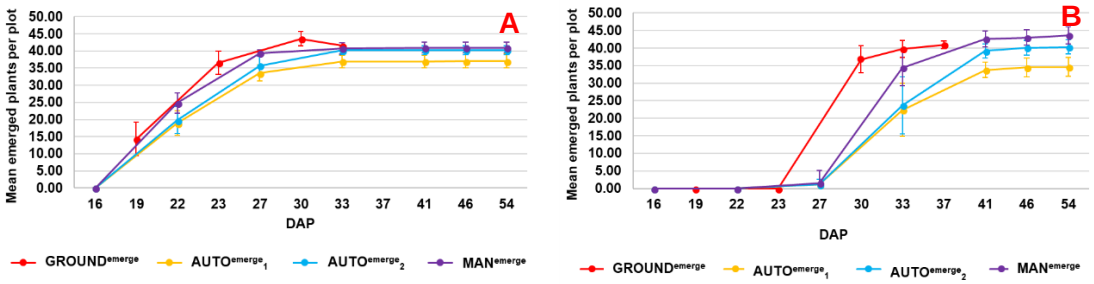

Figure 5-8: (A) Mean emerged Maris Piper plants at DAP; (B) Mean emerged Harmony plants at DAP.

Both ground and aerial surveys were conducted at 33 DAP so direct comparisons could be made (table 5-2, figure 5-9). For the Maris Piper plots, the $AUTO^{emerge}{}_1$ and $AUTO^{emerge}{}_2$ methods showed a significant moderate correlation to $GROUND^{emerge}$ whilst the MAN^{emerge} showed a significant strong correlation with $GROUND^{emerge}$. However, for all methods, no significant correlation was achieved for the later emerging Harmony plots. $AUTO^{emerge}{}_1$, $AUTO^{emerge}{}_2$ and MAN^{emerge} methods indicated that all plants had emerged by 54 DAP, however final plant counts were not recorded by $GROUND^{emerge}$ so this could not be directly compared.

*Table 5-2: Correlation analysis between $GROUND^{emerge}$ emerged plant counts and the three analysis methods at 33 DAP. Shows correlation per variety and a combination of both varieties (r correlation coefficient, s slope, i intercept, p p-value, n number of pairs, *Not significant at α = 0.05).*

Method	Variety	*r*	*s*	*i*	*n*	*p*
$AUTO^{emerge}{}_1$	Maris Piper	0.43	0.18 ± 0.08	34.86 ± 3.02	24	0.0373
	Harmony	0.29*	0.09 ± 0.07	37.67 ± 1.56	24	0.1673
	(Combined)	0.52	0.11 ± 0.02	37.31 ± 0.85	48	0.0002
$AUTO^{emerge}{}_2$	Maris Piper	0.47	0.27 ± 0.11	30.72 ± 4.38	24	0.0215
	Harmony	0.29*	0.09 ± 0.06	37.70 ± 1.53	24	0.1621
	(Combined)	0.52	0.10 ± 0.02	37.41 ± 0.83	48	0.0002
MAN^{emerge}	Maris Piper	0.94	0.63 ± 0.13	16.11 ± 5.16	5	0.0156
	Harmony	0.07*	-0.04 ± 0.33	39.31 ± 11.37	5	0.9147
	(Combined)	0.50*	0.29 ± 0.18	28.95 ± 6.80	10	0.1436

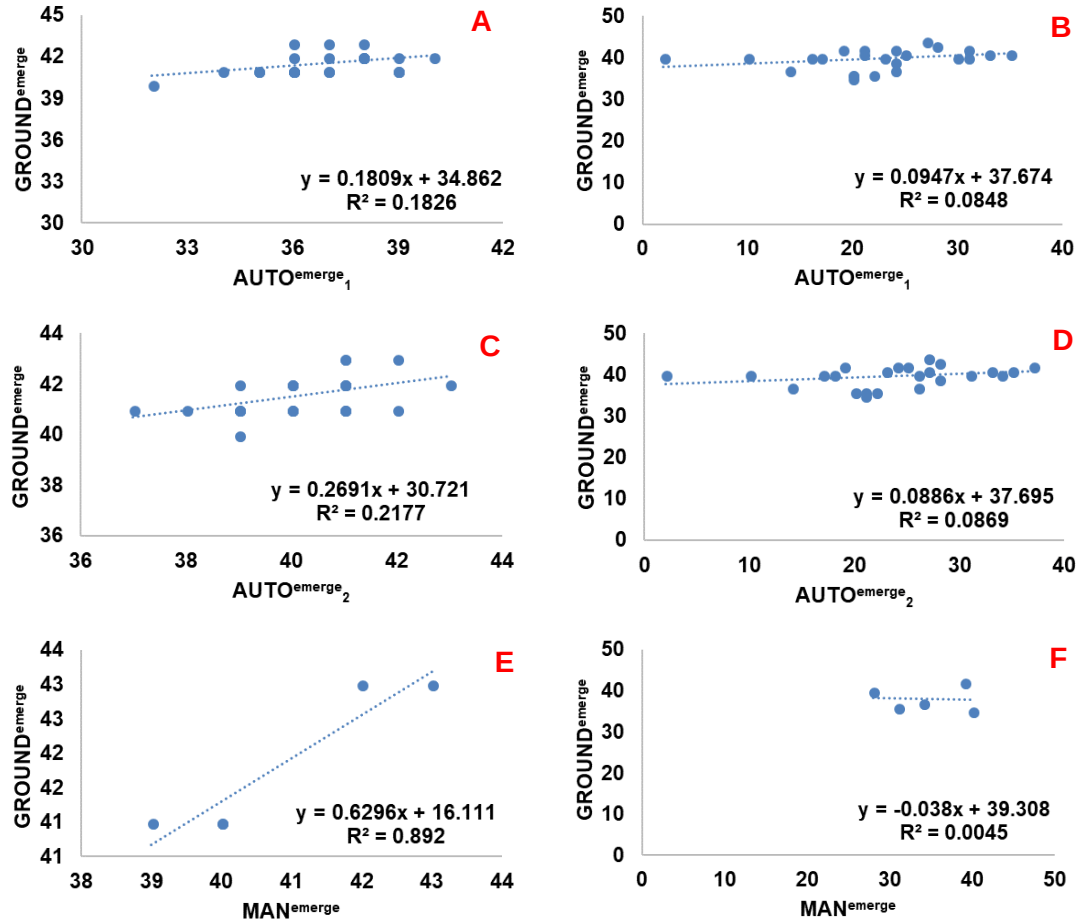

Figure 5-9: Maris Piper plant emergence correlation at 33 DAP between $GROUND^{emerge}$ and (A) $AUTO^{emerge}{}_1$; (C) $AUTO^{emerge}{}_2$; (E) MAN^{emerge}; Harmony plant emergence correlation at 33 DAP between $GROUND^{emerge}$ and (B) $AUTO^{emerge}{}_1$; (D) $AUTO^{emerge}{}_2$; (F) MAN^{emerge}.

5.4.2 Ground cover

Direct comparisons of potato leaf ground cover could be made for 54 and 61 DAP and for both sensing dates, $GROUND^{cover}$ reported a larger percentage of potato leaf ground cover in general. However, $AUTO^{cover}{}_{54}$ and $AUTO^{cover}{}_{61}$ both showed a strong positive correlation for both varieties that were also highly significant (table 5-3; figure 5-10).

Table 5-3: Correlation analysis results between GROUND^{cover} potato leaf ground cover and the two automatic analysis methods. Shows correlation per variety and a combination of both varieties (r correlation coefficient, s slope, i intercept, p p-value, n number of pairs).

Method	Variety	*r*	*i*	*s*	*n*	*p*
AUTO$^{cover}_{54}$	Maris Piper	0.81	12.64 ± 7.09	0.99 ± 0.15	24	< 0.0001
	Harmony	0.75	12.59 ± 7.39	1.32 ± 0.24	24	< 0.0001
	Combined	0.73	23.71 ± 4.44	0.82 ± 0.11	48	< 0.0001
AUTO$^{cover}_{61}$	Maris Piper	0.82	14.09 ± 9.12	0.90 ± 0.14	24	< 0.0001
	Harmony	0.66	27.15 ± 7.60	0.69 ± 0.16	24	0.0004
	Combined	0.80	22.60 ± 4.90	0.78 ± 0.09	48	< 0.0001

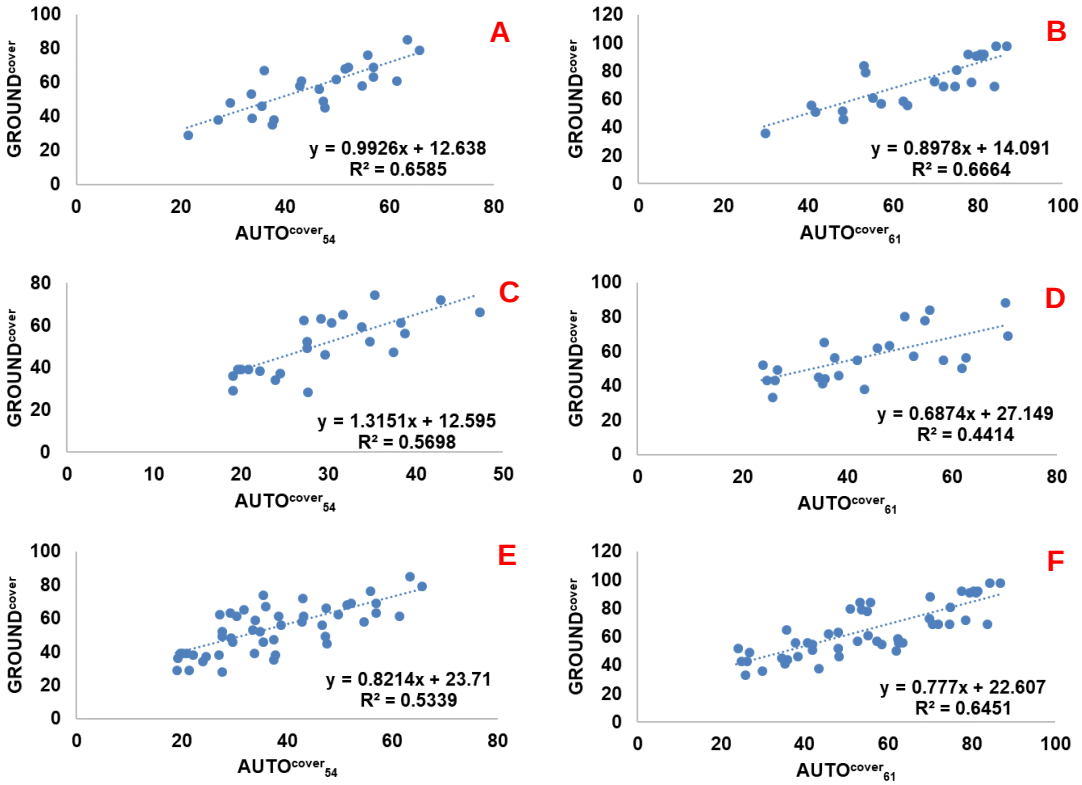

Figure 5-10: Potato leaf ground cover correlation at 54 DAP between GROUND^{cover} and AUTO$^{cover}_{54}$ for (A) Maris Piper; (C) Harmony; (E) Combined (both varieties); Potato leaf ground cover correlation at 61 DAP between GROUND^{cover} and AUTO$^{cover}_{61}$ for (B) Maris Piper; (D) Harmony; (F) Combined (both varieties).

5.5 Discussion

5.5.1 Emergence

From the emergence results it is clear that the resolution of the aerial imagery was not sufficient to be able to detect emerging shoots (for either automatic method) until they had started to develop some leaves (i.e. a leaf area > 1 cm^2; figure 5-11a), whereas the ground-based assessment could detect emergence just as the mother tuber sprout had breached the surface of the soil (pre-first leaf). This partly explains why all the methods showed significant correlation for the Maris Piper plots at 33 DAP compared to the Harmony plots, as the Maris Piper plants were larger because they had started to emerge at 19 DAP, whereas the Harmony plots had only started to emerge at 27 DAP (figure 5-11b).

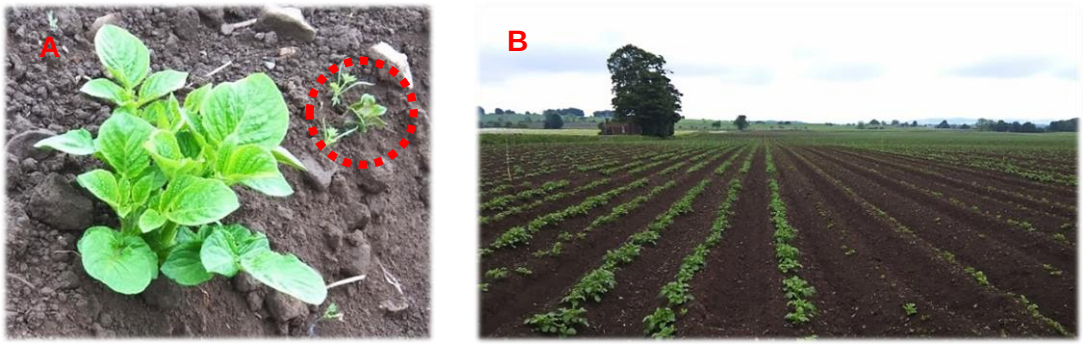

Figure 5-11: (A) An emerged potato plant of a few days that would be detected next to a just emerging plant (highlighted) that would not; (B) The difference in plant emergence by 33 DAP, showing Maris Piper plots (left hand side) and Harmony plots (right hand side).

Being able to detect emergence at the point that it occurs is a key measurement, as the 50% emergence measure (half of the plot has emerged) can be used to predict the tuber initiation growth stage (O'Brien *et al.*, 1998) as well as identify disease or issues that may have been initiated by the treatments applied to the trial plots (Sankaran *et al.*, 2017). However, to be able to do this from the air would be difficult as higher resolution imagery would be needed by either flying lower or using a different sensor with a larger focal length or pixel count. Both options are likely to lead to an increase in flight times for the same area covered and the extra imagery captured would also increase the time required to process the data.

The ~1 cm GSD resolution acquired should however have been sufficient to get accurate plant counts for the Maris Piper plots by 33 DAP, as capacity for this had already been shown by Gibson-Poole *et al.* (2017) (chapter 4). However, this was hampered by intermittent irregular tuber spacing caused by tubers rolling during the

planting operation, which was unfortunate for the trial as tuber spacing is an important factor in the development of the crop (Bussan *et al.*, 2007). Because of this, some plants emerged much closer to their neighbours (and conversely others further away), with those in closer proximity entering intra-row canopy merging at a much earlier stage. This resulted in lower plant counts at 33 DAP for $AUTO^{emerge}_{1}$ and $AUTO^{emerge}_{2}$ as some plants could not be distinguished from their neighbours (two plants being counted as one). $AUTO^{emerge}_{1}$ consistently produced lower plant counts for both varieties as it was not robust enough to handle this irregularity in planting and although this improved with $AUTO^{emerge}_{2}$ the final plant counts per plot was still generally lower than that produced by $GROUND^{emerge}$ (figure 5-12).

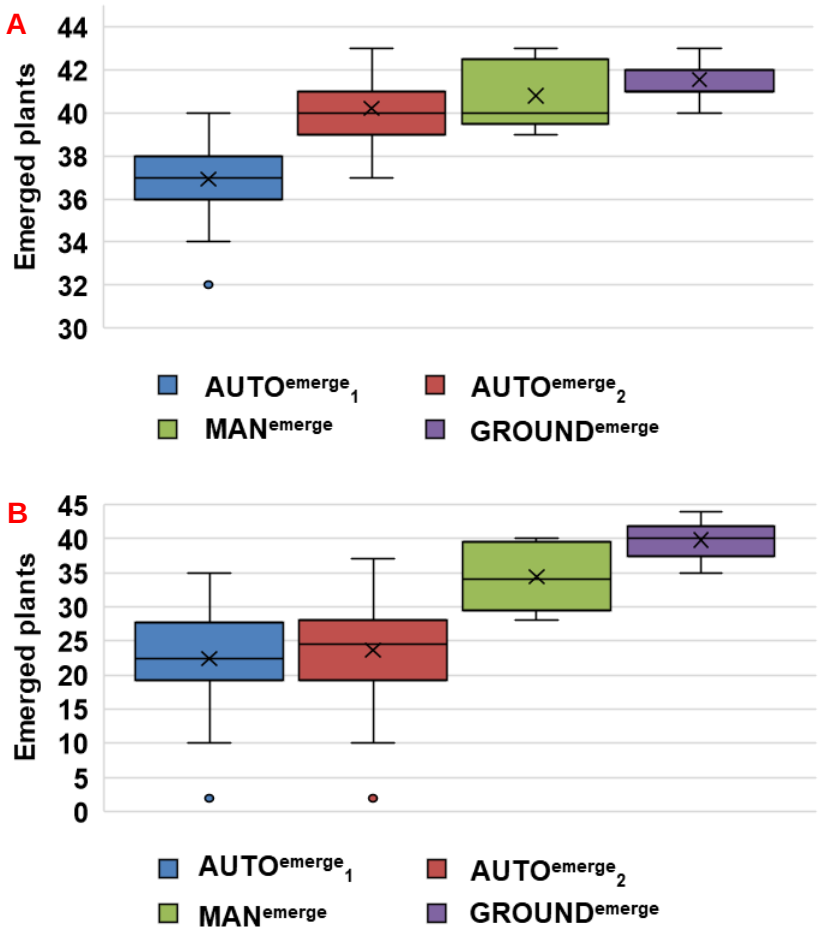

Figure 5-12: Box plot of plant counts at 33 DAP for (A) Maris Piper and (B) Harmony varieties (mean, median, standard deviation and outliers shown for each method).

In contrast to the automatic methods, MAN^{emerge} showed much better correlation with $GROUND^{emerge}$ for the Maris Piper plots by 33 DAP but was from a smaller sample size and the actual emerged points for the plots analysed were still not an

exact match. It did however show a considerably worse correlation for the Harmony plots and this was primarily due to the level of weeds appearing within the plots, which resulted in either overestimation (weeds counted as plants) or underestimation (plants thought to be weeds). The reason for this high level of weeds was attributed to the very dry weather experienced during application of the weed barrier (Griffin-Walker, 2016). Whatever the reason, it caused complications for emergence detection and ground cover assessment and was an issue that Gnädinger & Schmidhalter (2017) also commented on when trying to count maize plants.

At the time of writing only a study by Sankaran *et al.* (2017) had also investigated potato emergence using a UAS. They also used a COTS modified to detect NIR and applied a pixel-based thresholding method to delineate vegetation from soil. They tested three methods, with one using a sizing parameter to only select a potential emerged plant if it was greater than 100 cm^2. They also experienced issues with the sizing method due to earlier than expected intra-row canopy closure and were unable to determine final counts from 43 DAP due to intra-row canopy closure, as they didn't model the location and development of the plants, simply thresholded at each sensing date.

Sankaran *et al.* (2017) were operating their UAS at a much lower altitude (15 m AGL) with a 16 mega pixel camera, so the GSD of their imagery would have been finer, although they did not report what it was (it would likely have been ~0.5 cm GSD). However, their analysis methods still under recorded emergence plant counts compared to their ground-based data, which highlights the difficulty in attempting this via remote sensing. Including plant sizing as another parameter in $AUTO^{emerge}{}_2$ could have improved the emergence model and the thresholding proposed by Sankaran *et al.* (2017) also has merit. Making more use of height data could also improve delineation of plants whose canopies have merged by attempting to identify the crowns of each plant and would be an option worth pursuing. Sankaran *et al.* (2017) may not have this option available as they did not report processing their data into and orthomosaic.

5.5.2 Ground cover

Aerial ground cover analysis initially looked poor when the raw numbers were compared as $GROUND^{cover}$ reported higher ground cover in general (figure 5-13),

but $AUTO^{cover}_{54}$ and $AUTO^{cover}_{61}$ both correlated well. The classification methods used for the two different sensing dates used different workflows due to the nature of the different sensors used, however some similarities remained, with the use of height data as part of the classification for both methods being key in discriminating plants from weeds. Height data obtained from a UAS using COTS cameras has been used successfully in several studies looking at trials of smaller plants such as wheat (Holman *et al.*, 2016; Madec *et al.*, 2017) and barley (Bendig *et al.*, 2014; Bareth *et al.*, 2016) and more recently in larger row crop plants such as Chinese cabbage and white radish (Kim *et al.*, 2018), where the height data was used inform on the development of the plants.

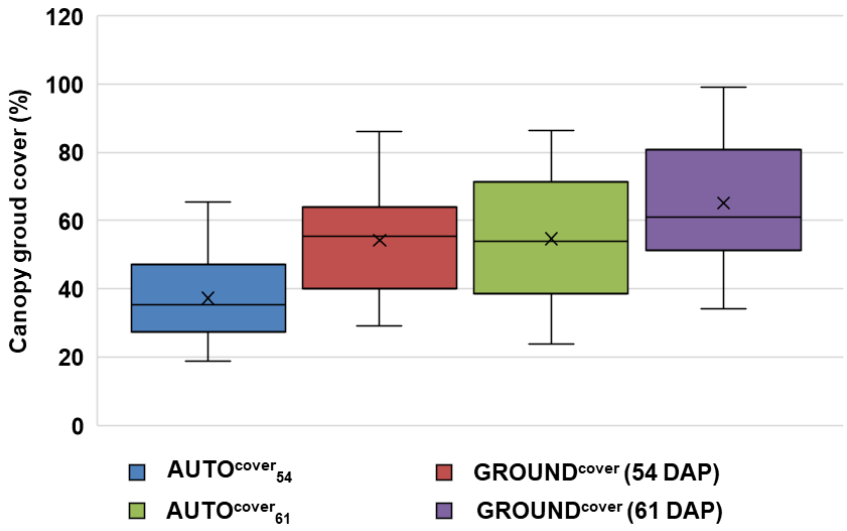

Figure 5-13: Box plot of potato canopy groundcover at 54 and 61 DAP for all varieties (mean, median, standard deviation shown for each method).

Further investigation into the mechanics of the ground data collection revealed why the raw numbers may have differed so much. A plot was viewed manually using the handheld grid of 100 equally size squares and ground stakes were placed on the ground within the viewing maxima of the grid (the four corners). The position of these stakes was then measured and revealed that due to the perspective that the observer has when looking at a plot on the ground using a grid, only ~1.65 m wide and ~1.2 m long area of the plot was being measured (figure 5-14a; Fenton, 2017a). Although this is a standard measure used for trials analysis it does highlight that the measurement could be skewed if the plot ground cover is very variable and larger plants within the viewing area could also occlude smaller plants behind them. Similarly, as this is a manual estimation, if two different observers used the same

grid to look at the same plot, the actual ground cover estimated by the two people would likely not be the same (although it would be close).

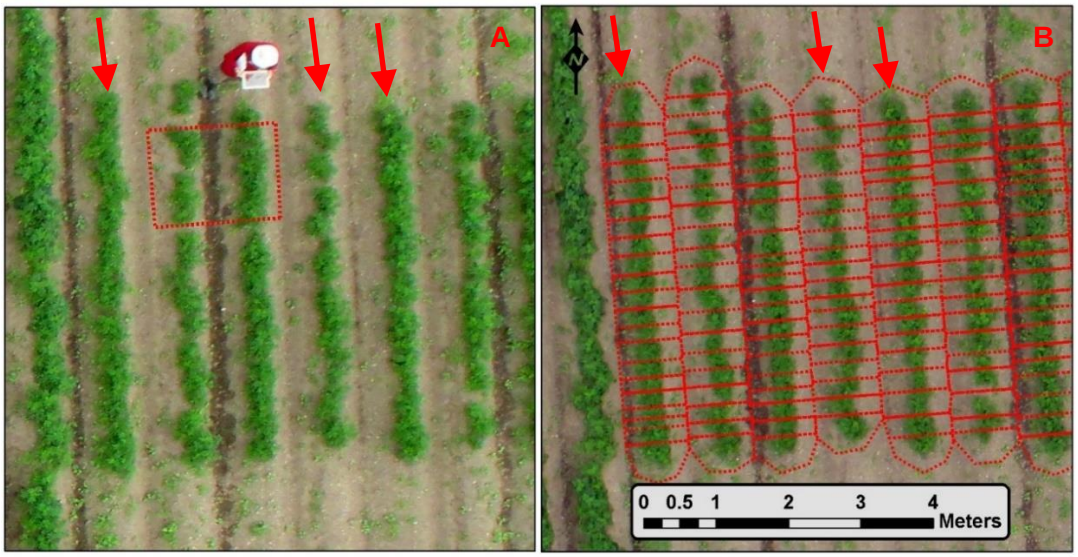

Figure 5-14: (A) Manual identification of ground cover showing approximate area of trial actually measured (red box; ~1.65 m wide and ~1.2 m long), guard rows also shown (red arrows); (B) automatic identification of ground cover showing p^{ROI} being measured (red polygons), guard rows also shown (red arrows) and can also be measured if required.

In contrast to this, the nadir viewpoint from aerial imagery allows the entire plot to be viewed and ground cover to be estimated directly against the area being measured (figure 5-14b), even if the plot has a large variation in the height between individual plants within the plot. This indicates that estimation of canopy cover from imagery obtained by a UAS is likely to be a more representative measure and that if effectively processed, georeferenced and classified, would give a much more standardised result against each plot.

5.5.3 Survey effort

The ground-based methods for emergence and ground cover are fast and efficient measures that are targeted specifically to give data that represents variability between plots. To measure emergence over the number of plots in this study took an observer 1~2 hours, whereas ground cover analysis was much quicker at 60~30 minutes as observations become quicker as the amount of canopy increases (Fenton, 2017b). In contrast to this, aerial data collection with the UAS took only 10 minutes, although more time was required to setup and especially to layout GCPs (~1 hour in total per survey visit, with at least a third this time required to deploy and retrieve GCPs). Processing of the aerial imagery (orthomosaic generation and

classification) also took some time (~2 hours per dataset), however most of this was automated and with further optimisation could be completely automated. The only exception to this is again the GCPs, which required manual placement during orthomosaic generation and can take at least 20 minutes per survey to place.

Therefore, surveying using a UAS is not necessarily faster than taking ground-based measurements, but it does cover a larger area and could include measurements of guard plots as well as measures not typically taken from the ground. The photogrammetry process used in this study produces high resolution DSM as well as orthomosiac data, so the ability to measure the height of the plants surveyed is also possible, would be much quicker than measuring by hand (Holman *et al.*, 2016) and would further add to trial analysis as plant height has input in predicting yield within potato crops (Arslan, 2007).

5.5.4 Impact of weed development

The level of weeds within this trial caused problems for all the automatic methods and also for the ground-based assessment at later stages, simply because the weeds (primarily *Fumaria officinalis* and *Convolvulus arvensis*) overwhelmed the potato plants that had emerged later (the Harmony plots; figure 5-15a) or were developing at slower rates due to the effects of PCN and the treatments that had been applied. Gnädinger & Schmidhalter (2017) also encountered issues with weeds affecting the accuracy of plant counts and ground cover assessment of maize plants, although studies on the detection of weeds at early plant growth stages have been shown to be successful for maize (Peña *et al.*, 2013) and sunflower crops (Peña *et al.*, 2015).

At the later stages of plant development in this study, the weeds had become integrated within the canopy of the plants being measured making separation of weed from plant challenging. By 79 DAP weed coverage for some plots reached almost 100 % (figure 5-15b) and although the actual accuracy of the classification at 54 and 61 DAP was not directly verified using an error matrix, its comparison with the results of the ground assessment showed a good correlation indicating that weeds can be effectively separated from potato vegetation even if within the canopy of the potato plants.

Figure 5-15: (A) Example of weeds within plots at 61 DAP (potato plant indicated with red arrow, the lighter green plants are Fumaria officinalis); (B) Example weeds dominating plots at 79 DAP, with some plots showing near 100 % weed coverage (potato plant indicated with red arrow, the flowering plants are Fumaria officinalis).

5.6 Conclusion and future thoughts

This study has shown that further development of models that are more sensitive and robust are required to be able to effectively identify potato emergence, however ground cover assessment from a UAS is effective and likely to be a more representative measure compared to traditional ground-based analysis. Also, for a similar survey effort as that required for a ground-based assessment, data acquired from a UAS can enable measurements of more aspects of the trial to be captured (e.g. height). Further to this, being able to view and analyse the trial as individual plants rather than just plots or rows could allow more detailed analysis of trial development and issues, as a finer scale of variability within a row or plot could be achieved without increasing survey effort. In the future, the use of highly accurate GNSS systems onboard the UAS could help negate the need to use GCPs, thus speeding up survey and image processing time alike and the use of narrowband multispectral cameras specifically designed for agriculture that can capture red, green, blue, NIR and rededge reflectance (the sharp transition seen in vegetation between red to NIR wavelengths) will also give more information relating to the health and development of each plant (Nebiker *et al.*, 2016; Pauly, 2016).

To conclude, as small UAS can only really be used in fair weather conditions (i.e. not raining and wind speeds < 8 m/s to ensure safe operation), they are unlikely to replace traditional ground-based methods completely. The results from this chapter highlight the need for effective classification software, indicating that OBIA can be effective in allowing the separation of weeds from plants of interest, further adding to the evidence for the 3rd objective of this PhD project. It also meets part of the 4th objective as trials analysis is one of the core agricultural research activities that

SRUC undertake. Even though ground-based and aerial measures correlated there were still differences, partly because ground-based measures can be subjective and not necessarily representative of the conditions on the ground. Therefore, aerial based assessment would bring an element of standardisation to this activity, as well as providing a wider coverage of measures that could benefit trials monitoring and analysis in the future.

Chapter 6. Environmental applications – Monitoring the spread of invasive non-native vegetation along riparian habitats

6.1 Introduction

In the UK, invasive non-native species (INNS) are those that have been introduced to an environment outside of its normal distribution via a third party (typically though a human inter-action), and INNS are broadly defined in the Non-Native Species Framework Strategy for Britain as "*species whose introduction and/or spread threaten biological diversity or have other unforeseen impacts*" (Defra, 2015)

INNS covers a wide range of species, both flora and fauna, whose spread can result in damage or degradation of land and infrastructure used for agricultural, conservation or urban uses, and which has an estimated overall cost to the British Economy of ~£1.7 billion annually (Williams *et al.* 2010). Riparian habitats are considered to be particularly susceptible to INNS as the waterway aids in the spread of their seeds, and the nature of riverbanks and sediment deposits makes initial establishment more likely (Tickner *et al.* 2001).

In Scotland, regulations regarding the spread of INNS are covered by Section 14 of the Wildlife and Countryside Act 1981, as amended by the Wildlife and Natural Environment (Scotland) Act 2011. These regulations denote that it is an offence to release or allow to escape from captivity, any species to a place out with its native range. However, many INNS are already established in the UK and within Scotland, three species that typically inhabit riparian habitats can be commonly seen; Himalayan Balsam (*Impatiens glandulifera*), Japanese Knotweed (*Fallopia japonica*) and Giant Hogweed (*Heracleum mantegazzianum*).

UAS have already been used to monitor riparian habitats (Husson *et al.*, 2014; Rusnák *et al.*, 2018) and to identify various riparian INNS including alligator weed (*Alternanthera philoxeroides*; Göktoğan *et al.*, 2010), kariba weed (*Salvinia molesta*; Göktoğan *et al.*, 2010), saltmarsh cordgrass (*Spartina alterniflora*; Wan *et al.*, 2014) and yellow flag iris (*Iris pseudacorus L.*; Hill *et al.*, 2016). Himalayan balsam (Michez *et al.*, 2016), Japanese knotweed (Michez *et al.*, 2016; Müllerová *et al.*, 2017b; Martin *et al.*, 2018) and giant hogweed (Michez *et al.*, 2016; Müllerová *et al.*, 2017b) have also all been investigated using UAS, with varying levels of success.

This exploratory chapter addresses the 3rd and 4th objective of this PhD project as it investigates the use of an UAS as a monitoring tool to identify the level of infestation of giant hogweed within, and adjacent to, a riparian habitat. With the approval of Clackmannanshire Council (Andy Macpherson) and Stirling Council (Guy Harewood), the study site was monitored over two years. The results from the first survey were presented at the University of Edinburgh, School of GeoSciences Postgraduate Research Conference in March 2016, and at the 16th National Biodiversity Network Conference (Edinburgh, November 2016).

6.1.1 Himalayan Balsam

First recorded in the wild in 1855, this species was brought to Britain as an attractive garden plant in the early 19th century (Booy *et al.*, 2008c). It is an annual herbaceous plant that can grow up to 2 m in height and forms dense stands of vegetation (Booy *et al.*, 2008c; Tanner *et al.*, 2013). It overshadows native flora reducing both plant and invertebrate biodiversity above and below ground (Tanner *et al.*, 2013) and when it dies back in the winter it can leave exposed patches of soil or riverbank that can be more easily eroded (Booy *et al.*, 2008c). It spreads through its seeds, which are small and easily dispersed as the seed heads burst when ripe (Booy *et al.,* 2008c), and its estimated annual cost to the British economy is £1,000,000 (Williams *et al.*, 2010).

6.1.2 Japanese Knotweed

Introduced to Britain in the mid-nineteenth century as an ornamental garden plant it is now widespread through Britain (Williams *et al.*, 2010; Booy *et al.*, 2008b). It is an herbaceous perennial plant that forms dense monospecific stands that can grow up to 3 m high, which can shade out native vegetation (Jones *et al.*, 2011; Booy *et al.*, 2008b). It has also hybridised with other similar species including Giant Knotweed (*Fallopia sachalinensis*), which has much larger leaves, to create the hybrid Bohemian Knotweed (*Fallopia x bohemica*), however these are all still non-native species (Jones *et al.*, 2011; Booy *et al.*, 2008b).

It rarely produces viable seed in Britain but it spreads rapidly via vegetative regeneration from very small amounts of its rhizome (0.7 gram of rhizome can produce a new plant in 10 days), and it can also be highly damaging to buildings and infrastructure (including flood defences), as it can grow up through some hard surfaces (Williams *et al.*, 2010; Jones *et al.*, 2011; Booy *et al.*, 2008b). Due to its

ability to grow through hard surfaces and the rapidity of growth from small pieces of rhizome, it is very expensive to control and costs the British economy an estimated £165,609,000 annually, of which ~£5,637,000 is attributed towards riparian habitats (Williams *et al.*, 2010).

6.1.3 Giant Hogweed

First recorded in Britain in 1817 (Nielsen *et al.*, 2005), giant hogweed is an herbaceous monocarpic perennial plant that originates from the Caucasus Mountains and other parts of Central Asia. It is the tallest herbaceous species in Europe and at full maturity can have inflorescences up to 80 cm wide, can reach up to a height of 5 m (figure 6-1), and have large, wide leaves up to 2.5 m long (Nielsen *et al.*, 2005; Booy *et al.*, 2008a; Müllerová *et al.,* 2013). It outcompetes other vegetation due to the shade of its large leaves which grow early in the year, and as it dies bank in the winter it can leave bare patches of ground or riverbank, making them more likely to be eroded (Harewood, 2014). The plant can also be a host for certain fungi such as *Sclerotinia spp.* (Seier & Evans, 2007), which can be a blight to many crops including oilseed rape and potatoes (Clarkson *et al.* 2017), both of which are important crops for Scotland's agricultural sector.

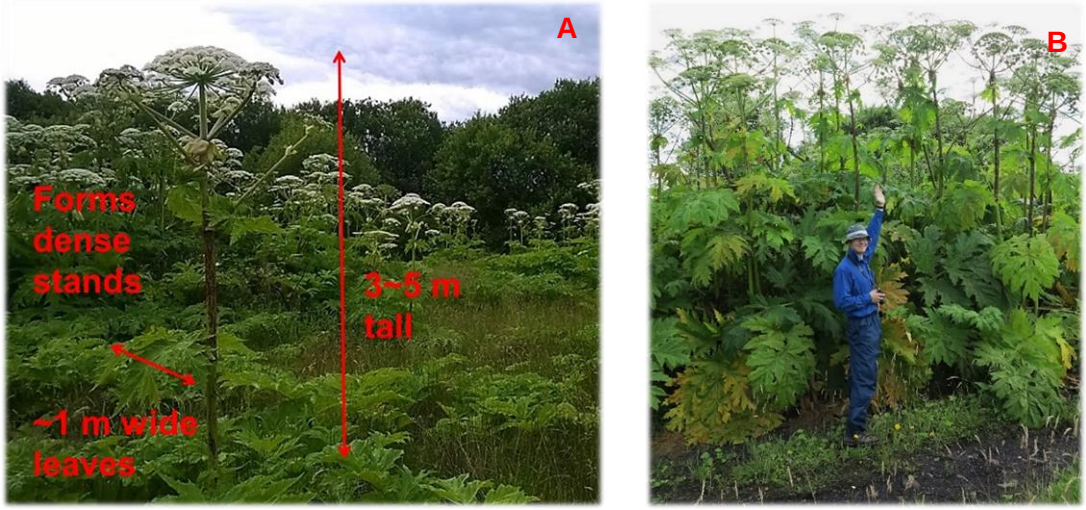

Figure 6-1: (A) Example attributes of giant hogweed; (B) Calum Tyler (approx. 2 m tall) showing approximate height of giant hogweed at the site.

However, giant hogweed is also a public health concern as it also contains a phytophototoxic sap that can induce phytophotodermatitis (burning of the skin when exposed to ultraviolet radiation) in humans and livestock with unpigmented skin (Nielsen *et al.*, 2005). As it is a monocarpic species, it typically lives for 3-5 years and when flowering it has been estimated that it can produce 5000 to more than

100,000 seeds, but more typically an average of 20,000 seeds (Nielsen *et al.*, 2005; Perglová *et al.*, 2006). These seeds can be easily transported along waterways and persist in the soil for at least three years (Pergl *et al.*, 2011; Perglová *et al.*, 2006). Annually giant hogweed costs the British economy an estimated £2,362,000, with £964,995 directly related to its effects and management along riparian habitats (Williams *et al.* 2010).

6.2 Aim of the case study

The aim of this case study is to identify if a UAS equipped with COTS cameras can be used to effectively map the current extent of the invasive non-native species giant hogweed.

The aerial data collected for this study was from a single site and only for a single INNS (giant hogweed), as a pilot study to identify the effectiveness of the UAS for vegetation surveys of this type. This study was one of the first active uses of the UAS system outlined in chapter 3 and although the study site was surveyed more than once, full processing and analysis was only attempted on the first dataset and normalisation was not carried out as an effective method had not been identified at the time of analysis. The intention was to revisit this data, perform normalisation and include all the surveys in order to refine and improve the classification algorithm, however there was insufficient time to complete this work.

6.3 Methods

6.3.1 Study site

The site chosen for this case study was a brownfield site called Manor Powis Bing. Originally a coal mine bing, the site has then been used for various applications, including as a municipal tip and more recently a 4x4 training circuit (Hackett, 2003). The site is jointly owned by Stirling and Clackmannanshire councils and is bounded by two transport mechanisms that could be important to facilitate the spread of INNS seeds; the Alloa-Stirling railway to the North and the River Forth to the South (figure 6-2).

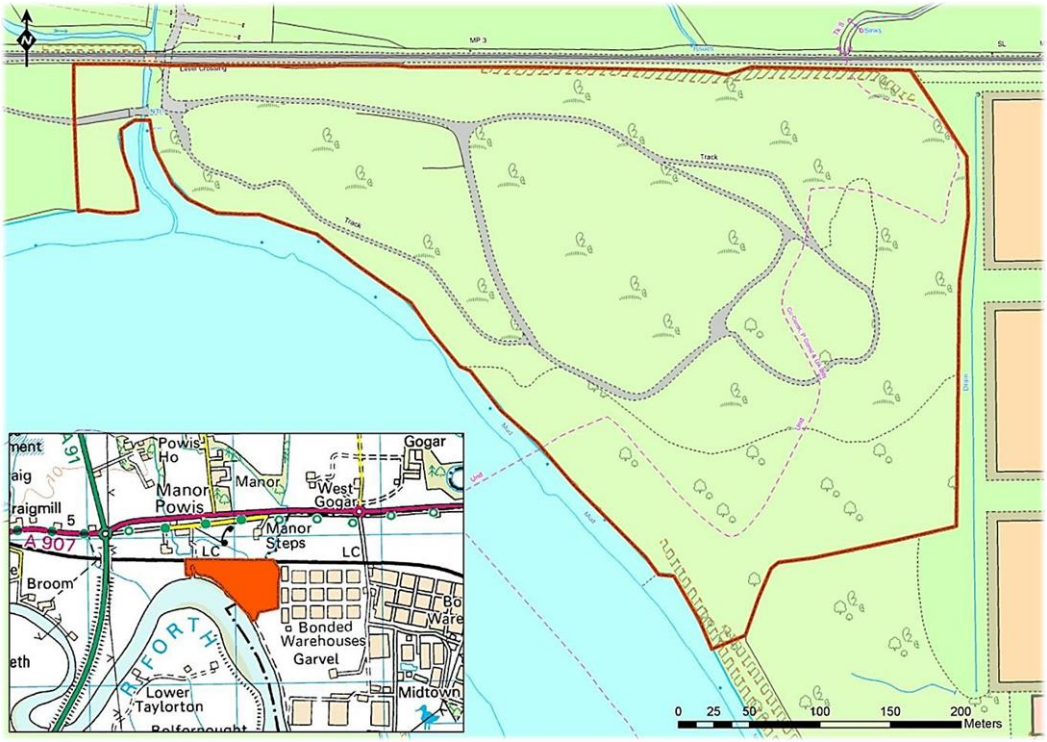

Figure 6-2: The Manor Powis Bing study site (orange boundary), ~18 ha; Inset shows area (orange) and contains Ordnance Survey data © Crown copyright and database right 2015.

6.3.2 Ariel data collection

Aerial data was acquired using the UAS and sensor package indicated in chapters 2 & 3, with the first survey conducted on the 6th July 2015 to capture giant hogweed during its flowering phase (anthesis). Further surveys were conducted to capture the phenological changes of giant hogweed, at varying times of the day and environmental conditions (full sunlight ~ overcast; table 6-1); 1st October 2015 (post-anthesis); 20th April 2016 (emergence); 21st July 2016 (waning anthesis).

Table 6-1: Time each survey conducted, and environmental conditions encountered.

DAP	Time	Conditions
6th July 2015	11:00	Overcast
1st October 2015	11:00	Sunny
20th April 2016	12:30	Sunny
21st July 2016	15:00	Overcast

For each survey, all data was acquired using pre-programmed automatic flights, travelling at 5 m/s and at 115 m AGL, to capture imagery at ~3.2 cm GSD. For each survey date, two flights were required to cover the entire area, and a 70 % forward and 72 % side overlap was used due to sensor limitation of 6 seconds between successive image captures (figure 6-3a). In total the area surveyed covered ~24.19 ha and included the Manor Powis site itself and the immediate area around it. Georectification of imagery was assisted using 16 GCPs (easily recognisable features; figure 6-3b) that had been surveyed at a later date using a Leica GPS 1200 survey grade RTK GPS (Leica Geosystems, Heerbrugg, Switzerland) with an expected accuracy of ±2 cm (Leica, 2008).

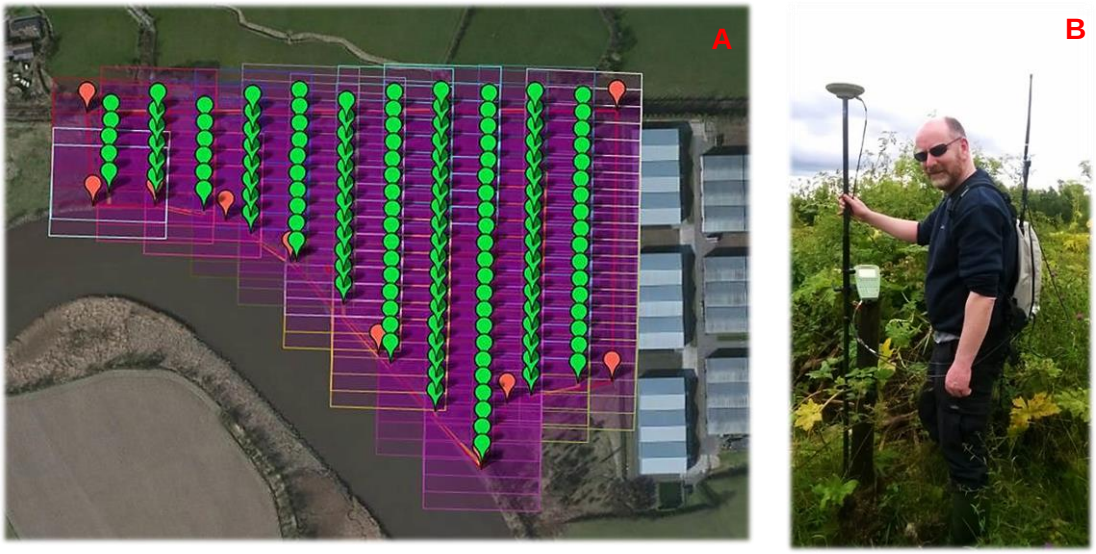

Figure 6-3: (A) Standard lawnmower pattern at 115 m AGL capturing 141 images for both RGB and NIR; Purple boxes show expected image footprint; Green dots show image capture locations; (B) Capturing point data (Alistair Hamilton); Ground points were captured post survey using noticeable features within the imagery.

6.3.3 Image processing

For the first survey (6th July 2015), image pre-processing was carried out as indicated in chapter 3, however normalisation was not performed (for the remaining surveys, only the visual dataset of each was processed). Some exceptions from the processing flow indicated in chapter 3 were also made to allow for the creation of height data across the scene surveyed. The linear RGB and NIR datasets were processed using Agisoft Photoscan (v1.2.0; Agisoft LLC, St. Petersburg, Russia), using high settings (image alignment highest; dense cloud high quality; depth filtering mild) and optimised using the 16 GCPs (using an estimated accuracy of 0.15 m). However, the visual dataset was processed using the ultra-quality dense cloud option (figure 6-4), and the DSM from this process was used rather than the DSM of the linear RGB dataset. The reason for this was twofold, firstly so that a DSM with the lowest possible GSD (i.e. ~3.2 cm GSD; figure 6-5) was available to be processed into a vegetation height layer, and secondly, to enable the creation of a DTM from within Agisoft Photoscan itself, which required the use of data with more visual clarity, so that obvious ground points could be identified.

Figure 6-4: The visual orthomosaic of the area surveyed. Dense stands of flowering hogweed can be clearly seen throughout the site (example area indicated with red arrow).

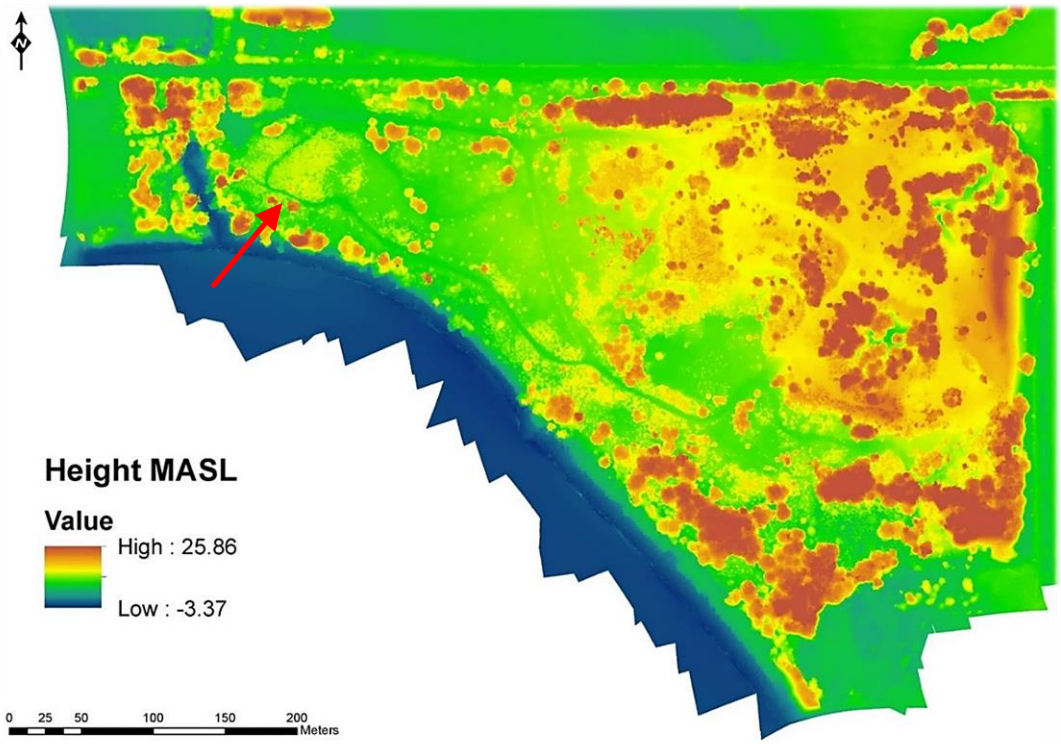

Figure 6-5: The digital surface model of the area surveyed, in meters above sea level (MASL). Again, the dense stands of giant hogweed can be seen due to the height of the vegetation (example indicated with red arrow).

6.3.3.1 Vegetation height layer creation

As giant hogweed is a relatively tall species, having detailed vegetation height information would be important as part of the classification process. The best available DTM for the study site (from Ordnance Survey) was at a resolution of 5 m GSD, and therefore gave a poor level of detail compared to the ~3.2 cm GSD imagery that had been captured. Therefore the 'Classify Ground Points' tool within Agisoft Photoscan was used to interpolate a surface using the parameters; maximum angle 15°, maximum distance 0.06 m and cell size 75 m. This initial ground point classification was not perfect and was manually modified (insertion of more ground points) to enable better coverage around areas of denser vegetation, along the riverbank and on the more raised area to the east of the study site. This modified ground point classification was then used to create a DTM of the scene surveyed (figure 6-6), which was then processed within ArcGIS (v10; ESRI, Redlands, USA) to create a vegetation height model (DSM – DTM; figure 6-7).

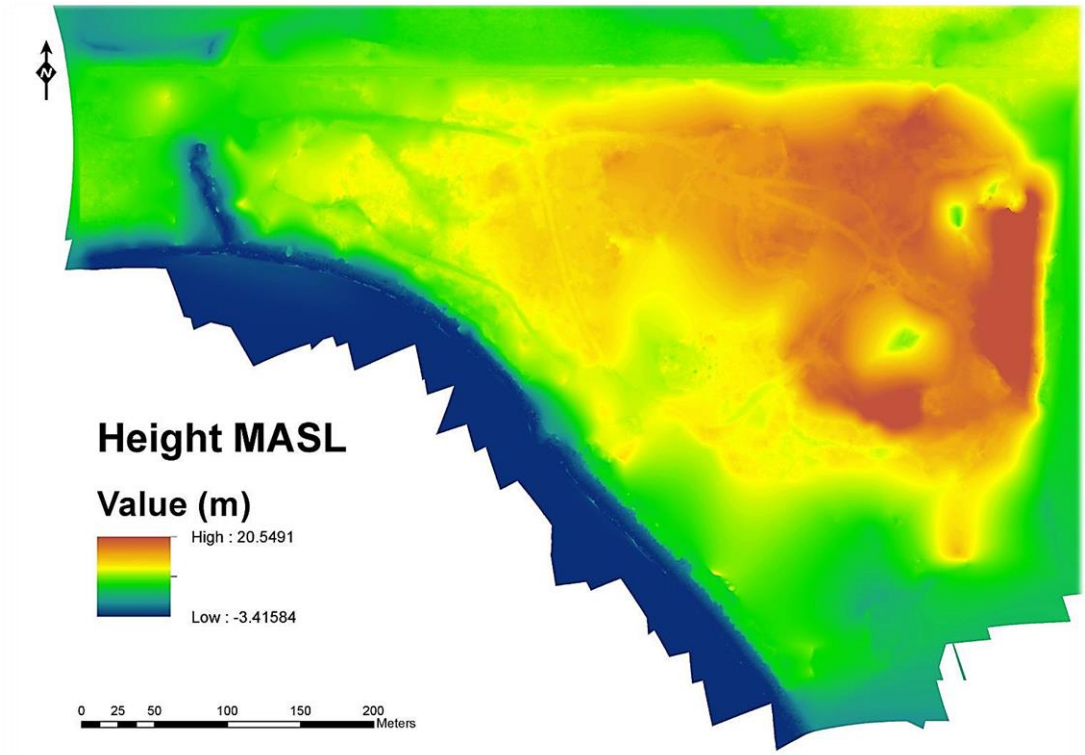

Figure 6-6: The digital terrain model of the area surveyed (in meters above sea level), derived from the visual dataset using Agisoft Photoscan.

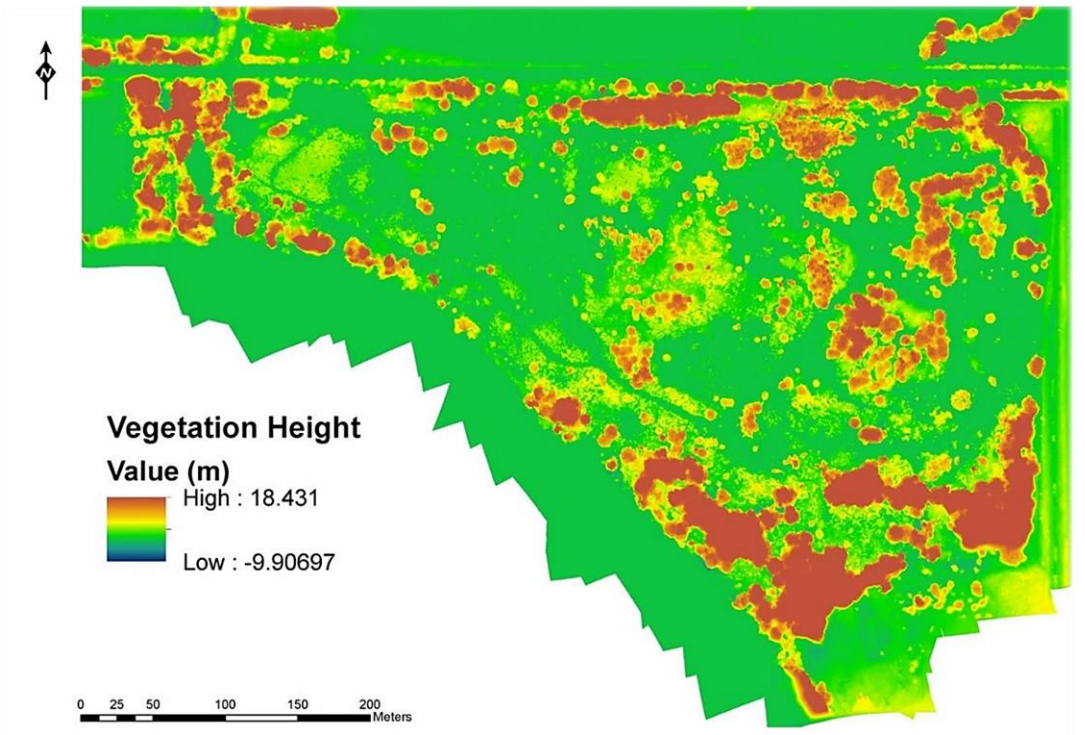

Figure 6-7: The vegetation height model derived using ArcGIS (DSM-DTM). The very low vegetation height indicated on the scale was caused by occasional points of noise within the DSM and DTM, primarily at the edges of the data over the river forth.

6.3.3.2 Orthomosaic co-registration

As the visual dataset was used to create the DSM, DTM and vegetation height layer, the linear RGB and NIR orthomosaics needed to be aligned to the visual dataset. An offset could be seen between the datasets, most likely due to a combination of factors including the use of natural features as GCPs (the centres of which may not have been perfectly identified within the different datasets), the visual dataset being processed differently, as well as the extra distortion created from the 585 nm long pass filter applied to the modified camera. ArcGIS was used to georeference both linear datasets to the visual dataset using 17 control points and a third order polynomial transformation, giving RMS errors of 0.02 m for the RGB dataset and 0.04 m for the NIR dataset, that enabled the datasets to be used together (figure 6-8).

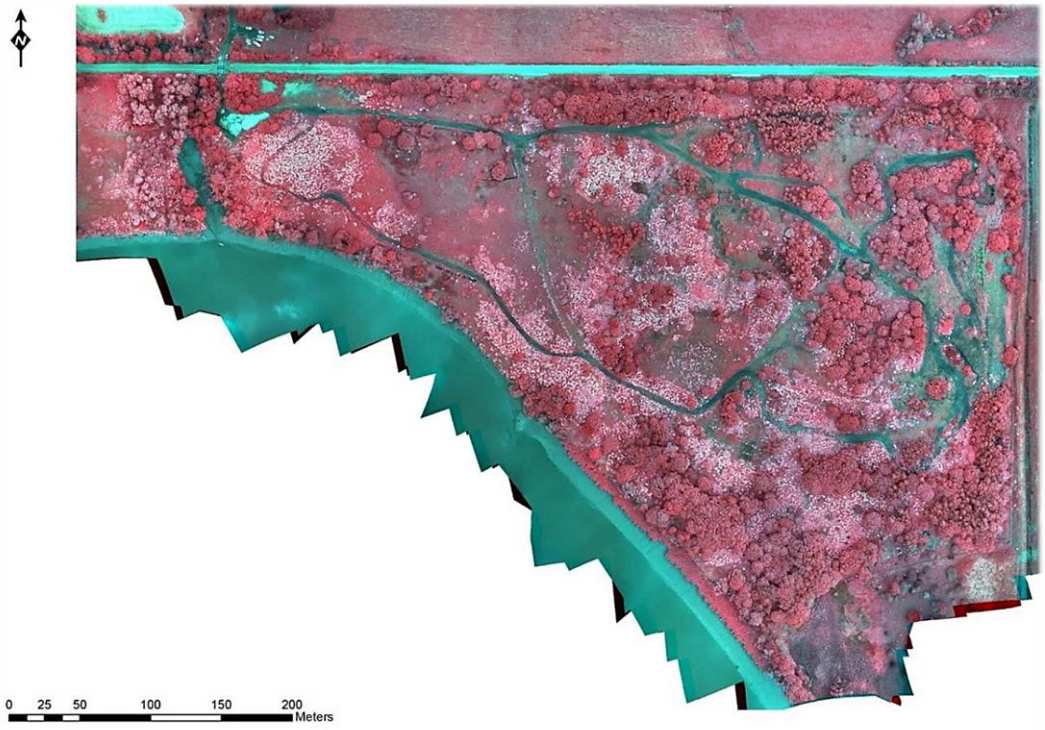

Figure 6-8: A false colour composite (colour infra-red) of the area surveyed.

6.3.3.3 Preparation for classification

Due to the image size limitations of the OBIA software package Interimage (v1.43; Camargo *et al.,* 2012), the orthomosaic datasets needed to be trimmed to a size that would allow them to be processed. To facilitate this ArcGIS was used to create a four band orthomosaic that only contained the red, green and blue bands from the

RGB linear orthomosaic and the blue band from the NIR linear orthomosaic (i.e. the band containing just NIR wavelengths of light). This four band orthomosaic and the vegetation height layer were then split into 391 individual blocks (of 1000 x 1000 pixels; figure 6-9), to allow each one to be processed independently using Interimage.

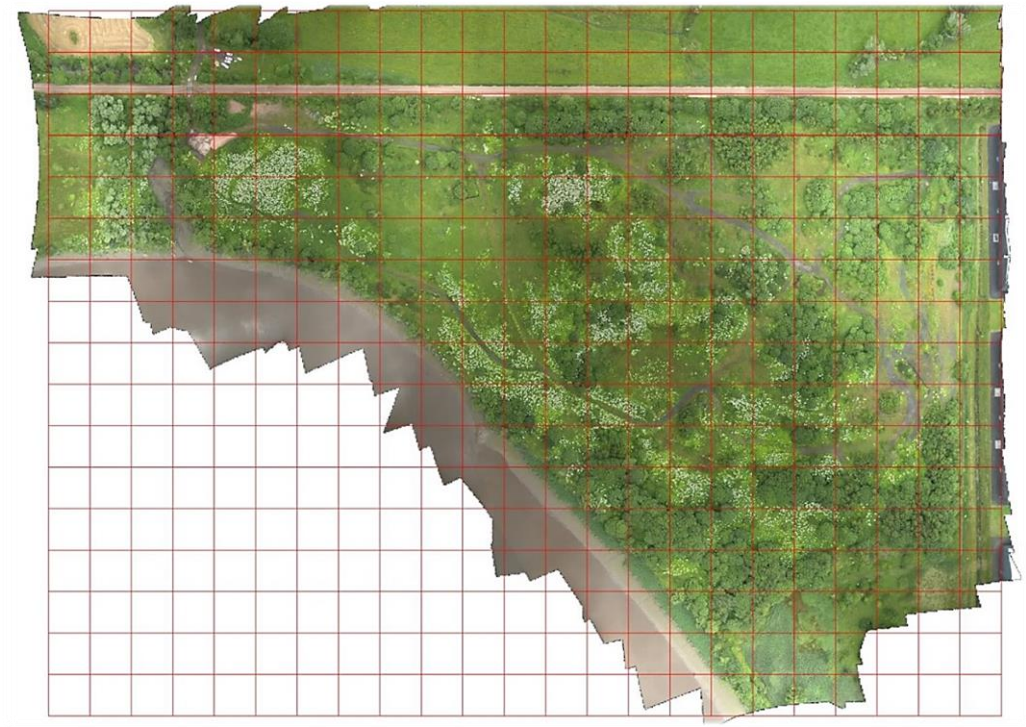

Figure 6-9: An example of the orthomosaic split into 391 image blocks (red squares) of 1000 x 1000 pixels, to enable their use within the classification process.

6.3.4 Automatic giant hogweed classification method

To enable the separation of giant hogweed from the other vegetation at the study site, a processing flow (termed semantic net) was created within Interimage and run against each of the 391 image blocks in turn. The semantic net used a rules-based approach with nine classes over two levels to classify the entire scene (figure 6-10).

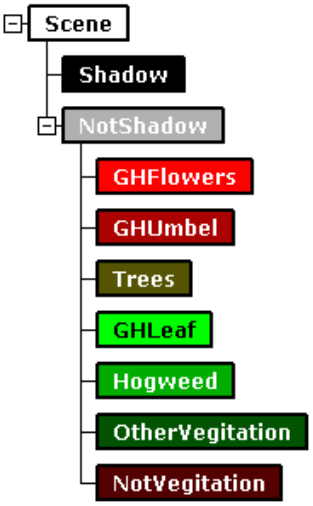

Figure 6-10: The semantic net used, showing all classes and

At the first level the scene was simply split to show areas that were shadowed or not, using the TA_Arithmetic operator (a pixel-based

thresholding operator) using the following *levels.* thresholds:

- Shadow = $\frac{DN_R+DN_G+DN_B}{3} \leq 4500$
- NotShadow = $\frac{DN_R+DN_G+DN_B}{3} > 4500$

Where DN_R refers to the DN from the red channel of the unmodified camera, DN_G refers to the DN from the green channel of the unmodified camera and DN_B refers to the DN from the blue channel of the unmodified camera.

Anything not classed as a shadow was processed further within a second level using either the TA_Arithmetic operator or the TA_Baatz_segmenter operator (a multiresolution segmentation operator), using decision rules to enable each object to be classified if certain criteria were met (table 6-2). Three vegetation indices were used as part of these decision rules (Eq. 6-1, 6-2 and 6-3).

$$NDVI = \frac{DN_{NIR} - DN_R}{DN_{NIR} + DN_R} \quad \text{(6-1)}$$
(Rouse *et al.* 1973)

$$ExG = (2 \cdot DN_G - DN_R - DN_B) \quad \text{(6-2)}$$
(Woebbecke *et al.*, 1995)

$$ExR = (1.4 \cdot DN_R - DN_G) \quad \text{(6-3)}$$
(Meyer & Neto, 2008)

Where DN_{NIR} refers to the DN from the blue channel of the modified camera DN_G refers to the DN of the green channel of the unmodified camera, DN_R refers to the DN of the red channel of the unmodified camera and DN_B refers to the DN of the blue channel of the unmodified camera.

Table 6-2: The operators, decision rules and reliability scores used for each class within the Interimage processing flow. For the decision rules, each item refers to the properties of the object being assessed; Brightness and Ratio are attributes within Interimage; GLCM stands for grey-level co-occurrence matrix (a textural attribute).

Class	Operator	Decision Rule	Reliability
GHFlowers	TA_Baatz	Height < 3.9 m Height > 0.5 m Size ≥ 14 pixels Brightness ≥ 15000 Mean GLCM (Blue) ≥ 14000	0.7
GHUmbel	TA_Baatz	Height < 3.9 m Height > 0.5 m ExG ≥ 20000 Within 50 pixels of GHFlowers	0.6
Trees	TA_Baatz	Height > 3.9 m	0.5
GHLeaf	TA_Baatz	Height ≤ 2 m Ratio (Blue) < 0.128033 Mean GLCM (Green) ≥ 14000	0.4
Hogweed	TA_Baatz	Height ≤ 3.9 m Size ≥ 10 pixels ExG ≥ 12000 ExR ≤ -4000 Within 50 pixels of GHFlowers Neighbouring GHLeaf	0.3
OtherVegetation	TA_Arithmetic	NDVI ≥ 0	0.2
NotVegitation	TA_Arithmetic	NDVI < 0	0.2

The classes within this second level of processing represented specific features of importance. GHFlowers are the actual flower heads of each giant hogweed plant. GHLeaf are the brighter and more distinct green leaves of giant hogweed. Hogweed represents the darker (semi shadowed) green leaves of giant hogweed, which were difficult to separate from other vegetation and so used proximity to either GHFlowers or GHLeaf objects as verification. Similarly, GHUmbels also used proximity to GHFlowers, as they represent giant hogweed vegetation directly surrounding the flowers, or flower heads that no longer have flowers and have started to go to seed. The trees class represent trees, OtherVegetation is any other vegetation and NotVegetation is anything that is not vegetation.

All of the classes (figure 6-10) used top down decision rules to create an object hypothesis for each class, and the final allocation of these classes was further

governed by priorities (the reliability score). This reliability score allows a class hypothesis to be given a higher priority over another if there is a spatial conflict (i.e. objects covering the same spatial area and being potentially more than one single class). These conflicts and identification of proximity to other objects were all resolved at the end of the process, via a single bottom up decision rule within the NotShadow class, spatially resolving the entire classification (Interimage, 2010).

6.4 Results

The output from all 391 image blocks was integrated into a single layer within ArcGIS to show the classification across the area surveyed (figure 6-11) and identify the amount of ground covered by giant hogweed plants (table 6-3).

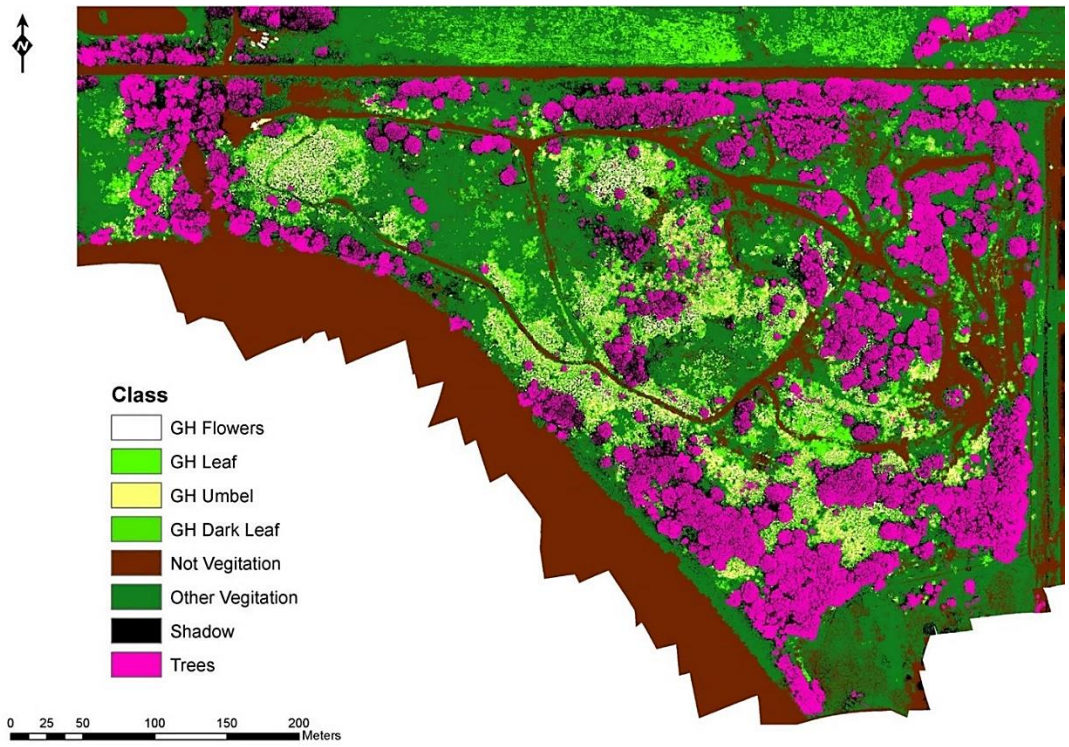

Figure 6-11: The final classification of the area surveyed showing all the classes (the class indicated as GH Dark Leaf is the Hogweed class).

Table 6-3: Ground cover in ha and as a percentage of the area surveyed (~24.19 ha) for each of the eight classes.

Class	Area (ha)	% of area surveyed
GHFlowers	0.35	1.44
GHUmbel	0.74	3.06
GHLeaf	1.24	5.12
Hogweed	1.14	4.73
Trees	4.04	16.37
OtherVegetation	8.21	33.92
NotVegitation	5.96	24.63
Shadow	2.50	10.37

To identify the accuracy of the classification, an error matrix was created so that kappa (Ǩ) statistics (eq. 6-4) could be generated to give an indication to the level of accuracy. As only the presence or absence of giant hogweed was important for this study, all of the giant hogweed related classes (GH flowers, GH leaf, GH Umbel and Hogweed) were amalgamated into a single combined class (giant hogweed; 3.47 ha; 14.36 % of area surveyed) and all of the other classes into a second class (not giant hogweed; 20.71 ha; 85.64 % of area surveyed). Across the area surveyed, 225 randomly placed 1 x 1 m plots were visually checked for the presence or absence of giant hogweed and compared with the results from the automatic classification (similar in method to Müllerová *et al.* 2013).

$$\check{\mathrm{K}} = \frac{Po - Pc}{1 - Pc} \qquad (6\text{-}4)$$

Where Po represents actual agreement and Pc represents chance agreement (Weih *et al.*, 2010).

The error matrix (table 6-4) showed an overall accuracy (OA) of 88 %, with a producers accuracy (PA) of 95 % and users accuracy (UA) of 68 % for the presence of giant hogweed. It resulted in a kappa statistic (Ǩ) of 0.71 which indicates a good level of agreement between the automatic and visual classification methods.

Table 6-4: Error matrix of giant hogweed presence or absence for the visual and automatic classification.

		Producer (Visual classification)			
		Giant Hogweed Present	**Giant Hogweed Not Present**	**Total**	**UA**
User (Automatic classification)	**Giant Hogweed Present**	52	24	76	0.68
	Giant Hogweed Not Present	3	146	149	0.98
	Total	55	170	(225)	
	PA	0.95	0.86		**OA** (0.88)

6.5 Discussion

Although four surveys were carried out for this study, only the first dataset was fully processed and classified as a pilot study to identify how effective UAS could be in detecting the presence of giant hogweed. This classification gave an OA of 88%, PA of 95%, UA of 68% and Ǩ of 0.71, which, when using the same indication of real-world accuracy as indicted in Chapter 4 (OA >= 85%, PA/UA >= 70 % and Ǩ > 0.61), indicates that classification method used in this study is not yet effective enough to be a reliable measure of the presence of giant hogweed.

There are several areas that need improvement, with the memory limitations of InterImage being one of the first areas to address. Splitting the area surveyed into small blocks introduced errors as height data was used extensively to filter out different layers of vegetation (i.e. trees, shrubs and giant hogweed itself as it is a very tall plant), but these features could be split by the borders of the image blocks, resulting in misclassifications (figure 6-12). Other plant species were also misclassified as giant hogweed, such as the shrub Elder (*Sambucus nigra*), which was misclassified as giant hogweed flowers due to the height of the shrub being similar to giant hogweed, and their flowering phase (also relatively large clusters of white flowers) occurring at the same time. To the north of the railway line, creeping buttercup (*Ranunculus repens*) was present across a large area within a field, and this was misclassified as giant hogweed leaf due to its textural and spectral qualities being similar.

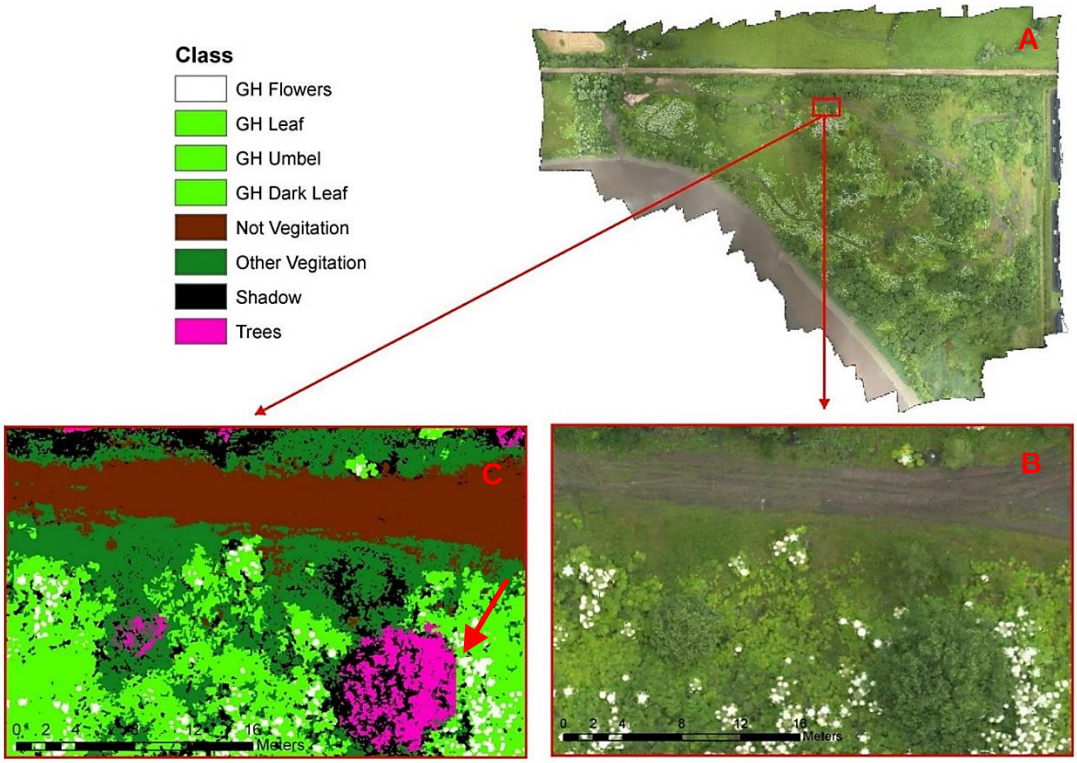

Figure 6-12: (A) Overview of brown field site surveyed for giant hogweed in July 2015; showing (B) inset of detailed section; (C) classification of detailed section, with class legend shown. The red arrow indicates a small misclassification of giant hogweed due to the tree being split by an image block (the shape of the tree should be rounder and not have a flat side).

There are a small number of researchers specifically looking at this this species and other INNS species using UAS (Müllerová *et al.*, 2017b; Michez *et al.*, 2016) and all have had varied amounts of success with mapping giant hogweed using COTS. Michez *et al.* (2016) used a fixed wing UAS with modified and unmodified COTS cameras but did not appear to use height data as part of their classification method. Their study showed effective results (OA 97% and Ǩ 0.93) when using an OBIA approach, however they did not report UA or PA and appeared to only be classifying the flowers (or clusters of flowers) and not the full extent of giant hogweed vegetation (or non-flowering giant hogweed).

The study by Müllerová *et al.* (2017b) also used a fixed wing UAS with modified and unmodified COTS cameras. They also did not specifically indicate that height data was being used, although a prior study by a co-researcher (Dvořák *et al.*, 2015) did indicate that height was used as part of their classification routine. They reported very high accuracy (OA 100%, PA 99%, UA 100% but Ǩ was not reported) when using an OBIA approach for surveying giant hogweed in its flowering stage but

reported difficulty with detecting the giant hogweed leaves surrounding the flowering umbels. Their study also highlighted that phenological changes (differences between flowering stage and die back) could assist with the detection of INNS species, a concept supported by other researchers investigating various INSS through remote sensing (Dorigo *et al.*, 2012; Bradley, 2014; Martin *et al.*, 2018).

Although the extra surveys carried out in October 2015, April 2016 and July 2016, were not used directly in this study, the combined use of data showing different phenological stages of giant hogweed (figure 6-13) could be useful in improving the classification result, allowing maps of the extent of giant hogweed to be created and therefore used to inform future management decisions on the control of the species. As giant hogweed is estimated to cost the British economy ~£2,362,000 annually, with £964,995 directly related to its effects and management along riparian habitats (Williams *et al.* 2010), the ability to monitor it remotely would aid in reducing these costs, and could help highlight vectors for the spread of seed from areas adjacent to riparian habitats.

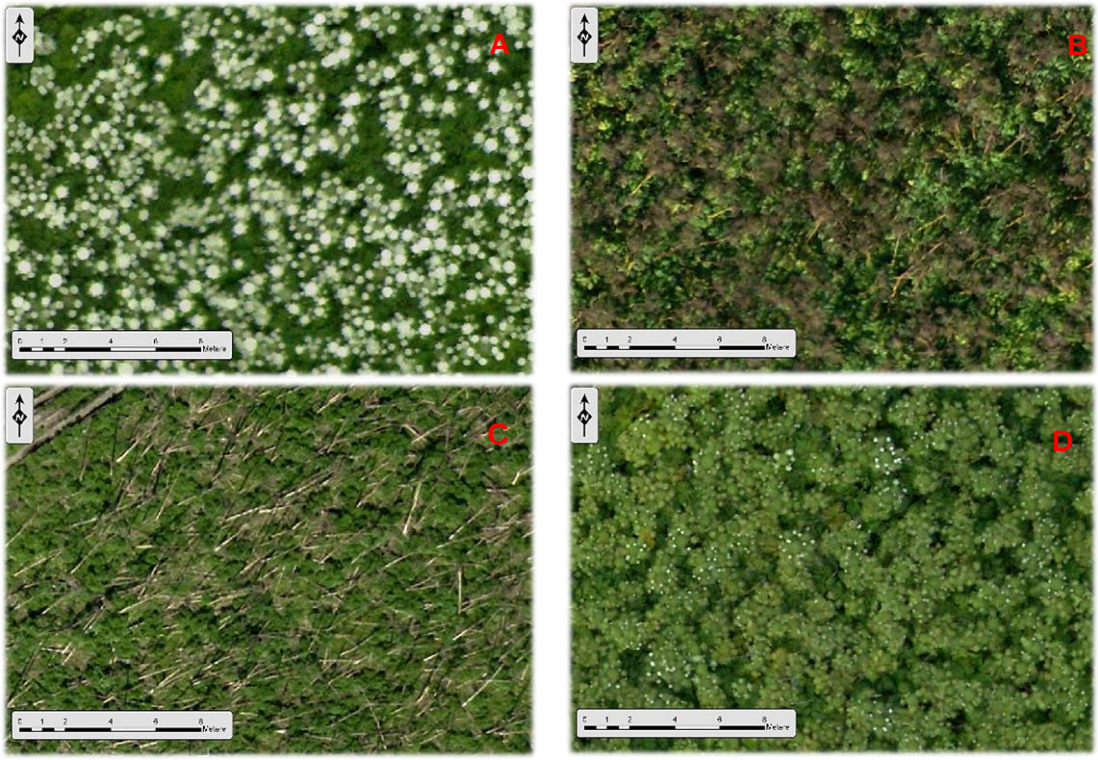

Figure 6-13: Phenological changes of a dense stand of giant hogweed; (A) 6th July 2015 (anthesis), flowering can be seen (white flowers); (B) 1st October 2015 (post-anthesis), dead stalks of flowering plants can be seen; (C) 20th April 2016 (emergence), newly emerging plants dominating the ground; (D) 21st July 2016 (waning anthesis), less flowers visible as they ripen into seed heads.

Manual methods of surveying for giant hogweed are labour intensive, with one example using a group of 10 volunteers led by two experienced rangers to survey ~24 km of a stretch of the River Allen (Stirlingshire) over a period of five days (Harewood, 2014). This equates to ~5 km per day but only up to a maximum of 50 m on either side of the river was mapped, with the position of plants (or length of dense stands) mapped using handheld GPS. If a UAS had been used, then a similar (or even greater) length of river could have been surveyed per day but would have also covered larger stretches of the riverbank and would only require two or three people to complete. Pergl *et al.* (2011) suggests covering as large an area as possible, as just 1% of the seed set from an average giant hogweed plant could result in 200 seedlings, and therefore the presence of giant hogweed out with the riparian habitat could well be a vector for seed dispersal back into it. There would of course be regulatory issues to overcome when using a UAS, due to the proximity of urban areas and public rights of way, and heavily wooded areas would likely be difficult or impossible to survey from the air, but the use of a UAS would allow for a more expanded survey for a similar effort.

At the actual Manor Powis site itself, a manual survey undertaken by Currie & Bairner (2013), showed the approximate distribution of giant hogweed (including dense patches) within the site in 2013 (data collected in March & August). In total, Currie & Bairner (2013) estimated that ~9.8 ha of the site was affected by Giant Hogweed in 2013, of which ~1.75 ha was classed as dense stands. The results of this study indicate that ~2.89 ha of ground is directly covered by giant hogweed in 2015 (within the bounds of the study site, not the entire area surveyed), with most of the site now hosting giant hogweed to some degree (figure 6-14). Both the position and size of the dense stands of giant hogweed appear to have increased since 2013, however Currie & Bairner (2013) only gave the approximate distribution of giant hogweed (they were actually cataloguing invertebrates), and as the classification accuracy of this study is not yet effective, it cannot be reliably said that giant hogweed is increasing across the site. However, as the first recorded sighting of giant hogweed at Manor Powis appears in 1995 and only in the south east of the study site (NBN Atlas, 2018; figure 6-14), it is likely that the species has been spreading steadily through the area, most likely aided by the use of the site as a 4x4 training circuit.

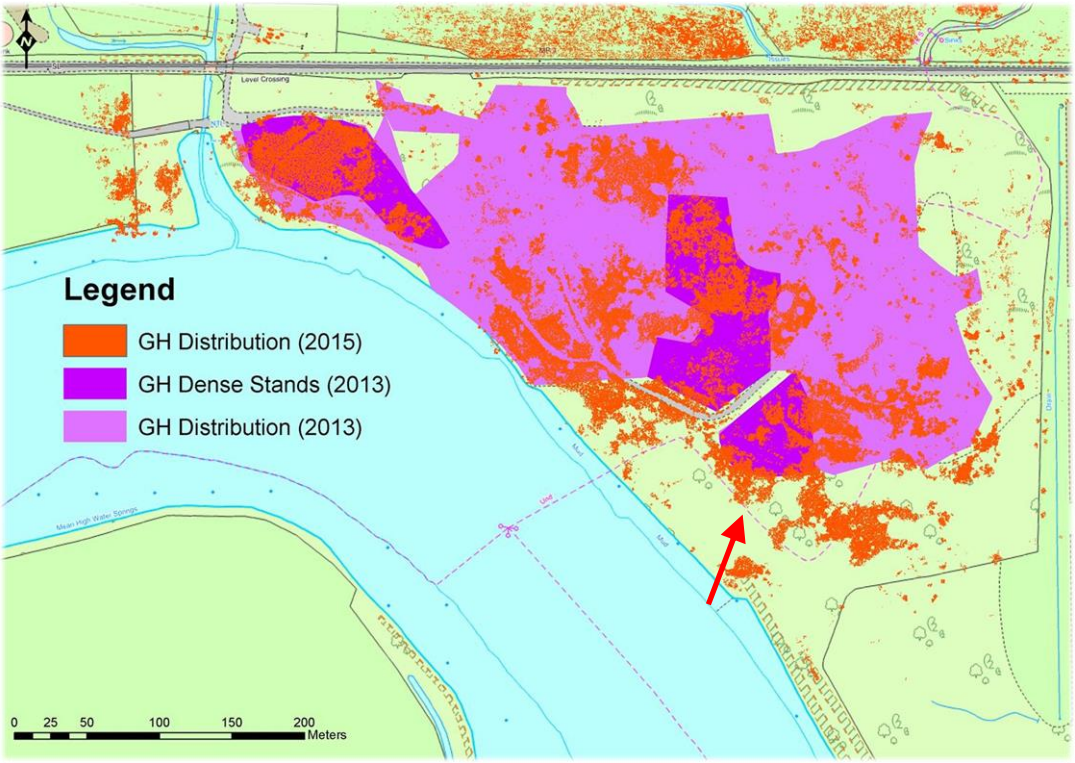

Figure 6-14: Extent of giant hogweed in 2013 (purple polygons) and 2015 (orange points). Red arrow indicates the approximate position of giant hogweed noted in 1995 (NBN Atlas, 2018). Contains Ordnance Survey data © Crown copyright and database right 2015.

Although further work is required on the classification method used in this study, the identification of flowering giant hogweed does look promising, as shown by Müllerová *et al.* (2017b) and Michez *et al.* (2016). If the classification can be improved to reliably show the size of individual flowering umbels (or approximation of the number of mature plants) then there is also the possibility of estimating the amount of seed that could be produced, as this can differ per plant based on a number of factors, including the size, number and position of flowering umbels (figure 6-15; Perglová *et al.* 2006).

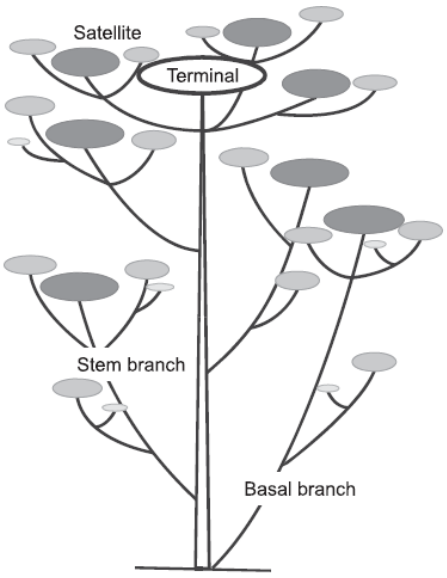

Figure 6-15: Schematic representation of the ordering of umbels and their position within the hierarchaical inflorence system of giant hogweed (Perglová et al. 2006).

The majority of seeds from mature plants (60-90%) are likely to fall within only 4 m of its parent plant (Nielsen *et al.*, 2005), however the remaining could travel via wind dispersal from 10-50 m (Caffery, 1994). Identification of the amount of seed created (and at what points and what height of the seed heads) could then be modelled with the distances they are likely to travel and used to identify how far the species could spread into neighbouring areas. If this could be reliably done at the Manor Powis site, then an indication of the number of seeds getting onto the railway line could be made as well as an indication of the number of seeds entering into the River Forth.

Either of these transport mechanisms could enable the seeds to travel further, via the slipstream of fast-moving trains or via the ability of the seeds to float from 8 hours up to 3 days (Moravcová *et al.*, 2007). The knowledge of potential seed dispersal has value to land managers trying to tackle this species and would aid in its eradication, as the Wildlife and Countryside Act 1981 holds individuals criminal responsible for spreading INNS. One example of this being the management of the railway line itself as active management of giant hogweed along the railway margins was observed on the 6th of July 2015. Being able to identify the source (and scale) of the invasion onto the railway could result in a shift of management decisions into trying to tackle the source of the seed, rather than just the plants in the margins of the railway line itself, which if done cooperatively with neighbouring landowners could prove more successful in eradicating the problem (Wade, 2015).

6.6 Conclusion and future thoughts

This study shows that the high resolution data provided by UAS can be used to classify giant hogweed and that the height data produced can be used to split up the layers of vegetation, assisting in the classification of tall species such as giant hogweed from the surrounding vegetation. If taken further, then classifications of this kind could also aid in modelling the spread of giant hogweed, which in turn could be of great benefit to land managers who are trying to control INSS. Although this study was not completely successful in its current form, the work of other researchers (e.g. Müllerová *et al.*, 2017b; Michez *et al.*, 2016) indicates that the remote sensing of giant hogweed and other INNS using UAS is worth pursuing, and therefore UAS could become valuable tools to aid in the eradication of problem plant species.

To conclude, this chapter meets part of the 4th objective of this PhD project through showing the ability to detect INNS species, although further work is required to refine the automatic classification method and bring it up to a similar standard of other studies. This would be aided by the use of OBIA software that does not require the data to be split into individual image blocks, which in turn adds to the requirements for the 3rd objective of this PhD project. Future collaboration with Clackmannanshire and Stirling council should also be pursued so that optimum survey methods to enable effective monitoring of this species along riparian habitats can be identified, especially as the nature of riparian habitats (typically long and winding) may require the use of a UAS with longer endurance than that used in this study (e.g. a fixed wing UAS).

Chapter 7. Experimental applications – Upscaling greenhouse gas estimations from different land use types

7.1 Introduction

Climate change has been linked to anthropogenic effects (Forster *et al.*, 2007) and is being driven by the increasing emissions of greenhouse gases (GHG; figure 7-1), such as carbon dioxide (CO_2), methane (CH_4) and nitrous oxide (N_2O). Although these GHG are biogenic and natural in the environment, the way that humans manage the land can influence how much of each GHG is produced. This is especially true for CH_4 and N_2O, both of which have a much higher global warming potential compared to CO_2 than, over a 100-year lifetime (298 and 34 times respectively; Myhre *et al.*, 2013).

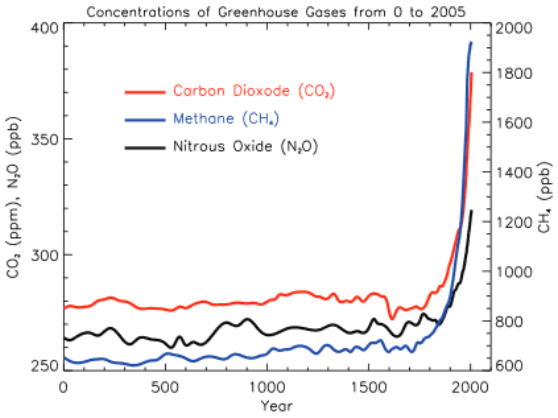

Figure 7-1: Atmospheric concentrations of important long-lived green-house gases over the last 2,000 years. Increases since about 1750 are attributed to human activities in the industrial era. Concentration units are parts per million (ppm) or parts per billion (ppb), indicating the number of molecules of the greenhouse gas per million or billion air molecules, respectively, in an atmospheric sample (Forster et al., 2007).

UAS have already been used to directly sample GHG emissions, sometimes for industrial applications such as detecting CH_4 leaks along pipelines or over landfill sites (Barchyn *et al.*, 2017; Emran *et al.*, 2017), or for sampling CH_4, CO_2 and water vapour to help with climate modelling in remote or dangerous areas, such as over forest fires (Berman *et al.*, 2012). This direct sampling method requires complicated GHG specific detectors, so an alternative method is to use optical sensors to map features on the ground that have known GHG fluxes (the exchange of gases). This spatial information can then be used to upscale and identify the total GHG flux for the area surveyed, as Davidson *et al.* (2017) showed when using high resolution satellite data to map arctic tundra vegetation, to allow for the upscaling of CH_4 emissions.

This exploratory chapter address the 4th objective of this PhD projects as it highlights two case studies that investigated the classification of microtopography

from two different land use types (forestry and grasslands), to allow the upscaling GHG emissions. The studies were both in collaboration with other researchers who were specialists in the field of climate change mitigation and adaptation, and whose data forms part of ongoing analysis. Therefore, these studies do not go into the technical aspects of upscaling the actual GHG emissions but concentrate on the utility of the UAS in classifying the microtopographical features of interest.

7.2 Experimental case study 1 – Classifying microtopographical features across an area of clear fell forestry

7.2.1 Introduction

Earlier on within this PhD project the opportunity arose to test the UAS over a large area of clear felled forestry as part of the GREENHOUSE project (Generating Regional Emissions Estimates with a Novel Hierarchy of Observations and Upscaled Simulation Experiments), a NERC funded project in collaboration with colleagues from York University, The University of Edinburgh, Forest Research and others, investigating greenhouse gas emissions over a range of managed habitats (GREENHOUSE, 2018). This project was primarily to identify GHG emissions (CO_2, CH_4 and N_2O) following the felling of a mature Sitka spruce (*Picea sitchensis*) stand in an upland forest in northern England (Harwood forest).

GHG fluxes were captured using traditional (e.g. static sampling chambers and eddy covariance towers) and novel gas sampling equipment such as the skyline system, an automated sampling system that can sample gases continuously (day and night) at varied points across an 18 m transect (Keane, 2015). This sampling revealed differences in emissions from different microtopographical features, such as at the top of a ridge and the hollow between two ridges (the ridges were formed as part of the planting process of the trees), as well as within ditches and between wet and dry areas of soil.

7.2.2 Aim of the case study

This experimental case study details the steps used to create a classified microtopography of a region of a clear-felled forest, to enable estimates to be made with regards to the level of greenhouse gas emissions that emanate from clear-felled areas. The report details the classification method, result and accuracy of the

classification, but does not indicate the upscaling of GHG emissions, as this area of research was handled by other members of the GREENHOUSE project and is still under development.

7.2.3 Methods

7.2.3.1 Aerial data collection

All data was collected on the 30th June 2015 (prior to Skyline installation), under mixed cloudy/sunny conditions and using the custom-built multi-rotor UAS and sensor package as indicated in chapter 3. Approximately 30 ha of the clear-felled area was selected to be surveyed, as this covered the intended locations of the various GHG measurement installations (figure 7-2). This was achieved via three separate flights at 115 m AGL, to capture imagery at a GSD of ~3.2 cm per pixel and with an image overlap of 78 % and side overlap of 60%. The UAS was flown at a speed of 5 m/s and collected 253 images in total (per camera).

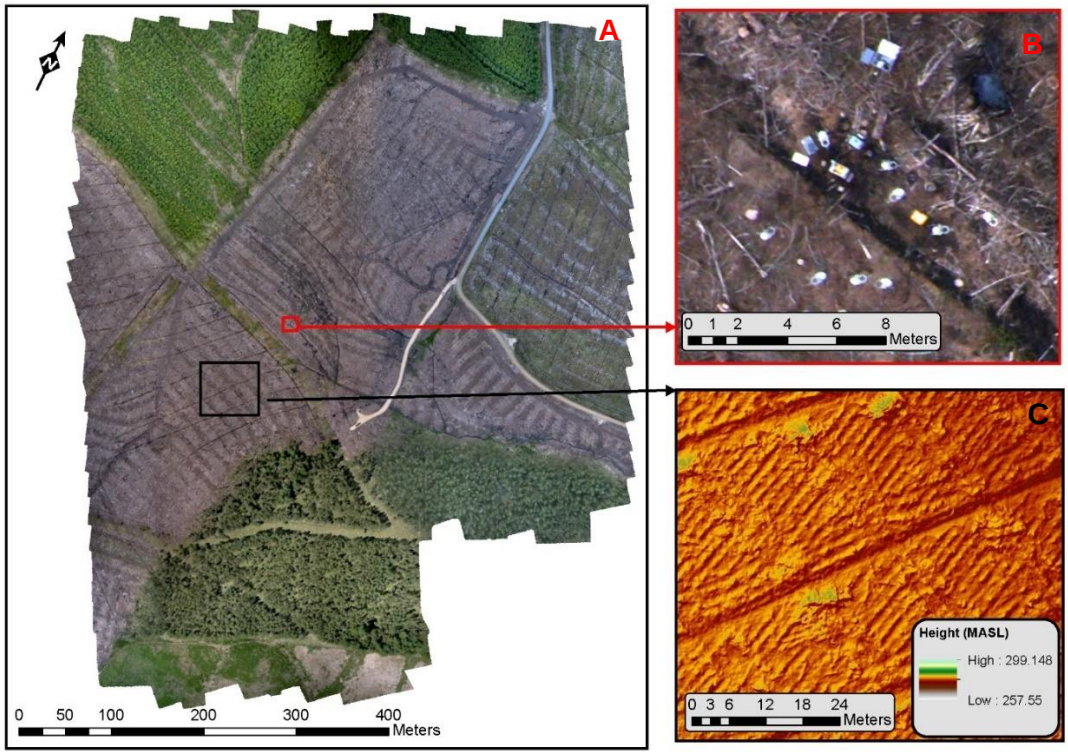

Figure 7-2: (A) The entire area covered by the UAS, Harwood Forest, Northumberland, England (June 2015); (B) example of detail visible showing automatic gas sampling chambers and ancillary equipment; (C) DSM of a section of the site showing ditch lines (East-West) and ridge and hollow lines (North-South).

7.2.3.2 Ground control point data collection

To ensure accurate positioning of the aerial data in relation to the 'SkyLine' system, eddy covariance measurement tower and other GHG measurement installations, GCPs needed to be dispersed evenly across the area to be surveyed. Unfortunately, there were only a limited number of GCPs available (orange discs of 20 & 30 cm diameter) so some were moved for each flight so that at least 10 would be visible within each 10 ha section surveyed, ensuring that each individual flight's data could still be used independently in case of failure during any single flight. The position of each GCP was noted with a Garmin eTrex 10 handheld GNSS (Garmin International Inc, Kansas, USA) and the most prominent (i.e. the larger GCP's that had been positioned on tree stumps) were surveyed again a month later using a Leica GPS 1200 survey grade RTK GPS (Leica Geosystems, Heerbrugg, Switzerland) with an expected accuracy of ±2 cm (Leica, 2008). In total 16 GCPs that had been surveyed with the high accuracy GNSS were visible across the area surveyed and available to be used for image processing.

7.2.3.3 Image processing and orthomosaic co-registration

Image pre-processing was carried out as indicated in chapter 3 however normalisation was not performed. The data was processed using Agisoft Photoscan (v1.2.5; Agisoft LLC, St. Petersburg, Russia), using the highest possible settings (image alignment highest; dense cloud ultra-quality; depth filtering mild) and optimised using the 16 GCPs dispersed throughout the scene surveyed (using an estimated accuracy of 0.15 m). Each complete dataset took ~12 hours to process, creating a linear red, green, blue (RGB) orthomosaic, a digital surface model (DSM), and a linear near infra-red (NIR) orthomosaic, and an orthomosaic enhanced for improved visually clarity (VIS).

Due to the use of much higher accuracy GCPs, the co-registration of the unmodified and modified cameras appeared to be effective when viewing clear features such as vegetation or ditches or relatively flat features and wet areas. However, alignment seemed poorer over piles of brash (raised features of broken tree trunks and branches), possibly due to the much nosier imagery created by the modified camera causing differences in the depth reconstruction of these features compared to the unmodified camera. Attempts to remedy this using ArcGIS (v10; ESRI, Redlands, USA) were not successful, so co-registration remained as it was originally processed.

7.2.3.4 Feature classification

The original intention for the classification method was to attempt to automatically classify features of interest across the entire area surveyed, however difficulties were encountered in trying to identify ridges and hollows effectively, so a smaller area was chosen that could be classified by hand (manually) using ArcGIS, so that it could be used as an initial assessment of the potential for upscaling GHG emissions (see appendix G for the report of this process in more detail).

A rectangular region of interest (ROI; figure 7-3) was chosen that was large enough to encompass the intended location of the skyline system, a tower installation housing an eddy covariance system and the mean GHG flux footprint sampled from this tower. This GHG flux footprint data was supplied by Forest Research and is indicative of the GHG fluxes for which 50% came from an area within 200 m from the eddy covariance tower at a wind direction of 220-260 degrees (Xenakis, 2016).

Figure 7-3: Overview of the area selected as a ROI (red box), ~2.1 ha; Also indicated are the locations of the flux tower (pink square), skyline system (red dots) and other gas sampling locations.

The four main microtopographical features to be classified were the ridges, hollows, drainage ditches and wet ground, however other features were present, such as vegetated areas and features covered by brash mats (the offcuts and woody residue of the harvesting operation that are used to create a track for the harvesting machinery to operate from). Therefore, they were also included in case they could be of value in later analysis and in total thirteen features of interest were identified, as indicated in table 7-1.

Table 7-1: Explanation of the features for each of the 13 classes.

Class (abbrev.)	Explanation of class
Brashed Ditches (BD)	Drainage ditches that had a brash mat overlying them.
Vegetated Ditches (VD)	Drainage ditches that cut through vegetation or had vegetation within them.
Ditches (D)	Drainage ditches.
Brashed Rough Ground (BRG)	Uncultivated ground that had a brash mat overlying it.
Vegetated Rough Ground (VRG)	Uncultivated ground that had growing vegetation.
Rough Ground (RG)	Uncultivated ground.
Brashed Ridges (BR)	Ridges used for tree planting that had a brash mat overlying them.
Vegetated Ridges (VR)	Ridges used for tree planting that had vegetation growing on them.
Ridges (R)	Ridges used for tree planting.
Brashed Hollows (BH)	Hollows between ridges used for tree planting that had a brash mat overlying them.
Vegetated Hollows (VH)	Hollows between ridges used for tree planting that had vegetation growing on them.
Hollows (H)	Hollows between ridges used for tree planting.
Wet Ground (WG)	Any area of ground that appeared to be wet or was standing water (but was not a ditch).

7.2.4 Results

The 13 classes were resolved from the manually classified layers of the drainage ditches, ridges, rough ground, vegetated areas, brash mats and wet ground to produce a final classification of the entire ROI (figure 7-4).

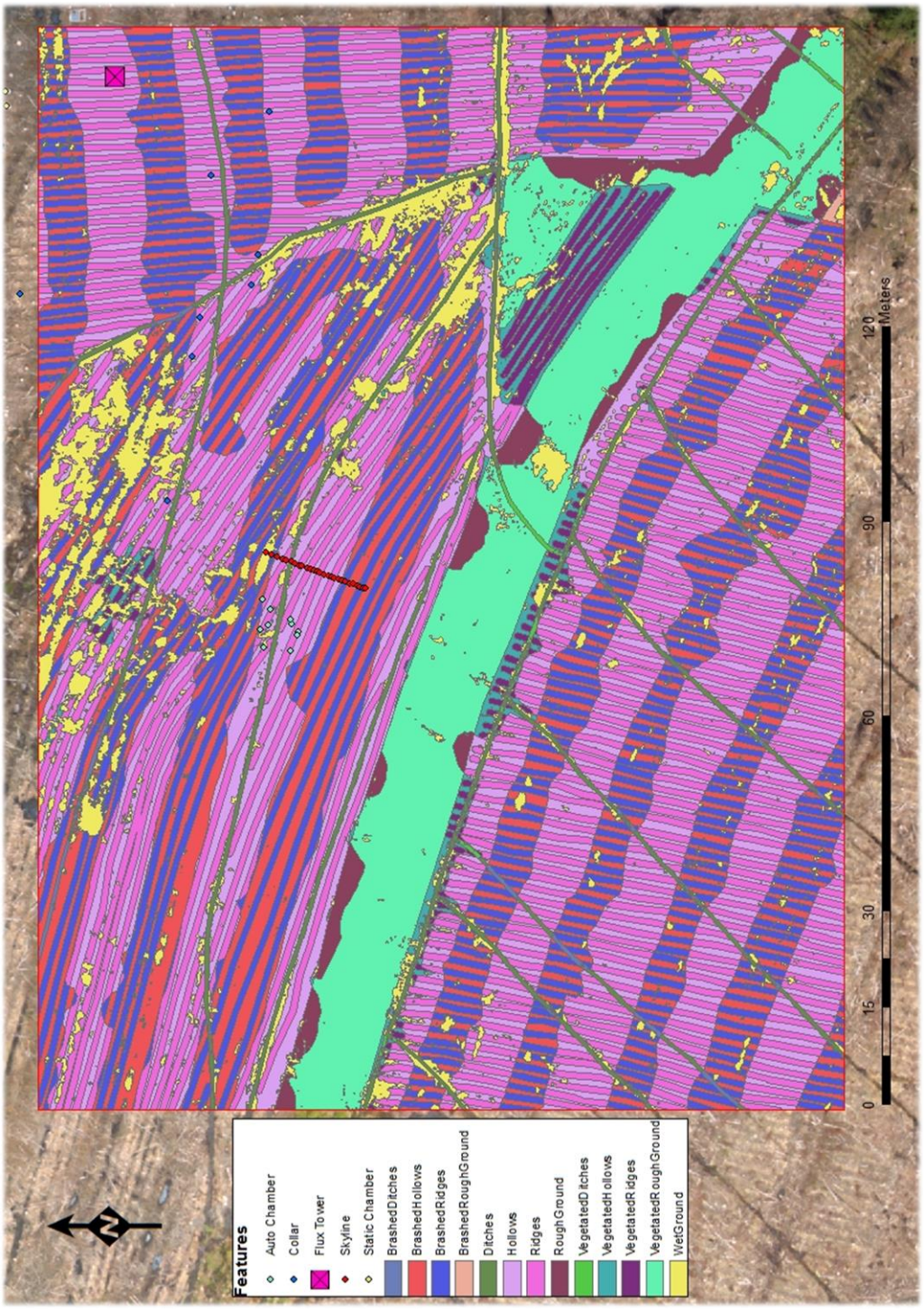

Figure 7-4: Final classification of ROI into 13 separate classes.

7.2.4.1 Classified area and percentage cover of ROI

The total area of the ROI is ~2.1 ha and the area and percentage cover of each class can be seen in table 7-2.

Table 7-2: Total area and percentage cover of each class within the ROI.

Class	Total Area (m^2)	Ground Cover (%)
BD	66.85	0.32
BH	3091.28	14.85
BR	3921.94	18.84
BRG	8.52	0.04
D	561.34	2.70
H	3540.58	17.01
R	4746.46	22.81
RG	365.50	1.76
VD	46.80	0.22
VH	291.79	1.40
VR	341.52	1.64
VRG	2203.91	10.59
WG	1625.23	7.81
TOTAL	***20811.73***	***100.00***

7.2.4.2 Classification accuracy

In order to give a level of error to the accuracy of the classification, 650 randomly placed points were created within the ROI and classified visually using the same class types of the main classification. These points were then compared against the main classification, creating an error matrix (table 7-3) that could be used to give an indication of accuracy using kappa (Ǩ) statistics (eq. 7-1). The overall accuracy was 79%, with Ǩ = 0.75, indicating a good level of agreement. However, some classes showed lower user or producers accuracies because a lot of the ridges and hollows contained brash even though they were not covered by a brash mat.

$$\check{K} = \frac{Po - Pc}{1 - Pc} \qquad (7\text{-}1)$$

Where Po represents actual agreement and Pc represents chance agreement (Weih *et al.*, 2010).

Table 7-3: Error matrix of all 13 classes (PA = Producers Accuracy; UA = Users accuracy).

Producer (what was visual observed)

User (what was classified)	BD	BH	BR	D	H	R	RG	VD	VH	VR	VRG	WG	Total	UA
BD	1	0	0	0	0	0	0	0	0	0	0	0	**1**	**1.00**
BH	0	110	0	0	1	0	0	0	0	0	0	0	**111**	**0.99**
BR	0	0	117	0	0	0	0	0	0	0	0	1	**118**	**0.99**
D	1	0	0	14	1	1	0	3	0	0	0	0	**20**	**0.70**
H	0	50	0	2	59	10	0	0	1	0	0	7	**129**	**0.46**
R	0	2	33	0	7	91	0	0	0	0	0	3	**136**	**0.67**
RG	0	0	0	0	0	0	16	0	0	0	0	1	**17**	**0.94**
VD	0	0	0	0	0	0	0	2	0	0	0	0	**2**	**1.00**
VH	0	0	0	0	0	0	0	0	6	0	0	1	**7**	**0.86**
VR	0	0	0	0	0	0	0	0	0	12	0	1	**13**	**0.92**
VRG	0	0	0	0	0	0	1	0	0	0	57	2	**60**	**0.95**
WG	0	1	3	1	1	0	0	0	0	2	1	27	**36**	**0.75**
Total	**2**	**163**	**153**	**17**	**69**	**102**	**17**	**5**	**7**	**14**	**58**	**43**		
PA	**0.50**	**0.67**	**0.76**	**0.82**	**0.86**	**0.89**	**0.94**	**0.40**	**0.86**	**0.86**	**0.98**	**0.63**		

7.2.5 Discussion and conclusions

The terrain at the Harwood Forest site was extremely challenging simply due to the amount of debris left after the clear-fell operation (figure 7-5). Although each flight only took ~13 minutes, over an hour was required to lay out and retrieve the ground control points for each survey. The full area of clear-felled forestry under investigation was larger than the section captured in this case study (~45 ha of just clear-fell), so a fixed wing UAS would potentially have been a better choice to use as UAS of that type are likely to be able to capture the entire area within a single flight (Dvořák *et al.*, 2015). However, the terrain itself would make it very difficult to land a fixed wing UAS without damage, which shows one of the benefits of using a multirotor design, as its VTOL capability meant it required a minimal amount of space to operate from.

Figure 7-5: The UAS in flight over the gas sampling towers and difficult terrain of the clear-fell area at Harwood Forest.

The actual GHG upscaling methods were investigated by other members of the GREENHOUSE project group and therefore not reported in this case study, but the intention was to use the classification results to show the microtopographical features that are important for GHG flux modelling, allowing the spatial and temporal distribution of GHG emissions to be understood. Summary results detailing the GHG measurements taken and proposed methods of upscaling the GHG emissions were presented at the EGU General Assembly Conference 2016 by members of the GREENHOUSE project (Toet *et al.*, 2016), however more research is needed before it can be said to be a robust solution as considerable differences were found between methods attempted (Toet, 2016).

Despite being a manual process, the accuracy of the classification was not as effective as expected. This was mainly due to set widths being used for certain features (e.g. ridges were set to be 1 m wide), which in fact varied a lot more than expected. Likewise, many more features were covered with brash out with the areas that were covered by brash mats, causing further misclassification. The manual classification itself was a laborious process and took several days of GIS work to complete, so identifying ways to automate the process would be required before trying to apply the method to an area larger than the ~2.1 ha of this case study.

However, a recent study by Lovitt *et al.* (2018) shows that automatic classification of microtopographic features such as ridges and hollows is possible, as they also used a multirotor UAS to survey the microtopography of a peat bog in Northern Alberta, Canada, in order to identify hummocks and hollows across the site. They pre-classified the scene to remove large features such as trees from their digital

elevation model (DEM), before creating a reference surface using a low-pass filter against their modified DEM, allowing features below this surface to be classified as hollows and above as hummocks. These microtopographical changes gave indications to differences in the level of the water table across the site, which in turn relate directly to CH_4 emissions as more CH_4 is release if the water table is at or near the surface (Lovitt *et al.*, 2018). Although Lovitt *et al.* (2018) were also unsure of the accuracy of their CH_4 flux estimates, their method of automatically classifying microtopographical features derived from a UAS seems worth pursuing further.

7.3 Experimental case study 2 – Classifying urine patches across a crop of grass being grown for silage

7.3.1 Introduction

Further collaborative research was also undertaken with a fellow colleague at SRUC (Juliette Maire) who was investigating the variability of nitrous oxide (N_2O), ammonia (NH_3), and nitrate (NO_3^-) emissions within grazed fields due to the deposition of faeces and urine from livestock. The deposition of these extra nutrients causes patches of grass within the field to appear taller and lusher, and they emit differing levels of GHG compared to other areas in the field. These emissions were being measured using static gas chambers at strategic positions within the field (i.e. over areas with and without patches), but to upscale the data and estimate the variability across the whole field, these patches needed to be mapped.

7.3.2 Aim of the case study

This experimental case study highlights how and why the UAS system was used to enable mapping of urine patches, but does not go into detail regarding the actual method of urine patch classification or the method of upscaling GHG emissions, as this research was conducted by Juliette Maire herself as part of her ongoing PhD (variations of which are still being developed for her research).

7.3.3 Methods

7.3.3.1 Aerial data and ground control point collection

The custom-built multi-rotor UAS and sensor package as indicated in chapter 3 was deployed over a field site to the South West of Edinburgh on the 6th June 2016 (figure 7-6) under full sun conditions. Approximately 5 ha of the field was surveyed at 35 m AGL to provide imagery at ~1 cm GSD with an image overlap of 60 % and

side overlap of 80%. The speed of the UAS was limited to 2 m/s to allow for the integration time of the cameras. Four flights in total were required to cover the entire area, and as the area sloped from North-West to South-East, two take off positions were used to ensure a more even GSD across the site. 12 GCPs were used (the collars of each of the static gas chambers) to provide georeferencing and were measured using the Piksi (Swift Navigation, San Francisco, USA) real-time kinematic GPS with an expected accuracy of ±8 cm.

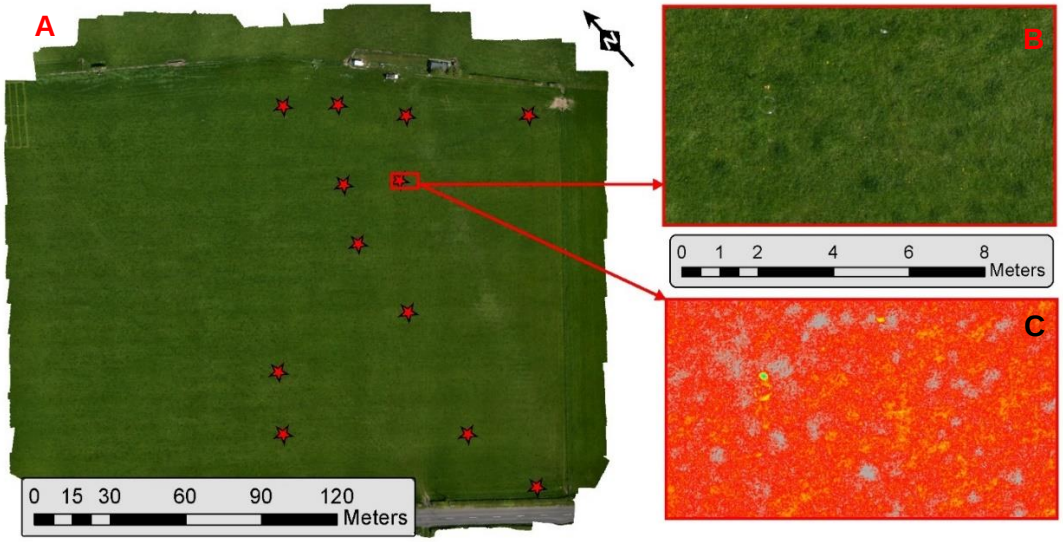

Figure 7-6: (A) Overview of entire field surveyed showing GCP points (red stars) (West of Edinburgh, Scotland, June 2016); (B) detail inset showing urine patches (darker green) and one of the gas sampling rings used as GCPs; (C) NDVI output of the same detailed inset, showing urine patches more clearly (grey/white).

7.3.3.2 Image processing and orthomosaic co-registration

Image pre-processing was carried out as indicated in chapter 3 however normalisation was not performed. The data was processed using Agisoft Photoscan (v1.2.5; Agisoft LLC, St. Petersburg, Russia), using the high settings (image alignment highest; dense cloud high quality; depth filtering mild) and optimised using the 12 GCPs dispersed throughout the scene surveyed (using an estimated accuracy of 0.15 m). A linear red, green, blue (RGB) orthomosaic, a digital surface model (DSM), a linear near infra-red (NIR) orthomosaic, and an orthomosaic enhanced for improved visually clarity (VIS) were produced. Co-registration between the different orthomosaics was visually checked and appeared to be effective and so was left as originally processed.

7.3.4 Urine patch detection method and results

The method for identifying urine patches within the field used an unsupervised pixel-based classification method employing K-means clustering (Jain, 2010), and was created using a custom-made algorithm within the open source statistical analysis program R (R Core Team, 2018). Five 15 x 15 m (225 m^2) sections of the field were processed using this algorithm as a proof of concept, resulting in the effective detection of urine patches (figure 7-7), allowing upscaling of urine patch N_2O emissions across the scene surveyed.

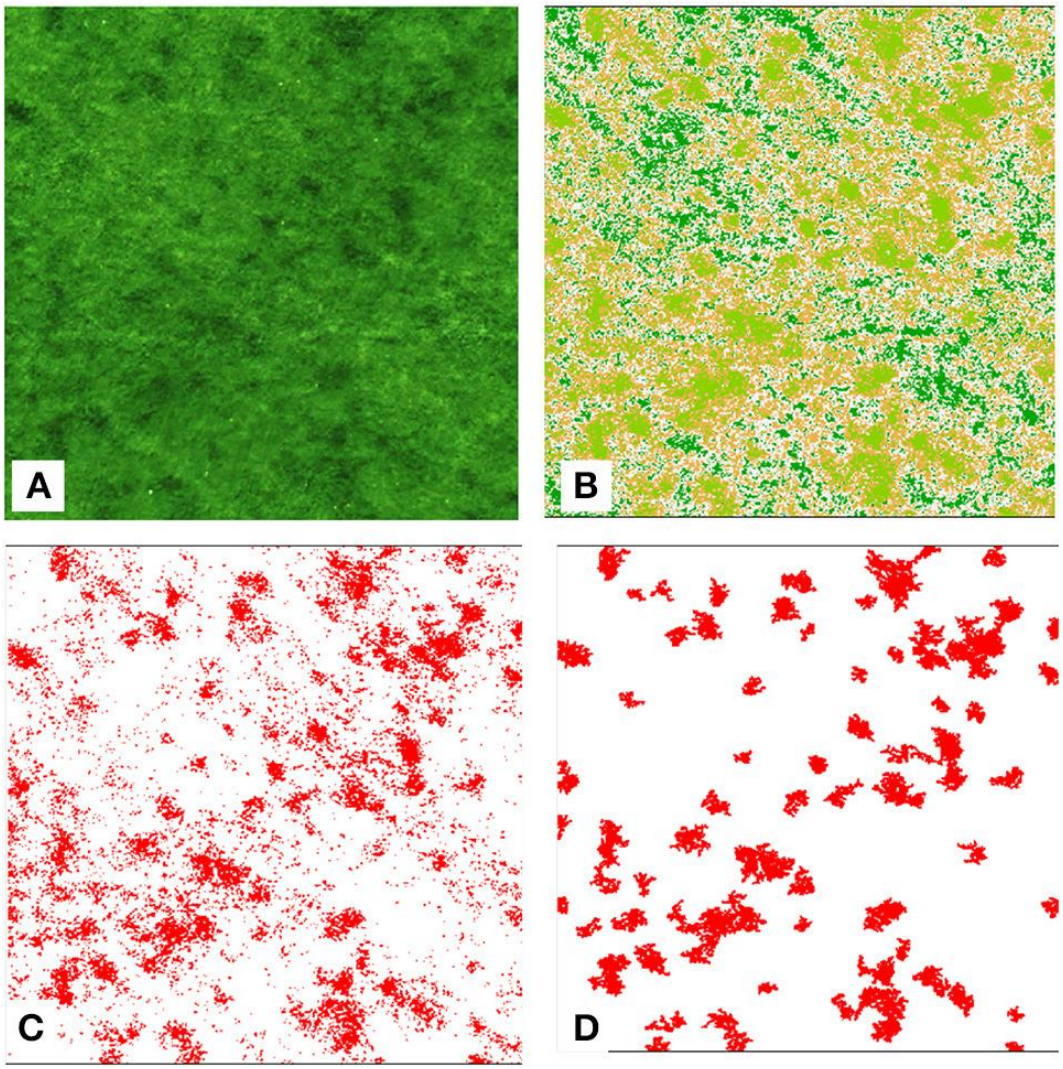

Figure 7-7: Examples of results from urine patch detection script on a 15 by 15 m square of grassland; (A) RGB image; (B) K-means clustering results; (C) selected cluster; and (D) patch isolation results (Maire et al., 2018).

The algorithm and method for upscaling GHG emissions were devised by Juliette Maire as part of her ongoing PhD project, so full details of the process and results

are not indicated in this case study. However, a full explanation of the methods employed, and results obtained can be seen appendix H, as the successful results of this exploratory analysis were published in Frontiers in Sustainable Food Systems (Maire *et al.*, 2018).

7.3.5 Discussion and conclusions

Identification of livestock waste deposition has traditionally involved large amounts of manual work, requiring 24-hour surveys to observe the livestock and map any deposition as it occurs (Auerswald *et al.*, 2010; Dennis *et al.*, 2011). Alternatives to this require the use of devices fitted to the livestock themselves, such as GNSS collars and thermal sensors to detect and note the positions of each urination event as the livestock move around the field (Betteridge *et al.*, 2010), or flow rate sensors to identify the volume and urinary nitrogen concentration of each urination event (Misselbrook *et al.*, 2016).

These methods can supply valuable information on urination events but are only applicable to small scale studies due to their costs and difficulty in setting up, so being able to view at a wider scale is required. Remote sensing of urine patches using a UAS should be able to provide this, as Dennis *et al.* (2013) demonstrated. However, the UAS used by Dennis *et al.* (2013) was piloted manually and image analysis was also conducted manually using RGB images directly off the camera (i.e. not orthophotos). Their results were promising, as the method was much faster and allowed more precise measurements of the distribution and shape of urine patches compared to traditional manual methods.

The results of this experimental study also showed promise (see Maire *et al.*, 2018) and the method itself is an evolution of that initiated by Dennis *et al.* (2013). With further refinement of the algorithm or use of other image analysis techniques such as OBIA, it should prove effective in allowing the rapid detection of the development of urine patches and the deposition of dung over field scale areas. However, although this study was focused on GHG emissions due to deposition of livestock waste, it also highlights the multidisciplinary advantages that using a UAS can bring to grassland management.

For instance, the patches being monitored within this study could also be of benefit within precision agriculture as there would be no need to apply extra fertilizer to these areas. Therefore, the data could be used as part of a prescription map for variable rate fertilisation (a map detailing the required fertilizer input), thereby reducing input costs for farmers (Roten *et al.*, 2017). Likewise, if attempting to mitigate the GHG emissions from these patches, the locations of each patch could be used to enable targeted application of urease inhibitors (reducing NH_3 emissions), as Bates & Quin (2013) highlighted using small unmanned ground vehicles (UGV).

Other areas could include the identification of optimum livestock stocking density (Dennis *et al.*, 2011) and acceptability of the pasture to livestock could also be modelled, as dung patches are often avoided by cattle (Dittrich & Helden, 2012). Finally, as these dung patches are often avoided by livestock, they therefore grow taller than the rest of the sward and can become home to different assemblages of arthropods. Knowledge of the size and distribution of these patches would be of great interest to ecologists, enabling them to better understand the diversity of grassland ecosystems (Dittrich & Helden, 2012).

7.4 Concluding remarks

This chapter shows further evidence for the 4th objective of this PhD project as both exploratory case studies show the potential utility of the UAS system as a tool to allow the upscaling of GHG emissions, though the identification of microtopographical features from varied land uses. Undertaking these studies also showed areas where the UAS system could be improved. For instance, for the urine patch detection study, two take off positions were used to ensure a more even GSD of the imagery captured, due to the field sloping relatively steeply (there was ~20 m difference in ground height from one side of the field to the other). If the UAS system had been equipped with the facility to actively track the terrain beneath it (e.g. though the use of a laser ranger finder) then this would not have been required. Although a minor issue for this particular study, it could be of use for future studies as it would further reduce the complexity of capturing imagery across undulating terrain (as is often encountered).

Likewise, the case study surveying the area of clear-felled forestry highlighted the difficulty of conducting surveys across uneven and broken ground. The total flight time required to capture imagery of ~30 ha of clear-felled forest was less than 45 minutes, but more than 3 hours was required to lay out and retrieve the GCPs. If the UAS had been equipped with a high accuracy RTK GNSS then this step may not have been required, resulting in a considerable saving of time. Finally, these studies also highlighted other potential applications where the UAS and sensor package could be applied, indicating that the UAS could provide utility to multiple areas of land-use management.

Chapter 8. Discussion and conclusion

This thesis has demonstrated the creation and testing of a UAS and its sensor package, which could then be deployed for a number of different land-use scenarios. Whenever embarking on a project with the intention of using a UAS, one must always remember that the aircraft itself is just an aerial platform that enables the capture of aerial data and creating a UAS from scratch should not be seen as a barrier to entry. UAS are a rapidly developing technology and the market for pre-built 'ready-to-fly' (RTF) UAS has expanded considerably since this project began, with over 2 million consumer (referred to as personal in figure 8-1) and 174,000 commercial UAS estimated to have been sold worldwide in 2016 (Standage, 2017; Garrett *et al.*, 2018; figure 8-1).

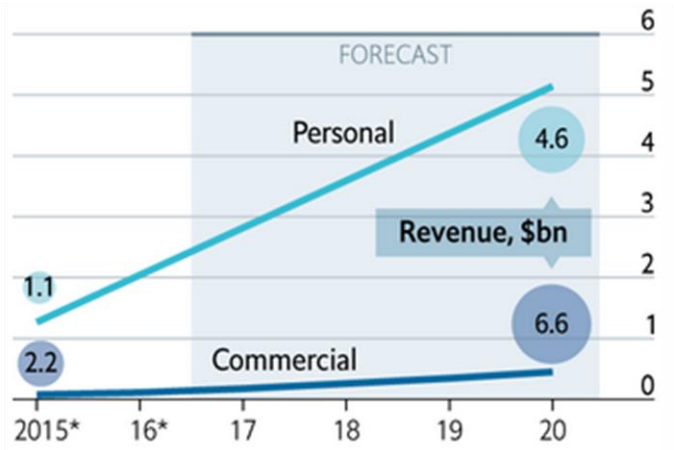

Figure 8-1: Number of UAS manufactured (in millions) by year; 2015 and 16 are estimates 2017-2020 are forecasts (Standage, 2017).

Consumer UAS will include a large number of very small aircraft that are essentially toys, however companies such as Da-Jiang Innovations (DJI), who currently dominate the consumer drone industry (Standage, 2017; Bateman, 2017), produce a wide range of effective RTF multirotor UAS equipped with built in cameras that can perform a variety of roles, with aerial videography as their main selling point, but with the capability to also perform aerial photography and therefore surveying as well. Other companies such as SenseFly and QuestUAV are more solidly in the commercial market, producing both multirotor and fixed wing designs, with far more emphasis on their ability as survey platforms to support industries such as agriculture, construction and mineral resource extraction.

The evolution of consumer grade UAS has allowed many researchers to access UAS technology and apply it to different research areas, such as Wei *et al.* (2017) using a DJI Phantom 4 Pro to monitor structural changes to agricultural terraces in Southwest China, and Hill *et al.* (2016) using a DJI Phantom 3 Pro to survey for the invasive plant yellow flag iris (*Iris pseudacorus* L.) in British Columbia, Canada. The author of this thesis has also used a DJI Phantom 4 (DJI, Shenzhen, China) to provide aerial data for undergraduate student projects investigating the encroachment of bracken on rough grazing land (figure 8-2a) and the quality of turf grass on a golf course (figure 8-2b), so their utility to a wide variety of research topics is very evident and their ease of use and excellent quality cameras (often better than those in this project) makes them ideal platforms in certain situations.

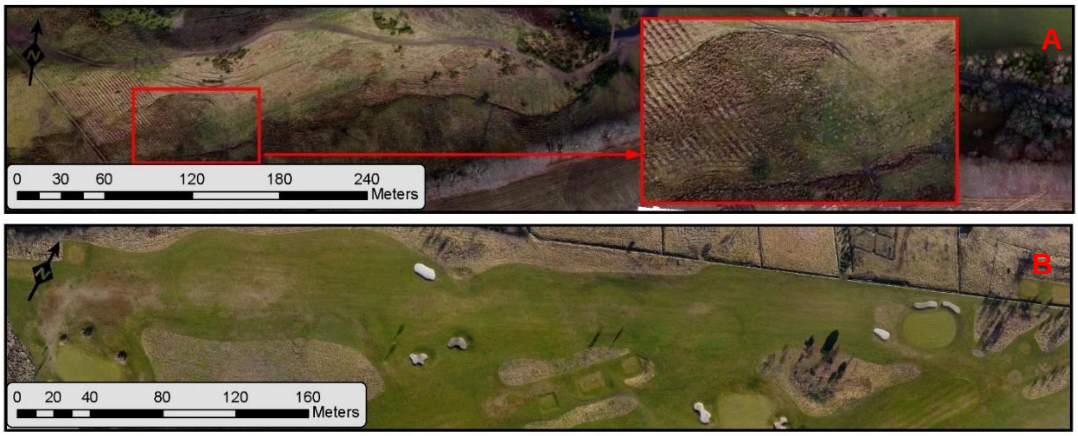

Figure 8-2: Example data collected for undergraduate student projects; (A) identification of bracken over upland rough pasture (West of Edinburgh, Scotland, February 2018); (B) evaluation of turf quality over a golf course (South-West of Cupar, Scotland, February 2018)

8.1 Custom built vs consumer RTF UAS

Building from scratch does however have its advantages, with the most obvious being a better understanding of how all of the components of as UAS work together and therefore being able to make your own repairs should something go wrong, which would be useful if working in remote places (Duffy *et al.*, 2017; Garrett *et al.*, 2018). Sensor integration is another area where working with a custom built UAS (using an open source autopilot) has its advantages over an RTF UAS, as RTF UAS often have tightly integrated sensors to optimise the design of the aircraft, which is part of what makes them appealing to operators. However, this can make the deployment of extra or different sensors not necessarily designed for that model of aircraft more difficult, which was experienced by the author of this thesis when

assisting with the setup and initial testing and operation of a UAS to be used for the ATEC project (Advanced Technologies for Efficient Crop management).

ATEC is a joint project between the University of Edinburgh and SRUC and "*aims to enhance the sustainable and efficient production of two major UK crops – wheat and potato*" (ATEC, 2018). This ongoing project utilised a DJI M600 heavy lift hexacopter (DJI, Shenzhen, China) with an AUW of ~14 kg, that was customised to carry an array of sensors including a very high-resolution digital camera (42 megapixels), a nine-band multispectral camera, a thermal camera and a spectrometer. However, some difficulties were encountered with the integration of these sensors with the autopilot (to allow triggering), which although eventually resolved, would have been relatively easy to integrate with the 3DR Pixhawk autopilot used for this PhD project. Geofence restrictions now also exist for aircraft using DJI autopilots, which while practical from a safety aspect as the geofence essentially stops the UAS being used in areas designated as no-fly zones (e.g. around airports, prisons and power facilities; DJI, 2016), requires extra steps to unlock the location (i.e. direct communication with DJI; DJI, 2018b). This could be a hinderance for some UAS operators, but is something that is not currently implemented (and could be circumvented) when using an open source autopilot (Garrett *et al.*, 2018)

The ability to add ancillary sensors to improve the autopilot itself is also more accessible for custom built UAS using open source autopilots, as features such as rangefinders (LiDAR/Sonar) can be added relatively easy (Ardupilot, 2016c), allowing terrain following functions within missions (Ardupilot, 2016d) or object avoidance (Ardupilot, 2016e), which can be of great benefit if surveying over undulating ground or within confined environments (Raimundo *et al.*, 2017). Some of these features are not always available in RTF UAS, so if required as part of a project then this should be taken into account. The differences in price between custom built and RTF UAS is difficult to quantify as considerably more time is required to both construct and test a custom-built aircraft, however if time is available then this author would recommend taking the custom build route in order to learn more about the aircraft they intend to operate, and potentially save some money at the same time. Whichever route is taken, the main point to remember is that the UAS must have the endurance and payload carrying qualities suitable for the aims of the project.

8.2 Aircraft size and weight

The size of the aircraft used for this project was somewhat larger than was necessary to carry the intended sensor package, however this was to enable the integration of other sensors and hardware at a later date. Size is an important factor to consider if working in remote areas that can only be accessed by foot, as in those situations a smaller UAS would definitely be easier to transport compared to the one designed for this project (see Duffy *et al.*, 2017 for a guide to working in varied, remote and challenging locations). The size of the aircraft also denotes its visibility and in order to be compliant with CAA VLOS regulations, as the UAS must be within unaided visual site at all times, which for smaller aircraft (such as the DJI phantom) may not be up to the recommended maximum of 500 m (CAA CAP722, 2015). The larger size of the aircraft designed for this project is easily visible from 500 m and potentially further, which could allow for an extension to the VLOS horizontal distance restriction if an effective safety case were to be submitted to the CAA (CAA CAP722, 2015).

The AUW of the aircraft is directly linked to the regulations governing its use and staying below 7 kg AUW reduces the regulatory burden as for heavier UAS, such as that used for the ATEC project, prior approval from air traffic control is required if wanting to operate within controlled airspace (The Air Navigation Order 2016). If the operator has not undergone an NQE certification course to become a CAA approved UAS operator for a < 20 kg aircraft, then the likelihood of this approval being gained is slim (as was experienced by the UAS operators on the ATEC project). This means that large areas within the vicinity of airports cannot be operated within, as the control zones of many larger airports extend for several km and are valid from surface level upwards (figure 8-3).

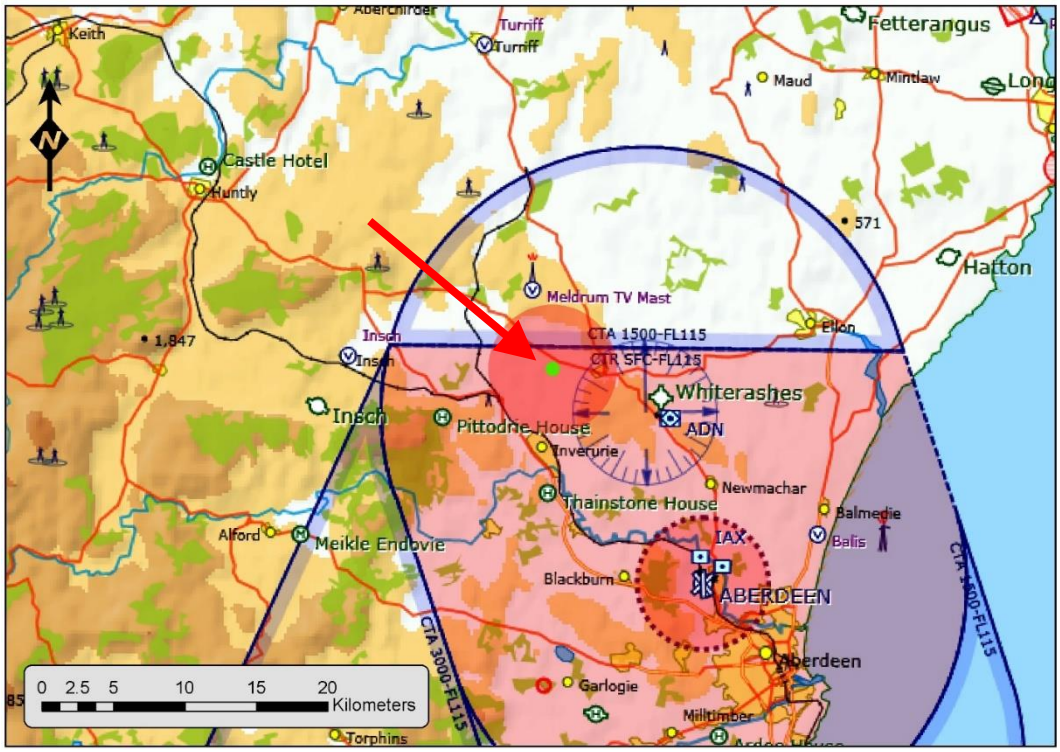

Figure 8-3: Example VFR chart indicating an intended operating site (red arrow, green point) that is within Aberdeen airport control zone (pink shading), which is class D airspace, from surface level to 11,500 feet (amended from SkyDemonLight, 2018).

8.3 Regulations, certification and insurance

As indicated right at the beginning of this thesis (chapter 1), the regulations governing UAS operation are flexible in relation to their use for research related projects, and operators don't necessarily need to be approved operators by the CAA. However, as Cunliffe *et al.* (2017) point out, many research collaborators (e.g. landowners over whose land you intend to operate from) now require CAA approved operators who are insured in case of failure of the UAS during flight. Gaining certification will also educate the operator in the safe operation of the aircraft, as most NQE courses will have a ground school element that instructs in areas such as interpreting visual flight rule (VFR) charts, identification of ground and aerial hazards as well as the regulations directly surrounding UAS operations.

The author of this thesis was fortunate to be able to attend an NQE course through funding supplied by SRUC from the Scottish Funding Council Knowledge Exchange program. It entailed two days of ground school training, with an exam to ensure the basics had been learnt, plus a flight exam to ensure that the safety aspects of UAS operation (identification of airspace and hazards both on the ground and in the air)

were being put into practise, as well as the operator being able to demonstrate safe operation of the UAS itself (i.e. pilot competence). Once completed and certification has been achieved, an operations manual detailing how the company responsible for UAS operations (in this case SRUC) will operate and maintain their aircraft needed to be submitted to the CAA to enable accreditation and obtain a Permission for Commercial Operation (PfCO).

As Cunliffe *et al.* (2017) also experienced, the operations manual is an extensive document and takes quite some time to complete (see appendix E) but was successfully created and a PfCO awarded by the CAA on 8th May 2016 (CAA ID 2086; CAA CAP1361, 2018). The advice of Cunliffe *et al.* (2017) would have been most welcome if the study had been published a year earlier, but their study is definitely worth investigating to gain advice and insight on obtaining UAS certification, creating an operations manual and the ancillary documents that go with it, although recent regulation changes brought about by the Air Navigation Order 2016 and The Air Navigation (Amendment) Order 2018 need to be taken into consideration.

Despite the amount of time it takes to complete, obtaining a PfCO is a worthwhile endeavour as once obtained, the minimum operating distance to congested (i.e. urban) areas is reduced to just 50 m (compared to 150 m), making work near to such areas possible. It also allows (and requires) insurance to be obtained, which can be upgraded to include the aircraft and sensors and could be invaluable should expensive hardware be used. Finally, as a fully certified, insured and CAA approved UAS operator, it can allay the fears of landowners or other project collaborators as well as allow the possibility for commercial work should it arise.

8.4 Sensors and image processing

The sensor package created as part of this project was effective in some areas but certainly not ideal. They were selected because they were very low cost (< £100 for three cameras – one was damaged during modification – the long pass filter and the aluminium housing), lightweight and known to be modifiable, allowing the capture of NIR wavelengths of light, as well as use scripting via CHDK to capture RAW imagery. However, they had a very small sensor size (1/2.3 inch) which gave them poor results in low light conditions (essentially whenever it was vaguely cloudy), making the use of fixed settings for ISO and shutter speed unreliable as the images

would often be under or over exposed, especially during mixed environmental conditions (aperture was fixed and could not be altered).

The use of the CHDK KAP UAV script resolved this issue, allowed images to be captured on command from the autopilot, reduced focusing time delay (as focus was set to infinity), which allowing effective image capture, as other studies have also reported (Glendell *et al.*, 2017; Müllerová *et al.*, 2017a; Szantoi *et al.*, 2017). However, as the ISO and shutter speed would be adjusted during flight, further issues were encountered as these settings could differ from image to image within a single flight, with any image having an ISO value of 200 or higher being considerably nosier, reducing image clarity (i.e. loss of fine detail). The addition of the 585 nm long pass filter made this situation worse for the modified camera, as the filter reduced transmission of light (by ~10 %) and excluded blue and green wavelengths, resulting in the camera typically selecting high ISO values to gain desired image exposure.

The use of RAW imagery also produced some challenges as these cameras, although capable of producing it, are not designed to do so. This meant that image capture was slow (5~6 seconds per image), requiring the speed of the UAS to be reduced to allow effective image overlap and thus reducing the area that could be surveyed, especially when operating at lower altitudes. For the small trial areas (1~2 ha) surveyed in chapter 4 and 5 this was not an issue but would mean that this system would not be suitable to implement effectively over larger areas at low altitude. The RAW files produced were also considerably larger than JPG imagery, potentially creating an issue if storage space is limited, and require further post processing to be useable.

The post processing routine was required to first fix bad pixels within each image before converting the RAW image into a linear 16-bit TIFF file. The conversion process used pre-made dark images to reduce dark current signal noise that would increase due to higher ISO and lower shutter speeds (Verhoeven *et al.*, 2009) and could be altered to produce either linear TIFF images with all white balance set to a value of 1 or enhanced true colour images with improved highlights. The enhanced images were superior to their corresponding JPG image allowing more effective visual analysis, as Verhoeven (2010) also described.

However, the TIFF images produced were often still quite noisy despite the correct methods used (especially the modified camera), so smoothing of the imagery was performed to rectify this. This step may have inadvertently reduced the effectiveness of later image classification, as the smoothing process could reduce the textural quality of the images (the change in frequency and pattern of tones; Blaschke *et al.*, 2014), making textural measures within OBIA classification less effective. Textural measures were investigated as part of the classification in chapter 5 but were found to be ineffective in aiding the discrimination between weeds and potato vegetation, and this could well have been due to the image smoothing.

The final step was to correct distortion in the TIFF file due to lens of the camera (as it was relatively wide angled) and crop the edges of the image to reduce the effects of vignetting (image darkening in a circular gradient from the image centre to its borders; Lelong *et al.*, 2008; Lebourgeois *et al.*, 2008). The corrections performed were adequate to reduce the worst areas of vignetting (the image corners and borders), however, to correct fully for the effects of vignetting, flat field correction would be required as demonstrated by Berra *et al.*, (2017). However, this method may not have been practical for this project as flat field correction is only valid based on the camera settings used to identify it (Lelong *et al.*, 2008), whereas the settings of the cameras used in this project could change between successive image captures. The effects of vignetting were however further reduced through the process of creating the final orthomosaic of the scene, as Agisoft Photoscan only uses a portion of each image (towards the centre of the image) to create the final mosaic, which will vary depending on the amount of image overlap (figure 8-4).

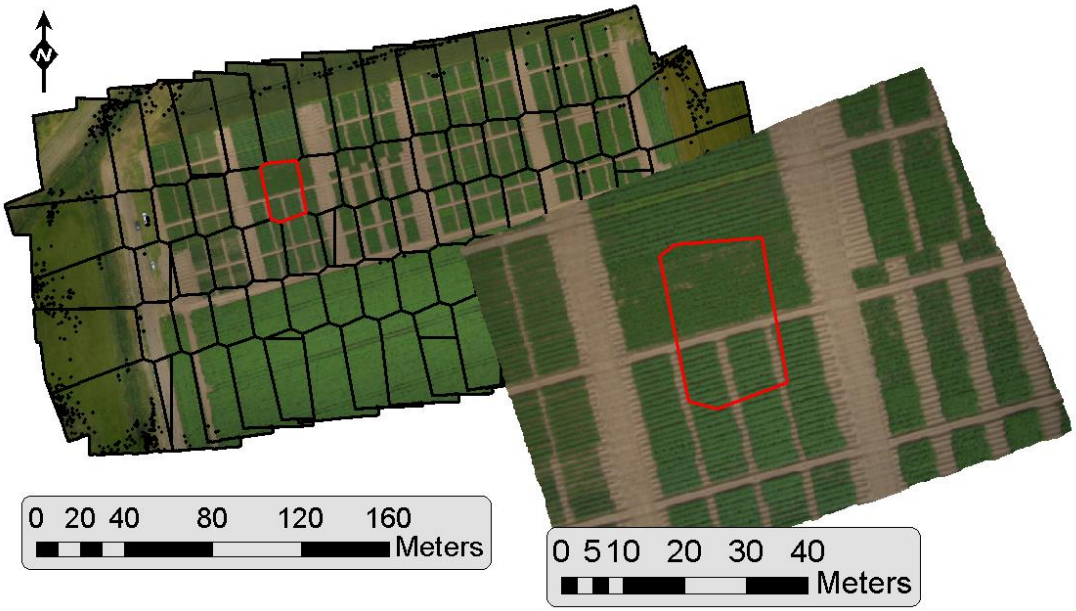

Figure 8-4: Example stitching seams from Agisoft Photoscan, showing inset orthophoto with proportion of image used in the final mosaic (red polygon).

The true spectral qualities of the cameras were not fully tested as they were not directly compared to other calibrated sensors (e.g. spectrometer measurements). Therefore, the effects on spectral quality (positive or negative) of the image processing routine are not known and further experimentation would be required before a judgment could be made. The use of linear TIFF images created from RAW imagery should however provide a more quantitative measure compared to using JPEG imagery alone (Verhoeven, 2010; Pauly, 2014), and if the imagery had been calibrated against known reflection surfaces (e.g. using the empirical line method; Smith & Milton, 1999), then the sensor package could potentially have been used as a true multispectral sensor as Berra *et al.*, (2017) and Pauly (2016) have demonstrated.

The image brightness normalisation routine indicated in chapter 3 and used in chapter 5, followed the method of Troscianko & Stevens (2015) and appeared to be effective but again was not fully tested by comparison with other sensors. There are likely to have been errors in the use of this method as the camera settings could change during the flight, and therefore the image taken of the calibration target at take-off and landing (if illumination had changed considerably) may not have had the same settings as the images during the flight. The calibration target itself was also most likely not a Lambertian surface (scattering reflected light equally in all directions; Troscianko & Stevens, 2015), so calibration would vary depending on the

time of day and angle of the sun. Troscianko & Stevens (2015) method was essentially designed to calibrate single stills of scene to remove illumination effects between different captures and allow measurement of features important to visual ecologists. However, it was specifically geared towards the calibration of linear 16-bit TIFF images extracted from RAW files, so was appropriate to use for this project but would require further testing to validate its effectiveness.

8.5 Diversity of application

From the literature review in chapter 1 an indication of the variety of scientific areas and different land-use types where UAS have been used can be seen. Over the course of this PhD project the author has also experienced the applicability of RS using the UAS designed for this this project for a variety of different research applications. For instance, simply providing high resolution backdrop imagery of an area being investigated can enable more context to be given to projects, such as that provided to SRUC masters students investigating possible contamination from lead mine tailings (figure 8-5a) or capturing the moment that a reservoir had been drawn down to its minimum water so that the bathymetry of the reservoir could be seen (figure 8-5b). The latter (in collaboration with Roseanne McDonald from the Centre for Ecology & Hydrology) would have been an event only observable for a very limited period of time, again showing the utility of using UAS as they can be deployed at short notice whenever environmental conditions are suitable (Zhang & Kovacs, 2012; Shahbazi *et al.* 2014).

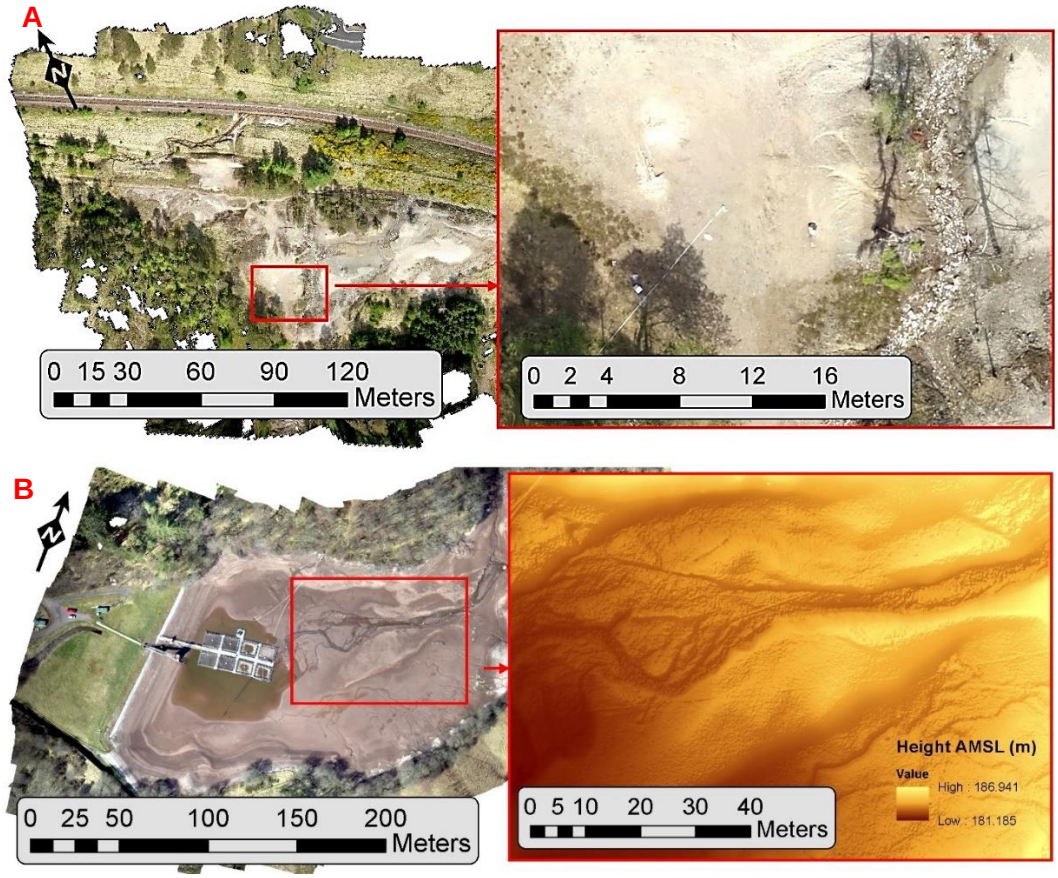

Figure 8-5: (A) Overview and detail inset of study lead mine tailings near Tyndrum, Scotland (June 2016); (B) Overview and detail inset (showing DSM) of Waltersmuir damn near Stirling, Scotland (April 2016).

Even though the sensor package designed for this project was not ideal, simply the ability to generate aerial images with good visual clarity can make a big difference to researchers who typically take all their measurements from the ground. For instance, during initial testing of the UAS and sensor package, different agricultural trials were investigated using the pixel-based thresholding method of identifying vegetative fraction (eq. 8-1) indicated by Torres-Sánchez *et al*. (2014). Both the early development of winter wheat (see appendix F) and oil seed rape (figure 8-6) trials were evaluated and although not fully explored or expanded on, experienced trials officers who were overseeing the trials were immediately able to get a better understanding of the condition of their trial plots simply from visual observation of the aerial data.

$$VF = \frac{Pixels\ classified\ as\ vegetation\ (in\ a\ deliminated\ area)}{Total\ pixels\ (in\ a\ deliminated\ area)} * 100 \qquad (8\text{-}1)$$

Where VF is the vegetative fraction, the percentage of green vegetation per unit of ground surface (Torres-Sánchez *et al*., 2014).

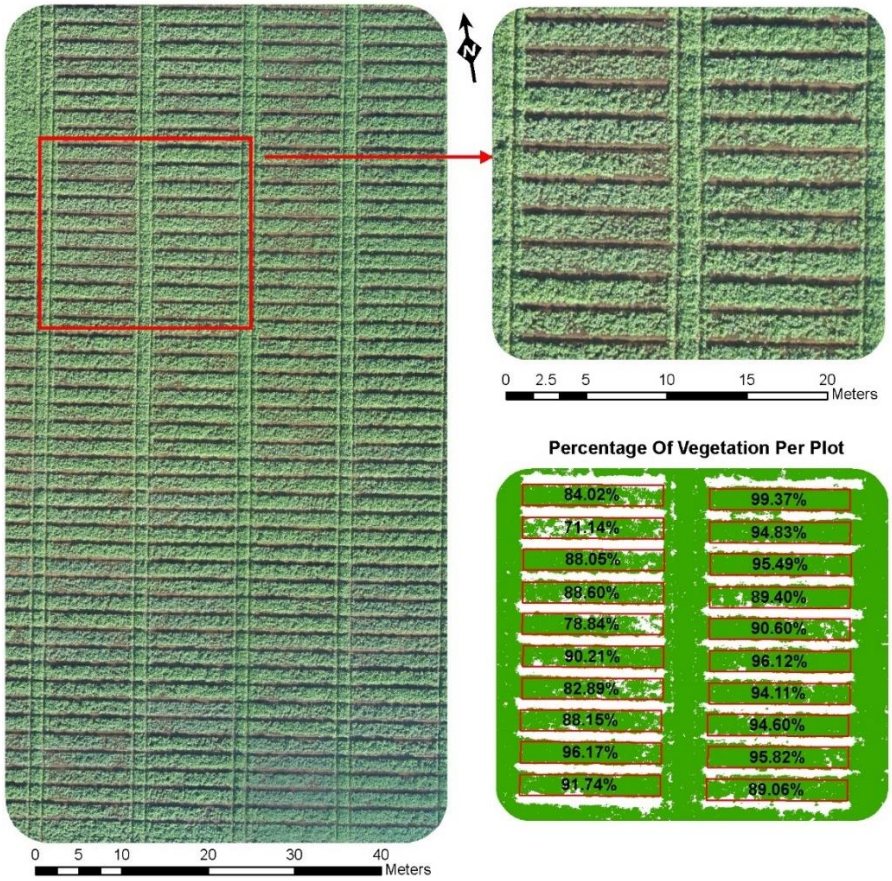

Figure 8-6: Example of identification of oil seed rape canopy cover, the vegetative fraction (West of Edinburgh, Scotland, November 2015).

Similarly, the late development of weeds within an infield trial of winter wheat was also explored (figure 8-7) and again got a positive reaction from the experienced trials officers involved. This indicated that the UAS and its sensor package could be useful for a variety of precision agriculture applications, and so led onto the two case studies looking at potatoes.

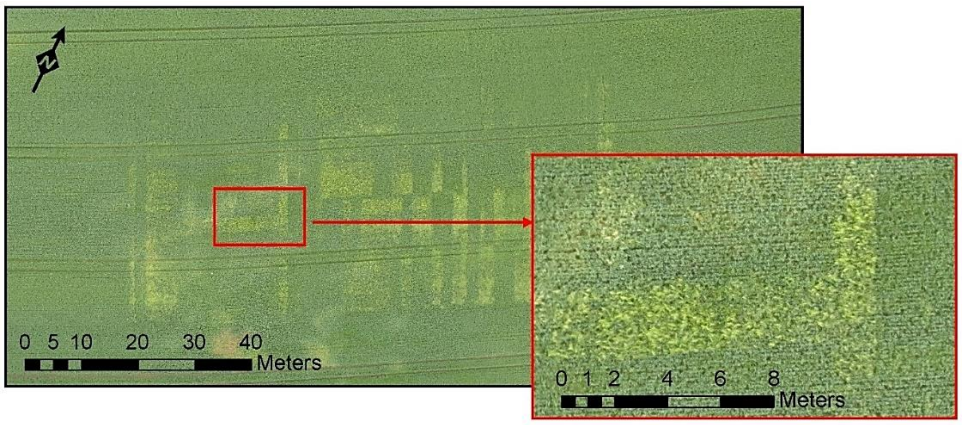

Figure 8-7: Example imagery of Brome (Bromus sterilis) growing through winter wheat within an infield trial system (North-West of Edinburgh, Scotland, June 2015).

Throughout this project the UAS system and its sensor package has been applied to a relatively diverse range of land-uses that can be found within Scotland, including agricultural crop trials, grassland, forestry and riparian. These are some of the key areas for SRUC's research aims but by no means all of them, as SRUC research aims include all rural land-use types within Scotland, including more upland areas such as moorland and peatbogs. Sadly, not all areas could be covered within this PhD project, but the general utility of the UAS system and its sensor package (as shown by the variety of applications already covered within this project) means that it could well be applied to any land-use area.

8.6 Objectives summary

8.6.1 1st Objective - Identify, assemble and test a sensor package that can be applied to a variety of land use areas that are key to SRUC research aims.

The creational aspects of this objective were covered in the first and second chapters, and showed that a very cost effective, broad-band multi-spectral sensor can be created. However, during its application across the remaining chapters its faults were also revealed. Firstly, the cameras were being coerced into operating in ways they were not meant to (the capturing of RAW imagery) and were therefore slow to operate. This imposed limitations to flight planning (e.g. reducing flight speed), meaning that the UAS system would cover less area of ground than it otherwise could. Secondly, the cameras had poor low light ability due to the very small size of the sensor within each camera and the compact design of the lens. This made getting reliable image exposures more difficult without the use of the CHDK script to vary shutter speed and ISO, which in turn made these cameras less

effective to be used for quantitative spectral measurements, as getting a reliable calibration would be difficult.

Other researchers have used modified COTS cameras effectively (e.g. Pauly, 2016; Sankaran *et al.*, 2017; Rasmussen *et al.*, 2018; Wan *et al.*, 2018) and some have shown how they can be effective, calibrated, broad band multispectral sensors (Berra *et al.*, 2017). Due to their broad band nature they are not as effective as narrow band multispectral sensors for spectral analysis, the very high resolution of COTS cameras, which is typically much higher than that of narrow band multispectral sensors (Pena *et al.*, 2015; Pauly, 2016), gives them a larger image footprint, allowing for more expensive surveys. It also makes them more effective for creating crop surface models and detecting fine details, and therefore aiding in areas such as plant disease detection (Nebiker *et al.*, 2016; Pauly, 2016, Rasmussen *et al.*, 2016). Ultimately the quality of the cameras used in this project were not all that could be desired, however their cost (~£100) was considerably cheaper than any alternatives at that time, especially if compared the Parrot Sequoia (Parrot, Paris, France; ~£3,000), which is one of the cheapest narrow band multispectral cameras that has recently become available to purchase. Therefore, the 1st objective of this project was met, but ideally higher quality cameras should have been acquired.

8.6.2 2nd Objective - Determine the UAS requirements of key SRUC research aims, and design, build and test an appropriate UAS that can accommodate the sensor package.

The design ethos for this projects UAS was to ensure that it could; a) carry the sensor package that had already been created; and b) be as flexible as possible for carrying other sensors or equipment in the future, up to an AUW of 7 kg. This practically mandated the use of a multirotor type of airframe, as its ability to work within contained areas and fly both very low and slow would work better with the sensor package and give it far more utility compared to a fixed wing design. A fixed wing design would have given far more endurance (Dvořák *et al.*, 2015), however at a potential AUW of 7 kg, such a design would have also needed extra ground equipment to get airborne (e.g. a catapult launcher).

Creating a quadcopter design with larger motors and propellers would have increased the endurance of the UAS (perhaps up to 20 minutes or more), however

the security given by the extra motors of the octocopter were favoured due to its potential future application with more expensive sensors. In total ~27 hours of actual flight time were logged during this project (144 individual flights), and no significant issues were encountered (i.e. hardware failures), indicating that it is a robust design. However, its physical size does reduce its practical use in locations that cannot be easily accessed with a vehicle (Duffy *et al.*, 2017), which could be a limitation for some of SRUC's aspirations for environmental work in more remote locations. Overall, the design, build and application of the UAS was successful, meeting the aims of the 2nd objective, and the UAS is still in use to this day.

8.6.3 3rd Objective - Determine software requirements linked to sensor and data requirements, and design appropriate data processing workflows.

As the sensors used in this project were producing RAW imagery, they had to be converted into a more useable form for further analysis. This was achieved through the use of a custom script, to both convert the images into linear 16-bit TIFF files, whilst attempting to correct areas of noise (e.g. bad pixels, dark current and distortion). Although a bit slow, this process was fully automated and gave data sets that were more useful for further analysis than the native JPG imagery from each camera alone. This area of imager pre-processing was successful, except that the smoothing steps may have reduced the textural quality of the images, reducing the ability to use that aspect effectively for later image classification.

The processing of the converted images into orthomosaic datasets using photogrammetry software based on SfM techniques (e.g. Agisoft Photoscan) was a semi-automatic process that is the preferred method in use by many researchers using UAS (e.g. Bendig *et al.*, 2015; Jensen & Mathews, 2016; Müllerová *et al.*, 2016). The main area of improvement that would make the process almost completely automated would be the ability to capture imagery with very high accuracy GNSS information, as this would likely have negated (or reduced) the use of GCPs to allow effective georectification. Some researchers have already shown that this is possible (Du *et al.*, 2017; Forlani *et al.*, 2018; Tomaštík *et al.*, 2019) and some of the latest commercially available UAS have this facility built, such as the DJI Phantom 4 RTK (DJI, Shenzhen, China), however the cost of such systems is very high (~£5,000). This could be a price worth paying however, as the precision

given would not only reduce human operator time processing the imagery, it would also reduce the time required in the field to deploy and retrieve the GCP.

Analysis and classification were performed using a mixture of pixel based and OBIA techniques, along with modelling using GIS software. As Blaschke, 2010 and others (Kelcey & Lucieer, 2013; Torres-Sánchez *et al.,* 2015) have indicated, OBIA image analysis is the preferred method to use for very high resolution imagery, due to the spectral changes that can be seen at this level of detail resulting in 'salt and pepper' noise if single pixels are analysed independently. The other main advantage of OBIA software is the ability to combine several data layers at the same time (e.g. orthomosiac, height model and thematic layers, such as the position of crop rows). Theses layers, along with object size, shape, texture and location of objects to other objects (or features), can then all be used to aid in the final classification of the scene surveyed.

Although fully featured and freely available, the OBIA software Interimage (Camargo *et al.* 2012) was not the ideal software to use, primarily due to the limitations in the sizes of imagery that could be used with it, meaning that the data had to be split up and processed independently. This made processing both slow and caused classification errors. Trimble eCogniton was a far superior OBIA product, and although not free (an academic license cost ~£3,000), it did not have any of the limitations of Interimage and if it had been available earlier in this PhD project, then the results from chapters 4 and 6 could well have been improved. Overall, the requirements for the 3rd objective were met, however the effectiveness of image normalisation (which was only applied for the 5th chapter) were not fully assessed and may well have not been effective if trying to rely on spectral measurements alone for time series analysis of data.

8.6.4 4th Objective - Through collaboration with existing projects, demonstrate the utility of UAS acquired data to these projects by addressing specific questions within those projects.

The 4th objective was met through the aims of the five different case studies that made up chapters 4-7, a summary of each indicated in the following sections.

8.6.4.1 Agricultural applications - disease detection

The aim of this case study was "*to identify if a UAS equipped with COTS cameras can detect and map the onset of disease within a crop of potatoes, with an effective level of accuracy*". Other studies have investigated the development of disease within a potato crop, namely the onset of late blight (Franceschini *et al.*, 2017; Sugiura *et al.*, 2016) as well as detecting its possible arrival from the air (Techy *et al.*, 2008), but none so far (to the authors knowledge) have investigated blackleg disease caused by *Pectobacterium spp.* The early detection of this disease (and removal of infected plants) is important as it can spread to neighbouring plants or infect progeny tubers (Toth *et al.*, 2003; Charkowski, 2015) and its presence within a potato crop can affect the certification of potential potato seed being produced, thereby resulting in financial loss for farmers (SASA, 2017).

Due to the likely spectral issues with the sensor package, this study focused on the structural aspects of the plants, to identify if the onset of disease could be detected through a reduction in canopy growth, height or volume, when compared with the mean measurements of the plant population as a whole. This required the modelling of each plant over time, with the detection of an emerged plant being the initial point to monitor from. The use of Thiessen polygons to denote plant growth space and monitor the development of each plant individually is also novel from the perspective of RS from a UAS and despite issues encountered due to alterations in position of orthomosaics between dates, the measures used with the automatic method produced a good estimation of the onset and development of disease within the trial (overall accuracy 92 %, producers and users accuracy 85 % and Kappa 0.79).

The results cannot be directly compared with another study, as the closest the author identified would be that of Sugiura *et al.* (2016), who used a standard digital camera on their UAS to assess the development of disease (late blight). They employed a pixel-based method but did not use height (structural) data, and they only produced a severity rating per plot and not per plant. However, whilst they had good results that also compared well with ground-based measurements they also encountered issues with the canopy of certain plants encroaching on their neighbours, causing errors in their estimation of disease severity, which highlights the need to find ways of tracking and separating one plant from another.

The methods employed in this study are essentially the initial foundations of a disease detection model and could most likely be improved through the use of

further spectral measures using calibrated multispectral imagery, as changes in leaf pigment (e.g. chlorophylls) could then also be monitored (Franceschini *et al.*, 2017). However, despite the study by Franceschini *et al.* (2017) using a hyperspectral imager onboard a UAS to detect the early stages of blight development, they still found that structural changes in the plants (e.g. loss of canopy) were a more important indicator of disease compared to the spectral measurements alone.

Over areas larger than the small trial of this study, surveying with a UAS using the methods outlined in this study would be considerably quicker than a full ground-based assessment, and the disease maps produced would help focus the efforts of potato inspectors and roguers. However, one issue remains that cannot be avoided, in that regular surveys are required, ideally more than once a week. Further work should be undertaken to reduce this requirement though the identification of each plant even when intra and inter row closure has occurred (perhaps through height analysis), as this requirement for regular surveys could be overly burdensome, as Hunt & Rondon (2017) also highlighted when they used daily images from a UAS to detect damage to potato plants from a Colorado potato beetle (*Leptinotarsa decemlineata*) infestation.

Improvements could also be made with more accurate orthomosaic and DSM positioning between survey dates (e.g. though the use of onboard high accuracy GNSS) and refinements to the image classification process, by using more effective image analysis software. However, overall the aim of this case study was met as the results indicate an effective level of disease detection, but the actual type of disease was not discerned in this case. Knowing what other plant stressors (biotic and abiotic) are present (or likely) would be important in quantifying disease severity, something that Duarte-Carvajalino *et al.* (2018) also indicate from their study investigating late blight.

8.6.4.2 Agricultural applications - trials analysis

The aim of this case study was "*to identify if a UAS equipped with COTS cameras is able to detect the emergence and change in canopy cover of potato plants to the same fidelity as that of traditional ground-based techniques*". Conducting trials analysis of potatoes is a relatively time-consuming activity from the ground so simply speeding up the process would be worthwhile. As would enabling a more

standardised methodology, as measures taken from the ground (especially for canopy cover estimation) can be subjective and will vary from person to person, as Sugiura *et al.* (2016) also encountered with ground-based assessment of blight. This study tried to address these issues by utilising the plant growth model developed for disease detection, but outputting on a per row (or plot) basis rather than per plant, to match that of ground-based observations.

The emergence detection method employed initially for disease detection did not fare well with this larger trial and even when updated to make it more robust, it still lagged behind the observations made from the ground. To give the model autonomy it would need to be improved by taking into consideration environmental factors that could alter the growth rate of plants (e.g. temperature, rain, nutrient application), as this would allow the growth rate per day to be varied rather than the fixed 2 cm per day that was implemented. However, the resolution of the imagery was not fine enough to detect shoots as they emerged, and the slightly irregular plant spacing plus the development of weeds led to an increase in false positive and negative results. The latter two factors, both of which are suboptimal conditions for typical potato development (Bussan *et al.*, 2007), were not encountered by Sankaran *et al.* (2017), who also investigated emergence within a potato crop using a UAS equipped with a modified digital camera. However, weed development was encountered by Gnädinger & Schmidhalter (2017), were the presence of weeds reduced accuracy when trying to count maize plants, and by Li *et al.*, (2019), who also indicted some miscounting of emerging potatoes due to the presence of weeds.

Sankaran *et al.* (2017) showed significant correlation between UAS and manual emergence counts ($r > 0.8$ for two different varieties) which was better than the best result of this trial ($r = 0.47$ for the Maris Piper variety), although this difference could be attributed to the poor plant spacing and weed development, as the visual analysis of the Maris Piper varieties also gave a significant and highly correlating result ($r = 0.94$). Sankaran *et al.* (2017) also reported difficulties in detecting emergence once intra-row canopy merging had occurred, which the model in this study could overcome to a point. Li *et al.*, (2019), used a standard digital camera to capture emerging potatoes using a pixel-based approach, but only from a single survey (at ~50% emergence). They indicated a high level of correlation between manual and UAS acquired emergence ($R^2 = 0.96$), however they may have been fortunate in capturing imagery at the perfect time (when the majority of plants were

distinct from each other) as they also indicated under and over estimation of plant counting where neighbouring plant canopies had merged.

Detection of canopy cover was more straight forward compared to emergence, although weeds were difficult to split from the potato vegetation, and to improve this a calibrated multispectral camera may prove to be more effective at being able to discriminate between the two, as Peña *et al.* (2015) reported higher accuracies for weed detection using such a system compared to a COTS camera. Peña *et al.* (2015) also used an OBIA approach for their classification of weeds, highlighting the applicability of this method when dealing with the very high-resolution imagery produced by UAS, as others have also reported (Torres-Sánchez *et al*., 2015; Pérez-Ortiz *et al.*, 2016).

The ground cover analysis correlated significantly with the ground-based measurements and although the ground-based measurements were generally higher, the reason for this was identified due to the way those measurements were taken, resulting in a reduced view of the plot being measured, especially towards the later growth stages when the canopy is quite high. Coupled with the subjective nature of the ground-based measurements, the use of RS from a UAS for this purpose is likely to give a much more representative and standardised measure of each plot (if classification is effective). Further to this, as the development of each plant was being monitored, far more intra-plot variability could be produced. With the addition of height data and potentially calibrated spectral measures to identify chlorophyll content, a wealth of detail not typically captured from the ground could be supplied, but for a similar survey effort as that required for traditional ground-based analysis.

Therefore, the aims of this case study were met, and indicate that further work is required to improve the methods (both data capture and analysis) before the use of UAS gives the same results as that of traditional techniques with regards to emergence counting. However, for ground cover assessment, the advantages in the use of UAS are much more apparent, but the differences seen between the aerial and traditional method need to be assessed further, perhaps through the use of a more representative (but potentially much slower) method of quantifying canopy cover from the ground.

8.6.4.3 Environmental applications – invasive non-native species monitoring

The aim of this case study was "*to identify if a UAS equipped with COTS cameras can be used to effectively map the current extent of the invasive non-native species giant hogweed*". Monitoring the distribution of invasive species along riparian habitats is also a time-consuming process when performed manually and often only covers direct features of interest (e.g. the immediate banksides of a river) and not the wider area surrounding them (Harewood, 2014). A study by Hill *et al.* (2016) also highlighted that manual surveys for INNS cannot always accurately capture the full scale of invasion (the area covered by INNS), as the measurements are often coarser. This was due to both time constraints and the ability to view the area in depth, as their view could be obscured by other vegetation, leading to under estimation of the area covered by INNS. They identified that visual interpretation of UAS captured imagery gave the most accurate indication of the area covered by INNS but their automatic classification (using pixel-based methods) overestimated the scale of invasion. However, visual interpretation of imagery does not scale very well to larger areas as it will take far too much time (Hill *et al.*, 2016), so improvements for their automatic classification would be required.

The OBIA classification method employed in the pilot study of this thesis also over-estimated the area of ground covered by giant hogweed but with improvements should become representative of the true scale of the problem, especially as a study by Müllerová *et al.* (2017b) showed an effective level of accuracy with their classification (which used a similar method), but only during certain phenological stages (i.e. when the plants were flowering). This was also noted as important by Hill *et al.* (2016), for even though the species being investigated was different, yellow flag iris (*Iris pseudacorus L.*), the flowering stage allowed more effective identification from surrounding vegetation. As these phenological stages can be brief and can vary in their timing year to year, the ability to be able to conduct a survey when required highlights another advantage of the use of UAS, for they can be deployed at very short notice.

Overall, the aims of this case study were met, as it showed that the UAS and sensor package could be used to map the extent of giant hogweed invasion, although further work is required to refine the automatic classification method and bring it up to a similar standard of other studies. Likewise, the multirotor UAS used for this case study might not be the best aerial platform to use, as the increased endurance of a

fixed wing UAS would allow for much more expanded surveys, which Pergl *et al.* (2011) suggests is wise to do when surveying for INNS. For just this reason, the studies by Müllerová *et al.* (2017b) and Michez *et al.* (2016) both used fixed wing UAS, so further work in this area should consider focussing on identifying optimum survey methods using a fixed wing type of aerial platform.

8.6.4.4 Experimental applications – greenhouse gas estimation upscaling

The two collaborative exploratory studies of chapter 7 were both focussed on a similar goal, that of identifying microtopographical features that were linked to differing emissions of greenhouse gases. Due to difficulties encountered trying to find an automated solution, the study classifying features within clear-fell forestry used a manual classification approach. This gave results that were not as effective as expected, partly due to the method employing fixed widths for certain features, which was expedient but not realistic to the true conditions on the ground. Expediency was key for this study at that time however as manually classifying features by hand is a very slow process. Scaling up the process to the entire area surveyed would have been an arduous task (hence why it was not undertaken), so the development of an automatic process along the lines of that shown by Lovitt *et al.* (2018) is required to enable the effective use of a UAS for studies of this type.

Likewise, for the study investigating urine patches, manual classification of the imagery would also have been laborious, so the pixel-based method employed by Maire *et al.* (2018) was a far more practical solution. This method did not show the true accuracy of the classification as actual livestock urination events were not captured, so therefore could not be compared directly to the features seen on the ground. However, statistical analysis of the spectral differences between detected “patch” and “non-patch” areas were shown to be significant and therefore likely to be actual patches. Manual methods of identifying when, where and how much urine is deposited by livestock are extremely time consuming (Auerswald *et al.*, 2010; Dennis *et al.*, 2011), so this method (once validated) would be a step forward in this area of research.

Therefore, the aims of both exploratory case studies were met, however both require further work to validate the accuracy of upscaling GHG emissions from the different features that were classified, although this concept itself is supported by

other researchers (Davidson *et al.*, 2017; Lovitt *et al.*, 2018). They also both showed how the UAS and its sensor package could be deployed over very different areas of land-use, conducting low altitude RS to aid in answering specific research questions.

8.7 Key considerations using UAS for precision agriculture and land conservation

One of the key points of precision agriculture is understanding in intra field variability between soils and crop yield (Hunt & Daughtry, 2018), as being able to react to this in a timely manner typically reduces field input requirements (which is a boon for farmers and the environment), whilst enhances yield and makes harvesting easier (Hunt & Daughtry, 2018). The condition of soils can be identified though ground based surveys measuring electrical conductivity and analysis of soils to identify key nutrients (Pedersen & Lind, 2017), and yield can be monitored by harvesting machinery (Pedersen & Lind, 2017). However, the monitoring of crop growth is also key, and this is where UAS can best be used.

A paper by Hunt & Daughtry (2018) nicely outlines the three main niches where UAS can be used to aid precision agriculture; crop scouting, monitoring and planning (table 8-1), all of which can be applied to UAS operations of land-use in general. For farmers and agricultural consultants, the use of commercial grade RTF UAS equipped with standard digital cameras are ideal for the scouting role. They allow more extensive (or quicker) field walking to note problem areas, simply by viewing the real time video feedback from the UAS, without the need for any further image processing (so cost would simply be the aircraft itself). Any problem areas discovered can then be investigated in more detail on the ground to enable more informed management decision to be made. However, relying on using a UAS alone for field walking may mean that certain insect pests or the very early development of disease or weeds could be missed if the resolution of the data being viewed is not sufficient (Hunt & Daughtry, 2018).

Table 8-1: The three niches of UAS remote sensing for precision agriculture (Hunt & Daughtry, 2018).

Characteristic	Scouting	Monitoring	Planning
Sensors	Camera (visible, CIR, thermal)	Multispectral	Multispectral, hyperspectral
Sensor calibration	Not required	Up-looking sensor	Rigorous
Area covered	Specific locations	Whole field	Whole field
Output	GNSS tagged photographs	GIS map of field	Decision support model
Spatial accuracy	Low	Medium	High
Orthomosaicing required	No	Depends on data product	Yes
Timing	Immediate	About 1–2 days	About 3 days to 3 months
Cost	Low	Medium	High
Economic benefits	Marginal	Depends on action taken	Economically optimum rates
Environmental benefits	Marginal	Depends on action taken	Most reduction of agro-chemicals
Applications	Check locations in fields that may have problems	Yield potential, occurrence of weeds, pests, and diseases	Variable rate application

Similarly, conservation land managers can also make use of this lower cost scouting niche for the management of their own land. For instance, the River Forth Fisheries Trust (RFFT) used RTF UAS to give context to the scale of INNS species along riverbanks they were managing using the following method:

- "*Initial quick surveys are taken from bridges or easily accessed areas where a long section of river can be seen. Evidence of invasive species is noted (either present or absent) so that it can be followed up in more detail later.*
- *Follow up ground-based surveys are undertaken by volunteers or staff and typically map the linear extent of the species along the riverbank but not the density, as this data is not required by RFFT for identifying the spread along the Forth catchment*". (Louis, 2014)

These manual surveys only indicate the extent of infestation and not necessarily the density of patches, although this might be recorded sometimes along with a digital photograph of particularly bad patches (Louis, 2014), and as they are done on foot, they might not show the true extent of invasion if certain areas are too difficult to access easily. This is where the monitoring niche comes into play, requiring full mapping of an areas under investigation. However, potentially more investment in both UAS hardware, sensors, image processing and analysis software would need to be made (as demonstrated in chapter 6 of this thesis), along with time for conducting surveys over regular time frames.

For precision agriculture, applications such as monitoring the development of weeds, disease and insect pests could be carried out (as indicated in chapters 4 and 5 of this thesis), as well as indicating potential yield. Companies such as DroneDeploy (San Francisco, USA) and Pix4D (Lausanne, Switzerland) are offering both mission planning software for RTF UAS and online or personal computer-based software that can process collected imagery into orthomosaics and surface models, as well as provide analytical routines to aid in identifying in field variability, plant establishment, plant count, weed and pest analysis routines (DroneDeploy, 2018). However, the literature for the effectiveness and accuracy of these routines is grey and may only apply to certain crops or when surveyed under ideal environmental conditions or at optimum crop growth times. This grey literature suggests that uncalibrated standard digital cameras can be used, especially if calibrated through ground truthing (e.g. Wrangham, 2017), however Hunt & Daughtry (2018) suggest the use of calibrated multispectral sensors as monitoring examines changes over time, and therefore calibration needs to be done to avoid changes due to illumination. A paper by Maes & Steppe (2018) gives a good indication of how applicable each type of sensor is for a variety of precision agriculture applications (table 8-2).

Table 8-2: Overview of the applications and suitability of different sensors used for UAS enabled precision agriculture. HS = highly suited; S = suited; S[b] indicates calculation of sun-induced fluorescence from hyperspectral data (Maes & Steppe, 2018).

Application		Type of sensor/camera			
		RGB	Multispectral (broad band)	Hyperspectral (narrow band)	Thermal
Drought stress	Detection in early stages	–	–	S[b]	HS
	Long-term consequences	–	HS	HS	S
Pathogen detection	Detection in early stages	–	–	HS	HS
	Severity of infection	HS	HS	HS	S
Weed detection	Spectral discrimination	–	S	HS	–
	Object based	HS	HS	–	–
Nutrient status		S	HS	HS	S
Growth vigor	Growth stage	HS	–	–	–
	Canopy height and biomass	HS	HS	–	–
	Lodging	HS	–	–	S
Yield prediction		S	HS	–	–

The planning niche is less applicable for conservation land managers as monitoring can supply them with the information required to plan for land management activities, but it is the ideal application of UAS for precision agriculture. The planning niche involves the creation prescription maps for variable rate application of field inputs (e.g. fertilizer and pesticides), enabling optimum inputs to be applied and reducing input costs and therefore impacts to the environment in the process (e.g. less GHG emissions and nutrient runoff). To ensure geolocation accuracy, the UAS system will also require high accuracy GNSS (or use GCPs) and ideally calibrated multispectral sensors so that biomass can be evaluated with more confidence (Hunt & Daughtry, 2018; Maes & Steppe, 2018). The data captured needs to be processed into orthomosaic and surface models, potentially combined with other sources of data such as soil conductivity and nutrient analysis (Maes & Steppe, 2018) and analysed within GIS (or farm management software) with ground truth information in order to create a variable rate prescription map.

The costs for obtaining and using data of this type are therefore higher (for UAS equipment, sensors, data processing and potentially time required for data capture) and this niche also requires more expensive variable rate farm machinery (Pedersen & Lind, 2017). Interestingly, Hunt & Daughtry (2018) indicate that comparisons between nutrient prescription maps created using UAS RS data vs those created from yield maps or proximal sensors (e.g. active sensors mounted on tractor cabs to enable 'on the go' variable rate applications), have not been completed with any rigour for multi-year applications. Further to this, Maes & Steppe (2018) also suggest that variable rate management machinery typically in use today (e.g. boom sprayers) are currently too coarse in their application abilities (around 10 m), and therefore the full commercial potential of using UAS derived high resolution prescription maps may not be apparent for some time.

Finally, both environmental and agricultural research areas make use of UAS with high precision GNSS and often combinations of sensors, with one area that is showing a marked increase in interest being the use of UAS for rapid plant phenotyping. This particular aspect of agricultural research is partly driven by the changing environmental factors caused by climate change, where tolerance to drought or specific pests or disease needs to be identified to ensure that crop yields can be maintained in the future (Chapman *et al.*, 2014; Sankaran *et al.*, 2015 ; Haghighattalab *et al.*, 2016; Gracia-Romero *et al.*, 2019). Often termed high

throughput plant phenotyping (HTPP), this technique requires the monitoring of plant growth information without the need for destructive sampling, identifying desirable traits such as water stress tolerance, disease resistance and yield (Rahaman *et al.*, 2015; Shakoor *et al.*, 2017). To understand and identify these traits within an infield setting (rather than a laboratory), a considerable amount of manual work is required if only capturing data from the ground (often using a combination of handheld sensors). However, if UAS are used for HTTP then time savings can be made, reducing costs and enabling larger trials of more varieties and treatment types at the same time (Chapman *et al.*, 2014; Haghighattalab *et al.*, 2016; Gracia-Romero *et al.*, 2019).

8.8 Conclusions, limitations and future thoughts

As has been discussed in this thesis and highlighted in many other studies, the potential utility of UAS are legion. This project itself has covered a range of different land-use areas, showing the applicability of this technology as a tool for research and education, and detailed potential precision agriculture applications that could be further evolved into tools which would add value to commercial agricultural operations. From a purely research and education perspective multirotor UAS are very nearly already a perfect tool, allowing flexible deployment to a wide range of environments and with an effective level of autonomy, as long as areas to be investigated are relatively compact. The software available for processing and analysing the data is also prevalent and effective, however both software and UAS are still evolving. As is RS itself from these platforms, with new types of sensors being miniaturised to improve their utility, such as multispectral imagers designed for precision agriculture, that process data during flight using reduced image overlap (SlantRange, 2019). Further research is also ongoing to identify the best methods to employ with these sensors, to ensure reliable and representable data capture (Assmann *et al.*, 2018).

However, there are still many hurdles to overcome before they can be more effectively integrated for land-use activities on a grander scale, in particular for precision agriculture applications. From a technological perspective, power sources (i.e. batteries) need further improvements to provide longer endurance and therefore allow the coverage of larger areas, especially at lower altitudes to gain the highest resolution data. Positional accuracy is another area where further gains need to be made, although the development of RTK and PPK (post processing kinematic) GNNS receivers look well placed to provide centimetre accuracy for UAS derived data outputs (Du *et al.*, 2017; Forlani *et al.*, 2018; Tomaštík *et al.*, 2019). Positional accuracy is also required for further autonomy, for if UAS can be relied upon to perform their work with limited human interaction then their utility increases considerably (Davies *et al.*, 2018). Some researchers are already exploring this with the concept of using swarms of small UAS to inspect crops, allowing a greater area of coverage due to inter-robotic communication and the ability to self-recharge (Carbone *et al.*, 2018).

However, the main stumbling block for both improved UAS autonomy and/or increasing endurance (and therefore range from the operator), is regulations (Davies *et al.*, 2018; Maes & Steppe, 2018). For obvious safety reasons current regulations in the UK require a human to be in control, and for that human to be able to visually see the aircraft at all times. However, this greatly reduces the utility of UAS as often fields are longer than 500 m and therefore require the more than one flight to complete as the operator has to move position. The regulations are however changing, as can be seen with the recent introduction of the Air Navigation (Amendment) Order 2018, and more autonomy may be possible in the future as the UK emergency services already have permission to operate beyond visual line of site in emergency situations (CAA ORS4 No.1233, 2017). The weather will also always be a limiting factor for UAS use, although sensors and UAS themselves can be made waterproof and be built to handle stronger winds but getting effective data under adverse conditions would likely still be prohibitive.

Despite these challenges, the diverse utility of UAS means that the future use of them within the UK looks set to increase and provide a greatly needed productivity boost to many sectors of the UK economy; As a recently released report from PricewaterhouseCoopers (PwC, 2018) estimates that by 2030 some 628,000 jobs will be directly involved with aspects of UAS operation, support and data analysis, and an estimated 76,000 UAS will be in operation across a range of industrial sectors, with a large portion of them being used for education, research and precision agriculture (figure 8-8).

Sector	Estimated number of drones in 2030
UK wide	**76,233**
Public and Defence, Health, Education and other services	27,521
Agriculture, Mining, Gas and Electricity	25,732
Transport and Logistics	11,008
Construction and Manufacturing	4,816
Technology, Media and Telecommunications	4,541
Financial, Insurance, Professional and Administrative Services	2,514

Figure 8-8: Estimated number of UAS in UK skies in 2030, by sector (PwC, 2018).

Chapter 9. References

3DR (2018). *Pixhawk Support by Topic*. Available online at: https://3dr.com/support/pixhawk/ (accessed: 10/07/2018).

Abberton, M., Batley, J., Bentley, A., Bryant, J., Cai, H., Cockram, J., Costa de Oliveira, A., Cseke, L.J., Dempewolf, H., De Pace, C. and Edwards, D. (2016). Global agricultural intensification during climate change: a role for genomics. *Plant biotechnology journal*, 14(4), p.1095-1098.

Aber, J.S., Marzolff, I., Ries, J. (2010). *Small-Format Aerial Photography: Principles, techniques and geoscience applications*. Elsevier, Amsterdam, Netherlands.

Ahmadi, S.H., Agharezaee, M., Kamgar-Haghighi, A.A. and Sepaskhah, A.R. (2014). Effects of dynamic and static deficit and partial root zone drying irrigation strategies on yield, tuber sizes distribution, and water productivity of two field grown potato cultivars. *Agricultural water management*, 134, p.126-136.

AHDB (2016). *GB Potatoes: Market Intelligence 2016-2017*. Available at: https://potatoes.ahdb.org.uk/sites/default/files/GB%20Potatoes%202016-2017.pdf (accessed 14/07/2018)

Albetis, J., Duthoit, S., Guttler, F., Jacquin, A., Goulard, M., Poilvé, H., Féret, J.B. and Dedieu, G. (2017). Detection of Flavescence dorée grapevine disease using unmanned aerial vehicle (UAV) multispectral imagery. *Remote Sensing*, *9*(4), p.308.

AlphaUAS (2018). *Alpha 800 UAV*. Available at: https://alphaunmannedsystems.com/ (accessed: 10/07/2018).

Arducopter (2012). *Arducopter 3DR Quadcopter Assembly Instructions*. Available at: http://www.arducopter.co.uk/whats-new/arducopter-3dr-assembly-instructions (accessed: 10/07/2018).

Arducopter (2018). *ArduCopter - more than your average quadcopter*. Available at: https://www.arducopter.co.uk/ (accessed: 10/07/2018).

Ardupilot (2016a). *Frame Class and Type Configuration*. Available at: http://ardupilot.org/copter/docs/frame-type-configuration.html (accessed: 10/07/2018).

Ardupilot (2016b). *AutoTune*. Available at: http://ardupilot.org/copter/docs/autotune.html (accessed: 10/07/2018).

Ardupilot, (2016c). *Rangefinders (landing page)*. Available at: http://ardupilot.org/copter/docs/common-rangefinder-landingpage.html (accessed 24/07/2018).

Ardupilot, (2016d). *Terrain Following*. Available at: http://ardupilot.org/copter/docs/terrain-following.html#terrain-following (accessed 24/07/2018).

Ardupilot, (2016e). *RangeFinders (Sonar/Lidar) for Object Avoidance*. Available at: http://ardupilot.org/copter/docs/common-rangefinder-objectavoidance.html#common-rangefinder-objectavoidance (accessed 24/07/2018).

Arslan, B., (2007. Relationships among yield and some yield characters in potato (*S. tuberosum L.*). *Journal of Biological Sciences*, 7(6), pp. 973-976.

Assmann, J.J., Kerby, J.T., Cunliffe, A.M. and Myers-Smith, I.H. (2018). Vegetation monitoring using multispectral sensors-best practices and lessons learned from high latitudes. To be published in *NRC Journal of Unmanned Vehicle Systems* [Preprint]. *bioRxiv*, p. 334730.

ATEC (2018). *ATEC - Advanced Technologies for Efficient Crop management*. Available at: https://www.geos.ed.ac.uk/geosciences/research/projects/atec (accessed 24/07/2018).

Auerswald, K., Mayer, F. and Schnyder, H. (2010). Coupling of spatial and temporal pattern of cattle excreta patches on a low intensity pasture. *Nutrient cycling in agroecosystems*, 88(2), pp.275-288.

Baluja, J., Diago, M.P., Balda, P., Zorer, R., Meggio, F., Morales, F. and Tardaguila, J. (2012). Assessment of vineyard water status variability by thermal and multispectral imagery using an unmanned aerial vehicle (UAV). *Irrigation Science*, *30* (6), p.511-522.

Bărăscu, N., Duda, M.M., Olteanu, G. (2016). Study of dynamics SPAD and NDVI values of potato plants according to the differentiated fertilization. Bull. *UASVM, Agriculture*, 73 (1), p. 5–14.

Barchyn, T.E., Hugenholtz, C.H., Myshak, S. and Bauer, J. (2017). A UAV-based system for detecting natural gas leaks. *Journal of Unmanned Vehicle Systems*, 6(1), pp.18-30.

Bareth, G., Bendig, J., Tilly, N., Hoffmeister, D., Aasen, H. and Bolten, A. (2016). A comparison of UAV-and TLS-derived plant height for crop monitoring: using polygon grids for the analysis of crop surface models (CSMs). *Photogrammetrie-Fernerkundung-Geoinformation*, 2016(2), pp. 85-94.

Baronti, F., Fantechi, G., Leonardi, E., Roncella, R. and Saletti, R. (2011). Hierarchical platform for monitoring, managing and charge balancing of LiPo batteries. In *2011 IEEE Vehicle Power and Propulsion Conference (VPPC),* p. 1-6. IEEE.

Bateman, J. (2017). *China drone maker DJI: Alone atop the unmanned skies*. Available at: https://www.cnbc.com/2017/09/01/in-race-to-dominate-drone-space-west-is-no-match-for-chinas-dji.html (accessed 24/07/2018).

Bates, G., and Quin, B.F. (2013). Robotic urine-patch treatment and effluent application—Technology to support intensification of New Zealand dairy farming while protecting the environment. *Proceedings of the New Zealand Grassland Association* 75, pp.125 –130.

Bayer, B.E. (1976). *US Patent 3971065. Color Imaging Array*, 20 July 1976. Available online at: https://patents.google.com/patent/US3971065A/en (accessed: 22/06/2018).

Bendig, J., Bolten, A. and Bareth, G. (2012). Introducing a low-cost mini-UAV for thermal-and multispectral-imaging. *Int. Arch. Photogramm. Remote Sens. Spat. Inf. Sci*, 39, pp. 345-349.

Bendig, J., Bolten, A., Bennertz, S., Broscheit, J., Eichfuss, S. and Bareth, G. (2014). Estimating biomass of barley using crop surface models (CSMs) derived from UAV-based RGB imaging. *Remote Sensing*, *6*(11), pp. 10395-10412.

Bendig, J., Willkomm, M., Tilly, N., Gnyp, M.L., Bennertz, S., Qiang, C., Miao, Y., Lenz-Wiedemann, V.I.S. and Bareth, G. (2013). Very high resolution crop surface models (CSMs) from UAV-based stereo images for rice growth monitoring in Northeast China. *Int. Arch. Photogramm. Remote Sens. Spat. Inf. Sci*, 40, pp. 45-50.

Bendig, J., *Yu*, K., Aasen, H., Bolten, A., Bennertz, S., Broscheit, J., Gnyp, M.L. and Bareth, G. (2015). Combining UAV-based plant height from crop surface models, visible, and near infrared vegetation indices for biomass monitoring in barley. *International Journal of Applied Earth Observation and Geoinformation*, *39*, pp. 79-87.

Berni, J. A. J., Zarco-Tejada, P. J., Suárez, L., González-Dugo, V., & Fereres, E. (2009). Remote sensing of vegetation from UAV platforms using lightweight multispectral and thermal imaging sensors. *Int. Arch. Photogramm. Remote Sens. Spatial Inform. Sci*, 38(6), p. 6

Bernstein, R. (1976). Digital image processing of earth observation sensor data. *IBM Journal of research and development*, *20*(1), pp. 40-57.

Berman, E.S., Fladeland, M., Liem, J., Kolyer, R. and Gupta, M. (2012). Greenhouse gas analyzer for measurements of carbon dioxide, methane, and water vapor aboard an unmanned aerial vehicle. *Sensors and Actuators B: Chemical*, 169, pp.128-135.

Berra, E.F., Gaulton, R. and Barr, S. (2017). Commercial off-the-shelf digital cameras on unmanned aerial vehicles for multitemporal monitoring of vegetation reflectance and NDVI. *IEEE Transactions on Geoscience and Remote Sensing*, 55(9), pp. 4878-4886.

Berra, E., Gibson-Poole, S., MacArthur, A., Gaulton, R. and Hamilton, A. (2015). Estimation of the spectral sensitivity functions of un-modified and modified commercial off-the-shelf digital cameras to enable their use as a multispectral imaging system for UAVs. *The International Archives of Photogrammetry, Remote Sensing and Spatial Information Sciences*, 40(1), pp. 207-214.

Betteridge, K., Hoogendoorn, C., Costall, D., Carter, M. and Griffiths, W. (2010). Sensors for detecting and logging spatial distribution of urine patches of grazing female sheep and cattle. *Computers and Electronics in Agriculture*, 73(1), pp. 66-73.

BirdsEyeView (2018). *FireFLY6 PRO*. Available online at: https://www.birdseyeview.aero/products/firefly6 (accessed: 10/07/2018).

Blain, L. (2017). *SOAPdrones variable pitch quadcopter uses petrol power for heavy-lifting endurance*. Available online at: https://newatlas.com/soapdrones-variable-pitch-multirotor-endurance/48202/ (accessed: 10/07/2018).

Blaschke, T. (2010). Object based image analysis for remote sensing. *ISPRS journal of photogrammetry and remote sensing*, *65*(1), pp. 2-16.

Blaschke, T., Hay, G.J., Kelly, M., Lang, S., Hofmann, P., Addink, E., Feitosa, R.Q., Van der Meer, F., Van der Werff, H., Van Coillie, F. and Tiede, D. (2014). Geographic object-based image analysis–towards a new paradigm. *ISPRS journal of photogrammetry and remote sensing*, *87*, pp. 180-191.

Bondyra, A., Gardecki, S., Gąsior, P. and Giernacki, W. (2016). Performance of coaxial propulsion in design of multi-rotor UAVs. In *ICA 2016: Challenges in Automation, Robotics and Measurement Techniques.* 440, pp. 523-531.

Bongiorno, D. L., Bryson, M., Dansereau, D. G., & Williams, S. B. (2013). Spectral characterization of COTS RGB cameras using a linear variable edge filter. *In Proc. SPIE 8660, Digital Photography IX*, pp. 86600N

Booy, O., Wade, M. & White, V. (2008a). *Giant Hogweed*. [Online]. Available at: https://secure.fera.defra.gov.uk/nonnativespecies/downloadDocument.cfm?id=30 (accessed: 24/07/2018)

Booy, O., Wade, M. & White, V. (2008b). *Japanese Knotweed*. [Online]. Available at: https://secure.fera.defra.gov.uk/nonnativespecies/downloadDocument.cfm?id=369 (accessed: 24/07/2018)

Booy, O., Wade, M. & White, V. (2008c). *Himalayan Balsam*. [Online] Available at: https://secure.fera.defra.gov.uk/nonnativespecies/downloadDocument.cfm?id=33 (accessed: 24/07/2018)

Bradley, B.A. (2014). Remote detection of invasive plants: a review of spectral, textural and phenological approaches. *Biological invasions*, 16(7), pp.1411-1425.

Bradshaw, J. E. (2007). Potato breeding strategy. In: *Potato Biology and Biotechnology. Advances and Perspectives*. Chap. 8 pp. 157–177. Vreugdenhil, D.Ed. Elsevier, London

Brandelero, C., Berra, E.F., Backes, K.S., Pereira, R.S., & Brun, E.J. (2012). Espectrorradiometria na região do visível e do infravermelho próximo em povoamento de Eucalyptus grandis Hill ex Maiden. Ciência Florestal, 22, pp. 215-222

Braun, S.A., Newman, P.A. and Heymsfield, G.M. (2016). NASA's hurricane and severe storm sentinel (HS3) investigation. *Bulletin of the American Meteorological Society*, *97*(11), pp. 2085-2102.

Brodbeck, C., Sikora, E., Delaney, D., Pate, G. and Johnson, J. (2017). Using Unmanned Aircraft Systems for Early Detection of Soybean Diseases. *Advances in Animal Biosciences*, 8(2), pp. 802-806.

Brooklyn *Museum* (2004). *Brooklyn Museum - Nadar Élevant la Photographie à la Hauteur de l'Art - Honoré Daumier.jpg*. Available at: https://upload.wikimedia.org/wikipedia/commons/3/32/Brooklyn_Museum_-_Nadar_%C3%89levant_la_Photographie_%C3%A0_la_Hauteur_de_l%27Art_-_Honor%C3%A9_Daumier.jpg (accessed 24/07/2018).

Bussan, A. J., Mitchell, P. D., Copas, M. E., & Drilias, M. J. (2007). Evaluation of the effect of density on potato yield and tuber size distribution. *Crop Science*, 47(6), pp. 2462-2472.

CAA (2018). *UAVEnquiries Auto Response*. [E-mail]. Message to: Gibson-Poole, S. 11th June *2018*.

CAA CAP1361 (2018). *CAP1361: Small Unmanned Aircraft (SUA) operators holding a valid CAA permission*. Available at: http://publicapps.caa.co.uk/modalapplication.aspx?appid=11&mode=detail&id=7078 (accessed 24/07/2018).

CAA CAP *722* (2015). *Unmanned Aircraft System Operations in UK Airspace – Guidance*. Available at: https://publicapps.caa.co.uk/docs/33/CAP%20722%20Sixth%20Edition%20March%202015.pdf (accessed 24/07/2018).

CAA ORS4 No.1233 (2017). *Small Unmanned Aircraft - Emergency Services Operations*. Available at: http://publicapps.caa.co.uk/docs/33/1233.pdf (accessed 24/07/2018).

Caffrey, J.M. (1994). Spread and management of Heracleum mantegazzianum along the Irish river corridors. In *Ecology and Management of Invasive Riverside Plants* (eds. Waal, L.C., Child, L.E., Wade, P.M., and Brock, J.H.), pp. 67-76. West Sussex, England: John Wiley & Sons Ltd.

Clarkson, J.P., Warmington, R.J., Walley, P.G., Denton-Giles, M., Barbetti, M.J., Brodal, G. and Nordskog, B. (2017). Population structure of Sclerotinia subarctica and Sclerotinia sclerotiorum in England, Scotland and Norway. *Frontiers in microbiology*, 8(490), pp.1-18.

Camargo, F. F., Almeida, C. M., Costa, G. A. O. P., Feitosa, R. Q., Oliveira, D. A. B., Heipke, C., & Ferreira, R. S. (2012). An open source object-based framework to extract landform classes. *Expert Systems with Applications*, 39(1), pp. 541-554.

Cantwell, M. (1996). A review of important facts about potato glycoalkaloids. *Perishables Handling Newsletter*, 87, pp. 26-27.

Carbone, C., Garibaldi, O. and Kurt, Z. (2018). Swarm robotics as a solution to crops inspection for precision agriculture. *KnE Engineering*, 3(1), pp. 552-562.

Chabot, D. (*2018*). Trends in drone research and applications as the Journal of Unmanned Vehicle Systems turns five. *Journal of Unmanned Vehicle Systems*, *6*(1), pp. vi-xv.

Chabot, D. *and* Bird, D.M. (2012). Evaluation of an off-the-shelf unmanned aircraft system for surveying flocks of geese. *Waterbirds*, *35*(1), pp. 170-174.
Chapman, S.C., Merz, T., Chan, A., Jackway, P., Hrabar, S., Dreccer, M.F., Holland, E., Zheng, B., Ling, T.J. and Jimenez-Berni, J. (2014). Pheno-copter: a low-altitude, autonomous remote-sensing robotic helicopter for high-throughput field-based phenotyping. *Agronomy*, *4*(2), pp. 279-301.
Chao, H., *Cao*, Y. and Chen, Y. (2010). Autopilots for small unmanned aerial vehicles: a survey. *International Journal of Control, Automation and Systems*, *8*(1), pp. 36-44.
Charkowski, A. O. (2015). Biology and control of Pectobacterium in potato. *American Journal of Potato Research*, 92(2), pp. 223-229.
Ortiz, O., Mares, V. (2017). The historical, social, and economic importance of the potato crop. In *The Potato Genome* (Chakrabarti, S.K., Xie, C. and Tiwari, J.K. eds.). pp 1-10. Cham, Switzerland: Springer International Publishing.
CHDK (2016). *KAP UAV Exposure Control Script*. Available at: http://chdk.wikia.com/wiki/KAP_UAV_Exposure_Control_Script (accessed: 10/07/2018).
CHDK (2018a). *CHDK RAW: Unleash the Power in your Canon Powershot*. Available at: http://chdk.wikia.com/wiki/CHDK (accessed: 22/06/2018).
CHDK (2018b). *A2200*. Available at: http://chdk.wikia.com/wiki/A2200 (accessed: 22/06/2018).
CHDKPTP (2014). *DNG Processing*. Available at: https://app.assembla.com/spaces/chdkptp/wiki/DNG_Processing (accessed: 10/07/2018).
Clarkson, J.P., Warmington, R.J., Walley, P.G., Denton-Giles, M., Barbetti, M.J., Brodal, G. and Nordskog, B. (2017). Population structure of Sclerotinia subarctica and Sclerotinia sclerotiorum in England, Scotland and Norway. *Frontiers in microbiology*, 8(490), pp. 1-18.
Clewley, D., Bunting, P., Shepherd, J., Gillingham, S., Flood, N., Dymond, J., Lucas, R., Armston, J. and Moghaddam, M. (2014). A python-based open source system for geographic object-based image analysis (GEOBIA) utilizing raster attribute tables. *Remote Sensing*, 6(7), pp. 6111-6135.
Coffin, D. (2015). *Dcraw User Commands*. Available online at: https://www.cybercom.net/~dcoffin/dcraw/dcraw.1.html (accessed: 10/07/2018).
Coffin, D. (2018). *DCraw*. Available at: http://www.cybercom.net/~dcoffin/dcraw/ (accessed: 22/06/2018).
Colomina, I., & Molina, P. (2014). Unmanned aerial systems for photogrammetry and remote sensing: A review. *ISPRS Journal of Photogrammetry and Remote Sensing*, *92*, pp. 79-97.
Cook, K.L. (2007). The silent force multiplier: the history and role of UAVs in warfare. In: *2007 IEEE Aerospace Conf.*, Big Sky, MT, USA, 3–10 March. pp. 1-7
Cunliffe, A.M., Anderson, K., DeBell, L. and Duffy, J.P. (2017). A UK Civil Aviation Authority (CAA)-approved operations manual for safe deployment of lightweight drones in research. *International journal of remote sensing*, 38(8-10), pp. 2737-2744.
Currie, N., & Bairner, S. (2013) *An assessment of invertebrate biodiversity on four brownfield sites in the Inner Forth Area. December 2013*. [Online] Available at: https://www.buglife.org.uk/assessment-invertebrate-biodiverity-four-brownfield-sites-inner-forth-area (accessed 22/06/2018)

Czajkowski, R., Pérombelon, M. C., van Veen, J. A., & van der Wolf, J. M. (2011). Control of blackleg and tuber soft rot of potato caused by Pectobacterium and Dickeya species: a review. *Plant pathology*, 60(6), pp. 999-1013.

Dandois, J.P. and Ellis, E.C. (2010). Remote sensing of vegetation structure using computer vision. *Remote Sensing*, *2*(4), pp. 1157-1176.

Dare, P. M. (2008). Small format digital sensors for aerial imaging applications. In *The international archives of the photogrammetry, remote sensing and spatial information sciences, Vol. XXXVII. Part B1. Beijing*. pp. 533-538.

Darrodi, M.M., Finlayson, G., Goodman, T., & Mackiewicz, M. (2015). Reference data set for camera spectral sensitivity estimation. *Journal of the Optical Society of America*, 32(3), pp. 381-391.

Dash, J.P., Watt, M.S., Pearse, G.D., Heaphy, M. and Dungey, H.S. (2017). Assessing very high resolution UAV imagery for monitoring forest health during a simulated disease outbreak. *ISPRS Journal of Photogrammetry and Remote Sensing*, 131, pp. 1-14.

Davidson, S., Santos, M., Sloan, V., Reuss-Schmidt, K., Phoenix, G., Oechel, W. and Zona, D. (2017). Upscaling CH4 fluxes using high-resolution imagery in Arctic tundra ecosystems. *Remote Sensing*, 9(12), pp. 2-21.

Davies, L., Bolam, R.C., Vagapov, Y. and Anuchin, A. (2018). Review of unmanned aircraft system technologies to enable beyond visual line of sight (BVLOS) operations. In *2018 X International Conference on Electrical Power Drive Systems (ICEPDS)*, pp. 1-6. IEEE.

Defra (2015). *The Great Britain Invasive Non-native Species Strategy. August 2015*. Available at: https://secure.fera.defra.gov.uk/nonnativespecies/downloadDocument.cfm?id=99 (accessed: 24/07/2018)

Dennis, S. J., Moir, J. L., Cameron, K. C., Di, H. J., Hennessy, D., and Richards, K. G. (2011). Urine patch distribution under dairy grazing at three stocking rates in Ireland. *Irish J. Agric. Food Res*. 50, pp. 149–160.

Dennis, S. J., Moir, J. L., Cameron, K. C., Edwards, G. R., and Di, H. J. (2013). Measuring excreta patch distribution in grazed pasture through low-cost image analysis. *Grass Forage Sci*. 68, pp. 378–385.

Dittrich, A. D. and Helden, A. J. (2012), Experimental sward islets: the effect of dung and fertilisation on Hemiptera and Araneae. *Insect Conservation and Diversity*, 5(1), pp. 46-56.

DJI (2016). *DJI GO App Now Includes GEO Geofencing System*. Available at: https://www.dji.com/newsroom/news/dji-go-app-now-includes-geo-geofencing-system (accessed 24/07/2018).

DJI (2018a). *Phantom 4 Visionary Intelligence. Elevated Imagination*. Available at: https://www.dji.com/phantom-4 (accessed: 10/07/2018).

DJI (2018b). *Fly Safe*. Available at: https://www.dji.com/flysafe (accessed 24/07/2018).

Dorigo, W., Lucieer, A., Podobnikar, T., & Čarni, A. (2012). Mapping invasive Fallopia japonica by combined spectral, spatial, and temporal analysis of digital orthophotos. Intern*ational Journal of Applied Earth Observation and Geoinformation*, 19, pp. 185-195.

DroneDeploy (2018). *Drones in Agriculture: The Ultimate Guide to Putting Your Drone to Work on the Farm*. Available at: https://dronedeploy-www.cdn.prismic.io/dronedeploy-www%2Fb6ac1117-09c8-42fe-b31b-53483050e3df_drones_in_agriculture_fv5.pdf (accessed: 10/04/2019).

Du, M., Noguchi, N., Okamoto, H. and Kobayashi, N. (2017). Topographic Mapping of Farmland by Integration of Multiple Sensors on Board Low-Altitude Unmanned Aerial System. *World Academy of Science, Engineering and Technology, International Journal of Computer, Electrical, Automation, Control and Information Engineering*, 11(11), pp. 1205-1209.

Duarte-Carvajalino, J., Alzate, D., Ramirez, A., Santa-Sepulveda, J., Fajardo-Rojas, A. and Soto-Suárez, M., (2018). Evaluating Late Blight Severity in Potato Crops Using Unmanned Aerial Vehicles and Machine Learning Algorithms. *Remote Sensing*, 10(10), p.1513.

Duffy, J.P., Cunliffe, A.M., DeBell, L., Sandbrook, C., Wich, S.A., Shutler, J.D., Myers-Smith, I.H., Varela, M.R. and Anderson, K. (2018). Location, location, location: considerations when using lightweight drones in challenging environments. *Remote Sensing in Ecology and Conservation*, 4(1), pp. 7-19.

Dunford, R., Michel, K., Gagnage, M., Piégay, H., & Trémelo, M. L. (2009). Potential and constraints of Unmanned Aerial Vehicle technology for the characterization of Mediterranean riparian forest. *International Journal of Remote Sensing*. 30 (19). p. 4915-4935.

Dvořák, P., Müllerová, J., Bartaloš, T. and Brůna, J. (2015). Unmanned aerial vehicles for alien plant species detection and monitoring. *International Archives of the Photogrammetry, Remote Sensing & Spatial Information Sciences*, XL-1/W4, pp. 83-90.

Ellicott, J. (2019) *RE: Flying and questions about potato inspections ...*. [E-mail]. Message to: Gibson-Poole, S. 3rd June 2019

Emran, B., Tannant, D. and Najjaran, H. (2017). Low-altitude aerial methane concentration mapping. *Remote Sensing*, 9(8), pp. 1-13.

Everaerts, J. (2009). NEWPLATFORMS-Unconventional Platforms (Unmanned Aircraft Systems) for Remote Sensing. Official Publication No. 56. *European Spatial Data Research (EuroSDR)*.

Fenton, B. (2017a) *RE: red is what I check*. [E-mail]. Message to: Gibson-Poole, S. 22nd September 2017.

Fenton, B. (2017b) *RE: 2016 PCN trial - ground cover from UAV*. [E-mail]. Message to: Gibson-Poole, S. 21st September 2017.

Fernández-Hernandez, J., González-Aguilera, D., Rodríguez-Gonzálvez, P. and Mancera-Taboada, J. (2015). Image-based modelling from unmanned aerial vehicle (UAV) photogrammetry: an effective, low-cost tool for archaeological applications. *Archaeometry*, *57*(1), pp. 128-145.

Ferreira, T. & Rasband, W. (2012). *ImageJ User Guide (IJ 1.46r)*. Available at: https://imagej.nih.gov/ij/docs/guide/user-guide.pdf (accessed: 10/07/2018).

Fleming, G. (2019) *Re: Enquiry into use of UAV's with Seed Potatoes* [E-mail]. Message to: Gibson-Poole, S. 11th April 2019

Foody, G. M. (2002). Status of land cover classification accuracy assessment. *Remote sensing of environment*, 80(1), pp. 185-201.

Forlani, G., Dall'Asta, E., Diotri, F., Cella, U.M.D., Roncella, R. and Santise, M. (2018). Quality assessment of DSMs produced from UAV flights georeferenced with on-board RTK positioning. *Remote Sensing*, 10(2), p.311.

Forster, P., V. Ramaswamy, P. Artaxo, T. Berntsen, R. Betts, D.W. Fahey, J. Haywood, J. Lean, D.C. Lowe, G. Myhre, J. Nganga, R. Prinn, G. Raga, M. Schulz and R. Van Dorland (2007): Changes in Atmospheric Constituents and in Radiative Forcing. In: *Climate Change 2007: The Physical Science Basis. Contribution of Working Group I to the Fourth Assessment Report of the Intergovernmental Panel on Climate Change [Solomon, S., D. Qin, M. Manning, Z. Chen, M. Marquis, K.B. Averyt, M.Tignor and H.L. Miller (eds.)]*. Cambridge University Press, Cambridge, United Kingdom and New York, NY, USA.

Franceschini, M.D., Bartholomeus, H., van Apeldoorn, D., Suomalainen, J. and Kooistra, L. (2017). Assessing changes in potato canopy caused by late blight in organic production systems through UAV-based pushbroom imaging spectrometer. *International Archives of the Photogrammetry, Remote Sensing and Spatial Information Science*, 42(2W6), pp. 109-112.

Gademer, A., B. Petitpas, S. Mobaied, L. Beaudoin, B. Riera, M. Roux, and J. P. Rudant (2010). Development a Low Cost Vertical Take off and Landing Unmanned Aerial System for Centimetric Monitoring of Biodiversity the Fontainebleau Forest Case. 2010 IEEE International Geoscience and Remote Sensing Symposium. *IEEE International Symposium on Geoscience and Remote Sensing IGARSS*, pp. 600 –603.

Garrett, B. and Anderson, K. (2018). Drone methodologies: Taking flight in human and physical geography. *Transactions of the Institute of British Geographers*. 43(3), pp. 341-359.

Gehrke, R., & Greiwe, A. (2014). RGBI images with UAV and off-the-shelf compact cameras: an investigation of linear sensor characteristics. *EARSeL eProceedings*, 13(S1), pp. 53-58.

GetFPV (2018). *Connex Falcore HD Racing Drone Package*. Available at: https://www.getfpv.com/ready-to-fly-quadcopters/connex-falcore-racing-drone-package.html (accessed: 10/07/2018).

Gibson-Poole S.J. (2013). An Evaluation Of The Potential Uses Of UAS Aerial Imagery For Vegetation Surveying: Methods And Feasibility. A thesis submitted in partial fulfilment of the requirements of the Scottish Agricultural College and the University Of Edinburgh for the Honours Degree in Environmental Protection. Edinburgh: Edinburgh University

Gibson-Poole (2017). *Using a drone to identify a giant herb*. Available at: https://nbn.org.uk/wp-content/uploads/2015/10/21.-Simon-Gibson-Poole-Using-a-drone-to-identify-a-giant-herb.pdf (accessed 24/07/2018).

Gibson-Poole, S., Fenton, B., Griffin-Walker, R. and Hamilton, A. (2018). Getting down to the plant level: Potato trials analysis using a UAV equipped with un-modified and modified commercial off-the-shelf digital cameras. In *Proceedings Crop Production in Northern Britain 2018*. Dundee, 27-28 February. pp. 231-236. Dundee: Crop Protection in Northern Britain.

Gibson-Poole, S., Humphris, S., Toth, I. and Hamilton, A. (2017). Identification of the onset of disease within a potato crop using a UAV equipped with un-modified and modified commercial off-the-shelf digital cameras. *Advances in Animal Biosciences*, 8(2), pp. 812-816.

Glendell, M., McShane, G., Farrow, L., James, M.R., Quinton, J., Anderson, K., Evans, M., Benaud, P., Rawlins, B., Morgan, D. and Jones, L. (2017). Testing the utility of structure-from-motion photogrammetry reconstructions using small unmanned aerial vehicles and ground photography to estimate the extent of upland soil erosion. *Earth Surface Processes and Landforms*, 42(12), pp. 1860-1871.

Göktoğan, A.H., Sukkarieh, S., Bryson, M., Randle, J., Lupton, T. and Hung, C. (2010). A rotary-wing unmanned air vehicle for aquatic weed surveillance and management. *Journal of Intelligent and Robotic Systems*, 57, pp.467-484.

Gnädinger, F. and Schmidhalter, U., (2017). Digital Counts of Maize Plants by Unmanned Aerial Vehicles (UAVs). *Remote Sensing*, 9(6), p. 544.

Gracia-Romero, A., Kefauver, S.C., Fernandez-Gallego, J.A., Vergara-Díaz, O., Nieto-Taladriz, M.T. and Araus, J.L. (2019). UAV and Ground Image-Based Phenotyping: A Proof of Concept with Durum Wheat. *Remote Sensing*, 11(10), p.1244.

GREAT BRITAIN. *The Wildlife and Countryside Act 1981. Elizabeth II. Chapter 69*. (1981) [Online]. London: The Stationary Office. Available at: https://www.legislation.gov.uk/ukpga/1981/69/pdfs/ukpga_19810069_en.pdf (accessed 24/07/2018).

GREENHOUSE (2018). GREENHOUSE: *Generating Regional Emissions Estimates with a Novel Hierarchy of Observations and Upscaled Simulation Experiments*. Available at: http://www.greenhouse-gases.org.uk/projects/greenhouse (accessed 24/07/2018).

Griffin-Walker, R. (2016) *RE: PCN Trial near Murroes, a few questions*. [E-mail]. Message to: Gibson-Poole, S. 20th September 2016.

Gross, J.W. (2015). A comparison of orthomosaic software for use with ultra high resolution imagery of a wetland environment. *Center for Geographic Information Science and Geography Department, Central Michigan University, Mt. Pleasant, MI, USA*. Available from: https://imagininc.wildapricot.org/resources/SPPC/2015/papers/john_gross_paper.pdf (accessed: 10/07/2018).

Govender, M., Chetty, K. and Bulcock, H. (2007). A review of hyperspectral remote sensing and its application in vegetation and water resource studies. *Water SA*, 33 (2), pp. 145-152.

Hack, H., Gall, H., Klemke, T.H., Klose, R., Meier, U., Stauss, R., Witzen-berger, A. (2001). *The BBCH scale for phonological growth stages of potato (Solanum tuberosum L.)*. In: Meier, U. (Ed.), Growth Stages of Mono- and Dicotyledonous Plants, BBCH Monograph. Federal Biological Research Centre for Agriculture and Forestry.

Hackett, N. (2003). *Clackmannanshire Council: Stirling - Alloa - Kincardine railway (route re-opening) and linked improvements (Scotland) Bill: Environmental statement (Volume 2): Topic specific reports. February 2003*. [Online] Available at: https://www.clacks.gov.uk/document/1211.pdf (accessed: 10/07/2018)

Haghighattalab, A., Pérez, L.G., Mondal, S., Singh, D., Schinstock, D., Rutkoski, J., Ortiz-Monasterio, I., Singh, R.P., Goodin, D. and Poland, J. (2016). Application of unmanned aerial systems for high throughput phenotyping of large wheat breeding nurseries. *Plant Methods*, 12(1), p. 35.

Hanafi, D., Qetkeaw, M., Ghazali, R., Than, M.N.M., Utomo, W.M. and Omar, R. (2013). Simple GUI wireless controller of quadcopter. *International Journal of Communications, Network and System Sciences*, 6(01), p. 52.

Harder, P., Schirmer, M., Pomeroy, J. and Helgason, W. (2016). Accuracy of snow depth estimation in mountain and prairie environments by an unmanned aerial vehicle. *The Cryosphere*, 10(6), p. 2559.

Hardin, P.J. and Jensen, R.R. (2011). Small-scale unmanned aerial vehicles in environmental remote sensing: Challenges and opportunities. *GIScience & Remote Sensing*, *48*(1), pp. 99-111.

Harewood, G. (2014). Giant hogweed by the river Allan and part of the river Forth: charting the change 1985-2013. *The Forth Naturalist and Historian*, 37, pp. 111-120.

Harvey, P. (2018). *ExifTool*. Available at: https://www.sno.phy.queensu.ca/~phil/exiftool/ (accessed: 10/07/2018).

Havis, N.D., Burnett, F.J., Hughes, G., Mercer, P.C., Cooke, L.R., Fraaije, B.A., Hunter, E.A. and Oxley, S.J.P., (2014). Rhynchosporium Commune–Understanding the effects of variety, fungicide resistance and seed-borne infection on disease levels in barley. In *Proceedings Crop Production in Northern Britain 2014*. Dundee, 25-26 February. pp. 167-172. Dundee: Crop Protection in Northern Britain

Hawkes, J.G. and Francisco-Ortega, J. (1993). The early history of the potato in Europe. *Euphytica*, 70(1-2), pp. 1-7.

Hazelhurst, J. (2014). *Pixhawk Inforgraphic*. Available at: http://ardupilot.org/copter/_images/Pixhawk-Inforgraphic2.jpg (accessed: 10/07/2018).

Heaphy, M., Watt, M.S., Dash, J.P. and Pearse, G.D. (2017). UAVs for data collection-plugging the gap. *New Zealand Journal of Forestry*, 62(1), pp. 23-30.

Hill, D.J., Tarasoff, C., Whitworth, G.E., Baron, J., Bradshaw, J.L. and Church, J.S. (2016). Utility of unmanned aerial vehicles for mapping invasive plant species: a case study on yellow flag iris (Iris pseudacorus L.). *International journal of remote sensing*, 38(8-10), pp. 2083-2105.

Hodgson, A., Kelly, N. and Peel, D. (2013). Unmanned aerial vehicles (UAVs) for surveying marine fauna: a dugong case study. *PloS one*, *8*(11), p. e79556.

Holman, F.H., Riche, A.B., Michalski, A., Castle, M., Wooster, M.J. and Hawkesford, M.J. (2016). High throughput field phenotyping of wheat plant height and growth rate in field plot trials using UAV based remote sensing. *Remote Sensing*, 8(12), p. 1031.

Honkavaara, E., Saari, H., Kaivosoja, J., Pölönen, I., Hakala, T., Litkey, P., Mäkynen, J. and Pesonen, L. (2013). Processing and assessment of spectrometric, stereoscopic imagery collected using a lightweight UAV spectral camera for precision agriculture. *Remote Sensing*, *5*(10), pp. 5006-5039.

Hornign, N. (2012). *Canon A2200 NIR conversion*. Available at: https://publiclab.org/notes/nedhorning/9-25-2012/canon-a2200-nir-conversion (accessed: 22/06/2018).

Hughes, L. (2016). *NASA's Global Hawk being prepared for deployment to Florida to study Hurricane Matthew*. Available at: https://www.nasa.gov/sites/default/files/styles/full_width/public/thumbnails/image/afrc2016-0292-08.jpg?itok=OeYHQVTe (accessed 24/07/2018).

Hunt, E.R. and Daughtry, C.S. (2018). What good are unmanned aircraft systems for agricultural remote sensing and precision agriculture?. *International journal of remote sensing*, 39(15-16), pp.5345-5376.

Hunt, E. R., Hively, W. D., Fujikawa, S. J., Linden, D. S., Daughtry, C. S., & McCarty, G. W. (2010). Acquisition of NIR-green-blue digital photographs from unmanned aircraft for crop monitoring. *Remote Sensing*, 2(1), pp. 290-305

Hunt, E.R., Hively, W.D., McCarty, G.W., Daughtry, C.S.T., Forrestal, P.J., Kratochvil, R.J., Carr, J.L., Allen, N.F., Fox-Rabinovitz, J.R. and Miller, C.D. (2011). NIR-green-blue high-resolution digital images for assessment of winter cover crop biomass. *GIScience & remote sensing*, 48(1), pp. 86-98.

Hunt, E.R. and Rondon, S.I. (2017). Detection of potato beetle damage using remote sensing from small unmanned aircraft systems. *Journal of Applied Remote Sensing*, 11(2), p. 026013.

Humphirs, S. (2016) *RE: ECPA Draft Paper*. [E-mail]. Message to: Gibson-Poole, S. 8th December 2016

Husson, E., Hagner, O. and Ecke, F. (2014). Unmanned aircraft systems help to map aquatic vegetation. *Applied Vegetation Science*, *17*(3), pp. 567-577.

ICAO (2018). *Remotely piloted aircraft system (rpas) concept of operations (CONOPS) for international IFR operations*. Available at: https://www.icao.int/safety/UA/Documents/RPAS%20CONOPS.pdf (accessed 24/07/2018).

International Potato Centre (2018). *The Potato Plant*. Available at: https://nkxms1019hx1xmtstxk3k9sko-wpengine.netdna-ssl.com/wp-content/uploads/2013/08/Afiche-papa-ingles.jpg (accessed 14/07/2018)

InterImage (2010). *InterImage 1.41 User Guide*. Available at: http://www.lvc.ele.puc-rio.br/projects/interimage/documentation/files/InterImage%201.41%20-%20User%20Guide.pdf (accessed 14/07/2018)

Islam, A.S. and Bala, S.K. (2008). Assessment of potato phenological characteristics using MODIS-derived NDVI and LAI information. *Giscience & remote sensing*, 45(4), pp. 454-470.

IWM (2018). *Air Mechanic Cecil Haliday of the Royal Flying Corps demonstrates a C type aerial reconnaissance camera fixed to the fuselage of a BE2c aircraft*. Available at: https://media.iwm.org.uk/ciim5/36/133/large_000000.jpg (accessed 24/07/2018).

Jain, A.K. (2010). Data clustering: 50 years beyond K-means. *Pattern recognition letters*, 31(8), pp. 651-666.

James Hutton Institute (2016). *Potatoes in Practice 2016*. Available at: http://www.hutton.ac.uk/events/potatoes-practice-2016 (accessed 14/07/2018)

Jensen, J.L. and Mathews, A.J. (2016). Assessment of image-based point cloud products to generate a bare earth surface and estimate canopy heights in a woodland ecosystem. *Remote Sensing*, *8*(1), p. 50.

Jiang, J., Liu, D., Gu, J., & Susstrunk, S. (2013). What is the space of spectral sensitivity functions for digital color cameras? In *Applications of Computer Vision (WACV), 2013 IEEE Workshop*, pp. 168-179.

Jones, D., Pike, S., Thomas, M., & Murphy, D. (2011). Object-based image analysis for detection of Japanese knotweed sl taxa (Polygonaceae) in Wales (UK). *Remote Sensing*, 3(2), pp. 319-342.

Keane, J.B. (2015). *The development of novel automated technology to measure trace gas fluxes from agricultural systems*. A Thesis Submitted in partial fulfilment of the Requirements of the University of York for the Degree of Doctor of Philosophy.York: University of York.

Kelcey, J. and Lucieer, A. (2013). An adaptive texture selection framework for ultra-high resolution UAV imagery. In *Proceedings of the IEEE International Geoscience and Remote Sensing Symposium*, 21–26 July 2013, Melbourne, Australia. pp. 3883–388.

Kim, D.W., Yun, H.S., Jeong, S.J., Kwon, Y.S., Kim, S.G., Lee, W.S. and Kim, H.J. (2018). Modeling and Testing of Growth Status for Chinese Cabbage and White Radish with UAV-Based RGB Imagery. *Remote Sensing*, 10(4), p. 563.

Khot, L.R., Sankaran, S., Carter, A.H., Johnson, D.A. and Cummings, T.F. (2016). UAS imaging-based decision tools for arid winter wheat and irrigated potato production management. *International Journal of Remote Sensing*, 37(1), pp. 125-137.

KnightOptical (2018a). *585FAP*. Available at: https://www.knightoptical.com/_public/documents/1372681789_585nmlongpassfilteracryliccolour585fap.pdf (accessed: 22/06/2018).
KnightOptical (2018b). *590FCS*. Available at: https://www.knightoptical.com/_public/documents/1422454707_590fcsgraph.pdf (accessed: 22/06/2018).
Koh, L.P. and Wich, S.A. (2012). Dawn of drone ecology: low-cost autonomous aerial vehicles for conservation. *Tropical Conservation Science*, 5(2), pp. 121-132.
Kolbe, H. and Stephan-Beckmann, S. (1997). Development, growth and chemical composition of the potato crop (Solanum tuberosum L.). I. Leaf and stem. *Potato research*, 40(1), pp. 111-129.
Koslosky, E., de Oliveira, A.S., Wehrmeister, M.A. and Fabro, J.A. (2017). Designing Fuzzy Logic Controllers for ROS-Based Multirotors. In *Robot Operating System (ROS)*, pp. 41-82. Springer, Cham.
Kršák, B., Blišťan, P., Pauliková, A., Puškárová, P., Kovanič, Ľ., Palková, J. and Zelizňaková, V. (2016). Use of low-cost UAV photogrammetry to analyze the accuracy of a digital elevation model in a case study. *Measurement*, 91, pp. 276-287.
Kyratzis, A.C., Dimitrios P. Skarlatos, George C. Menexes, Vasileios F. Vamvakousis, and Andreas Katsiotis. Assessment of vegetation indices derived by UAV imagery for durum wheat phenotyping under a water limited and heat stressed mediterranean environment. *Frontiers in plant science,* 8, p. 1114.
Kyratzis, A.C., Skarlatos, D.P., Menexes, G.C., Vamvakousis, V.F. and Katsiotis, A. (2017). Assessment of vegetation indices derived by UAV imagery for durum wheat phenotyping under a water limited and heat stressed mediterranean environment. *Frontiers in plant science*, *8*, p. 1114.
Lacomme, C., Glais, L., Bellstedt, D.U., Dupuis, B., Karasev, A.V. and Jacquot, E. eds. (2017). *Potato virus Y: biodiversity, pathogenicity, epidemiology and management*. Springer International Publishing.
Landis, J.R. and Koch, G.G. (1977). The measurement of observer agreement for categorical data. *Biometrics*, pp. 159-174.
Lanzon, A., Freddi, A. and Longhi, S. (2014). Flight control of a quadrotor vehicle subsequent to a rotor failure. *Journal of Guidance, Control, and Dynamics*, 37(2), pp. 580-591.
Lebourgeois, V., Bégué, A., Labbé, S., Mallavan, B., Prévot, L., & Roux, B. (2008). Can commercial digital cameras be used as multispectral sensors? A crop monitoring test. *Sensors*, 8(11), pp. 7300-7322
Leica (2008). *Leica GPS1200+ Series Technical Data*. Available at: https://w3.leica-geosystems.com/downloads123/zz/gps/general/brochures-datasheet/gps1200_technicaldata_en.pdf (accessed: 10/07/2018).
Leica (2018). *Leica Viva GNSS GS10 receiver Datasheet*. Available at: https://w3.leica-geosystems.com/downloads123/zz/gpsgis/viva%20gnss/brochures-datasheet/leica_viva_gnss_gs10_receiver_ds_en.pdf (accessed: 10/07/2018).
Lelong, C.C., Burger, P., Jubelin, G., Roux, B., Labbé, S. and Baret, F. (2008). Assessment of unmanned aerial vehicles imagery for quantitative monitoring of wheat crop in small plots. *Sensors*, 8(5), pp. 3557-3585.
Li, B., Xu, X., Han, J., Zhang, L., Bian, C., Jin, L. and Liu, J. (2019). The estimation of crop emergence in potatoes by UAV RGB imagery. *Plant methods*, 15(1), pp.1-13.

Lim, H., Park, J., Lee, D. and Kim, H.J. (2012). Build your own quadrotor: Open-source projects on unmanned aerial vehicles. *IEEE Robotics & Automation Magazine*, 19(3), pp. 33-45.

Link, J., Senner, D. and Claupein, W. (2013). Developing and evaluating an aerial sensor platform (ASP) to collect multispectral data for deriving management decisions in precision farming. *Computers and electronics in agriculture*, 94, pp. 20-28.

Lippiello, V., Ruggiero, F. and Serra, D. (2014). Emergency landing for a quadrotor in case of a propeller failure: A PID based approach. In *Safety, Security, and Rescue Robotics (SSRR), 2014 IEEE International Symposium*, pp. 1-7.

Loianno, G., Mulgaonkar, Y., Brunner, C., Ahuja, D., Ramanandan, A., Chari, M., Diaz, S. and Kumar, V. (2015). Smartphones power flying robots. In *Intelligent Robots and Systems (IROS), 2015 IEEE/RSJ International Conference*, pp. 1256-1263.

Louis, J. (2014). *How RFFT conducts INNS surveys*. [Interview]. 8th August 2014.

Lovitt, J., Rahman, M.M., Saraswati, S., McDermid, G.J., Strack, M. and Xu, B. (2018). UAV Remote Sensing Can Reveal the Effects of Low-Impact Seismic Lines on Surface Morphology, Hydrology, and Methane (CH4) Release in a Boreal Treed Bog. *Journal of Geophysical Research: Biogeosciences*, 123(3), pp. 1117-1129.

Lowe, D.G. (1999). Object recognition from local scale-invariant features. In *Computer vision, 1999. The proceedings of the seventh IEEE international conference, Corfu, Greece*. pp. 1150-1157.

Lucieer, A., Jong, S.M.D. and Turner, D. (2014). Mapping landslide displacements using Structure from Motion (SfM) and image correlation of multi-temporal UAV photography. *Progress in Physical Geography*, 38(1), pp. 97-116.

Lucieer, A., Turner, D., King, D.H. and Robinson, S.A. (2014). Using an Unmanned Aerial Vehicle (UAV) to capture micro-topography of Antarctic moss beds. *International Journal of Applied Earth Observation and Geoinformation*, *27*, pp. 53-62.

Luijk, G. (2007). *What is DCraw*. Avaialble at: http://www.guillermoluijk.com/tutorial/dcraw/index_en.htm (accessed: 22/06/2018).

Madec, S., Baret, F., De Solan, B., Thomas, S., Dutartre, D., Jezequel, S., Hemmerlé, M., Colombeau, G. and Comar, A. (2017). High-throughput phenotyping of plant height: comparing unmanned aerial vehicles and ground LiDAR estimates. *Frontiers in plant science*, 8, p. 2002.

Maes, W.H. and Steppe, K. (2018). Perspectives for remote sensing with unmanned aerial vehicles in precision agriculture. *Trends in plant science*, 24(2), pp. 152-164.

Maire, J.L.M., Gibson-Poole, S., Cowan, N., Reay, D.S., Richards, K.G., Skiba, U., Rees, R.M. and Lanigan, G.J. (2018). Identifying urine patches on intensively managed grassland using aerial imagery captured from Remotely Piloted Aircraft Systems. *Frontiers in Sustainable Food Systems*, 2(10), pp.1-11.

Manwell, J.F., McGowan, J.G. and Rogers, A.L. (2009). *Wind energy explained: theory, design and application*. John Wiley & Sons.

MAPIR (2018). *3DR SOLO Accessory Bay Tilting Mount - Single Survey Camera - 3DR Gimbal Compatible*. Available at: https://www.mapir.camera/collections/mounts/products/3dr-solo-accessory-bay-tilt-mount-single (accessed: 10/07/2018).

Martin, F.M., Müllerová, J., Borgniet, L., Dommanget, F., Breton, V. and Evette, A., (2018). Using Single-and Multi-Date UAV and Satellite Imagery to Accurately Monitor Invasive Knotweed Species*. Remote Sensing*, 10(10), pp. 1-15.

Matese, A., Toscano, P., Di Gennaro, S.F., Genesio, L., Vaccari, F.P., Primicerio, J., Belli, C., Zaldei, A., Bianconi, R. and Gioli, B. (2015). Intercomparison of UAV, aircraft and satellite remote sensing platforms for precision viticulture. *Remote Sensing*, *7*(3), pp. 2971-2990.

Meyer, G.E. and Neto, J.C., (2008). Verification of color vegetation indices for automated crop imaging applications. *Computers and electronics in agriculture*, 63(2), pp. 282-293.

McLoud, P. R., Gronwald, R. & Kuykendall, H. (2007). Precision agriculture: NRCS Support for Emerging Technologies. *Agronomy Technical Note No. 1*. Natural Resources Conservation Service, US Dept. of Agriculture, Washington, DC.

Michez, A., Piégay, H., Jonathan, L., Claessens, H. and Lejeune, P. (2016). Mapping of riparian invasive species with supervised classification of Unmanned Aerial System (UAS) imagery. Internat*ional Journal of Applied Earth Observation and Geoinformation*, 44, pp. 88-94.

Misselbrook, T., Fleming, H., Camp, V., Umstatter, C., Duthie, C.A., Nicoll, L. and Waterhouse, T. (2016). Automated monitoring of urination events from grazing cattle. *Agriculture, Ecosystems & Environment*, 230, pp.191-198.

Moravcová L., Pyšek P., Krinke L., Pergl J., Perglová I. and Thompson K. (2007) Seed germination, dispersal and seed bank in Heracleum mantegazzianum. In: *Ecology and Management of Giant Hogweed (Heracleum mantegazzianum)* (eds. Pyšek, P., Cock, M.J.W., Nentwig, W. and Ravn, H.P.) pp. 74-91. CAB International.

Mori, T., Hashimoto, T., Terada, A., Yoshimoto, M., Kazahaya, R., Shinohara, H. and Tanaka, R. (2016). Volcanic plume measurements using a UAV for the 2014 Mt. Ontake eruption. *Earth, Planets and Space*, *68*(1), p. 49.

Motavalli, P., Nelson, K., Udawatta, R., Jose, S. and Bardhan, S. (2013). Global achievements in sustainable land management. *International Soil and Water Conservation Research*, 1(1), pp. 1-10.

Muller, M. (2018a). *xcopterCalc - Multicopter Calculator*. Available at: https://www.ecalc.ch/xcoptercalc.php (accessed: 10/07/2018).

Muller, M. (2018b). *xcopterCalc – Help - Hilfe*. Available at: https://www.ecalc.ch/calcinclude/help/xcoptercalchelp.htm (accessed: 30/03/2018).

Müllerová, J., Bartaloš, T., Brůna, J., Dvořák, P. and Vítková, M. (2017a). Unmanned aircraft in nature conservation: an example from plant invasions. *International journal of remote sensing*, 38(8-10), pp. 2177-2198.

Müllerová, J., Bråna, J., Dvořák, P., Bartaloš, T., and Vítková, M. (2016). Does the data resolution/origin matter? Satellite, airborne and UAV imagery to tackle plant invasions. *Int. Arch. Photogramm. Remote Sens. Spatial Inf. Sci*. XLI-B7, pp. 903–908.

Müllerová, J., Brůna, J., Bartaloš, T., Dvořák, P., Vítková, M. and Pyšek, P. (2017b). Timing is important: unmanned aircraft vs. satellite imagery in plant invasion monitoring. *Frontiers in plant science*, 8 (887), pp. 1-13.

Müllerová, J., Pergl, J., & Pyšek, P. (2013). Remote sensing as a tool for monitoring plant invasions: Testing the effects of data resolution and image classification approach on the detection of a model plant species Heracleum mantegazzianum (giant hogweed). *International Journal of Applied Earth Observation and Geoinformation*, 25, pp. 55-65.

Murphey, A. (2016). *Welcome to GPS Utility home page*. Available at: http://www.gpsu.co.uk/index.html (accessed: 10/07/2018).

Myhre, G., D. Shindell, F.-M. Bréon, W. Collins, J. Fuglestvedt, J. Huang, D. Koch, J.-F. Lamarque, D. Lee, B. Mendoza, T. Nakajima, A. Robock, G. Stephens, T. Takemura and H. Zhang (2013): Anthropogenic and Natural Radiative Forcing. In: *Climate Change 2013: The Physical Science Basis. Contribution of Working Group I to the Fifth Assessment Report of the Intergovernmental Panel on Climate Change [Stocker, T.F., D. Qin, G.-K. Plattner, M. Tignor, S.K. Allen, J. Boschung, A. Nauels, Y. Xia, V. Bex and P.M. Midgley (eds.)]*. Cambridge University Press, Cambridge, United Kingdom and New York, NY, USA

Nagai, M., Chen, T., Ahmed, A. and Shibasaki, R. (2007). UAV-borne mapping system for river environment. In *Proceedings of Asian Conference of Remote Sensing, Kuala Lumpur, Malaysia,* 12–16 November 2007 (Vol. 1216).

Nakamura, J. (2006). *Image Sensor and Signal Processing for Digital Still Cameras*. Boca Raton, FL, USA: CRC Press

NASA (2018). *Sketch of the Landsat 1 satellite*. Available at: https://landsat.gsfc.nasa.gov/wp-content/uploads/2012/12/erts.jpg (accessed 24/07/2018).

National Instruments (2011). *PID Theory Explained*. Available at: http://www.ni.com/white-paper/3782/en/ (accessed: 10/07/2018).

NBN Atlas (2018). *Record of Heracleum mantegazzianum Sommier & Levier "Giant Hogweed" by Brackenridge, W., R. (1995). Clackmannan District Habitat Contexting Survey – Scottish Natural Heritage*. [Online]. Available at: https://database.bsbi.org/record/2cd4p9h.1cgkts (accessed 10/07/2018)

Nebiker S., Lack, N., Abacherli, M., Landerach, S. (2016). Lightweight multispectral UAV sensors and their capabilities for predicting grain yield and detecting plant diseases. *ISPRS - International Archives of the Photogrammetry, Remote Sensing and Spatial Information Sciences, Prague, Czech Republic, 12–19 July 2016*; Volume XLI-B1; pp. 963–970.

Nielsen, C., H.P. Ravn, W. Nentwig and M. Wade (eds.) (2005). The Giant Hogweed Best Practice Manual. Guidelines for the management and control of an invasive weed in Europe. *Forest & Landscape Denmark*, Hoersholm, pp. 1-44.

Niemann, T. (2018). *PTLens*. Available at: https://www.epaperpress.com/ptlens/ (accessed: 10/07/2018).

Nijland, W., de Jong, R., de Jong, S.M., Wulder, M.A., Bater, C.W., & Coops, N.C. (2014). Monitoring plant condition and phenology using infrared sensitive consumer grade digital cameras. *Agricultural and forest meteorology*, 184, pp. 98-106.

Oborne, M. (2016). *Mission Planner Home*. Available at: http://ardupilot.org/planner/ (accessed: 10/07/2018).

O'Brien, P.J., Allen, E.J. and Firman, D.M., 1998. REVIEW: A review of some studies into tuber initiation in potato (Solanum tuberosum) crops. *The Journal of Agricultural Science*, 130(3), pp. 251-270.

Optronic (2002). *OL Series 750 Automated Spectroradiometric Measurement System*. Orlando, FL, USA: Optronics Lab., Inc.

Otsu, N. (1979). A threshold selection method from gray-level histograms. *IEEE transactions on systems, man, and cybernetics,* 9(1), pp. 62-66.

Palczewska, G., Vinberg, F., Stremplewski, P., Bircher, M.P., Salom, D., Komar, K., Zhang, J., Cascella, M., Wojtkowski, M., Kefalov, V.J. and Palczewski, K. (2014). Human infrared vision is triggered by two-photon chromophore isomerization. *Proceedings of the National Academy of Sciences*, 111(50), pp. E5445-E5454.

Pauly, K. (2014). Applying conventional vegetation vigor indices to UAS-derived orthomosaics: Issues and considerations. In *Proceedings of the 12th International Conference on Precision Agriculture, Sacramento, California, USA*. P.

Pauly, K., (2016). Towards calibrated vegetation indices from UAS-derived orthomosaics. In *Proc. of the 13th Int. Conf. on Precision Agriculture*, July 31 - August 4. pp. 2-12. International Society of Precision Agriculture, Monticello, Illinois.

Pena, J.M., Torres-Sánchez, J., de Castro, A.I., Kelly, M. and López-Granados, F. (2013). Weed mapping in early-season maize fields using object-based analysis of unmanned aerial vehicle (UAV) images. *PloS one*, 8(10), p. e77151.

Peña, J.M., Torres-Sánchez, J., Serrano-Pérez, A., de Castro, A.I. and López-Granados, F. (2015). Quantifying efficacy and limits of unmanned aerial vehicle (UAV) technology for weed seedling detection as affected by sensor resolution. *Sensors*, *15*(3), pp. 5609-5626.

Pérez-Ortiz, M., Peña, J.M., Gutiérrez, P.A., Torres-Sánchez, J., Hervás-Martínez, C. and López-Granados, F. (2015). A semi-supervised system for weed mapping in sunflower crops using unmanned aerial vehicles and a crop row detection method. *Applied Soft Computing*, 37, pp. 533-544.

Pérez-Ortiz, M., Peña, J.M., Gutiérrez, P.A., Torres-Sánchez, J., Hervás-Martínez, C. and López-Granados, F. (2016). Selecting patterns and features for between-and within-crop-row weed mapping using UAV-imagery. *Expert Systems with Applications*, *47*, pp. 85-94.

Pergl, J., Müllerová, J., Perglová, I., Herben, T. and Pyšek, P. (2011). The role of long-distance seed dispersal in the local population dynamics of an invasive plant species. *Diversity and Distributions*, 17(4), pp. 725-738.

Perglova, I., Pergl, J., & Pyšek, P. (2006). Flowering phenology and reproductive effort of the invasive alien plant Heracleum mantegazzianum. *Preslia*, 78(3), pp. 265-285.

Pérombelon, M. C. M. (2002). Potato diseases caused by soft rot erwinias: an overview of pathogenesis. *Plant Pathology*, 51(1), pp. 1-12.

Pedersen, S.M. and Lind, K.M. eds. (2017). *Precision Agriculture: Technology and Economic Perspectives*. Springer International Publishing, Cham, Switzerland.

Photoscan (2018). *Agisoft PhotoScan User Manual Professional Edition, Version 1.4*. Available at: http://www.agisoft.com/pdf/photoscan-pro_1_4_en.pdf (accessed: 10/07/2018).

Portlock, J.N. and Cubero, S.N. (2008). Dynamics and Control of a VTOL quad-thrust aerial robot. In *Mechatronics and Machine Vision in Practice.* pp. 27-40. Springer, Berlin, Heidelberg.

Pringle, R.M., Syfert, M., Webb, J.K. and Shine, R. (2009). Quantifying historical changes in habitat availability for endangered species: use of pixel-and object-based remote sensing. *Journal of Applied Ecology*, 46(3), pp. 544-553.

PublicLabs (2018). Infragram convertible cameras. Available at: https://publiclab.org/wiki/infragram-convertible-cameras (accessed: 22/06/2018).

PwC (2018). *Skies without limits: Drones – taking the UK's economy to new heights*. Available at: https://www.pwc.co.uk//intelligent-digital/drones/Drones-impact-on-the-UK-economy-FINAL.pdf (accessed 24/07/2018).

Quan, Q. (2017). *Introduction to multicopter design and control*. Singapore: Springer Singapore.

Quaternium (2017). *Hybrix.20 The first petrol-electric multicopter*. Available at: http://www.quaternium.com/uav/hybrix-20/ (accessed: 10/07/2018).

QuestUAV (2018a). *Q200 Surveyor Pro*. Available at: https://www.questuav.com/drones/q200-survey-drone/attachment/q200-surveyor-pro-4/ (accessed: 10/07/2018).
QuestUAV (2018b). *Kaz Minerals Q200 Launch Preparation*. Available at: https://www.questuav.com/media_category/q-200/page/9/ (accessed: 10/07/2018).
QuestUAV (2018c). *DATAhawk AG Agriculture Drone*. Available at: https://www.questuav.com/drones/datahawk-agriculture/ (accessed: 10/07/2018).
R Core Team (2018). *The R Project for Statistical Computing*. Available at: https://www.r-project.org/ (accessed 24/07/2018).
Rabatel, G., Gorretta, N., & Labbé, S. (2014). Getting simultaneous red and near-infrared band data from a single digital camera for plant monitoring applications: Theoretical and practical study. *Biosystems Engineering*, 117, pp. 2-14
Rahaman, M., Chen, D., Gillani, Z., Klukas, C. and Chen, M. (2015). Advanced phenotyping and phenotype data analysis for the study of plant growth and development. *Frontiers in plant science*, 6, p.619.
Raimundo, A., Peres, D., Santos, N., Sebastião, P. and Souto, N. (2017). Using Distance Sensors to Perform Collision Avoidance Maneuvres on Uav Applications. *The International Archives of Photogrammetry, Remote Sensing and Spatial Information Sciences*, 42, p. 303.
Rasmussen, J., Nielsen, J., Streibig, J.C., Jensen, J.E., Pedersen, K.S. and Olsen, S.I. (2018). Pre-harvest weed mapping of Cirsium arvense in wheat and barley with off-the-shelf UAVs. *Precision Agriculture*, pp.1-17.
Rasmussen, J., Ntakos, G., Nielsen, J., Svensgaard, J., Poulsen, R.N. and Christensen, S. (2016). Are vegetation indices derived from consumer-grade cameras mounted on UAVs sufficiently reliable for assessing experimental plots?. *European Journal of Agronomy*, 74, pp. 75-92.
Redulla, C.A., Davenport, J.R., Evans, R.G., Hattendorf, M.J., Alva, A.K. and Boydston, R.A. (2002). Relating potato yield and quality to field scale variability in soil characteristics. *American journal of potato research*, 79(5), pp. 317-323.
Rees, W.G. (2013). *Physical principles of remote sensing*. Cambridge University Press.
Rogan, J., Franklin, J. and Roberts, D.A. (2002). A comparison of methods for monitoring multitemporal vegetation change using Thematic Mapper imagery. *Remote Sensing of Environment*, 80(1), pp. 143-156.
Ronan, P (2007). EM Spectrum. Available at: https://commons.wikimedia.org/wiki/File:EM_spectrum.svg#/media/File:EM_spectrum.svg (accessed: 22/06/2018).
Roten, R.L., Fourie, J., Owens, J.L., Trethewey, J.A., Ekanayake, D.C., Werner, A., Irie, K., Hagedorn, M. and Cameron, K.C. (2017). Urine patch detection using LiDAR technology to improve nitrogen use efficiency in grazed pastures. *Computers and Electronics in Agriculture*, 135, pp.128-133.
Rouse, J. W., Haas, R. H., Schell, J. A., & Deering D. W. (1973). Monitoring vegetation systems in the great plains with ERTS. In *Proceedings of the 3rd ERTS symposium*, NASA, SP-351 I, pp. 309-317.
Roze, A., Zufferey, J.C., Beyeler, A. and McClellan, A. (2014). *eBee RTK accuracy assessment*. Available at: https://www.sensefly.com/app/uploads/2017/11/eBee_RTK_Accuracy_Assessment.pdf (accessed: 10/07/2018).

Rusnák, M., Sládek, J., Kidová, A. and Lehotský, M. (2018). Template for high-resolution river landscape mapping using UAV technology. *Measurement*, 115, pp.139-151.

Ryan, N.A., Duffy, E.M., Cassells, A.C. and Jones, P.W. (2000). The effect of mycorrhizal fungi on the hatch of potato cyst nematodes. *Applied Soil Ecology*, 15(2), pp. 233-240.

Sankaran, S., Khot, L.R., Espinoza, C.Z., Jarolmasjed, S., Sathuvalli, V.R., Vandemark, G.J., Miklas, P.N., Carter, A.H., Pumphrey, M.O., Knowles, N.R. and Pavek, M.J. (2015). Low-altitude, high-resolution aerial imaging systems for row and field crop phenotyping: A review. *European Journal of Agronomy*, 70, pp. 112-123.

Sankaran, S., Quirós, J.J., Knowles, N.R. and Knowles, L.O. (2017). High-Resolution Aerial Imaging Based Estimation of Crop Emergence in Potatoes. *American Journal of Potato Research*, 94(6), pp. 658-663.

SASA (2015). *Scottish seed potato classification scheme explanatory leaflet 2015*. Available at: http://www.sasa.gov.uk/sites/default/files/GCI_Leaflet_2015.pdf (accessed 14/07/2018).

SASA (2017). *Scottish Seed Potatoes (SPCS Leaflet v14)*. Available at: https://www.sasa.gov.uk/sites/default/files/SPCS%20Leaflet%20English%20v14.pdf (accessed 14/07/2018).

SASA (2018). *Blackleg.jpg*. Available at: https://www.sasa.gov.uk/sites/default/files/blackleg.jpg (accessed 14/07/2018).

Schindelin, J., Arganda-Carreras, I., Frise, E., Kaynig, V., Longair, M., Pietzsch, T., Preibisch, S., Rueden, C., Saalfeld, S., Schmid, B. and Tinevez, J.Y. (2012). Fiji: an open-source platform for biological-image analysis. *Nature methods*, 9(7), pp. 676-682.

Scottish Government (2018). Agriculture facts and figures. Available at: https://www.gov.scot/binaries/content/documents/govscot/publications/statistics/2018/06/agriculture-facts-figures-2018/documents/00536433-pdf/00536433-pdf/govscot%3Adocument/00536433.pdf (accessed 04/06/2019).

SCOTLAND. *Wildlife and Natural Environment (Scotland) Act 2011. Elizabeth II*. (2011) [Online]. The Stationary Office. Available at: http://www.legislation.gov.uk/asp/2011/6/pdfs/asp_20110006_en.pdf (accessed 24/07/2018).

Seier, M.K., Evans, H,C. (2007). Fungal Pathogens Associated with Heracleum mantegazzianum in its Native and Invaded Distribution Range. In: *Ecology and management of giant hogweed (Heracleum mantegazzianum)* (eds. Pyšek, P., Cock, M.J.W., Nentwig, W. and Ravn, H.P.). pp. 189-208. CAB International.

Shahbazi, M., Théau, J. and Ménard, P. (2014). Recent applications of unmanned aerial imagery in natural resource management. *GIScience & Remote Sensing*, *51*(4), pp. 339-365.

Shakoor, N., Lee, S. and Mockler, T.C. (2017). High throughput phenotyping to accelerate crop breeding and monitoring of diseases in the field. *Current opinion in plant biology*, 38, pp. 184-192.

Sidea, A.G., Brogaard, R.Y., Andersen, N.A. and Ravn, O. (2014). General model and control of an n rotor helicopter. In *Journal of Physics: Conference Series* (Vol. 570, No. 5, p. 052004). IOP Publishing.

Skelsey P., Elphinstone J.G., Saddler G.S., Wale S.J. and Toth I.K. (2016). Spatial analysis of blackleg affected seed potato crops in Scotland. *Plant Pathol*. 65, pp. 570-576.

SkyDemonLight (2018). *SkyDemonLight*. Available at: http://www.skydemonlight.com/ (accessed 24/07/2018).

SlantRange (2019). *SlantRange 3p*. Available at: https://www.slantrange.com/product/slantrange-3p/#mounting-kit (accessed 10/06/2019).
Snavely, N., Seitz, S.M. and Szeliski, R. (2008). Modeling the world from internet photo collections. *International journal of computer vision*, *80*(2), pp. 189-210.
SRUC (2017a). *CS/POT/003:2017. Potato growth stage determination*. Edinburgh: SRUC.
SRUC (2017b). *CS/POT/29/06:2017. Assessment of ground cover in potato plots using transparent grids*. Edinburgh: SRUC.
SRUC (2018). *Roguers.jpg*. Available at: https://www.sruc.ac.uk/directory_record/34326/potato_roguing (accessed 14/07/2018).
SRUC (2019a). *About Us - Strong in our Heritage: Ambitious for Our Future*. Available at: https://www.sruc.ac.uk/info/120359/about_us (accessed 04/06/2019).
SRUC (2019b). *Our Mission, Vision, Aims & Values*. Available at: https://www.sruc.ac.uk/info/120393/our_mission_vision_aims_and_values (accessed 04/06/2019).
SRUC (2019c). *Potatoes*. Available at: https://www.sruc.ac.uk/directory_record/3189/potatoes (accessed 04/06/2019).
Standage, T. (2017). *Technology Quarterly Taking flight: Civilian drones*. Available at: https://www.economist.com/technology-quarterly/2017-06-08/civilian-drones (accessed 24/07/2018).
Stichelbaut, B. (2006). The application of First World War aerial photography to archaeology: the Belgian images. *Antiquity*, *80*(307), pp. 161-172.
Struik, P.C. (2007). Above-ground and below-ground plant development. In: *Potato Biology and Biotech-nology. Advances and Perspectives*. Chap. 11 pp. 219-236. Vreugdenhil, D.Ed. Elsevier, London
Sugiura, R., Tsuda, S., Tamiya, S., Itoh, A., Nishiwaki, K., Murakami, N., Shibuya, Y., Hirafuji, M. and Nuske, S. (2016). Field phenotyping system for the assessment of potato late blight resistance using RGB imagery from an unmanned aerial vehicle. *Biosystems engineering*, *148*, pp. 1-10.
Suzuki, T., Amano, Y., Takiguchi, J., Hashizume, T., Suzuki, S., & Yamaba, A. (2009). Development of low-cost and flexible vegetation monitoring system using small unmanned aerial vehicle. In *ICCAS-SICE*, 2009, pp. 4808-4812.
Swift Navigation (2016). *Piksi Datasheet*. Available at: http://docs.swiftnav.com/pdfs/piksi_datasheet_v2.3.1.pdf (accessed: 10/07/2018).
Swift Navigation, (2017). *Frequently Asked Questions: What is the accuracy of Piksi?*. Available at: http://docs.swiftnav.com/wiki/Frequently_Asked_Questions#What_is_the_accuracy_of_Piksi.3F (accessed 14/07/2018)
Szantoi, Z., Smith, S.E., Strona, G., Koh, L.P. and Wich, S.A. (2017). Mapping orangutan habitat and agricultural areas using Landsat OLI imagery augmented with unmanned aircraft system aerial photography. *International journal of remote sensing*, 38(8-10), pp. 2231-2245.
Tanner, R. A., Varia, S., Eschen, R., Wood, S., Murphy, S. T., & Gange, A. C. (2013). Impacts of an invasive non-native annual weed, Impatiens glandulifera, on above-and below-ground invertebrate communities in the United Kingdom. *PloS one*, 8(6), pp. 1-13.

Thamm, H.P. (2011). SUSI62 a robust and safe parachute UAV with long flight time and good payload. *International Archives of the Photogrammetry, Remote Sensing and Spatial Information Sciences*, 38(1), p. C22.

Techy, L.; Woolsey, C.A.; Schmale, D.G. (2008). Path planning for efficient UAV coordination in aerobiological sampling missions. In *Proceedings of 2008 IEEE Conference on Decision and Control, Cancun, Mexico, 9–11 December*; pp. 2814–2819.

Tickner, D. P., Angold, P. G., Gurnell, A. M., & Mountford, J. O. (2001). Riparian plant invasions: hydrogeomorphological control and ecological impacts. *Progress in Physical Geography*, 25(1), pp. 22-52.

The Air Navigation Order 2016. (SI 2016/765).

The Air Navigation (Amendment) Order 2018. (SI 2018/623).

The Seed Potatoes (Scotland) Regulations 2015. (SI 2015/395).

Thomlinson, J.R., Bolstad, P.V. and Cohen, W.B. (1999). Coordinating methodologies for scaling landcover classifications from site-specific to global: Steps toward validating global map products. *Remote Sensing of Environment*, 70(1), pp. 16-28.

Toet, S., Keane, B., Yamulki, S., Blei, E., Gibson-Poole, S., Xenakis, G., Perks, M., Morison, J. and Ineson, P. (2016). Upscaling of greenhouse gas emissions in upland forestry following clearfell. In *EGU General Assembly Conference, 17-22 April,* 18, p. 13775.

Toet, S. (2016) *DEMs for Harwood: clearfell, Crichton, Lincolnshire?*. [E-mail]. Message to: Gibson-Poole, S. 4th August 2016.

Tomaštík, J., Mokroš, M., Surový, P., Grznárová, A. and Merganič, J. (2019). UAV RTK/PPK Method—An Optimal Solution for Mapping Inaccessible Forested Areas?. *Remote Sensing*, 11(6), p.721.

Torres-Sánchez, J., Peña-Barragán, J.M., Gómez-Candón, D., De Castro, A.I. and López-Granados, F. (2013). Imagery from unmanned aerial vehicles for early site specific weed management. In *Precision agriculture'13*, pp. 193-199.

Torres-Sánchez, J., López-Granados, F., De Castro, A.I. and Peña-Barragán, J.M. (2013). Configuration and specifications of an unmanned aerial vehicle (UAV) for early site specific weed management. *PloS one*, *8*(3), p. e58210.

Torres-Sánchez, J., López-Granados, F. and Peña, J.M. (2015). An automatic object-based method for optimal thresholding in UAV images: Application for vegetation detection in herbaceous crops. *Computers and Electronics in Agriculture*, *114*, pp. 43-52.

Torres-Sánchez, J., Peña, J.M., de Castro, A.I. and López-Granados, F. (2014). Multi-temporal mapping of the vegetation fraction in early-season wheat fields using images from UAV. *Computers and Electronics in Agriculture*, *103*, pp. 104-113.

Toth, I., Humphris, S., Brierley, J., Skelsey, P., Saddler, G., Cahill, G. and Wale, S. (2016). *Final Report: Routes of blackleg contamination of high grade potato seed stocks by Pectobacterium species - Ref: R475 - Reporting Period: April 2013 – May 2016*. Available at: https://potatoes.ahdb.org.uk/sites/default/files/publication_upload/R475%20Final%20Report%20for%20publication.pdf (accessed 14/07/2018).

Toth, I.K., Sullivan, L., Brierley, J.L., Avrova, A.O., Hyman, L.J., Holeva, M., Broadfoot, L., Pérombelon, M.C.M. and McNicol, J. (2003). Relationship between potato seed tuber contamination by Erwinia carotovora ssp. atroseptica, blackleg disease development and progeny tuber contamination. *Plant Pathology*, 52(2), pp. 119-126.

Toth, I. K., Van Der Wolf, J. M., Saddler, G., Lojkowska, E., Hélias, V., Pirhonen, M., & Elphinstone, J. G. (2011). Dickeya species: an emerging problem for potato production in Europe. *Plant Pathology*, 60(3), pp. 385-399.

Troscianko, J. and Stevens, M. (2015). Image calibration and analysis toolbox–a free software suite for objectively measuring reflectance, colour and pattern. *Methods in Ecology and Evolution*, 6(11), pp. 1320-1331.

Turner, D., Lucieer, A., Malenovský, Z., King, D.H. and Robinson, S.A. (2014). Spatial co-registration of ultra-high resolution visible, multispectral and thermal images acquired with a micro-UAV over Antarctic moss beds. *Remote Sensing*, 6(5), pp. 4003-4024.

Turner, D., Lucieer, A. and Wallace, L. (2014). Direct georeferencing of ultrahigh-resolution UAV imagery. *IEEE Transactions on Geoscience and Remote Sensing*, 52(5), pp. 2738-2745.

Turner, D., Lucieer, A. and Watson, C. (2012). An automated technique for generating georectified mosaics from ultra-high resolution unmanned aerial vehicle (UAV) imagery, based on structure from motion (SfM) point clouds. *Remote sensing*, 4(5), pp. 1392-1410.

U-blox (2017). *LEA-6 / NEO-6/ MAX-6u-blox 6 GLONASS, GPS & QZSS modules: Hardware Integration Manual*. Available at: https://www.u-blox.com/sites/default/files/products/documents/LEA-NEO-MAX-6_HIM_%28UBX-14054794%29_1.pdf (accessed: 10/07/2018).

Ullman, S. (1979). The interpretation of structure from motion. *Proc. R. Soc. Lond. B*, 203(1153), pp. 405-426.

Verhoeven, G.J. (2010). It's all about the format-unleashing the power of RAW aerial photography. *Int. J. Remote Sens.*, 31(8), pp. 2009-2042.

Verhoeven, G. (2011). Taking computer vision aloft–archaeological three-dimensional reconstructions from aerial photographs with photoscan. *Archaeological prospection*, 18(1), pp. 67-73.

Verhoeven, G., Doneus, M., Briese, C. and Vermeulen, F. (2012). Mapping by matching: a computer vision-based approach to fast and accurate georeferencing of archaeological aerial photographs. *Journal of Archaeological Science*, *39*(7), pp. 2060-2070.

Verhoeven, G.J., Smet, P.F., Poelman, D., & Vermeulen, F. (2009). Spectral Characterization of a Digital Still Camera's NIR Modification to Enhance Archaeological Observation. Geoscience and Remote Sensing, *IEEE Transactions on Geoscience and Remote Sensing*, 47(10), pp. 3456-3468.Von Bueren, S., Burkart, A., Hueni, A., Rascher, U., Tuohy, M. and Yule, I. (2014). Comparative validation of UAV based sensors for the use in vegetation monitoring. Biogeosci Discuss, 11(3), pp.3837-3864.

Von Bueren, S.K., Burkart, A., Hueni, A., Rascher, U., Tuohy, M.P. and Yule, I.J. (2015). Deploying four optical UAV-based sensors over grassland: challenges and limitations. *Biogeosciences*, *12*(1), pp.163-175.

VulcanUAV (2016). *Raven*. Available at: http://vulcanuav.com/aircraft/#raven (accessed: 10/07/2018).

Wade, M. (2015). *Hogweed: Why councils and transport managers should be concerned*. Available at: https://www.transport-network.co.uk/Hogweed-Why-councils-and-transport-managers-should-be-concerned/12058 (accessed: 10/07/2018).

Wan, L., Li, Y., Cen, H., Zhu, J., Yin, W., Wu, W., Zhu, H., Sun, D., Zhou, W. and He, Y., (2018). Combining UAV-based vegetation indices and image classification to estimate flower number in oilseed rape. *Remote Sensing*, 10(9), p.1484.

Wan, H., Wang, Q., Jiang, D., Fu, J., Yang, Y. and Liu, X. (2014). Monitoring the invasion of Spartina alterniflora using very high resolution unmanned aerial vehicle imagery in Beihai, Guangxi (China). *The Scientific World Journal*, 2014. pp. 1-7.

Wang, C., Myint, S.W., Price, K.P., Wang, H. and An, N. (2015). A simplified empirical line calibration method for sUAS-based remote sensing. *Red*, 590, p. 680.

Wei, Z., Han, Y., Li, M., Yang, K., Yang, Y., Luo, Y. and Ong, S.H. (2017). A small UAV based multi-temporal image registration for dynamic agricultural terrace monitoring. *Remote Sensing*, 9(9), p. 904.

Weih, R.C., Riggan, N.D. (2010). Object-based classification vs. pixel-based classification: comparative importance of multi-resolution. *International Archives of the Photogrammetry, Remote Sensing and Spatial Information Sciences* XXXVIII-4/C7 pp. 1–6 (Ghent, Belgium).

Williams, F., Eschen, R., Harris, A., Djeddour, D., Pratt, C., Shaw, R. S., Varia, S., Lamontagne-Godwin, J., Thomas, S.E. & Murphy, S. T. (2010). *The economic cost of invasive non-native species on Great Britain. November 2010*. Available at: http://b3.net.nz/gerda/refs/429.pdf (accessed: 10/07/2018)

Whitehead, K. and Hugenholtz, C.H. (2014). Remote sensing of the environment with small unmanned aircraft systems (UASs), part 1: a review of progress and challenges. *Journal of Unmanned Vehicle Systems*, *2*(3), pp. 69-85.

Woebbecke, D.M., Meyer, G.E., Von Bargen, K. and Mortensen, D.A., 1995. Color indices for weed identification under various soil, residue, and lighting conditions. *Transactions of the ASAE*, 38(1), pp.259-269.

Wrangham, J (2017). *Case Study - Variable Rate Nitrogen Application*. Available at: https://droneag.farm/variable-rate-nitrogen-application/ (accessed 10/06/2019).

Wright, A (2017). *Breaking down UK potato exports in 2016/17*. Available at: https://potatoes.ahdb.org.uk/publications/breaking-down-uk-potato-exports-201617 (accessed 14/07/2018).

Yamada, I. (2016). Thiessen Polygons. In *International Encyclopedia of Geography: People, the Earth, Environment and Technology* (eds D. Richardson, N. Castree, M. F. Goodchild, A. Kobayashi, W. Liu and R. A. Marston). pp. 1-6.

Xenakis, G. (2016) *RE: Data from clearfell*. [E-mail]. Message to: Toet, S., Gibson-Poole, S., Keane, B. 1st April 2016.

Xu, Z., Yang, J., Peng, C., Wu, Y., Jiang, X., Li, R., Zheng, Y., Gao, Y., Liu, S. and Tian, B. (2014). Development of an UAS for post-earthquake disaster surveying and its application in Ms7. 0 Lushan Earthquake, Sichuan, China. *Computers & Geosciences*, *68*, pp. 22-30.

Zhang, C. and Kovacs, J.M. (2012). The application of small unmanned aerial systems for precision agriculture: a review. *Precision agriculture*, *13*(6), pp. 693-712.

Zhang, D., Zhou, X., Zhang, J., Huang, L. and Zhao, J. (2017). Developing a small UAV platform to detect sheath blight of rice. In *Geoscience and Remote Sensing Symposium (IGARSS), July 2017 IEEE International*. pp. 3190-3193.

Zhou, J., Pavek, M. J., Shelton, S. C., Holden, Z. J., & Sankaran, S. (2016). Aerial multispectral imaging for crop hail damage assessment in potato. *Computers and Electronics in Agriculture*, 127, pp. 406-412.

Appendix A – ImageJ script commands and macro script

Script for dark-corrected images generation

1) To generate a dark frame using the dark image (RAW format), execute the command “dcraw -v -D -4 -j -t 0 darkimagefilename.rawfileextension” (table A-1).

2) Afterwards, the dark frame can be subtracted from the RAW images being processed by using the script command “dcraw -v -r 1 1 1 1 -q 0 -o 0 -4 -j -t 0 –T –K darkimagefilename.pgm *.rawfileextension”, which it will generate linear dark-corrected 16-bit tiff images.

Table A-1: DCRaw command parameters explanation, according to Luijk (2007) & DCRaw (2015)

-v	Provides textual information about the RAW conversion process.
-D	Returns raw data with the original unscaled pixel values.
-4	Generates a linear 16-bit file as its output.
-j	Does not stretch the image.
-t 0	Disables flipping the output images.
-r 1 1 1 1	Custom white balance for the four channels (1 red, 1 blue, 2 green) by choosing the individual multiplying factors. Using 1 as factor assures that no white balance will be performed.
-q 0	Sets the Bayer demosaicing algorithm to be bilinear.
-o 0	Sets the output colour profile to be none (no colour management).
-T	Specifies a TIFF image file as the output file type
-K	Subtracts a dark frame from the raw data.

Image Processing using Fiji (ImageJ)

1) Installation: Download the latest stable version (http://fiji.sc/Downloads#Fiji) and then unpack the zip (there is no install).

2) Setup directories: Create an input and an output directory, making sure that there is a RED, GREEN and BLUE subdirectory, and copy the images you want to analyse into the input directory.

3) Execute the script: Execute ImageJ-win64.exe to start Fiji, and from the main menu bar select Plugins->Macros->Edit. Copy the custom script (Appendix 2) into the edit window. On the macro window select Language -> IJ1 Macro and alter the input and output variables to match the input and output directories that you have created. Click on the Run button and the script will process the images showing a log that will say “—PROCESSING COMPLETE—“ when finished.

4) Batch analysis: Return to the Fiji main menu and select Analyze->Set Measurements and ensure that mean grey value and standard deviation value are selected. Go back to the Fiji main menu and selecting Process->Batch->Measure and select your output directory for the relevant colour

channel. It should show a results window detailing all of the cropped images and each ones accompanying data.

ImageJ macro script

```
// NOTE this should work for any image file size, both tiff (16 bit) and jpg (24 bit)

// input and output directories
// NOTE ensure only image files are present in input and output directory contains RED, GREEN and BLUE folders that are empty!

Input = “C:\\??\\??\\”;
output = “C:\\??\\??\\”;

// run in batch mode to speed things up (does not open files etc to the GUI
setBatchMode(true);

// get the file list from the input directory
file = getFileList(input);

// loop the file list and process the function
for (i = 0; i < file.length; i++)
	SplitAndCrop(input, output, file[i]);

setBatchMode(false);

print ("--PROCESSING COMPLETE--");

// this function will open a file, split it into RGB channels,
// crop each channel to a central 9x9 pixel window and the save the crop as a tiff
function SplitAndCrop(input, output, filename) {
//	open the first file
	open(input + filename);
	print ("Opened " + filename);
	selectWindow(filename);
//	select the newely created RGB image (8 bit) and split it into three channels
//	set the scale to pixels
	run("Set Scale...", "distance=0 known=0 pixel=1 unit=pixel");
	print ("Set Scale Done");
//	Identify the height and width and set the centre point to use
	Cwidth = (getWidth()/2)-5;
	print ("Width = " + getWidth() + "; Cwidth = " + Cwidth);
	Cheight = (getHeight()/2)-5;
	print ("Height = " + getHeight() + "; Cheight = " + Cheight);
// identify bit depth (effects the active window names)
	Bdepth = bitDepth();
	print ("Bit depth = " + Bdepth);
//	split the channels
	if (Bdepth == 8) {
		run("RGB Color");
		print ("8 Bit Image Converted");
	}
	run("Split Channels");
	print ("Split Channels Done");

//	select the blue channel image, crop it and save it as tiff
	if (Bdepth == 16) {
		selectWindow("C3-" + filename);
	} else {
		selectWindow(filename + " (blue)");
	}
	makeRectangle(Cwidth, Cheight, 9, 9);
	run("Crop");
	print ("Cropped " + filename + " BLUE");
	saveAs("Tiff", output + "BLUE\\" + filename + "_BLUE.tif");
	print ("Saved " + filename + " BLUE");
	close();
	print ("Closed BLUE Channel");

//	select the green channel image, crop it and save it as tiff
```

```
		if (Bdepth == 16) {
			selectWindow("C2-" + filename);
		} else {
			selectWindow(filename + " (green)");
		}
		makeRectangle(Cwidth, Cheight, 9, 9);
		run("Crop");
		print ("Cropped " + filename + " GREEN");
		saveAs("Tiff", output + "GREEN\\" + filename + "_GREEN.tif");
		print ("Saved " + filename + " GREEN");
		close();
		print ("Closed GREEN Channel");

//		select the red channel image, crop it and save it as tiff
		if (Bdepth == 16) {
			selectWindow("C1-" + filename);
		} else {
			selectWindow(filename + " (red)");
		}
		makeRectangle(Cwidth, Cheight, 9, 9);
		run("Crop");
		print ("Cropped " + filename + " RED");
		saveAs("Tiff", output + "RED\\" + filename + "_RED.tif");
		print ("Saved " + filename + " RED");
		close();
		print ("Closed RED Channel");
}
```

Appendix B – Image pre-processing script

```
// S Gibson-Poole 22/06/2016
// V1 - utility to convert raw images


// run in batch mode to speed things up (does not open files etc to the GUI
setBatchMode(true);

// Check that the tools needed exist
DCRAW = "E:\\SJGP_ImageProcessing\\RawProcessing\\TOOLS\\dcraw.exe";
EXIFTool = "E:\\SJGP_ImageProcessing\\RawProcessing\\TOOLS\\exiftool.exe";
PTLens = "C:\\Program Files\\ePaperPress\\PTLens\\PTLens.exe";
PTLensDir = "C:\\Program Files\\ePaperPress\\PTLens";

// if DCRAW not found go find it
if (File.exists(DCRAW)!=1) {
	DCRAW = File.openDialog("Select the location of DCRAW.");
	if (DCRAW == "") exit;
	print ("DCRAW selected here " + DCRAW);
}

// if EXIFTool not found go find it
if (File.exists(EXIFTool)!=1) {
	EXIFTool = File.openDialog("Select the location of EXIFTool.");
	if (EXIFTool == "") exit;
	print ("EXIFTool selected here " + EXIFTool);
}

// if PTLens not found go find it
if (File.exists(PTLens)!=1) {
	PTLensDir=getDirectory("Select the location of the PTLens program.");
	if (PTLensDir == "") exit;
	print ("PTLens selected here " + PTLensDir);
}

//open PTlens so that the parameters can be checked before processing continous
exec("cmd.exe /c \""+PTLens+"\"");

// ask which way to process
Choice = getBoolean("Select 'Yes' For Visual or 'No' for Linear processing");

// ask if RGB or NIR data
Sensor = getBoolean("Select 'Yes' For RGB data or 'No' for NIR data");

if (Sensor == 1) {
	print("Processing RGB data");
	Sensor = "RGB";
	DarkFramesDir = "E:\\SJGP_ImageProcessing\\RawProcessing\\DarkImages\\RGB\\";
} else{
	print("Processing NIR data");
	Sensor = "NIR";
	DarkFramesDir = "E:\\SJGP_ImageProcessing\\RawProcessing\\DarkImages\\NIR\\";
}

// ask for raw file source directory
RAWDir = getDirectory("Select the location of the raw files to process.");
print("Processing RAW files located here "+RAWDir);

if (RAWDir == "") {
	print ("RAWDir not selected, aborting.");
	exit;
}

// check for existance of directory to copy to and quit if there already
if (Choice == 0) {
	if (File.isDirectory(RAWDir+"LIN\\")==1) {
		print ("LIN Subdirectory already exists! check and remove before trying again.");
//		exit;
	}
	File.makeDirectory(RAWDir+"LIN\\");
```

```
		print("Processing linear data");
		Type = "LIN\\";
}

if (Choice == 1) {
		if (File.isDirectory(RAWDir+"VIS\\")==1) {
			print ("VIS Subdirectory already exists! check and remove before trying again.");
//			exit;
		}
		File.makeDirectory(RAWDir+"VIS\\");
		print("Processing visual data");
		Type = "VIS\\";
}

// ask for georefereced jpg directory
JPGDir = getDirectory("Select the location of the georeferenced JPG files.");
print("Geotagged files are here "+JPGDir);

if (JPGDir == "") {
		print ("JPGDir not selected, aborting.");
		exit;
}

// now we want to get the file list and do a loop processing each in turn
RAWFile = getFileList(RAWDir);
for (i = 0; i < RAWFile.length; i++) {

		//		Only process DNG files
		if (endsWith(RAWFile[i],"DNG")) {
			print ("Processing "+RAWFile[i]);

			// first off get the iso info from the JPG
			iso = exec("cmd.exe /c "+EXIFTool+" -T -iso
"+JPGDir+"IMG"+substring(RAWFile[i],3,(lengthOf(RAWFile[i])-4))+"_geotag.JPG");

			// clean it up as it adds a return statement to the end of the value and is a string
			iso = parseInt(substring(iso,0,lengthOf(iso)-1));

			// make sure it is range with the dark frame images we have
			if (iso==80 || iso==100 || iso==125 || iso==160 || iso==200 || iso==250 || iso==320 || iso==400) {
				print("ISO is __"+iso+"__");
			} else {
				print("ISO is out of range at __"+iso+"__");
				exit;
			}

			// now get and check the shutter speed info from the JPG
			Sspeed = exec("cmd.exe /c "+EXIFTool+" -T -shutterspeed
"+JPGDir+"IMG"+substring(RAWFile[i],3,(lengthOf(RAWFile[i])-4))+"_geotag.JPG");

			// clean it up as it adds a return statement to the end of the value and is a string
			Sspeed = parseInt(substring(Sspeed,2,lengthOf(Sspeed)-1));

			print("Shutter Speed read as __"+Sspeed+"__");

			// set the range to use going for the dark image correction
			if (Sspeed <= 200) {
				Sspeed="200";
			} else if (Sspeed <= 250) {
				Sspeed="250";
			} else if (Sspeed <= 400) {
				Sspeed="320";
			} else if (Sspeed > 400 && Sspeed <= 640) {
				Sspeed="500";
			} else if (Sspeed > 640 && Sspeed <= 2000) {
				Sspeed="1000";
			} else {
				print("Shutter Speed is out of range at __"+Sspeed+"__");
				exit;
			}
			print("Shutter Speed set to "+Sspeed);
```

```
                        // Check dark frame to use
                        DarkFrame = DarkFramesDir+Sensor+"_iso"+iso+"_ss"+Sspeed+".pgm";
                        print("Using dark frame "+DarkFrame);

                        if (File.exists(DarkFrame)!=1) {
                                print("Dark frame "+DarkFrame+" does not exist!");
                                exit;
                        }

                        // take first file and convert using dcraw into the same folder as the dng
                        if (Choice == 0) {
                                exec(DCRAW+" -r 1 1 1 1 -f -o 0 -4 -j -t 0 -T -K "+DarkFrame+"
"+RAWDir+RAWFile[i]);
                        } else {
                                exec(DCRAW+" -w -f -o 1 -H 2 -4 -j -t 0 -T -K "+DarkFrame+" "+RAWDir+RAWFile[i]);
                        }

                        if (File.exists(RAWDir+substring(RAWFile[i],0,(lengthOf(RAWFile[i])-4))+".tiff")==1) {
                                print(RAWDir+substring(RAWFile[i],0,(lengthOf(RAWFile[i])-4))+".tiff created");
                        }

                        // run imagej despecle outputting into the VIS or LIN folder
                        open(RAWDir+substring(RAWFile[i],0,(lengthOf(RAWFile[i])-4))+".tiff");
                        selectWindow(substring(RAWFile[i],0,(lengthOf(RAWFile[i])-4))+".tiff");
                        run("Despeckle");
                        saveAs("Tiff",RAWDir+Type+substring(RAWFile[i],0,(lengthOf(RAWFile[i])-4))+"_ds.tiff");
                        close();

                        // check the file exists
                        if (File.exists(RAWDir+Type+substring(RAWFile[i],0,(lengthOf(RAWFile[i])-4))+"_ds.tiff")==1) {
                                print(RAWDir+Type+substring(RAWFile[i],0,(lengthOf(RAWFile[i])-4))+"_ds.tiff
created");
                        }

                        // run ptlens to correct and clip the image in the vis or lin folder
                        exec("cmd.exe /c cd \""+PTLensDir+"\" & start /wait PTLens -Q
"+RAWDir+Type+substring(RAWFile[i],0,(lengthOf(RAWFile[i])-4))+"_ds.tiff");

                        // rename the file (delete existing file in case this is a re-run)
                        exec("cmd.exe /c del "+RAWDir+Type+substring(RAWFile[i],0,(lengthOf(RAWFile[i])-
4))+"_ds_pt.tiff & ren "+RAWDir+Type+substring(RAWFile[i],0,(lengthOf(RAWFile[i])-4))+"_ds.tiff
"+substring(RAWFile[i],0,(lengthOf(RAWFile[i])-4))+"_ds_pt.tiff");

                        // check that the file exists
                        if (File.exists(RAWDir+Type+substring(RAWFile[i],0,(lengthOf(RAWFile[i])-4))+"_ds_pt.tiff")==1)
{
                                print(RAWDir+Type+substring(RAWFile[i],0,(lengthOf(RAWFile[i])-4))+"_ds_pt.tiff
created");
                        }

                        // run imagej to sharpen the image if VIS
                        if (Choice == 1) {
                                open(RAWDir+Type+substring(RAWFile[i],0,(lengthOf(RAWFile[i])-4))+"_ds_pt.tiff");
                                selectWindow(substring(RAWFile[i],0,(lengthOf(RAWFile[i])-4))+"_ds_pt.tiff");
                                run("Sharpen");
                                saveAs("Tiff",RAWDir+Type+substring(RAWFile[i],0,(lengthOf(RAWFile[i])-
4))+"_ds_pt.tiff");
                                close();

                                // rename the file (delete existing file in case this is a re-run)
                                exec("cmd.exe /c del "+RAWDir+Type+substring(RAWFile[i],0,(lengthOf(RAWFile[i])-
4))+"_ds_pt_sh.tiff & ren "+RAWDir+Type+substring(RAWFile[i],0,(lengthOf(RAWFile[i])-4))+"_ds_pt.tiff
"+substring(RAWFile[i],0,(lengthOf(RAWFile[i])-4))+"_ds_pt_sh.tiff");

                                // check that the file exists
                                if (File.exists(RAWDir+Type+substring(RAWFile[i],0,(lengthOf(RAWFile[i])-
4))+"_ds_pt_sh.tiff")==1) {
                                        print(RAWDir+Type+substring(RAWFile[i],0,(lengthOf(RAWFile[i])-
4))+"_ds_pt_sh.tiff created");
                                }

                                // run exiftool to set the GPS
```

```
                                    exec("cmd.exe /c "+EXIFTool+" -TagsFromFile
"+JPGDir+"IMG"+substring(RAWFile[i],3,(lengthOf(RAWFile[i])-4))+"_geotag.JPG
"+RAWDir+Type+substring(RAWFile[i],0,(lengthOf(RAWFile[i])-4))+"_ds_pt_sh.tiff");
                                    print(RAWDir+Type+substring(RAWFile[i],0,(lengthOf(RAWFile[i])-4))+"_ds_pt_sh.tiff
geotagged with JPG data");

                                    // run exiftool to take information from the CRW
                                    exec("cmd.exe /c "+EXIFTool+" -TagsFromFile
"+RAWDir+substring(RAWFile[i],0,(lengthOf(RAWFile[i])-4))+".tiff
"+RAWDir+Type+substring(RAWFile[i],0,(lengthOf(RAWFile[i])-4))+"_ds_pt_sh.tiff");
                                    print(RAWDir+Type+substring(RAWFile[i],0,(lengthOf(RAWFile[i])-4))+"_ds_pt_sh.tiff
geotagged with RAW data");

                                    // delete the orignal tiff and renamed tiff images
                                    exec("cmd.exe /c del "+RAWDir+Type+substring(RAWFile[i],0,(lengthOf(RAWFile[i])-
4))+"_ds_pt_sh.tiff_original & del "+RAWDir+substring(RAWFile[i],0,(lengthOf(RAWFile[i])-4))+".tiff");
                                } else {
                                    // run exiftool to set the GPS
                                    exec("cmd.exe /c "+EXIFTool+" -TagsFromFile
"+JPGDir+"IMG"+substring(RAWFile[i],3,(lengthOf(RAWFile[i])-4))+"_geotag.JPG
"+RAWDir+Type+substring(RAWFile[i],0,(lengthOf(RAWFile[i])-4))+"_ds_pt.tiff");
                                    print(RAWDir+Type+substring(RAWFile[i],0,(lengthOf(RAWFile[i])-4))+"_ds_pt.tiff
geotagged with JPG data");

                                    // run exiftool to take information from the CRW
                                    exec("cmd.exe /c "+EXIFTool+" -TagsFromFile
"+RAWDir+substring(RAWFile[i],0,(lengthOf(RAWFile[i])-4))+".tiff
"+RAWDir+Type+substring(RAWFile[i],0,(lengthOf(RAWFile[i])-4))+"_ds_pt.tiff");
                                    print(RAWDir+Type+substring(RAWFile[i],0,(lengthOf(RAWFile[i])-4))+"_ds_pt.tiff
geotagged with RAW data");

                                    // delete the orignal tiff and renamed tiff images
                                    exec("cmd.exe /c del "+RAWDir+Type+substring(RAWFile[i],0,(lengthOf(RAWFile[i])-
4))+"_ds_pt.tiff_original & del "+RAWDir+substring(RAWFile[i],0,(lengthOf(RAWFile[i])-4))+".tiff");
                                }
                        }
// select the next file
}
//End Loop

setBatchMode(false);

print ("-- "+Type+" PROCESSING COMPLETE --");
```

Appendix C – Potato disease detection paper

Please see the file ***Appendix_C_PotatoDiseaseDetectionPaper.pdf*** within the supporting documentation CD Rom.

Appendix D – Potato trials analysis paper

Please see the file ***Appendix_D_PotatoTrialsAnylsisPaper.pdf*** within the supporting documentation CD Rom.

Appendix E – SRUC Operations manual and site safety assessment template for commercial UAS operations

Please see the file ***Appendix_E_SRUC-UAS-OM-0001_1.5_20180611.pdf*** (the operations manual) and ***Appendix_E_SRUC-UAS-OM-0002_2.3_20180521.pdf*** (the site safety assessment template) within the supporting documentation CD Rom.

Appendix F – Report on experimental analysis of winter wheat trial plots

Please see the file ***Appendix_F_CauldshielTrialsResults.pdf*** within the supporting documentation CD Rom.

Appendix G – Report on experimental classification of topographical features within a clear-felled forest

Please see the file ***Appendix_G_HarwoodClearfellClassificationReport.pdf*** within the supporting documentation CD Rom.

Appendix H – Urine patch detection paper

Please see the file ***Appendix_H_UrinePatchDetectionPaper.pdf*** within the supporting documentation CD Rom.

(The End)